

**Self-Assembling Peptide Nano-Apatite Hybrid Material for
Dentine Mineralisation**

Sam Alan Whitworth

Submitted in accordance with the requirements for the degree of
Doctor of Philosophy

The University of Leeds

Doctoral Training Centre in Tissue Engineering and Regenerative
Medicine

School of Mechanical Engineering

September 2018

The candidate confirms that the work submitted is their own. The candidate confirms that appropriate credit has been given within the thesis where reference has been made to the work of others.

This copy has been supplied on the understanding that it is copyright material and that no quotation from the thesis may be published without proper acknowledgement

The right of Sam Alan Whitworth to be identified as Author of this work has been asserted by him in accordance with the Copyright, Designs and Patents Act 1988.

Acknowledgements

I would like to thank everyone who has helped me during the course of this thesis. In particular I would like to thank Professor Jennifer Kirkham, Professor David Wood and Dr Robert Philip Wynn Davies for all their supervision, hard work and guidance.

I would like to also thank the Division of Oral Biology and the Institute of Medical and Biological Engineering for all their support, and the EPSRC for funding my work.

I would like to thank my parents Claire Woodman and John Whitworth who have supported me my entire life, you have been a constant source of encouragement and advice which at times was greatly needed.

Finally, I would like to thank my partner Emmanuelle Lemaire who has helped me in more ways than I could have ever hoped. You have been an endless supply of positivity and I cannot thank you enough.

Abstract

Dentine sensitivity continues to be a problem for patients who experience painful symptoms associated with the condition and there is a clear clinical need for the development of new treatments to manage the problem. Currently available treatments often require frequent application or do not produce the required alleviation of symptoms. The aim of this thesis was to establish if self-assembling peptides (SAPs) combined with nanohydroxyapatite seed crystals could be an effective treatment for the occlusion of human dentine tubules and so potentially alleviate the symptoms of dentine sensitivity.

Nanohydroxyapatite (nanoHA) seed crystals were produced via hydrothermal synthesis and characterised using x-ray diffraction, dynamic light scattering, scanning electron microscopy and transmission electron microscopy. This confirmed the presence of highly crystalline rod shaped crystals with a median size of 45 nm (longest axis). A steady state *in vitro* nucleation and crystal growth assay (IVNCG) was used to determine the minimum nanoHA seed crystal density in agarose required to generate a total phosphate mass (indicative of quantity of mineral formed) comparable to that produced by the poly-L-glutamic acid positive control after 5 days exposure to buffers containing calcium and phosphate ions at physiological concentrations, pH and temperature. A transition in crystal morphology and composition, reflecting a shift from an OCP-like towards a HA-like chemistry and appearance, was seen on increasing nanoHA seeding density from 20 $\mu\text{g/mL}$ to 30 $\mu\text{g/mL}$. SAPs (P₁₁₋₁₃ and P₁₁₋₁₄, complementary pair) were then combined with nanoHA seed crystals to produce a novel hybrid material. Its ability to support HA crystal growth was assessed using the IVNCG, without success, due to precipitation of the hybrid material. A novel precipitation assay was developed and used alongside a ¹H NMR study to determine the cause of the observed precipitation. Precipitation was found to be associated with interaction and aggregation of the P₁₁₋₁₃ peptide with nanoHA in the presence of calcium ions at the same concentration as those used in the IVNCG assay, possibly through calcium bridging.

SAP/nanoHA hybrid material and P₁₁₋₄ were applied to human dentine samples and their ability to reduce dentine permeability assessed using a fluid filtration

method after initial application and following 7 days incubation in artificial saliva (AS). Surprisingly, following treatment with the hybrid material, dentine permeability increased after 7 days in AS, possibly due to P₁₁₋₁₃ interaction with the dentine tubule wall (as suggested by the ¹H NMR experiments) resulting in compression of the non-slip layer. In contrast, P₁₁₋₄ treated dentine showed a decrease in permeability after 7 days incubation in AS which was statistically insignificant compared to the positive control (I Bond universal, Kulzer)($p>0.05$). The reduction in fluid flow was attributed to the formation of a 10 μm thick layer of crystals, believed to be HA, present 20 μm down the tubule and seen in the SEM analysis.

In conclusion the P_{11-13/14} self-assembling peptides combined with nanoHA treatment produced no evidence of human dentine tubule occlusion and actually resulted in an *increase* in fluid flow through dentine. P₁₁₋₄ treatment, in contrast, resulted in reduced dentine permeability and should be considered a candidate for further development as a dentine sensitivity treatment.

Table of Contents

Acknowledgements	i
Abstract	ii
Table of Contents	iv
List of Figures	ix
List of Tables	xx
List of Abbreviations	xxii
Chapter 1 - Introduction	1
1.1 General Introduction	1
Chapter 2 - Literature Review	3
2.1 Anatomy and Development of the Dental Tissues.....	3
2.1.1 Tooth Anatomy	3
2.1.2 Enamel	4
2.1.3 Dentine.....	5
2.1.4 Dental Pulp.....	6
2.2 Tooth Development	6
2.2.1 Amelogenesis.....	8
2.2.2 Dentinogenesis	10
2.3 Hydroxyapatite	12
2.3.1 Biological Hydroxyapatite	13
2.3.2 Synthesis Methods.....	14
2.3.3 Characterisation Techniques.....	16
2.4 Mechanisms of Mineralisation	18
2.4.1 Nucleation	20
2.4.2 Crystal Growth	22
2.4.3 Mineralisation in Biological Systems	23
2.5 Clinical Challenge of Dentine Sensitivity	25
2.5.1 Definition, Causes and Prevalence of Dentine Sensitivity	25

2.5.2	Mechanism of Dentine Sensitivity	27
2.5.3	Dentine Sensitivity Treatments.....	28
2.5.4	Nerve Desensitisation Treatments	29
2.5.5	Occlusion Treatments	30
2.5.6	“At Home” Occlusion Treatments	30
2.5.7	“In Clinic” Occlusion Treatments	32
2.6	Measurement of Dentine Permeability.....	33
2.6.1	<i>In Vitro</i> Techniques	33
2.6.2	Clinical Trials.....	34
2.7	Inspiration from Nature	35
2.8	Biomimetics	36
2.9	Peptide Biomimetics	36
2.10	Self-Assembling Peptides.....	40
2.11	Concluding Remarks	44
2.12	Project aim	46
Chapter 3 – Synthesis and Characterisation of Nano-sized Hydroxyapatite Seed Crystals.....		47
3.1	Introduction.....	48
3.2	Methods.....	50
3.2.1	Hydrothermal Synthesis of Nanohydroxyapatite	50
3.2.2	Powder Characterisation	51
3.3	Results	53
3.3.1	Hydrothermal Synthesis of NanoHA Batches.....	53
3.3.2	X-Ray Diffraction of NanoHA Batches.....	53
3.3.3	Scanning Electron Microscopy of NanoHA Batches.....	56
3.3.4	Dynamic Light Scattering Analysis of NanoHA Batches.....	57
3.3.5	Transmission Electron Microscopy of NanoHA Batches	58
3.4	Discussion	63
3.5	Conclusion.....	69
Chapter 4 - <i>In Vitro</i> Nucleation and Crystal Growth Assay Validation with Assessment of the Effect of Nanohydroxyapatite Seeding.		70
4.1	Introduction.....	71
4.2	Methods.....	79
4.2.1	<i>In Vitro</i> Nucleation and Crystal Growth Assay (IVNCG) Validation	79

4.2.2	Determination of Phosphate Content in Agarose Controls Recovered from IVNCG After 5 Days.....	80
4.2.3	IVNCG Statistical Analysis	81
4.2.4	Effect of IVNCG Run Time on Buffer Calcium and Phosphate Content	82
4.2.5	Determination of Buffer Phosphate Concentration	82
4.2.6	Determination of Buffer Calcium Concentration	83
4.2.7	Determination of Minimum NanoHA Seeding Density Required to Produce Increased HA Formation Compared to Controls Using IVNCG.....	83
4.2.8	Isolation and Analysis of Mineral Formed in NanoHA Seeded Agarose After 5 Days in IVNCG	85
4.2.9	Effect of Shortening the IVNCG Run Duration with Respect to Crystal Growth	86
4.2.10	Comparison of NanoHA Synthesised in this Work to Other Synthetic NanoHA with Respect to Crystal Growth in IVNCG	86
4.3	Results	87
4.3.1	Validation of <i>In Vitro</i> Nucleation and Crystal Growth Assay (IVNCG)	87
4.3.2	Effect of IVNCG Run Time on the Calcium and Phosphate Concentrations of the Reservoir Buffers	90
4.3.3	Determination of Minimum NanoHA Seeding Density in Agarose Required to Produce Increased HA Formation Compared to Controls Using IVNCG.....	92
4.3.4	Isolation and Analysis of Mineral Formed in NanoHA Seeded Agarose after 5 Days in IVNCG	95
4.3.5	Effect of Shortening the Duration of the IVNCG Run with Respect to Crystal Growth	100
4.3.6	Comparison of Synthesised NanoHA Produced in this Work to Other Synthetic NanoHA Using the IVNCG over a 4-Day Test Period.....	101
4.4	Discussion	103
4.5	Conclusion.....	115
Chapter 5 – IVNCG Assay Assessment and Optimisation of Self-Assembling Peptide/Nano-Apatite Hybrid Material With Respect to its Mineral Forming Potential.		116
5.1	Introduction.....	117
5.2	Methods.....	123

5.2.1	Assessment of Mineralisation Potential of P _{11-13/14} SAP Seeded with 30 µg/mL NanoHA Using the IVNCG Assay...	123
5.2.2	Effect of Decreasing the NanoHA Seeding Density and IVNCG Assay Run Length on Quantity of Mineral Formed by the Hybrid Material	124
5.2.3	Effect of Using a Benzoylated Dialysis Membrane on Quantity of Mineral Formed In The Presence of the Hybrid Material Using the IVNCG Assay	124
5.2.4	Investigation of Peptide Precipitation	125
5.2.5	Quantitative Precipitation Study Comparing IVNCG to Artificial Saliva Calcium and Phosphate-Containing Buffers with Respect to Hybrid Material Precipitation.	127
5.2.6	The Use of ¹ H NMR Analysis to Probe Peptide Aggregation with Respect to IVNCG NanoHA, Ionic Calcium and Ionic Phosphate Concentrations.	128
5.3	Results	130
5.3.1	Assessment of Mineralisation Potential of P _{11-13/14} SAP Seeded with 30 µg/mL NanoHA (the “Hybrid Material”) Using the IVNCG Assay	130
5.3.2	Effect of Decreasing the NanoHA Seeding Density of P _{11-13/14} and Experiment Duration on Quantity of Mineral Formed Using the IVNCG Assay	132
5.3.3	Effect of Using a Benzoylated Membrane on P _{11-13/14} on Quantity of Mineral Formed Using the IVNCG Assay.....	133
5.3.4	Precipitation Studies	134
5.3.5	Quantitative Precipitation Study Comparing IVNCG to Artificial Saliva (AS) Calcium and Phosphate Concentrations with Respect to Hybrid Material Precipitation.	138
5.3.6	¹ H NMR Analysis of Peptide Monomers Interaction with NanoHA Particles in Ionic Calcium Environment.....	144
5.4	Discussion	146
5.5	Conclusion.....	152
Chapter 6 – Application of Self-Assembling Peptide/Nano-Apatite Hybrid Material to Dentine		153
6.1	Introduction.....	154
6.2	Methods.....	158
6.2.1	Dentine Disk Production.....	158
6.2.2	Fluid Filtration Device.....	159
6.2.3	Fluid Filtration Validation.....	161

6.2.4	Fluid Filtration Assessment of the Hybrid Material's Tubule Occlusion Ability After 7 Days in Artificial Saliva.	162
6.2.5	Scanning Electron Microscopy Imaging Assessment of 7-Day Fluid Filtration Study Treatment Groups	168
6.3	Results	169
6.3.1	Dentine Disk Production.....	169
6.3.2	Fluid Filtration System Validation	169
6.3.3	Effect of Application of Hybrid Material to Dentine Disks on Dentine Permeability After Initial Application and after 7 Days Incubation in Artificial Saliva Solution.....	170
6.3.4	Effect of Various Treatments on the Ultrastructural Appearance of Dentine.....	175
6.4	Discussion	179
6.5	Conclusion.....	187
Chapter 7 - General Discussion.....		188
7.1	Development of an Optimised Hybrid Material for Dentine Tubule Occlusion.....	193
7.2	Suitability of SAPs for Use as Dentine Occlusion Treatments.....	198
Chapter 8 – Summary and Conclusion		207
8.1	Summary	207
8.2	Future work	209
8.3	Conclusion.....	210
Chapter 9 – Bibliography		211

List of Figures

- Figure 2-1 Schematic showing the main tooth tissues modified from Blausen.com (2014).4
- Figure 2-2 Schematic of tooth development describing the stages of tooth development. Thickening stage occurs through oral epithelium growth into the mesenchyme. Mesenchyme then thickens in response to ingrowing epithelium resulting in the bud stage. As the epithelium grows deeper into the mesenchyme it wraps around the condensing mesenchyme producing the cap stage. The epithelium continues to grow into the mesenchyme producing a bell shape of condensed mesenchyme, differentiation of the epithelium cell occurs at the point of contact between the epithelium and condensed mesenchyme producing a layer of odontoblasts on the condensed mesenchyme and a layer of ameloblasts above the odontoblasts which go on to produce the enamel and dentine respectively. Image reproduced with permission from Tucker & Sharpe (2004).8
- Figure 2-3 Schematic representation of hydroxyapatite structure showing sites of hydroxyl, oxygen, calcium and phosphorus in the hydroxyapatite structure. Image reproduced with permission from Brunton *et al.* (2013). (<https://creativecommons.org/licenses/by/3.0/>)12
- Figure 2-4 Schematic describing the nucleation of a crystal phase from a saturated solution with respect to the crystal phase. The formation of a crystal with a radius below the critical cluster size is energetically unfavourable and the equilibrium will be in favour of ions. A small number will grow above the critical cluster radius resulting in a stable crystal with respect to dissolution. Size of arrow indicative of favoured equilibrium position.21
- Figure 2-5 Schematic diagram of the substrate surface showing the possible active sites for crystal growth. In order of largest to smallest binding energy: terrace vacancy, step vacancy, kink site, step side, terrace site (Davey & Garside, 2000a).23
- Figure 2-6 Smear layer covered human dentine. SL is the smear layer on the surface while SP is the penetration of the smear layer into the tubule. Image reproduced with permission from Pashley (2013). .27
- Figure 2-7 The 2 dentine sensitivity treatment strategies, nerve stabilisation through the use of numbing agents (Red) which diffuse down the tubule and prevent stimulation of the nerves. Tubule occlusion blocks the dentine tubule which prevents the change in fluid flow within the tubule due to dentine surface stimuli (Blue).29

Figure 2-8 - Schematic of proposed treatment mechanism of D8DS. Exposed and open dentine tubules were treated with E8DS peptide. NanoHA then brushed onto surface which would interact with the peptide not only on the surface but within the dentine tubules. Schematic from Wang <i>et al.</i> (2014).....	39
Figure 2-9 TEM images of nanoHA crystals used in Wang <i>et al.</i> (2014). Crystals are poorly resolved and look larger than the 20nm stated by the author. Image modified from Wang <i>et al.</i> (2014).....	40
Figure 2-10 Schematic of the hierarchical self-assembly of anti-parallel β-sheet forming peptides as a function of peptide monomer concentration. At low concentrations below the critical concentration (C^*) peptide monomers exist in solution. As the concentration increases above C^* the monomers interact to form β-sheet tapes which can then go on to interact to form ribbons, then fibrils and finally fibres with respect to increasing peptide monomer concentration. Image modified from Aggeli <i>et al.</i> (2001) Copyright (2001) National Academy of Sciences.	42
Figure 2-11 P₁₁₋₄ amino acid sequence protonation states at physiological pH (7.4). The glutamic acid residues are deprotonated (blue) producing a negative charge (-3) and the arginine side chain is protonated (red) producing a positive charged (+1) resulting in an overall charge per molecule of P₁₁₋₄ of -2. Hydrophobic side chains tryptophan and phenylalanine (lilac) provide sites for π-π interactions for stabilisation of the tape-tape interaction present in the ribbon level of β-sheet hierarchy. The peptide backbone and glutamine residues (black) form complementary hydrogen bonding between peptide molecules.	44
Figure 3-1 Graph showing XRD patterns produced from batch 1, 2, 3 and Sigma nanoparticles. Dashed line represent common peaks between samples (average standard deviation between peaks 0.02 2θ). Batch 1, 3 and Sigma all confirmed a hydroxyapatite crystal structure while batch 2 confirmed a hydrated form of hydroxyapatite.	55
Figure 3-2 SEM images of powders from A) batch 1, B) batch 2 and C) batch 3 all showing densely packed rod shaped particles. In contrast, D) Sigma powder showed spherical particles. Density of particles prevented measurement although morphology was clearly visible.....	56
Figure 3-3 Dynamic light scattering (DLS) data showing size distribution of particles as a function of the % of total particle number for batches 1, 2, 3 and Sigma powders. DLS measurements confirmed the bulk of the particles were in the 30-130 nm size range.....	58
Figure 3-4 TEM image showing rod shaped particles present in batch 1 powder. Images confirmed a range of particle sizes present within the sample, with the majority below 100 nm in length with respect to the longest axis. Scale bar 100 nm.	59

Figure 3-5 TEM image showing rod shaped particles present in batch 2 powder. Images confirmed a range of particle sizes present within the sample with the majority below 100 nm in length with respect to the longest axis. Scale bar 100 nm.59

Figure 3-6 TEM image showing rod shaped particles present in batch 3 powder. Images confirmed a range of particle sizes present within the sample with the majority below 100 nm in length with respect to the longest axis. Scale bar 100 nm.60

Figure 3-7 TEM image showing spherical shaped particles present in the Sigma powder. Images confirmed a range of particle sizes present within the sample with the majority below 100 nm in length with respect to the spherical particle diameter. Scale bar 100 nm.....60

Figure 3-8 Size distributions produced from TEM measurement data for batches 1, 2, 3 and Sigma particles. Measured length was of the longest axis for rods, or diameter for spheres. All synthesised batches and Sigma particles produced a similar particle size distribution.61

Figure 4-1 – Schematic of sample chamber described by De Jong *et al.* (1978), comprising of a polyacrylamide film with lead-containing solution on one side and phosphate-containing solution on the opposite side. The lead and phosphate ions would diffuse into the polyacrylamide film sample. Precipitation formed within the polyacrylamide film once the saturation limit with respect to lead phosphate was reached. Image modified from De Jong *et al.* (1978).73

Figure 4-2 – Schematic of sample holder used by Hunter and Goldberg (1993). Calcium-containing buffer would flow past one side of the agarose sample and phosphate-containing buffer would flow past the opposite side. The calcium and phosphate ions would diffuse into the agarose sample with the mass of mineral formed dependent on the macromolecules seeded within the agarose samples. Image modified from Hunter & Goldberg (1993) Copyright (1993) National Academy of Sciences.76

Figure 4-3 – Schematic representation of the IVNCG assay showing the position of the buffer compartments, A and D, Sample holder, B, and sample wells, C. Image modified from Sayed (2013).80

Figure 4-4 Typical calibration curve showing absorbance at 820 nm against phosphate concentration. The line of best fit showed a linear response with a R^2 value of 0.999. Error bars show 2x standard deviation, n=3.87

Figure 4-5 Bar histograms showing amounts of phosphate determined in positive (poly-L-glutamate in agarose, n=16) and negative (agarose, n=20) controls after 4 separate 5-day runs in the IVNCG. Greater amounts of phosphate were present in the positive controls compared with the negative controls on each occasion. Error bars show 2x standard deviation. * confirms statistically significant difference using independent t-test significance level of at least $p < 0.05$88

Figure 4-6 A) Scatter graph showing the phosphate concentration in phosphate-containing reservoir buffer (red) and calcium-containing reservoir buffer (black) during the IVNCG 5-day run period. B) Scatter graph showing the calcium concentration in the phosphate-containing reservoir buffer (red) and calcium-containing reservoir buffer (black) during the 5-day run period. Error bars show standard deviation. The concentration of phosphate in the phosphate-containing buffer and the concentration of calcium in the calcium-containing buffer remained reasonably constant over time, confirming the IVNCG system was in steady state over 5 days (n=3).91

Figure 4-7 Calibration curve showing absorbance at 820 nm against phosphate concentration up to 160 μM . The line of best fit shows a linear response with a R^2 value of 0.999 confirming linearity. Error bars show 2x standard deviation, n=3.92

Figure 4-8 Bar chart showing phosphate mass in samples of increasing nanoHA seeding density (n=3) after 5 days in IVNCG compared with positive and negative controls. Positive control was agarose with 10 $\mu\text{g}/\text{mL}$ poly-L-glutamic acid, negative control was agarose alone. Error bars show 2x standard deviation, N/S= no significant difference, *= significant difference ($p < 0.05$). The minimum seeding density of nanoHA required to produce a statistically significant increase in phosphate mass compared to the positive control was 30 $\mu\text{g}/\text{mL}$. Added phosphate in form of nanoHA 5.66 μg of phosphate per 10 μg of nanoHA added.93

Figure 4-9 Bar chart showing quantity of phosphate produced as a function of nanoHA seeding density after 5 days in the IVNCG. All 3 runs showed that a 30 $\mu\text{g}/\text{mL}$ nanoHA seeding density was the minimal seeding density required to produce statistically significant increase in phosphate mass compared to the 10 $\mu\text{g}/\text{mL}$ poly-L-glutamic in 1% agarose positive control (*= $p < 0.05$). Added Phosphate in form of nanoHA 5.66 μg of phosphate per 10 $\mu\text{g}/\text{mL}$ of nanoHA added. Error bars show 2x standard deviation. Samples n=10, controls n=3.95

Figure 4-10 Images of mineral precipitate formed within agarose gels and retrieved after 5 days in the IVNCG assay. A) Positive control (1% agarose with poly-L-glutamate at 10 µg/mL); B) Negative control (1% agarose only); C) 10 µg/mL nanoHA in 1% agarose; D) 20 µg/mL nanoHA in 1% agarose; E) 30 µg/mL nanoHA in 1% agarose. Images taken on the Bio-Rad ChemDoc™ MP imaging system using the Coomassie Blue standard protocol available on the ChemDoc™ software. Top row images show side-on view of the samples, bottom row shows gel from the perspective of the buffer interface with respect to position in the IVNCG assay. A change in precipitate appearance is visible when nanoHA seeding density increased from 20 µg/mL nanoHA (sparse regions of precipitate) to 30 µg/mL nanoHA (dense band of precipitate was visible).....96

Figure 4-11 SEM images of mineral recovered from samples retrieved from the IVNCG assay after a 5-day run. A) and B) Positive control 10 µg/mL poly-L-glutamic acid in 1% agarose C) and D) negative control 1% agarose, E) and F) 10 µg/mL nanoHA G) and H) 20 µg/mL nanoHA, I) and J) 30 µg/mL nanoHA seeded agarose. Changes in crystal morphology were seen when nanoHA seeding density was increased from 20 µg/mL to 30 µg/mL, from large (300-600 µm), single spherical aggregates to smaller (7-20 µm) plate-shaped individual crystals (arrowed) respectively. The crystals retrieved from samples containing 30 µg/mL nanoHA had a similar appearance to the positive control while the crystals retrieved from samples containing 10 and 20 µg/mL nanoHA looked similar to those seen in the negative control.....99

Figure 4-12 Bar chart showing phosphate mass produced in samples with different nanoHA seeding density after 4 days in the IVNCG assay, error bars show 2x standard deviation. All phosphate amounts detected in nanoHA seeded agarose samples were significantly lower compared to the positive control (p<0.05) except for the sample seeded at 30 µg/mL nanoHA in run 2 which contained a significantly increased level of phosphate (p<0.05). Added phosphate in form of nanoHA 5.66 µg of phosphate per 10 µg of nanoHA added.101

Figure 4-13 Bar chart showing effect of nanoparticle source (“small HA” from Sayed’s work, combined batches 1 and 3 nanoHA produced in this thesis and nanoHA purchased from Sigma) at varying seeding densities against phosphate mass in the samples after 4-day IVNCG assay runs (n=3). Red shows Poly-glutamic acid in agarose seeded with 30 µg/mL batch 1 3 nanoHA seeding density. Green bars show phosphate in samples with a 5 µg/mL nanoHA seeding density, orange bars show 10 µg/mL seeding density and blue bars how 30 µg/mL seeding density. Almost all samples contained significantly lower amounts of phosphate compared with the positive control. The exceptions were samples containing 30 µg/mL nanoHA produced in this thesis by combining batches 1 and 3. No significant differences were seen between these and the positive control (significance value $p < 0.05$). Added phosphate in form of nanoHA 5.66 µg of phosphate per 10 µg of nanoHA added. Error bars show 2x standard deviation.102

Figure 4-14 – Graph showing the model diffusion properties of the IVNCG system assuming a static system. The model holds only prior to the formation of mineral. Dashed lines indicate region where mineralisation is possible.....108

Figure 4-15 SEM micrographs of OCP coating reproduced from Lin *et al* (2015)114

Figure 5-1 Amino acid sequence of peptide P₁₁₋₄ with one letter amino acid code labels. At pH 7.4 the 3 glutamic acid residues (E) of P₁₁₋₄ are deprotonated ($pK_a < 4.25$, see section 2.10) and the Arginine (R) is protonated ($pK_a = 12.5$) producing an overall negative charge of 2-. Stereochemistry shown through dashed line representing behind the peptide backbone while thick black line represents in front of the peptide backbone.118

Figure 5-2 – Amino acid sequence of complementary peptides P₁₁₋₁₃ and P₁₁₋₁₄ with one letter amino acid code labels. At pH 7.4 the glutamic acid residues (E) of P₁₁₋₁₃ are deprotonated ($pK_a < 4.25$ see section 2.10) producing an overall negative charge of 6-. At pH 7.4 the ornithine residues (O) are protonated ($pK_a = 10.76$) producing an overall positive charge of 4+. Stereochemistry shown through dashed line representing behind the peptide backbone while thick black line represents in front of the peptide backbone.....119

Figure 5-3 - Schematic of the non-covalent interactions between one molecule of P₁₁₋₁₃ and one molecule of P₁₁₋₁₄ when in anti-parallel β-sheet formation under physiological conditions (pH 7.4, 150 mM NaCl). Lilac residues show position of charged groups present at pH 7.4. Blue residues show positions of hydrophobic residues at pH 7.4. Red atoms show position where hydrogen bonding occurs between peptide backbones. For simplicity only 2 units are shown although in reality a continuous repeating dimeric unit of P₁₁₋₁₃ and P₁₁₋₁₄ is present when critical concentration is reached.....121

Figure 5-4 Bar chart showing the effect of changing SAP concentration on the amount of phosphate produced in the IVNCG assay. P_{11-13/14} samples were seeded with 30 µg/mL nanoHA. One sample at 20 mM was not seeded with 30 µg/mL nanoHA to act as a control. Control samples were 1 % agarose with 10 µg/mL poly-L-glutamic acid (positive), 1% agarose (negative), 1 % agarose seeded with 30 µg/mL nanoHA (nanoHA positive control) and 20 mM P₁₁₋₄ (peptide positive control). * = p < 0.05 . Error bars show 2x standard deviation.131

Figure 5-5 Bar chart showing effect of varying peptide concentration in hybrid material on phosphate mass produced in IVNCG assay when seeded with 10 µg/mL nanoHA over 4 days. The phosphate masses produced confirmed a statistically significant lack of phosphate mass accumulation for all the P_{11-13/14} samples compared with the positive control (poly-L-glutamic acid). Error bars show 2x standard deviation.133

Figure 5-6 Bar chart showing varying hybrid material concentration IVNCG assay using benzoylated dialysis membrane. Hybrid material was seeded with 10 µg/mL nanoHA. Error bars show 2x standard deviation.134

Figure 5-7 – Daily photographs taken during precipitation assay showing effect of peptide concentration on rate and severity of precipitation under different buffer conditions. The white opaque appearance was indicative of peptide precipitation. Addition of calcium-containing buffer caused precipitation to occur at the fastest rate with samples containing the lower concentrations of peptide precipitating first. Addition of phosphate-containing buffer also resulted in precipitation but this was slower and less severe compared to the effects of the calcium-containing buffer. The addition of nanoHA also increased the severity and rate of precipitation compared to the unseeded P_{11-13/14} 20 mM control samples.136

Figure 5-8 Daily photographs taken during precipitation assay showing effect of IVNCG buffer concentration on rate and severity of precipitation in the hybrid material. White opaque appearance due to precipitation of peptide was visible in the calcium-containing buffer samples on day 5. Decrease in buffer calcium concentration resulted in a decrease in the rate and severity of precipitation over the 5-day test period.138

- Figure 5-9 Daily photographs showing severity of peptide precipitation under IVNCG and AS buffer conditions. Dark grey areas indicate peptide precipitation. All the P₁₁₋₄ samples maintain a slightly opaque grey throughout the 7-day experiment. The P_{11-13/14} samples under AS buffer conditions remained unchanged over the 7-day test period. The P_{11-13/14} under IVNCG calcium-containing buffer conditions increase in grey value as the experiment progresses with the nanoHA seeded sample producing the darkest grey due to the significant precipitation produced. Full 7-day results see appendix 1.3.140**
- Figure 5-10 Bar chart showing turbidity measurements of precipitation assay using 860 nm absorbance over the 7-day test period with buffer containing IVNCG and AS calcium ion concentrations. AS calcium-containing buffer samples remain nearly constant over time. The P_{11-13/14} samples with IVNCG calcium-containing buffer show a large increase in turbidity around day 6/7 corresponding to the development of opaque samples observed.141**
- Figure 5-11 Bar Chart showing the turbidity measurements of precipitation assay using 860 nm absorbance over the 7-day test period with buffer containing IVNCG and AS phosphate ion concentrations.142**
- Figure 5-12 Bar chart showing turbidity measurements of precipitation assay using 860 nm absorbance over the 7-day test period buffer containing IVNCG and AS phosphate/calcium ion concentrations.144**
- Figure 6-1 Pashley (1984) dentine disk split chamber device, test area determined by rubber “O” rings (black) are forced against dentine disk through tightening of external sample holder (not pictured).155**
- Figure 6-2 Schematic of the fluid filtration device developed with pressurised vessel to allow post-treatment fluid filtration measurements. Image reproduced with permission from Pashley & Galloway (1985).....156**
- Figure 6-3 Picture of a molar tooth cast into holder prior to cutting. Tooth was positioned to ensure cut was as perpendicular to the long axis of the tooth (root to crown) as possible.159**
- Figure 6-4 Photograph of dentine fluid filtration device based on the work of Pashley (1984). 1) Micro syringe 2) Inlet pressure regulator 3) Test pressure regulator 4) Purge pressure tap 5) Test pressure tap 6) Pressure evacuation tap 7) Pressure vessel 8) Pressure vessel pressure gauge 9) Glass capillary 10) Sample holder 11) Buffer reservoir A) 3 way tap B) 3 way tap with on/off tap.....160**

- Figure 6-5 Schematic of dentine fluid filtration device illustrated above. Black lines indicate gas system while grey lines indicate fluid system. Pressure is produced using nitrogen and regulated down to a purge pressure of 15 PSI or test pressure of 1 PSI. PBS is stored in pressure vessel and travels through the system and exits through the dentine sample (yellow rectangle in sample holder). The movement of the bubble within the glass capillary is used to record the fluid flow over the 5-minute test period.....160**
- Figure 6-6 Schematic of sample holder assembly cross-section showing the dentine disk “sandwiched” between the 2 PTFE washers via the rubber “O” rings. Fluid flows through the inlet, through the dentine disk and then out of the outlet. Speed of fluid flow is dependent on the permeability of dentine disk and pressure of fluid (of which pressure is held constant).161**
- Figure 6-7 Validation of fluid filtration device. Graph shows mean % reduction in fluid flow through dentine after application of positive control treatment (oxalic acid 5%) and negative control treatment (PBS) compared to the initial measurement (n=10). Statistical analysis using an independent t-test confirmed significant decrease in fluid flow in positive control compared to negative control. Error bars show 2x standard deviation. * Statistically significant at least $p < 0.05$170**
- Figure 6-8 Bar chart showing mean % reduction in fluid flow (dentine permeability) compared to fluid flow immediately after treatment application. A one-way Anova Test with *post hoc* Bonferroni correction showed that after initial application, there was no significant difference between the negative control (20 mM HEPES and 30 mM KCl), 20 mM P₁₁₋₄ and 30 µg/mL nanoHA treatment groups. The P_{11-13/14}, P_{11-13/14} seeded with 30 µg/mL nanoHA and iBond treatments were significantly more effective at decreasing fluid flow after initial application compared with the negative control and there was no significant difference between these 3 groups. Error bars show 2x standard deviation. * confirms statistically significant difference using one-way ANOVA Bonferroni test significance level of at least $p < 0.05$ (n=10).171**

Figure 6-9 Bar chart showing mean % reduction in fluid flow (dentine permeability) and standard deviation following a range of treatments and after 7 days incubation in artificial saliva. The 20 mM P_{11-13/14}, 20 mM P_{11-13/14} seeded with 30 µg/mL nanoHA and the 30 µg/mL nanoHA treatments (orange) were not considered due to their very high variability. After 7 days in AS solution there was a significant difference between the negative control and the 20 mM P₁₁₋₄ and iBond treatment groups. There was no significant difference between the P₁₁₋₄ and iBond treatments after 7 days in AS solution. Error bars show 2x standard deviation. * confirms statistically significant difference using one-way ANOVA Bonferroni test significance level of at least p<0.05 (n=10 unless stated different on graph).173

Figure 6-10 Bar chart showing mean % reduction in fluid flow (dentine permeability) immediately after treatment application and after 7 days in AS solution. The 20 mM P_{11-13/14}, 20 mM P_{11-13/14} seeded with 30 µg/mL nanoHA and the 30 µg/mL treatment groups all produced significant increase in mean % fluid flow after 7 days in AS solution. The 20 mM P₁₁₋₄ treatment group resulted in a significantly greater reduction in mean % fluid flow after 7 days in AS solution while the negative control and iBond treatments produced no significant change after incubation in AS solution. Error bars show 2x standard deviation. * confirms statistically significant difference using one-way ANOVA Bonferroni test significance level of at least p<0.05. (n=10 unless stated different on graph).174

Figure 6-11 Scanning electron micrographs of dentine surfaces of samples taken from different treatment groups after 7 days in AS solution. A) Negative control (PBS) showed no deposits with open tubules. B) nanoHA control showed no differences compared to negative control. C) P₁₁₋₄ produced no differences compared to negative control. D) iBond control produced a thick layer on the surface of the dentine with other areas showing resin filled tubules. E) P_{11-13/14} showed no differences compared to negative control. F) P_{11-13/14} with 30 µg/mL nanoHA showed no differences compared to negative control.....176

Figure 6-12 Scanning electron microscopy images of dentine tubules in samples from different treatment groups after 7 days in AS solution. A) Negative control of PBS treated dentine showed no deposits with open tubules. B) nanoHA treated dentine showed no obvious differences compared to negative control. C) P₁₁₋₄ treated dentine showed deposits 20 µm down the tubules with a deposit thickness of 20 µm, see orange arrows. D) iBond treated samples showed a thick layer of material on the surface of the dentine, see white arrows, although very little penetration is visible down the tubules. E) P_{11-13/14} treated samples showed no differences compared to negative control. F) P_{11-13/14} with 30 µg/mL nanoHA treated samples showed no differences compared to negative control..177

Figure 6-13 High magnification SEM micrograph showing the deposits associated with P₁₁₋₄ treatment of dentine disks after 7 days in artificial saliva. These deposits may have been the cause of the observed reduction in dentine permeability. These deposits localised to the test area approximately 20 µm away from the surface and were approximately 20 µm in thickness (deposit depth approximately 40 µm into dentine tubule at deepest point).....178

Figure 7-1 Schematic describing the hypothesised nanoHA seeding density dependent transition from what is believed to be OCP (this could be tested using XRD), at 20 µg/mL or below nanoHA seeding density to HA, when seeded at 30 µg/mL or above after 5 days in IVNCG assay. At both nanoHA seeding densities the sample well is undersaturated with respect to HA causing crystal seed dissolution. When nanoHA seeding is below 20 µg/mL, all the seed crystals dissolve and then recrystallise when calcium and phosphate ions from buffer reservoir diffuse into the sample well forming large crystal aggregates of what we believe to be OCP, see SEM image A) (scale bar 200 µm). When nanoHA seeding is 30 µg/mL or above, nanoHA seeds dissolve but some remain which then go on to grow, producing a large number of what we believe to be small HA crystals as seen in the SEM image, (scale bar 10 µm). Schematic not to scale.196

Figure 7-2 Schematic cross section of dentine tubule (not to scale) depicting the hypothesised decrease in non-slip length (dark blue) when hydrophobic SAP layer (magenta) assembles on tubule wall. The increase in diameter of D1 to D2 results in an increase in fluid not under non-slip condition (light blue) which, when under laminar pressure, would result in increased fluid flow.199

Figure 7-3 SEM images of A) the control dentine disks (after preparation, cleaning and without application of any agents); B) dentine disks treated with ACC toothpaste and C) dentine disks treated with P₁₁₋₄ gel product. Image reproduced with permission from Schlee *et al.* (2017).204

List of tables

Table 3-1 Table showing which reference samples matched the synthesised and Sigma powder samples. Batches 1, 3 and Sigma matched hydroxyapatite references while batch 2 matched a calcium deficient hydroxyapatite	54
Table 3-2 Calculated Ca/P molar ratios obtained from EDS data. Powders from synthesised batches 1, 3 and Sigma produced Ca/P molar ratios characteristic of stoichiometric hydroxyapatite (1.67) when the $\pm 3\%$ error in EDS measurements was taken into account (Ca/P error = ± 0.05). The synthesised batch 2 produced a calcium deficient Ca/P ratio.	57
Table 3-3 Table summarising median and interquartile range calculated from TEM measurement data for particles from batches 1, 2, 3 and Sigma samples.....	62
Table 3-4 Table summarising information provided by HA characterisation techniques used in this work with the limitations of each method.	66
Table 3-5 Table showing TEM and DLS nanoparticle size distribution compared with previously reported nanoparticle size following synthesis using the Earl <i>et al.</i> (2007) hydrothermal method.	67
Table 4-1 Output from Bonferroni statistical test carried out on the 4 separate IVNCG validation runs comparing the positive and negative controls. Statistically significant differences were found between the amounts of phosphate measured in the positive controls across the 4 runs. Statistically significant differences were also found between the amounts of phosphate measured across the negative control runs. SD shows significant difference while N/A shows no significant difference, significance level = 0.05.....	89
Table 4-2 Table showing Ca/P molar ratio of isolated crystals produced in different samples in the IVNCG after 5 days, determined through EDS analysis. The analyses suggest that crystals produced in the negative control, 10 and 20 $\mu\text{g}/\text{mL}$ nanoHA seeded samples were of similar Ca and P composition to OCP. The 30 $\mu\text{g}/\text{mL}$ nanoHA sample produced a Ca/P ratio similar to hydroxyapatite while the positive control Ca/P ratio suggested a calcium deficient hydroxyapatite.	98
Table 4-3 Table showing comparison of approximate phosphate masses produced during <i>in vitro</i> mineralisation studies normalised to $\mu\text{g}/\text{mL}$. The 70% values in brackets show expected phosphate concentrations when the decrease in surface area of sample in contact with calcium-containing and phosphate-containing buffer is taken into account due to the smaller sample wells used in the IVNCG assay.	106

Table 5-1 Composition of samples investigated using ¹H NMR analysis to determine if peptide material was assembling on the nanoHA crystals.129

Table 5-2 Integral of the 7-8 ppm region of the ¹H NMR spectra when normalised to the TMS reference peak. Results suggest that the P₁₁₋₁₃ monomer, when in the presence of ionic calcium at a concentration of 6.5 mM, could enter in to surface mediated self-assembly on the surface of the nanoHA particles.....145

Table 6-1 Table detailing application procedure for each treatment tested using the fluid filtration device to determine any effect on dentine permeability. After application procedure, the test surface was rinsed with DI H₂O and the test pressure applied. Each treatment was applied to 10 dentine disk samples with 3 fluid filtration measurements taken. The first measurement was taken before treatment application, the second directly after application and the final taken after 7 days in artificial saliva solution at 37 °C.....167

Table 7-1 Dentine fluid filtration measurements (converted into % reduction ± SD) after application of a novel bioglass HX-BGC formulated into a toothpaste and as a powder compared to Sensodyne repair (Novamin®) and distilled H₂O control. Treatments were assessed after initial application, 1 day of submersion in AS solution and after 7 days of daily treatment application followed by AS submersion (Zhong *et al.*, 2015). The fluid filtration % reduction for the P₁₁₋₄ monomer treatment produced in this work is shown in bold. * No repeated daily application of P₁₁₋₄ was done after initial application.....202

List of Abbreviations

AS – Artificial saliva

DLS – Dynamic light scattering

EDS - Energy-dispersive x-ray spectroscopy

HA – Hydroxyapatite

^1H NMR – Proton nuclear magnetic resonance spectroscopy

IVNCG – *In vitro* nucleation and crystal growth

NanoHA – Nano-sized hydroxyapatite

OCP - Octacalcium phosphate

SEM – Scanning electron microscopy

SAP – Self-assembling peptide

TEM – Transmission electron microscopy

XRD – X-ray diffraction

Chapter 1 - Introduction

1.1 General Introduction

The successful long-term treatment of dentine sensitivity remains a clinical challenge. Dentine sensitivity is defined as a short sharp pain arising from exposed dentine tubules in response to stimuli, typically thermal, evaporative, tactile, osmotic or chemical, which cannot be ascribed to any other dental defect or pathology (Holland *et al.*, 1997). There are a wide range of available treatments to prevent the painful response to the stimuli produced on the surface of open dentine tubules but to date no treatment has been defined as “gold standard”. For a treatment to be defined as gold standard it would be required to produce the following effects: non-irritant to the pulp, easily applied, rapid in action, effective for a long time, without staining effects, relatively painless on application and economically viable (Kimura *et al.*, 2000). As no treatment can claim to meet all of these desirable criteria, research into new materials using different treatment methodologies is ongoing.

In the work presented in this thesis, a rationally designed self-assembling peptide/nanoHA hybrid material was optimised and assessed to determine its efficacy in promoting occlusion of dentine tubules in human dentine samples. The self-assembling peptide (SAP) component of the hybrid material was comprised of peptides P₁₁₋₁₃ and P₁₁₋₁₄ which have been rationally designed such that when combined in equimolar ratio under physiological conditions and at sufficient peptide concentration, they follow a hierarchical self-assembly process producing a 3-dimensional fibrillar network (Kyle *et al.*, 2012). The P_{11-13/14} SAPs when combined with nano-sized hydroxyapatite (HA) have been shown to be effective in favouring the growth of nanoHA seed crystals (Sayed, 2013).

The following thesis will test the hypothesis that the self-assembling peptide/nanoHA hybrid material is effective in occluding human dentine tubules. The rationale behind the proposed self-assembling peptide/nanoHA hybrid material dentine sensitivity treatment is that a solution of P₁₁₋₁₃ seeded with

nanoHA and a second solution of P₁₁₋₁₄ seeded with nanoHA would be applied separately to the dentine surface one after the other. The first nanoHA seeded peptide solution would penetrate in to the dentine tubules. The subsequent addition of the second nanoHA seeded peptide solution would then initiate the self-assembly process, resulting in the formation of a SAP gel, not only on the dentine surface, but within the dentine tubules. The nanoHA seed crystals contained within and supported by the SAP gel could then grow, promoting the occlusion of the dentine tubules. To optimise the SAP/nanoHA hybrid material with respect to its crystal growth potential, a high throughput *in vitro* nucleation and crystal growth (IVNCG) assay was validated and utilised.

To assess the SAP/nanoHA hybrid material with respect to its ability to reduce fluid flow through human dentine, a fluid filtration device was developed and validated. The fluid filtration device was based on the work of Reeder *et al.* (1978) and allowed for the measurement of dentine permeability with respect to fluid flow through the dentine. The optimised SAP/nanoHA hybrid material was applied to human dentine samples and the permeability of the dentine assessed after initial application and after 7 days incubation in AS solution, using the fluid filtration device. P₁₁₋₄ SAP, the active ingredient in the commercially available Curodont dental regeneration/protection clinical products, was also tested in the same system to provide a comparison.

Chapter 2 - Literature Review

The following chapter will provide a review of the literature relevant to the work presented in this thesis. The review is not exhaustive but provides a background source of literature detailing the anatomy and development of the tooth, along with an introduction to hydroxyapatite and its synthesis, including a brief introduction to the thermodynamics and kinetics of mineral formation. The clinical challenge of dentine sensitivity is described along with a review of current treatments and measurement techniques used in the development of new treatments. The final section provides an introduction to biomimetic peptide-based treatments used in dental applications. Each subsequent chapter in this thesis contains a separate introduction which provides a more focussed and detailed review with respect to the topic covered in that chapter.

2.1 Anatomy and Development of the Dental Tissues

2.1.1 Tooth Anatomy

To understand the causes of dentine sensitivity and develop new treatments to address the problem, an understanding of the anatomy of the tooth and its tissues is required. Enamel covers the entire crown of the tooth protecting the underlying dentine. Enamel provides the hardness of the tooth's crown with a Young's modulus of 94 ± 5 GPa which is smaller than steel (approximately 200 GPa) but significantly larger than dentine (20 ± 2 GPa) (Xu *et al.*, 1998). The hardness of enamel confers wear-resistance properties which are required for the mastication of food (Lin and Douglas, 1994). Enamel, although displaying remarkable hardness properties, is brittle and requires the underlying dentine, which has a much lower Young's modulus to act as a cushion for loading transmission to prevent tooth failure (Lin and Douglas, 1994; Imbeni *et al.*, 2005). The bulk of the tooth is composed of dentine, overlaid by enamel, while the inner core of the tooth contains a chamber where the pulp (the living part of the tooth)

resides. Below the tooth crown, the roots are covered in a thin mineralised tissue layer called the cementum, see Figure 2-1.

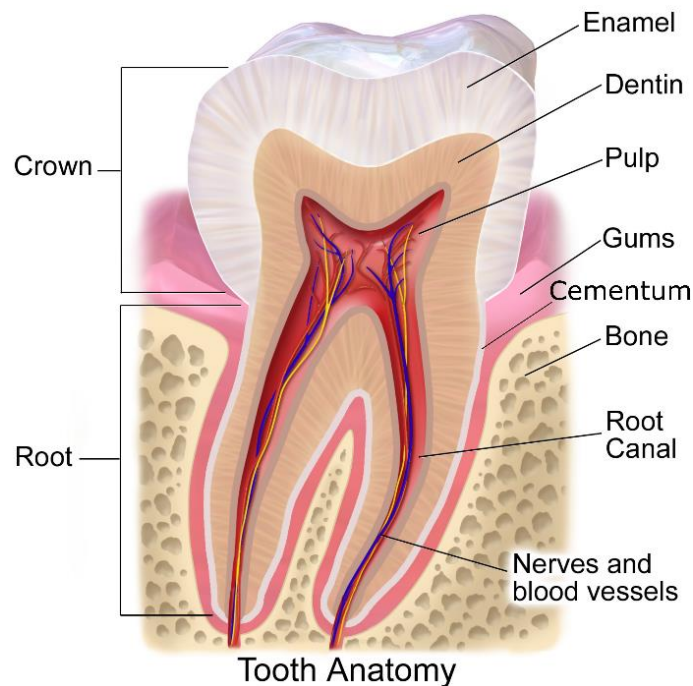


Figure 2-1 Schematic showing the main tooth tissues modified from Blausen.com (2014).

2.1.2 Enamel

Mature enamel is the most mineralised tissue in the body consisting of >95% apatite material by weight (LeFevre and Manly, 1938). The structure of enamel is complex and results in a highly mineralised tissue which can withstand the mechanical and abrasive forces required throughout the lifetime of the organism (Fincham *et al.*, 1999). As the tooth emerges from the oral cavity, the ameloblast layer, which is responsible for the formation of enamel, is lost, resulting in enamel being a non-vital and acellular tissue that cannot undergo cell-mediated regeneration (Nanci, 2013a), in contrast to bone, and dentine. Enamel can be said to have 3 levels of hierarchical structure (Ang *et al.*, 2012). The first level of structure are the apatite nanocrystals approximately 60 nm wide with a thickness of 25 nm (Daculsi and Kerebel, 1978) and a length of at least 100 μm (Daculsi *et al.*, 1984). These crystals are organised together to form rods (or prisms) approximately 3-4 μm in diameter which form the 2nd level of structure, and are thought to run from the enamel-dentine junction to the near surface of the tooth

enamel which is on average 2.5 mm thick (Oliveira *et al.*, 2010) . The regions between the rods are occupied by interrod (inter-prismatic) enamel which can be distinguished from rod enamel as its crystals are orientated at 60° compared to the rod (White *et al.*, 2001). The final level is the grouping of rods into Hunter and Schreger bands which can be seen under light microscopy due to changes in direction between cohorts of adjacent rods (Homma, 1990).

2.1.3 Dentine

Dentine, composed of 70% inorganic material, 20% organic material and 10% H₂O, makes up the bulk of the tooth tissue (Linde and Goldberg, 1993). Dentine is a mineralised tissue which has tubules running in parallel from the pulp to the enamel-dentine junction. Each of these tubules contains an odontoblast process which forms a layer at the pulpal-dentine interface (Ireland, 2006). Human dentine is a complex structure and can be of 3 different types: primary, secondary and tertiary dentine (Kuttler, 1959).

Primary dentine makes up the majority of the tooth and lines the pulp chamber; it is also known as circumpulpal dentine (Nanci, 2013b). Primary dentine is not itself a homogenous layer and is made up of intertubular dentine and peritubular dentine (Goldberg *et al.*, 2011). Intertubular dentine makes up the bulk of the primary dentine with the peritubular dentine lining the tubular lumen (inside space of the tubule) (Fearnhead, 1957). Intertubular dentine is comprised of a tightly woven network of type I collagen fibrils with apatite crystals deposited throughout while peritubular dentine is more highly calcified with less collagen present compared to intertubular dentine (Nanci, 2013b).

Once the tooth becomes functional in the mouth, the formation of secondary dentine begins (Arana-Chavez and Massa, 2004). The thickness of secondary dentine increases with age and results in the size of the pulp chamber decreasing over time (Solheim, 1992). There is little compositional difference between primary and secondary dentine but secondary dentine does differ morphologically as the curvature of the tubules is more accentuated due to the growth of the dentine into the pulp chamber, which results in a reduction of the space for the odontoblasts (Goldberg *et al.*, 2011).

The final type of dentine that can be present is tertiary dentine, also known as reactive dentine due to the fact that its formation is triggered through stimuli such as attrition, caries or dental procedures (Stanley *et al.*, 1966; Smith *et al.*, 1995).

2.1.4 Dental Pulp

The dental pulp is located in the central chamber of the tooth and is a soft connective tissue that supports the dentine and contains the “living” part of the tooth. The dental pulp can be split into 4 distinct zones (Nanci, 2013b).

The first zone is called the odontoblast layer and is found at the periphery of the pulp chamber. The odontoblasts form a lining around the pulp chamber and have extended processes that reach into the dentine. The second zone is called the cell-free zone and as its name suggests, this zone contains little to no cells although there are areas occupied by blood capillaries, nerve fibres and the processes of fibroblasts (Gotjamanos, 1969; Trowbridge and Kim, 1994). The third zone is the cell-rich zone which contains the fibroblasts whose function is to maintain the pulp matrix (Nanci, 2013b) as well as perivascular cells, undifferentiated mesenchymal cells (Sloan and Smith, 2007) and postnatal human dental pulp stem cells (Gronthos *et al.*, 2000). These cells are thought to ensure that the odontoblasts are repaired or regenerated if stimuli results in odontoblast damage/death (Smith *et al.*, 1995). The final zone is the pulp core which contains the major blood vessels and the nerves of the pulp (Nanci, 2013b). The nerve fibres (which when stimulated produce pain) have been shown to extend beyond the cell-free zone close to the odontoblast lining the pulp chamber (Dahl and Mjör, 1973).

2.2 Tooth Development

In humans, at around 37 days after conception, bands of thickened epithelium, called the primary epithelium bands, begin to form around the presumptive upper and lower jaws which initiate tooth development (Nanci, 2013c). The primary epithelium bands then grow into the neural crest derived mesenchymal forming the dental lamina which corresponds to the future position of the teeth (Pispa and Thesleff, 2003). Dental placodes then form which are localised thickenings

of the epithelium. These are thought to initiate which tooth type will form (incisor, canine, premolar, molar) (Mikkola, 2007). The mesenchyme then condenses around the ingrowing epithelium producing the tooth bud (Tucker and Sharpe, 2004). As the bud grows further into the mesenchyme, it drags along the dental lamina and wraps around the condensing mesenchyme producing a cap sitting on a ball of mesenchyme; this is known as the cap stage, see Figure 2-2 (Tucker and Sharpe, 2004). The cap on the ball of condensed mesenchyme is known as the dental organ but will eventually produce the enamel of the tooth while the condensed mesenchymal ball will become the dental papilla which will form the dentine and pulp (Nanci, 2013c). As the development of the tooth continues, it begins to take on the shape of a bell as the condensing mesenchyme deepens into the neural-crest derived mesenchyme, producing the bell stage (Nanci, 2013c). Towards the end of the bell stage, once the condensing mesenchyme is completely enclosed by the growing epithelium, the epithelial cells closest to the dental mesenchyme differentiate into enamel producing ameloblasts while the adjacent dental mesenchyme differentiates into dentine producing odontoblasts (Ruch *et al.*, 1995).

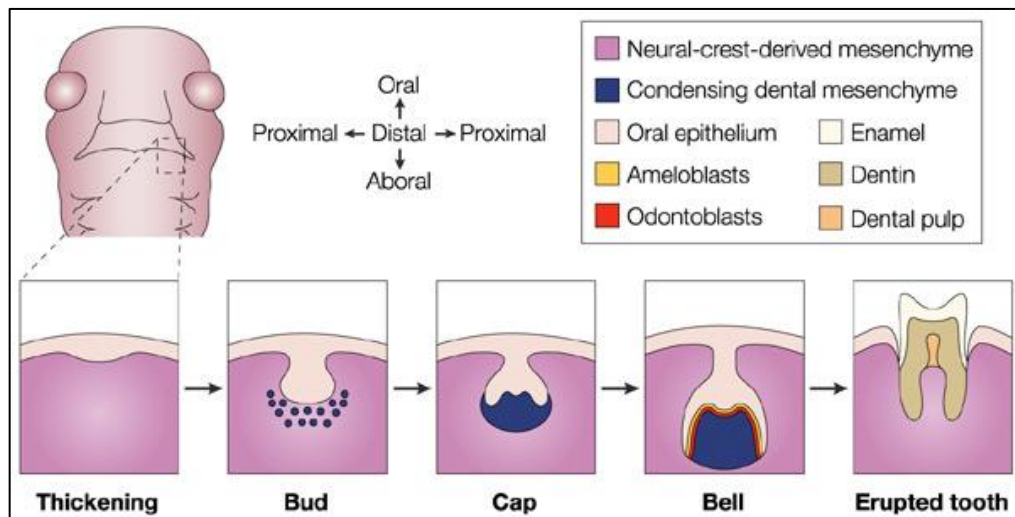


Figure 2-2 Schematic of tooth development describing the stages of tooth development. Thickening stage occurs through oral epithelium growth into the mesenchyme. Mesenchyme then thickens in response to ingrowing epithelium resulting in the bud stage. As the epithelium grows deeper into the mesenchyme it wraps around the condensing mesenchyme producing the cap stage. The epithelium continues to grow into the mesenchyme producing a bell shape of condensed mesenchyme, differentiation of the epithelium cell occurs at the point of contact between the epithelium and condensed mesenchyme producing a layer of odontoblasts on the condensed mesenchyme and a layer of ameloblasts above the odontoblasts which go on to produce the enamel and dentine respectively. Image reproduced with permission from Tucker & Sharpe (2004).

2.2.1 Amelogenesis

During the bell stage of tooth development, the process of amelogenesis (enamel formation) begins. The formation of enamel can be described as proceeding in 3 stages: pre-secretory stage, secretory stage and the maturation stage (Leblond and Warshawsky, 1979).

During the pre-secretory stage, the ameloblasts develop a protein synthesis apparatus which will enable the production and secretion of the organic matrix of enamel during the secretory stage (Nanci and Smith, 1999). The predominant protein present in the forming organic enamel matrix is amelogenin and its cleavage products, which constitute around 90% of the total organic enamel matrix although this can deviate depending on the amelogenesis stage (Terminie *et al.*, 1980). The amelogenin protein is alternatively spliced and subject to post-secretory degradation generating a wide spectrum of amelogenin proteins

(Gibson *et al.*, 1991). Amelogenins are mostly proteins 20-25 kDa (SDS molecular weight), primarily hydrophobic and rich in the amino acids proline (25%), glutamic acid (14%), leucine (9%) and histidine (7%) (Eastoe, 1960). The second most abundant protein present in the protein enamel matrix is called ameloblastin, which accounts for around 10% of the matrix composition. Ameloblastin is relatively large when compared to amelogenin, with a molecular weight of approximately 65 kDa (Nanci, 2013d). Ameloblastin is essential for the formation of enamel and has been shown to be responsible for the maintenance of the ameloblasts' phenotype and may facilitate the attachment of the ameloblasts to the matrix surface (Fukumoto *et al.*, 2004). The final major component of the protein enamel matrix is called enamelin and contributes approximately 1% of the total matrix composition. Enamelin is the largest structural protein found in the protein enamel matrix with a molecular weight of approximately 186 kDa (Nanci, 2013d). Enamelin has been found to be essential to ensure ameloblast integrity and for the formation of enamel (Hu *et al.*, 2014). Prior to the secretory stage, the ameloblasts begin to actively secrete enamel proteins which produce a thin layer of enamel containing no prisms. The ameloblasts then move away from the already formed dentine surface and form the Tomes' process at the enamel facing end of the cell (Nanci, 2013d).

The formation of the Tomes' process signals the beginning of the secretory stage. The Tomes' process is a specialised structure at the secretory end of the ameloblast which controls the formation of enamel rods and enamel interrod material. Once the Tomes' process has been formed, the secretion of enamel proteins occurs at 2 sites. The proximal site secretes proteins which form the interrod enamel, this process resulting in the formation of pits as the interrod enamel forms around the protruding distal part of the cell (Boyde, 1967). The pit is then filled with matrix secreted from the distal end site of the Tomes' process, and this matrix participates in the formation of the enamel rods (Leblond and Warshawsky, 1979). The earliest mineral crystals present during enamel formation have been reported as long thin crystals with dimensions of 1.5 nm thickness and 15 nm width (Kerebel *et al.*, 1979). Towards the end of the secretory phase, the amount of matrix protein decreases; this has been attributed to the withdrawal of protein following extracellular degradation

(Robinson *et al.*, 1981). It is also the case that as the ameloblasts reach the surface limit of the tissue, they secrete progressively less protein (Robinson *et al.*, 1988). Once the distal portion of the Tomes' process is lost, the ameloblasts become shorter and produce enamel similar to the initial enamel that contained no rods, this makes up the last few increments of the enamel structure (the "aprismatic layer") (Gwinnett, 1966).

The final stage in amelogenesis is the maturation stage. Enamel hardens as the level of protein decreases and is replaced by tissue fluid, there is a rapid increase in the width and thickness of the crystals. The study of the effect of bovine amelogenins on the growth of OCP crystals has shown that on removal of amelogenins, the crystal growth is primarily formed through the thickening of the individual crystals (width and thickness) (Iijima *et al.*, 2001). It was reported that the loss of protein from the secretory stage crystal surfaces is the cause of this rapid mineral accumulation at the maturation stage, which suggests that the proteins exert control over the morphology of mineral crystals (Robinson *et al.*, 1989).

2.2.2 Dentinogenesis

Dentine is formed by odontoblast cells that have differentiated from the condensed mesenchymal cells of the dental papilla. The odontoblasts then begin the secretion of a matrix which will produce the first dentine layer called the dentine mantle (Arana-Chavez and Massa, 2004). This matrix consists of large-diameter collagen type III fibres, known as Korff's fibres, which originate deep within the odontoblasts and extend towards the enamel organ (Nanci, 2013b).

As the odontoblasts continue to grow in size, they begin to produce smaller type I collagen fibrils which position themselves parallel to where the dentinoenamel junction will form. This process results in the formation of the dental mantle (Nanci, 2013b). The odontoblasts produce small membrane bound vesicles, known as a matrix vesicles, which bud off and lie near the basal lamina and embed themselves in the organic matrix of dentine which consists of around 90% collagen, primarily type I but types III and V are also present in small amounts (Goldberg and Takagi, 1993). The collagen acts as a scaffold which provides a surface for the matrix vesicles to form upon (Nanci, 2013b). The mechanism by

which mineral is nucleated in dentine (and bone) has not been conclusively reported although there are theories as to how mineral nucleation is achieved.

One widely accepted theory is that the mineral phase of dentine is initiated inside the matrix vesicle and as it grows it breaks through the vesicle and spreads a cluster of crystallites which interact and fuse with other erupting clusters of crystallites to produce a continuous mineral phase (Anderson, 1995). In dentine the formation of spherical matrix vesicles which imbed themselves within the surrounding collagen fibres has been reported (Eisenmann and Glick, 1972). The matrix vesicles have been shown to contain needle-like crystals suggesting that nucleation of calcium phosphate mineral occurs within these matrix vesicles (Eisenmann and Glick, 1972).

A contradicting theory involves the non-collagenous proteins which are present in the dentine organic matrix with phosphophoryns being the most abundant (Dimuzio and Veis, 1978). Phosphophoryns have been reported to be capable of HA nucleation, have been found at the mineralising front and have been linked to the nucleation of HA crystals *in vitro* (Nawrot *et al.*, 1976).

The precise mechanism of mineral nucleation in dentine is therefore currently unclear although matrix vesicles or phosphophoryns are possible nucleating agents. Once the dentine mantle has been formed, the odontoblasts cease to produce matrix vesicles and instead begin to produce several non-collagenous matrix proteins (Arana-Chavez and Katchburian, 1998).

The non-collagenous proteins include, but are not limited to, the previously described phosphophoryns, dentine matrix protein-1 and dentine sialoprotein. Dentine matrix protein-1 (DMP-1) is an acidic protein which has been shown to be capable of nucleating HA *in vitro* and control the morphology of the growing crystals into elongated rods (He *et al.*, 2003). Dentine sialoprotein (DSP) has been shown *in vitro* to have a limited effect on HA nucleation and crystal growth (Boskey *et al.*, 2000) but has been reported as a possible regulator of mesenchymal cell differentiation (Wan *et al.*, 2016). The odontoblasts are always separated from the mineralising front by a layer of pre-dentine due to the mineralisation lag. As the odontoblasts move towards the pulp, one of the cell processes, known as a Tomes' fibre, becomes accentuated and is left behind,

while the dentine matrix will mineralise around this cell process resulting in the formation of the dentine tubules (Arana-Chavez and Massa, 2004).

2.3 Hydroxyapatite

The mineral phase of enamel and dentine is apatitic. “Apatite” is the general name given to a family of inorganic compounds which share a similar hexagonal crystal structure and crystal lattice point group $P6_3/m$ (LeGeros, 1994). Apatite was first identified as a calcium phosphate salt in 1788 by Proust and Klaprota who also noted its similarity to bone (Smith, 1994). Calcium phosphate mineral can take the form of an apatite called hydroxyapatite which makes up the majority of the mineral content of vertebrates’ bone and teeth, although the composition of biological apatite can vary, see section 2.3.1, (Sadat-Shojai *et al.*, 2013). The structure of apatite can be described by the general formula $A_4B_6(MO_4)_6X_2$. In pure hydroxyapatite, calcium occupies 2 different sites, A and B, M is phosphorus and X is a hydroxyl group resulting in the formula $Ca_{10}(PO_4)_6OH_2$ (Kay *et al.*, 1964). Calcium’s occupation of two different sites is visible in Figure 2-3.

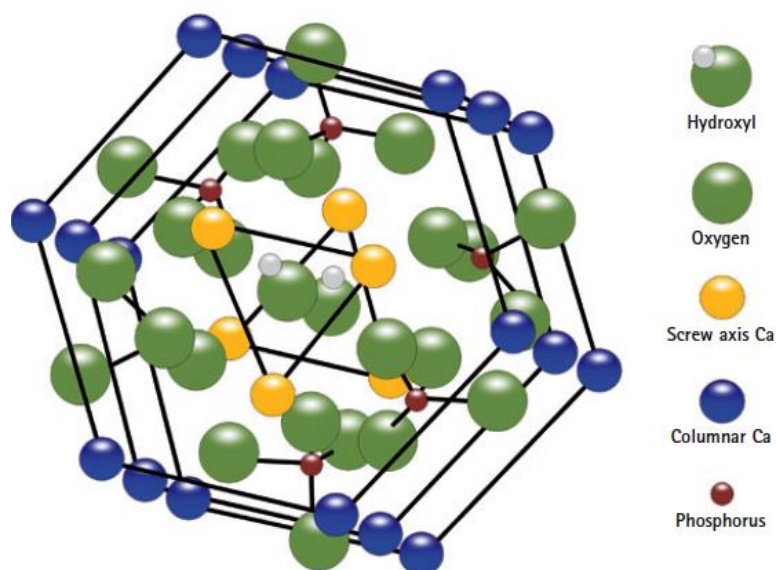


Figure 2-3 Schematic representation of hydroxyapatite structure showing sites of hydroxyl, oxygen, calcium and phosphorus in the hydroxyapatite structure. Image reproduced with permission from Brunton *et al.* (2013). (<https://creativecommons.org/licenses/by/3.0/>)

2.3.1 Biological Hydroxyapatite

Biological hydroxyapatite is not pure as substitutions within the mineral structure can and do occur, for example bone is relatively rich in a carbonate and magnesium analogue of pure hydroxyapatite (Boskey, 2003), while dentine and enamel have minor substituted components including, but not limited to, carbonate, magnesium and fluoride (Robinson *et al.*, 1995). Biological hydroxyapatite is always nano-dimensional and nano-crystalline with dimensions of a few to hundreds of nano-meters. One reason for this biological preference is thought to be the result of natural selection as this size range can form specific interactions with proteins which can exert control over the morphology of the crystals formed (Dorozhkin, 2010).

The substitutions within the crystal structure affect the resulting chemical properties of the mineral formed. The substitution of carbonate into the hydroxyapatite crystal structure can occur through the exchange of a hydroxyl ion (least common) (Elliott *et al.*, 1985) or phosphate ion (most common) (LeGeros *et al.*, 1967). The substitution of carbonate ions into the apatite crystals can result in a decrease in crystallinity due to a decrease in structural order caused by the replacement of the PO₄ group with the smaller carbonate group which increases mineral solubility (LeGeros, 1981). The substitution of magnesium ions for calcium ions in the apatite has been shown to inhibit the growth of apatite crystals through stabilising the formation of tricalcium phosphate or amorphous calcium phosphate of the crystal surface resulting in smaller sized crystals (LeGeros, 1981). The inclusion of magnesium in brushite cement formulations has been shown to retard the formation of hydroxyapatite through stabilising the tricalcium phosphate precursor phase preventing the formation of HA which decreases the compressive strength *in vivo* and increases the reabsorption of the cement (Lilley *et al.*, 2005). The substitutions of carbonate and magnesium which can occur in biological apatite have been shown to increase the dissolution of biological apatite under acidic conditions which is caused by the decrease in crystallinity associated with the substitution (Legeros *et al.*, 1995). Although when the organic component of the biological tissue was

present, dissolution under acidic conditions was reduced suggesting the organic component plays an important role in the protection of biological apatite under acidic conditions (Legeros *et al.*, 1995).

Fluoride ions can be incorporated into hydroxyapatite through substitution with the hydroxyl group (Young, 1974) and results in an apatite with reduced solubility under acidic conditions caused by the contraction of the apatite crystal structure caused by the electronegative fluoride ions substitution with the hydroxyl group (Buonocore and Bibby, 1945). Fluoride toothpastes, which result in the substitution of fluoride into enamel crystals, are extensively used to reduce enamel erosion and prevent the formation of enamel caries through producing an acid resistant fluorapatite layer on the tooth surface (Featherstone, 1999).

2.3.2 Synthesis Methods

It is generally accepted that hydroxyapatite nanoparticles are preferable to macro-sized particles when we are considering their use in hard tissue engineering. This preference is due to the poor bioresorbability and brittle characteristics of macro-sized particles compared to that of the nano-sized particles (Zakaria *et al.*, 2013). The demand for nano-sized particles of hydroxyapatite has resulted in a steady increase in the number of publications related to the synthesis of hydroxyapatite nanoparticles (nanoHA). A recent review carried out by Sadat-Shojai *et al.* (2013) found an increase from 25 publications in 1999 to 75 publications in 2011 indexed in Scopus, relating to methods of nanoHA synthesis (Sadat-Shojai *et al.*, 2013). This trend displays the increasing interest in hydroxyapatite nanoparticles as well as the challenges of producing them.

There are a number of different methods which can be used to synthesise nanoHA depending on the type of hydroxyapatite required, which in turn depends on its chosen application. Phase composition, purity, crystallinity, particle size, particle-size distribution, specific surface area, density and particle morphology can all be controlled through the synthesis methodology chosen (Abidi and Murtaza, 2014). Synthesis methods include but are not limited to sol-gel (Fathi *et al.*, 2008), hydrothermal (Earl *et al.*, 2006a), wet chemical precipitation (Abidi and Murtaza, 2014) and hydrolysis (Nakahira *et al.*, 1999).

Hydrolysis of various calcium phosphate minerals, examples being $\text{CaHPO}_4 \cdot 2\text{H}_2\text{O}$ (Shih *et al.*, 2004) and $3\text{Ca}_3(\text{PO}_4)_2$ (Durucan and Brown, 2000), using CaCO_3 has been shown to be effective in the synthesis of nanoHA. The hydrolysis method can proceed under a range of temperature and pH values. The calcium phosphate mineral to be hydrolysed (see above) is mixed with CaCO_3 at a Ca/P molar ratio of 1.67 and poured into a NaOH solution. The mixture then undergoes agitation at high temperature (below 100 °C) for a period of time. The reaction is then stopped through the addition of ice cold H_2O . The resulting suspension is then washed and dried. The suspension can then be heat-treated to remove undesired phases. The resulting nanoHA produced can vary in phase purity and size although single phase crystalline nanorod HA has been reported (Shih *et al.*, 2004).

The sol-gel methodology of nanoHA particle synthesis often involves the formation of a triethyl phosphite colloid suspension in anhydrous ethanol with a small amount of H_2O added to allow for hydrolysis (Liu *et al.*, 2001). Once hydrolysis is complete, a stoichiometric (Ca/P molar ratio of 1.67) amount of calcium nitrate dissolved in anhydrous ethanol is added dropwise to the solution under constant stirring. The ethanol is then removed through drying at 60 °C resulting in a gel product. The gel is then heated in a furnace at various temperatures to produce the final nanoHA product. The processing of the sol-gel method product has been shown to have a significant effect on the resulting Ca/P ratio of the powders formed (Bilton *et al.*, 2010).

Wet chemical precipitation is a common method used and is relatively easy to carry out; it can be used to produce large quantities of product and at cheap cost (Berzina-cimdina and Borodajenko, 2012). A calcium solution, normally calcium hydroxide or calcium nitrate, is prepared along with a phosphate solution, normally orthophosphoric acid or di-ammonium hydrogen phosphate, and both are added dropwise to each other under continuous stirring which results in the precipitation of hydroxyapatite. Once the addition is complete the suspension can then undergo further processes such as aging, washing, drying and thermal treatment which, depending on the method used to achieve these processes,

can alter the final structure of the nanohydroxyapatite crystals produced (Sadat-Shojai *et al.*, 2013).

A variation of the wet chemical precipitation method is the hydrothermal method which uses the same initial precipitation reaction but the suspension is then treated at high temperature and pressure to promote the 1-dimensional growth of crystals resulting in the production of nanorods (Earl *et al.*, 2006a). One issue with this method compared to others is the cost as expensive equipment is needed to obtain the required temperatures and pressures (Sadat-Shojai *et al.*, 2013).

2.3.3 Characterisation Techniques

Once hydroxyapatite has been synthesised, characterisation of the resulting nanoparticles is required to determine if the reaction has been successful. There are a number of techniques that can be used to determine the composition, size, shape and size distribution of the nanoparticles produced. A few of the main techniques will be introduced below along with the information that the technique provides.

Fourier transformed infrared spectroscopy (FTIR) provides information on the chemical bonds present in a material through exciting chemical bonds causing vibrations. The frequency at which a chemical bond absorbs energy is dependent on the strength of the bond, the atoms involved in the vibration and the vibrating bonds' interactions with the surrounding environment. FTIR produces an absorbance or transmission spectrum which can be assigned to specific bonds within a material. FTIR can be used in hydroxyapatite nanoparticle characterisation to assess 2 main parameters: maximum absorption which indicates composition and peak width which provides information concerning the degree of order within the material (Berzina-cimdina and Borodajenko, 2012). The characteristic chemical groups present in the FTIR spectrum of synthesised hydroxyapatite are commonly PO_4^{3-} , OH^- , CO_3^{2-} (Fathi *et al.*, 2008).

Dynamic light scattering provides information on the size distribution of particles suspended in solution (Müller *et al.*, 2014). The technique involves the passing of a laser through a particle suspension. The laser light interacts with the particles and is scattered. The scattered light is detected and the angle at which the

photon was scattered relative to the laser beam is used to calculate the size of the particle. The measurement of particle size when analysing nanoparticles can overestimate the size due to the instruments measurement of hydrodynamic radius, that is its hydrated size (Bhattacharjee, 2016). Measurement of hydrodynamic radius produces size values larger than the true size of the particle. This effect is negligible when considering micron sized particles but can produce a significant effect when using nm sized particles (Kaasalainen *et al.*, 2017).

X-ray diffraction (XRD) is a technique that is widely used to determine the structure of crystalline material. X-rays have wavelengths of approximately 10^{-10} m which is the same order of magnitude as the distances between atoms in molecules. This results in the diffraction of x-rays when they interact with a molecule (Housecroft and Sharpe, 2008). The peaks produced in an x-ray spectrum can provide information on the crystal structure and composition (Bragg, 1913), as diffraction patterns from experiments can be compared to reference spectra (Sudarsanan and Young, 1969). The degree of crystallisation can also be determined from x-ray diffraction spectra since the more defined the peaks are, the more crystalline the sample is, due to the alignment of crystal plains within a highly crystalline sample (Abidi and Murtaza, 2014).

Transmission electron microscopy (TEM) uses the same principles as a light microscope but utilises electrons instead of light. Electrons are accelerated then projected onto a thin sample (approx. 50 nm thick). As the electrons travel through the sample, they interact with the sample atoms in one of 2 ways. When an electron approaches the atom it can be deflected by the atoms nucleus (elastic scattering) and this deflection can divert the electron away from the detector. The second possible interaction is that the electron dislodges an electron in the specimen (inelastic scattering), producing a secondary electron of lower energy that does not reach the detector. Both of these interactions result in electron not forming the image. The electrons that reach the detector are used to form the final image (Dykstra and Reuss, 2003). This technique is used to determine the morphology of hydroxyapatite nanoparticles (Tao *et al.*, 2007; Fathi *et al.*, 2008).

Scanning electron microscopy (SEM) is similar to TEM although in SEM the electrons which interact with the sample are not the electrons that are used to produce the final image. The SEM performs a raster scan of the sample surface and detects secondary electrons which are produced from the beams interaction with the sample's surface. These secondary electrons are detected and used to form an image of the samples surface. SEM can be used to determine morphology of hydroxyapatite nanoparticles (Kumta *et al.*, 2005).

Energy-dispersive x-ray spectroscopy can also be used in the characterisation of hydroxyapatite nanoparticles. This technique uses an electron beam that interacts with the sample in the same manner as in SEM and TEM. One of the possible outcomes of the electron beam interacting with the sample is that an electron from the beam will collide with an orbital electron of the sample and cause it to be dislodged. This results in an unstable electron configuration and an electron from a higher shell will fall back to fill the electron vacancy. The difference in energy between the electron vacancy and the higher energy level electron results in the emission of an x-ray with energy equal to the difference between the 2 levels. These energies are characteristic of the atom in which they occur and this can be used to determine the elemental composition of the sample. In hydroxyapatite particle synthesis, this is useful as it enables the determination of the calcium to phosphate molar ratio which if equaling 1.67 is consistent with hydroxyapatite (He *et al.*, 2003). A comparison of the information provided by the characterisation methods used in this thesis and associated limitations is supplied in section 3.4.

2.4 Mechanisms of Mineralisation

Mineral crystal formation is a process whereby a system (solution which is saturated with respect to a mineral crystal phase) moves from a high energy state to a lower energy state through the formation of a crystal phase. The origin of the energy difference between the energy states is related to the solubility of the inorganic crystal phase that is produced. The solubility of an inorganic salt can be defined as the amount of pure solid that can dissolve in one litre of water. The change in energy that accompanies the dissolution of a solid into the

aqueous phase, the free energy of solution ΔG_S , is described by Equation 2.4-1 with ΔG_L , the free energy change for crystal lattice disruption. The 3 negative terms are hydration ΔG_H , ion pairing, ΔG_{IP} and complex formation, ΔG_C . The sum of all 4 terms produces the free energy of solution ΔG_S . If the resulting ΔG_S is negative the system will move towards dissolution.

$$\Delta G_S = \Delta G_L - (\Delta G_H + \Delta G_{IP} + \Delta G_C) \quad \text{Equation 2.4-1}$$

The solubility product K_{sp} is the product of the effective concentrations (activities) of ions at equilibrium with their corresponding solid phase, Equation 2.4-2. The K_{sp} of an inorganic salt is related to the free energy of solution ΔG_S through Equation 2.4-3 with R being the gas constant and T the temperature.

$$K_{sp} = [X^-] \cdot [M^+] \quad \text{Equation 2.4-2}$$

$$\Delta G_S = -RT \ln(K_{sp}) \quad \text{Equation 2.4-3}$$

The solubility product K_{sp} sets the thermodynamic point for the precipitation of a solid. The thermodynamic driving force for crystallisation is the supersaturation (SR) which is the difference between the activity product (AP) and the solubility product K_{sp} at equilibrium. Equation 2.4-4 shows this relationship. When SR is below 1 the solution is not saturated enough to produce a solid phase whereas if it is above 1 spontaneous formation of a solid phase is favourable.

$$SR = \frac{AP}{K_{sp}} \quad \text{Equation 2.4-4}$$

Supersaturation, S_R , is a measure of the difference between the system concentrations and the equilibrium concentrations and is a measure of how far the system is from the equilibrium state and is the thermodynamic driving force for crystallisation. Supersaturation can be achieved through a number of different methods for example chemical reactions, temperature changes, pH changes and solvent evaporation (Mann, 2001a).

2.4.1 Nucleation

The thermodynamic driving force for crystallisation is the supersaturation level in a given solution. However, this driving force is often overshadowed by significant kinetic effects that prevent crystallisation from occurring (Davey and Garside, 2000a). The process by which crystallisation is initiated in a supersaturated solution to produce a new solid phase is called nucleation. The nucleation process can be initiated through homogenous nucleation or heterogeneous nucleation. Homogenous nucleation involves the spontaneous formation of a new phase within the supersaturated system. This formation of a new phase is kinetically unfavourable as the nucleus of the new phase has to become large enough to be energetically stable. This nucleus size is known as the “critical cluster size”. Any nucleus below this critical cluster size is prone to dissolution and often dissolves back into solution before it has had the time to grow to the critical cluster size, see Figure 2-4. The origin of the critical cluster size is due to the energetically unfavourable formation of a new solid-liquid interface. The solid-liquid interface results in the solid phase having 2 classes of atoms, the interior atoms and the surface interface atoms. The interior ions have all their intermolecular interactions satisfied by other solid phase atoms while the surface interface atoms only have a portion of their total interactions satisfied. It is the unsatisfied interactions of the surface ions which are energetically strained producing a dissolution favouring energy called the interfacial tension γ .

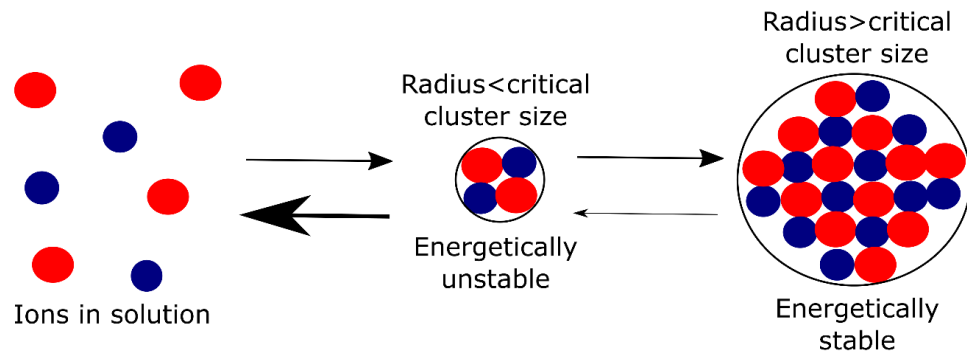


Figure 2-4 Schematic describing the nucleation of a crystal phase from a saturated solution with respect to the crystal phase. The formation of a crystal with a radius below the critical cluster size is energetically unfavourable and the equilibrium will be in favour of ions. A small number will grow above the critical cluster radius resulting in a stable crystal with respect to dissolution. Size of arrow indicative of favoured equilibrium position.

When we consider the energy of the 2 types of atoms in the solid phase Equation 2.4-5 can be produced with respect to the nucleation free energy ΔG_n , with G_i being the internal atoms free energy and G_e being the external ions free energy (Davey and Garside, 2000a).

$$\Delta G_n = G_i + G_e \quad \text{Equation 2.4-5}$$

The internal molecules stabilise the formation of the new solid phase and so act to lower the free energy. The surface molecules destabilise the new phase and raise the free energy. We can consider the nucleus as a sphere. The surface area is proportional to the number of surface ions and the volume is proportional to number of internal ions. The equations for the surface area, Equation 2.4-6, and volume, Equation 2.4-7, are shown below with r being the radius of the sphere.

$$\text{Area of sphere} = 4 \pi r^2 \quad \text{Equation 2.4-6}$$

$$\text{Volume of sphere} = \frac{4}{3} \pi r^3 \quad \text{Equation 2.4-7}$$

It can be seen, from the equations above, that as the sphere grows the number of surface atoms decrease with respect to the number internal atoms due to the

difference in powers of r . Initially the gain of free energy due to the surface atoms outweighs the loss from the internal atoms resulting in the nucleus dissolution. As the sphere grows, the positive free energy decreases until it becomes negative. At this point the cluster has reached the critical cluster size. Any addition growth in the cluster results in the favourable lowering of the free energy producing crystal growth.

The second form of nucleation, heterogeneous nucleation, is a modification of the homogeneous process and occurs when the system contains a foreign particulate contaminant or an added template seed. If the system contains foreign bodies, these can act as catalysts for nucleation as they act to reduce the G_e term in equation 2.4-5. This reduction in the dissolution favouring G_e free energy lowers the activation energy for nucleation favouring solid phase growth. The extent to which a foreign body lowers the G_e term is dependent on how well the foreign body mimics the structure of the resulting solid phase. Due to the difficulty in producing a system that is completely foreign body free, heterogeneous nucleation is the most common way in which a solid phase is produced (Davey and Garside, 2000a).

2.4.2 Crystal Growth

Once a stable nucleus has formed in a saturated system, the number of atoms joining the solid phase is greater than the number of atoms leaving. This results in the growth of the solid phase through secondary crystal growth. Secondary crystal growth requires the presence of solid crystal material and can occur at saturations lower than the values required for heterogeneous and homogenous nucleation. Secondary crystal growth can occur through different mechanisms but is driven by the clustering of ions in solution near the solid/liquid interface. The driving force for crystal growth is the availability of active sites on the crystal surface which, having high binding energies, lower the free energy of the system when ions are incorporated into these sites, resulting in the growth of the solid phase. Certain sites on the surface provide more stabilisation energy than others, see Figure 2-5 which shows the potential active sites on a crystal surface. The bigger the increase in surface area interaction between incoming ions and the solid phase, the higher the binding energy. The step vacancy produces the

largest surface area interaction between the solid and incoming ion (in the schematic the incoming ion would be a square the size of the step vacancy) while the terrace site would produce the lowest surface area interaction (Davey and Garside, 2000b).

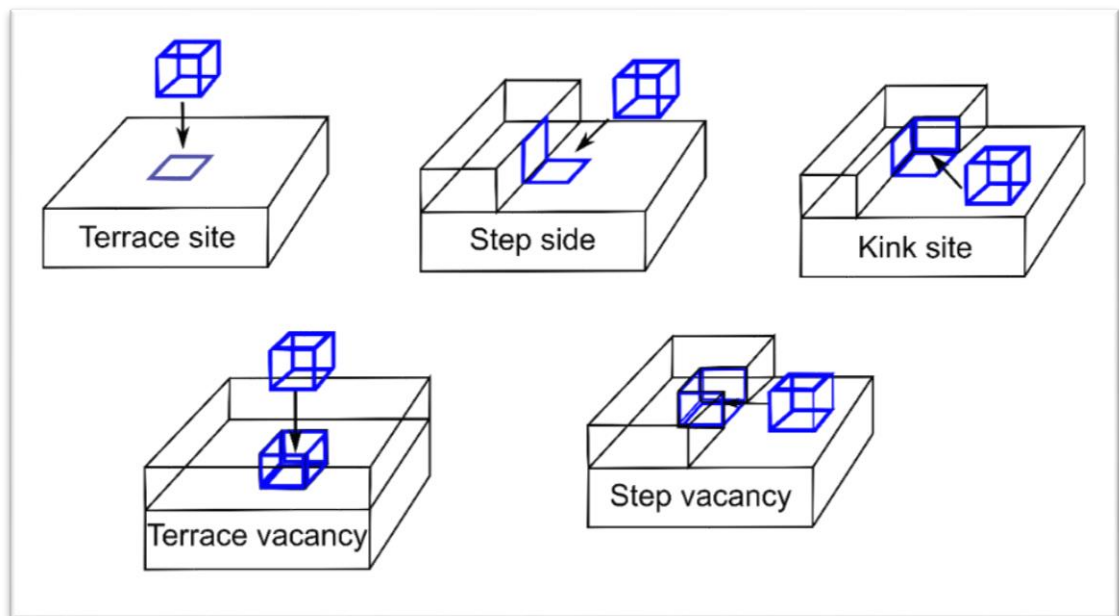


Figure 2-5 Schematic diagram of the substrate surface showing the possible active sites for crystal growth. In order of largest to smallest binding energy: terrace vacancy, step vacancy, kink site, step side, terrace site (Davey & Garside, 2000a).

2.4.3 Mineralisation in Biological Systems

The biological formation of hard tissues can be split into 2 groups depending on the level of cellular control over mineralisation. Biologically induced biomineralisation has the least amount of control while biologically controlled mineralisation has the highest degree of control over the resulting mineral phase (Lowenstam and Weiner, 1989). Biologically controlled mineralisation is a cell-mediated process that produces minerals with specific biological functions. Biominerals produced through controlled mineralisation have species-specific crystallochemical properties which are a direct result of the cellular control exerted during their formation (Mann, 2001b). These properties include, but are not limited to, high level of spatial organisation, higher order assembly into hierarchical structures and uniform particle size.

A distinctive feature of nearly all biologically controlled mineralisation is the sealing off of the mineralisation site known as space delineation (Wilbur, 1984). The sealing off of the mineralisation front allows the cell-mediated process to deliver the required ions to the mineralising matrix, thus preventing the need for a system wide supersaturation with respect to the mineral formed. The mechanism by which mineral is nucleated in developing enamel is not fully understood.

The amelogenin proteins have been shown to self-assemble to form nanosphere structures which have been identified as the principal structural component of the forming enamel organic matrix during the secretory stage (Robinson *et al.*, 1981). The self-assembly of amelogenin is hydrophobically driven and the resulting nanospheres have been shown to self-assemble into linear arrays of microribbons, which, when immersed in meta-stable calcium phosphate solution, produced ordered and aligned crystals along the long axis of the microribbons (Du *et al.*, 2005). The presence of mouse amelogenin has been shown to promote the nucleation of octacalcium phosphate (OCP) *in vitro* through a suggested lowering of the interfacial energy and increasing supersaturation with respect to hydroxyapatite (HA) and OCP (Tarasevich *et al.*, 2007). Previous studies carried out by Hunter *et al.* (1996) using a gel-based *in vitro* system determined that the presence of amelogenin did not increase the quantity or affect the morphology of the calcium phosphate mineral produced. The *in vitro* study by Tarasevich *et al.* (2007) did not identify the process that occurs *in vivo* but did determine that amelogenin is capable of calcium phosphate nucleation and crystal growth.

The formation of OCP as an initial precursor to enamel has been hypothesised although no consensus has been achieved (Brown *et al.*, 1987; Simmer and Fincham, 1995; Tarasevich *et al.*, 2007). The epitaxial growth (deposition of a crystalline overlayer) of HA on an OCP surface has been shown to have a “near perfect structural fit” producing a very low interfacial energy, see heterogeneous nucleation section 2.4.1, which would support the hypothesised OCP to HA transition process (Brown *et al.*, 1987). The process by which the mineralised tissues of the body are formed are complex which, as described in section 2.2,

involve a range of different biological processes which are not fully understood. When considering that these mineralised tissues can become damaged, it is a challenge to repair or replace them. One condition, caused through the exposure of dentine tubules to the oral environment, is dentine sensitivity which continues to be a difficult condition to treat.

2.5 Clinical Challenge of Dentine Sensitivity

2.5.1 Definition, Causes and Prevalence of Dentine Sensitivity

Dentine sensitivity is defined as a short sharp pain arising from exposed dentine in response to stimuli, typically thermal, evaporative, tactile, osmotic or chemical, which cannot be ascribed to any other dental defect or pathology (Holland *et al.*, 1997). Diagnosis of dentine sensitivity can be difficult as there are many other conditions that can result in the same symptoms, examples being caries, failed restorations and cracked cusps, which are treated and managed using different procedures (Addy and Peace, 1994). Conservative estimates of the prevalence of dentine sensitivity in the general population range from 3.8% to 35% depending on the population studied (Rees and Addy, 2002) and is most common in people aged between 20-40 years with its peak occurring in adults aged around 30 years old (Bartold, 2006). To be diagnosed as dentine sensitivity, the dentine tubules must be exposed and open.

In healthy teeth, the dentine is covered in a layer of enamel above the gingiva and with a layer of cementum below, with the point at which they meet being called the enamel-cementum junction. There are a number of aetiological and predisposing factors that can result in the removal of the enamel or cementum, rendering the dentine exposed, which can lead to the development of dentine sensitivity (Dababneh *et al.*, 1999).

Enamel can be removed through attrition, abrasion or erosion and it is often a combination of these processes that results in the exposure of the underlying dentine (Dababneh *et al.*, 1999). In the case of the removal of cementum, recession of the gingivae can expose the cementum to the oral environment. The cementum can be easily abraded away once exposed (for example through teeth

brushing) which in turn exposes the underlying dentine. Gingival recession is a condition that itself has a number of causes such as poor dental hygiene, improper brushing and general ageing (Marini *et al.*, 2004; Heasman *et al.*, 2017). In some people a developmental abnormality results in the enamel and cementum not meeting at the enamel-cementum junction which also results in a section of dentine being exposed (Bartold, 2006).

A key part of the definition of dentine sensitivity is not only that the dentinal tubules be exposed but that the dentine tubules must be open. Exposed dentine naturally acquires a layer of organic and inorganic material which covers the dentine surface and produces plugs which penetrate down into the dentine tubules, see Figure 2-6. This layer acts as an insulator, protecting the dentine from pain-causing stimuli. After dental procedures that involve cutting, through the use of chisels, reamers or files, small fragments of mineralised material are produced which can become lodged in the dentine tubules producing a “smear layer” (Eldarrat *et al.*, 2004). Once lodged in the tubules, the layer can become colonised by acid producing bacteria which result in the dissolution of the smear layer mineralised component after 7-10 days which can in turn result in the development of dentine sensitivity in the patient (Pashley, 2013).

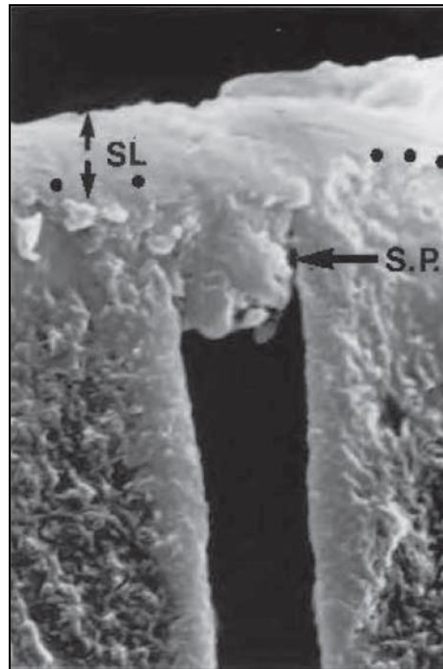


Figure 2-6 Smear layer covered human dentine. SL is the smear layer on the surface while SP is the penetration of the smear layer into the tubule. Image reproduced with permission from Pashley (2013).

2.5.2 Mechanism of Dentine Sensitivity

Several theories have been proposed to explain how stimuli acting on the surface of exposed dentine can be transmitted through the dentine and result in stimulation of the nerves within the pulp (Addy and Dowell, 1983a). The first of these theories is the innervation theory, which postulates that the direct stimulation of nerves within the dentine is what produces the pain response (Fearhead, 1957). If this theory was the true mechanism of dentine sensitivity, the numbing of the nerves within the dentine, and not the nerves of the pulp, would result in the prevention of pain. However, this was proven not to be the case and so it can be concluded that although the innervated nature of dentine could result in the sensing of stimuli and cause pain, it is not solely or at all dependent on the nerves present in the inner third of the dentine (Yu and Abbott, 2007). Another theory is that the odontoblasts act as receptor cells which, with their processes extending into the dentine and up to the enamel dentine junction, are directly stimulated before transferring this stimulation to the nerves within the pulp (Avery and Rapp, 1958). The issue with this theory is that the odontoblasts

are matrix forming cells and are not thought to be able to transmit stimuli as no synapses have been observed between the odontoblasts and the nerve endings (Yu and Abbott, 2007). The final theory, and the most popular one, is the hydrodynamic theory, which postulates that the movement of fluid within the dentine tubule in response to stimuli at the dentine surface causes the nerve ending in the pulp to excite as they are sensitive to a sudden change in pressure and fluid movement (Brannstrom, 1963). The hydrodynamic theory explains why the presence of local anaesthetics applied to dentine does not prevent pain as the nerves are stimulated within the pulp through a distortion of the pulpal pressure.

2.5.3 Dentine Sensitivity Treatments

There are a number of treatment options available to sufferers of dentine sensitivity for use at home and in the clinic. Treatments can be split into one of 2 categories depending on the method used to alleviate the painful symptoms, see Figure 2-7. The first category uses numbing agents which act through diffusing along the dentine tubule and into the pulp. These numbing agents then interact with the nerve endings to reduce their sensitivity to changes in pressure (Bartold, 2006). The second method utilised to provide relief from the symptoms of dentine sensitivity is through the occlusion of the dentine tubules, which prevents the dentine surface stimuli from interacting with the nerves.

As previously mentioned there are many different treatments available and the following section will provide a summary of the main treatment options currently used, along with some of the treatments currently under development. The reason for the large range of treatments available is due to a number of criteria which are thought to be required for a successful treatment. These requirements are: non-irritant to the pulp, easily applied, rapid in action, effective for a long time, without staining effects, consistently effective and relatively painless on application (Kimura *et al.*, 2000). The lack of any treatment which fulfils all the above criteria and the lack of a gold standard treatment to compare new treatments against have resulted in a varied array of treatments using different methods of action and chemical composition to be produced (Dababneh *et al.*, 1999).

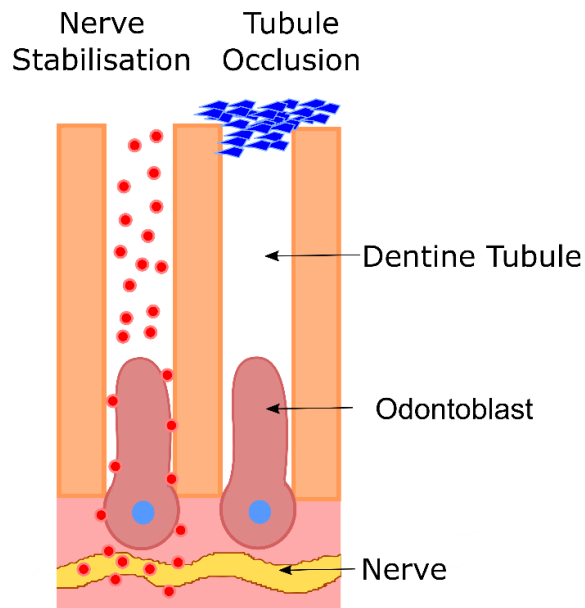


Figure 2-7 The 2 dentine sensitivity treatment strategies, nerve stabilisation through the use of numbing agents (Red) which diffuse down the tubule and prevent stimulation of the nerves. Tubule occlusion blocks the dentine tubule which prevents the change in fluid flow within the tubule due to dentine surface stimuli (Blue).

2.5.4 Nerve Desensitisation Treatments

Potassium salts are known as “numbing agents” and were used as pain relief before the discovery of anaesthetics. Potassium nitrate was first reported to be effective in the treatment of dentine sensitivity by Hodosh and fulfilled some of the criteria required for a successful treatment, these being its effectiveness, non-irritating and non-discolouring effects on teeth (Hodosh, 1974). The mechanism by which potassium nitrate alleviates the symptoms of dentine sensitivity is unknown but it is postulated that the increase in extracellular potassium ions surrounding the nerves could be the mode of action. The increased potassium concentration is thought to depolarise the nerve fibres preventing them from activating in response to a change in pressure or fluid movement (Markowitz *et al.*, 1991). Potassium nitrate, potassium chloride and potassium citrate are all used in nerve desensitising toothpastes. Potassium nitrate is the most commonly used potassium salt with the 2 largest manufacturers, GlaxoSmithKline and Colgate Palmolive, having respectively 9 and 2 different types of toothpaste containing potassium nitrate as their active ingredient (Beddis *et al.*, 2013). Nerve desensitising treatments do not lend

themselves well to clinical use due to the need for repeated applications to maintain the potassium concentration surrounding the nerves, hence their delivery via toothpaste and mouthwash. Potassium nitrate formulated into a mouthwash has recently been shown to be effective in the reduction of dentine sensitivity (Gillam et al., 2018) confirming earlier studies (Gillam *et al.*, 1996)

2.5.5 Occlusion Treatments

Occlusion of the dentine tubules is the other method used in the treatment of dentine sensitivity and there are a variety of different materials and techniques which are used to achieve the occlusion of open dentine tubules. Occlusion treatments can be split into 2 groups: the first occludes through the introduction of compounds which act to block the tubules through the formation of an insoluble layer that penetrates into the tubules and covers the dentine surface or promotes the formation of natural biological minerals within the tubules (Mantzourani and Sharma, 2013); the second group involves the formation of a plugging layer through mechanical means, examples being the brushing of dentine to produce fragments of natural hydroxyapatite which then diffuse into the tubules producing a smear layer (Knight *et al.*, 1993). The following 2 sections will describe a number of treatment options split between those applied at home, through dentifrices, and those applied in clinic by dental professionals.

2.5.6 “At Home” Occlusion Treatments

Strontium in the form of strontium chloride was the active ingredient in the original Sensodyne toothpaste and was first introduced commercially over 50 years ago although this has now largely been replaced by strontium acetate due to its superior clinical efficacy as it is compatible with fluoride (Mantzourani and Sharma, 2013). The mechanism by which strontium acts to alleviate the symptoms of dentine sensitivity is not fully understood but possible explanations of its mode of action include acceleration of the deposition of calcium-containing minerals in the dentine tubules reducing fluid movement and stabilisation of the nerve cell impulses resulting in nerve de-sensitisation (Addy and Dowell, 1983b). Strontium-based dentine sensitivity treatments have been reported to be clinically effective in the reduction of the painful symptoms associated with dentine sensitivity (Kishore *et al.*, 2002) but the evidence for the effectiveness of

strontium (and potassium) based treatments has been questioned and a systematic review carried out by Karim and Gillam concluded that, as yet, there is no clear evidence to support the effectiveness of these treatments (Karim and Gillam, 2013).

A relatively new treatment for dentine sensitivity utilises the amino acid arginine to promote the occlusion of dentine tubules. The treatment is delivered via toothpaste and is currently commercially available as Colgate sensitive Pro-Relief (Olley *et al.*, 2012). The active ingredients consist of arginine, calcium carbonate and fluoride which act to plug the open dentine tubules with a calcium carbonate layer and accelerate the natural mechanism of tubule occlusion through the deposition of dentine-like mineral within the tubules while forming a protective layer on the dentine surface (Petrou *et al.*, 2009). Clinical trials have reported its effectiveness at reducing the painful symptoms associated with dentine sensitivity (Ayad *et al.*, 2009; Schlee *et al.*, 2017). Another clinical trial reported that the arginine treatment was less effective when compared to the strontium acetate treatment when both underwent a dietary acid challenge which suggests that the calcium carbonate layer is more susceptible to acidic diets (Olley *et al.*, 2012).

Another class of compounds used in the treatment of dentine sensitivity are bioglasses. Bioglasses have been developed to consist of specific ratios of silicon dioxide, disodium oxide, calcium oxide and phosphorus pentoxide, and have been reported as effective in the occlusion of dentine tubules (Cochrane *et al.*, 2010; Zhong *et al.*, 2015). The mechanism through which tubule occlusion is produced proceeds in 5 stages. The first stage begins with the diffusion of the bioglass into the dentine and exposure of the glass to an aqueous environment, which results in the exchange of sodium ions within the glass with hydrogen ions in solution, thereby producing an increase in the local pH. The second stage is the loss of soluble silica through the breaking of silicon-oxygen-silicon bonds and the formation of silanols at the glass-aqueous interface. The third stage consists in the condensation of the silanols at the surface of the glass, producing a silicon rich layer. The fourth stage is the migration of calcium and phosphate from within the glass to the surface forming a calcium and phosphate rich layer, and the final

stage results in the crystallisation of an amorphous hydroxyapatite layer which incorporates hydroxyl, carbonate and fluoride anions present in solution (Hench, 1991). The bioglass '45S5' contains 45% silicon dioxide, 24.5% disodium oxide, 24.5% calcium oxide and 6% phosphorus pentoxide and for use in dental applications is marketed under the name "Novamin" (Cochrane *et al.*, 2010). Clinical data suggest that Novamin-based treatment is effective in the occlusion of dentine tubules (Pradeep and Sharma, 2010; Majji and Murthy, 2016). Research into new bioglasses is ongoing with a number of experimental bioglasses being assessed as potential dentine sensitivity treatments (Mitchell *et al.*, 2011; Zhong *et al.*, 2015).

2.5.7 "In Clinic" Occlusion Treatments

A range of topical treatments require application by a clinical professional due to the need for either dentine pre-treatment (drying of the dentine surface or smear layer removal) and direct application onto exposed dentine or application of the treatment in minimal amounts because of toxicity issues. Oxalate containing compounds have been reported to be effective in the occlusion of dentine tubules and a number of different oxalate containing compounds are utilised in treatment. These include, but are not limited to, potassium oxalate, oxalic acid, ferric oxalate and aluminium oxalate (Gillam *et al.*, 2001; Varoni *et al.*, 2017). The mechanism by which oxalates promote the occlusion of dentine tubules is through the reaction of the oxalate molecule with calcium ions present in the oral environment forming calcium oxalate crystals which block the dentine tubules (Mantzourani and Sharma, 2013), though oxalate-based treatments have been shown to poorly penetrate dentine tubules (Greenhill and Pashley, 1981). Clinical trials of oxalate-containing treatments have produced mixed results with some claiming their effectiveness while others concluded that they are no more effective than placebos (Cunha-Cruz *et al.*, 2011). The use of oxalate containing treatments as "at home" treatments are limited because of their toxicity (Guo and McMartin, 2005).

Other professionally applied treatments include resins and varnishes which are applied to promote the occlusion of dentine tubules. The components of these resin and varnish treatments include hydroxyethyl methacrylate, benzalkonium

chloride, glutaraldehyde and fluoride. Glutaraldehyde is thought to act through causing the precipitation of serum albumin from dentinal fluid, this precipitates then inducing the polymerisation of hydroxyethyl methacrylate which blocks the dentine tubules (Qin *et al.*, 2006). Fluoride-based varnishes use a highly concentrated lacquer that acts by inducing the formation of calcium fluoride crystals which block the dentine tubules by producing a layer on the dentine surface reducing fluid movement (Mantzourani and Sharma, 2013).

Laser therapy has also been used in the attempt to find a cure for dentine sensitivity. There are a number of different lasers which have been used in the treatment of dentine sensitivity with different mechanisms of action depending on their power output. Low output lasers, for example He-Ne and GaAlAs, are thought to act through producing an analgesic effect related to depressed nerve transmission (Kimura *et al.*, 2000). Clinical studies have shown that the use of low powered lasers can reduce the painful symptoms associated with dentine sensitivity (Hashim *et al.*, 2014). Higher powered lasers, such as Nd:YAG and Er,Cr:YSGG, have also been used in the treatment of dentine sensitivity. These high power lasers are thought to act through melting and recrystallisation of dentine mineral or through obliterating the dentine tubules by stimulating tertiary dentine production (Yilmaz and Bayindir, 2014). Studies have been carried out on the effectiveness of using high powered laser light and have reported its effectiveness *in vitro* (Kurt *et al.*, 2018) and in the clinic (Yilmaz and Bayindir, 2014). Surgical procedures can also be used in the treatment of dentine sensitivity and involve the grafting of healthy gingiva to the region of gingival recession, thereby re-sealing the exposed dentine, through the occlusion of the tubules. This type of treatment is invasive and, as it is a graft, will result in some form of donor site morbidity. Additionally good periodontal health is also required before surgical intervention (Tugnait and Clerehugh, 2001).

2.6 Measurement of Dentine Permeability

2.6.1 *In Vitro* Techniques

The ability to determine the potential of materials for occlusion of dentine tubules in the lab is an important step in the development and assessment of a dentine

sensitivity treatment. When we consider the mode of action of a dentine tubule occluding treatment, which is decreasing fluid movement within the tubule through blocking the tubule at the surface, the need to be able to determine the reduction in fluid flow through dentine, once the treatment material of interest has been applied, is required. One method used to determine the change in permeability of dentine is fluid filtration.

Fluid filtration is a technique which measures the volume of fluid which can be forced through a material of interest under a given hydrostatic pressure per unit area of time per unit of pressure (Ertürk and Kirzioğlu, 2007). The first generation fluid filtration dentine measurement apparatus required the visual observation of a bubble in a micropipette which was part of the fluid line. When the bubble was moved by fluid flow, the distance moved was noted which allowed for the calculation of the amount of fluid which had passed through the dentine (Reeder *et al.*, 1978). This technique was later improved through the use of an electronic flow detector which electronically tracked the movement of the bubble removing the need for visual recording of the movement. A full review of the fluid filtration technique is described in section 6.1. In brief, the fluid filtration technique is able to determine the bulk permeability of the dentine under test but other techniques are able to provide information on small areas of the dentine surface. One such technique is laser scanning confocal microscopy, which, under optimal conditions, could provide the fluid flow rate through a single tubule. The advantage of using a confocal-based technique is that it may be able to determine the treatment effectiveness with respect to differing dentine tubule structures (Williams *et al.*, 2008).

2.6.2 Clinical Trials

Clinical trials involving patients are essential for the testing of efficacy of dentine sensitivity treatments. There are a number of issues with regards to clinical trials which have made the comparison of clinical data difficult and are the cause of much confusion due to conflicting results (Holland *et al.*, 1997). The basic method used to conduct a clinical trial of a dentine sensitivity treatment is to apply a stimuli to a patient's sensitive dentine and record some type of pain response. The treatment is then applied before stimuli and pain response are recorded

again. The difference in the pain scores is then used to determine the effectiveness of the treatment. This seems very straight forward but there are a number of issues that need to be addressed before any conclusions on the effectiveness can be reported.

The method of stimulation is important as not all types of stimulation are suitable for quantifying dentine sensitivity, which may differ for different types of stimulation (Holland *et al.*, 1997). To negate these factors it has become generally accepted that thermal stimulation should be accompanied by a tactile stimulus (Orchardson and Collins, 1987) although the reproducibility of the tactile stimulus can be questionable due to the need for the clinician to manually scratch the dentine surface (Ide *et al.*, 2001).

The most common method for recording the pain scores produced through these studies is the visual analogue scale (VAS) which, although used widely in clinical research (Ide *et al.*, 2001; Haefeli and Elfering, 2006), has a number of disadvantages. The VAS measurement requires the patient to rate their pain along a line from “no pain” to “pain as bad as it could be” by placing a cross on the line. This method of pain rating can be useful but it is limited by the patient’s own interpretation of how painful “pain as bad as it could be” is to them, and when we consider a study that happens over a period of weeks the patients perception of pain could vary over a given time period (Wewers and Lowe, 1990).

A report into the reproducibility of clinical dentine sensitivity assessment concluded that the reproducibility was not as good as expected in clinical trials and that trials carried out on dentine sensitivity treatments were not as good as initially assumed due to the reasons given previously (Ide *et al.*, 2001).

2.7 Inspiration from Nature

The difficulty in producing effective dentine sensitivity treatments coupled with the challenge of assessing their effectiveness both *in vitro* and *in vivo* in reducing the pain symptoms associated with the condition has led to increased research into the development of materials which take inspiration from nature. As previously discussed, section 2.2, biological systems have developed complex processes to produce mineralised tissues. Although our current understanding

prevents the direct replication of the biological process, materials could be developed which mimic known biological mineralising agents to promote the occlusion of dentine tubules.

2.8 Biomimetics

The term biomimetic was coined by Otto H. Schmitt in 1969 and represents the field of study that aims to mimic nature's methods, designs and processes and is increasingly being applied to the fields of science and engineering (Bar-Cohen, 2006a). The process of evolution has allowed nature to experiment with numerous challenges and when successful has archived the information into the DNA of living systems. These solutions can range in complexity. Some are relatively easy to mimic, for example the use of fins in scuba diving to aid with swimming which have been copied from the legs of sea creatures such as seals (Bar-Cohen, 2006b). Other are far more complicated and the outcome of these solutions can have properties that are novel and surpass the capabilities of man-made ones. An example of this is the silk (composed of proteins) produced by spiders. Silks display remarkable properties such as having high ultimate tensile strength and mechanical stability at high temperatures (Bar-Cohen, 2006b). The complex biological processes that produce silk have made replicating its formation difficult although progress is being made (Carlson *et al.*, 2006).

The growing field of tissue engineering and regenerative medicine has increasingly been trying to use the principles of biomimicry to produce biomaterials that can provide a range of properties including, but not limited to, the characteristic extracellular matrix environment that is essential for the cellular decision process (Patterson *et al.*, 2010), controlled drug delivery (Biondi *et al.*, 2008) and protein templates in hard tissue repair/replacement (George and Ravindran, 2010).

2.9 Peptide Biomimetics

Synthetically derived peptides which can mimic the functionality produced by biological systems are increasingly seen as providing a route to new biomaterials for use in tissue engineering, drug delivery and therapeutics (Bello *et al.*, 2013).

The analysis of biological systems and the determination of the mechanism by which they achieve their function have allowed new materials with a range of applications to be produced. Examples include, but are not limited to, the synthesis of cyclic peptide antibiotics (Trauger *et al.*, 2000), the prevention of skin ageing (Gazitaeva *et al.*, 2017) and drug delivery (Bhattacharyya *et al.*, 2016).

With respect to dental applications, synthetic peptide-based materials have been developed with the goal of providing treatment for dentine sensitivity (Wang *et al.*, 2014), and for the regeneration of the hard tissues of the tooth (Kirkham *et al.*, 2007; Dogan *et al.*, 2018). One such peptide recently developed is a new amelogenin-derived 15-amino acid long peptide (ADP5). It has been developed through the screening of a cysteine-constrained M13 bacteriophage heptapeptide library against hydroxyapatite (HA) powder to identify HA binding affinity (Gungormus *et al.*, 2008). This screening resulted in the production of the peptide ADP5 which has been shown to produce a 10 μm thick layer of HA resembling enamel when applied to artificial white spot lesions of enamel followed by incubation for 1 hour in 4.80 mM Ca^{2+} /2.89 mM PO_4^{3-} (Dogan *et al.*, 2018). The ADP5 peptide was also tested after 1 hour incubation 4.80 mM Ca^{2+} /2.89 mM PO_4^{3-} with 1100 ppm F to determine if the peptide was compatible with fluoride levels found in toothpastes. SEM and EDS analyses of the crystal morphologies and compositions formed for both sets of experimental conditions confirmed a change in crystal morphology when fluoride was present. When no fluoride was present, the crystals formed produced a thick layer (10 μm) of HA nanorods while when fluoride was present, 2 crystal morphologies formed: clusters of 50-100 nm spherical nanoparticles, and structures composed of nanorods that were similar but less dense than the non-fluoride test. It was not possible to use the EDS technique to determine if the different mineral morphologies had different molar compositions of HA and FA due to the overlapping nature of the 2 phases but the overall molar Ca/F ratio was 8.74 ± 0.78 . The authors hypothesised that the small spherical nanoparticles could be FA while the nanorods were HA. The analysis of the newly formed HA layer showed integration with the underlying enamel supporting the development of peptide-based materials to treat damaged enamel.

A study produced by Wang *et al.* (2014) investigated the use of a collagen/calcium dual affinity peptide combined with nanoHA with respect to its ability to promote the mineralisation of dentine tubules (Wang *et al.*, 2014). The treatment developed by Wang *et al.* used a synthetic polypeptide designed to have affinity for both hydroxyapatite and collagen and combined it with commercial nanoHA powder. The dual affinity peptide was designed by connecting an 8 amino acid long glutamic acid peptide (EEEEEEEE) sequence inspired by bone sialoprotein, known to have a strong binding affinity to HA (Goldberg *et al.*, 2001), to a 9 amino acid sequence (DSpESpSpEEDR) inspired by DMP1 which has been identified as collagen interacting by peptide sequence mapping (He and George, 2004). The 2 peptide sequences were attached to produce the peptide E8DS peptide sequence (EEEEEEEEEDSpESpSpEEDR). The hypothesised treatment mechanism was that the E8DS peptide would bond to the acid etched demineralised dentine collagen and to the synthetic nanoHA crystals, thus promoting the attachment of the nanoHA to the surface of the dentine. It was also hypothesised that the nanoHA particles would penetrate into the tubules promoting occlusion deep within them, see Figure 2-8. The treatment methodology involved the application of the peptide to the dentine surface at a concentration of 1 mg/mL peptide followed by brushing with nanoHA crystals (25 mg/mL). The peptide treated samples were then washed continuously at a flow rate of 1 mL/min for 4 weeks and assessed using SEM to determine mineralisation of the dentine surface and dentine tubules. The results showed that the D8DS/nanoHA treatment did produce a compact layer of nanoparticles on the surface of the dentine but the predicted penetration into the tubules did not occur to the depth that was anticipated with no mineralisation visible within the dentine tubules (Wang *et al.*, 2014).

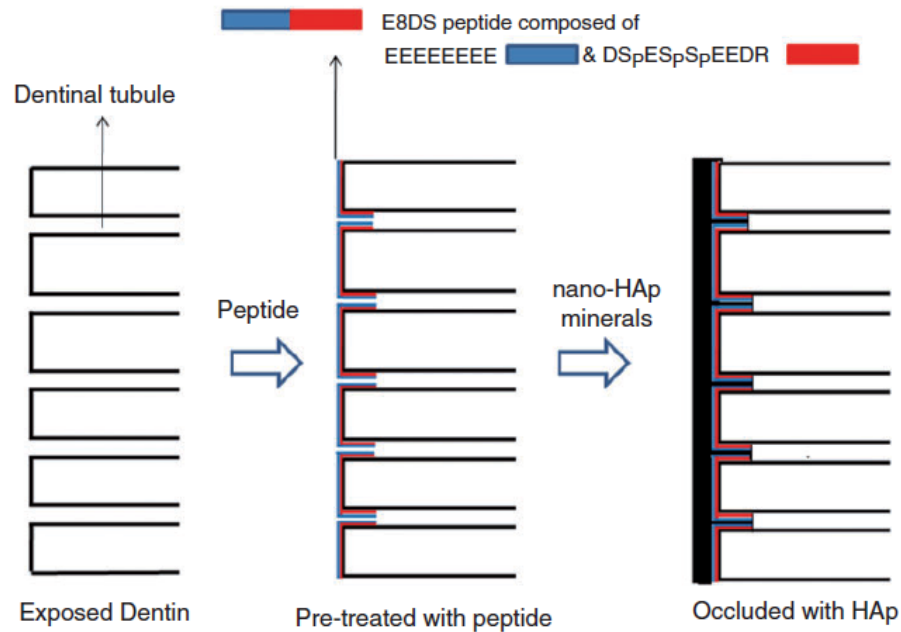


Figure 2-8 - Schematic of proposed treatment mechanism of D8DS. Exposed and open dentine tubules were treated with E8DS peptide. NanoHA then brushed onto surface which would interact with the peptide not only on the surface but within the dentine tubules. Schematic from Wang *et al.* (2014).

One issue which may have reduced the Wang *et al.* (2014) treatment's ability to penetrate the dentine tubules was the nanoHA crystals themselves. The stated size of the nanoHA crystals was 20 nm but on inspection of the TEM images produced, the crystals look amorphous in shape and were significantly larger when compared to the 20 nm scale bar. No particle characterisation techniques were published by the authors and on inspection it is difficult to determine if these are in fact individual particles aggregated together or very large amorphous crystals. The nanoHA suspension was placed under ultrasonic agitation for 30 minutes prior to addition but due to the lack of characterisation and confirmation of the nanoHA suspension, for example using DLS, it cannot be determined whether the nanoHA was still in an aggregated state or present as large amorphous crystals.

The second potential issue with respect to achieving the hypothesised nanoHA penetration into the dentine tubule was the treatment's application. The step wise addition of E8DS and then nanoHA could be improved through using the treatment components simultaneously, which could aid in dentine tubule

penetration. It was shown that the E8DS peptide penetrated the dentine tubule to a depth of 5 μm using fluorescence microscopy but no HA mineralisation was visible within the dentine tubules. Combining the E8DS peptide with the nanoHA, similar to the hybrid material assessed in this thesis, may well result in the nanoHA penetrating the dentine tubule with the peptide. The E8DS/nanoHA interaction would also need to be investigated to ensure the material maintained its functionality with respect to dentine adhesion.

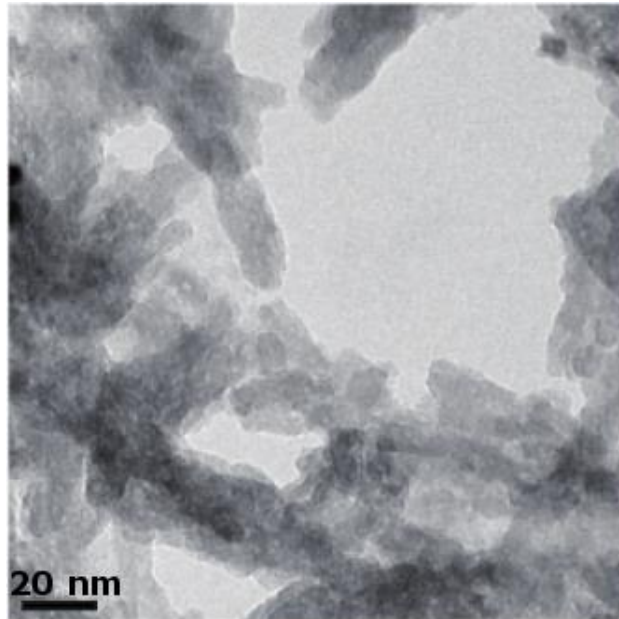


Figure 2-9 TEM images of nanoHA crystals used in Wang *et al.* (2014). Crystals are poorly resolved and look larger than the 20nm stated by the author. Image modified from Wang *et al.* (2014).

2.10 Self-Assembling Peptides

Self-assembling peptides (SAPs) are inspired by the understanding of protein self-assembly and are capable of forming a number of higher order structures (Aggeli *et al.*, 1997). SAPs are polypeptide molecules which can interact through non-covalent interactions in a hierarchical manner to produce structurally well-defined aggregates or “assemblies”. The structure and function of the aggregates produced are dependent on the isomeric form of the amino acids, the sequence of the amino acids in the polypeptide chain, the concentration of peptide in solution and the solution conditions, for example pH, temperature and ionic strength (Carrick *et al.*, 2007). There are a number of different nano-

structures that can be produced through peptide self-assembly. Examples include but are not limited to nanotubes (Hartgerink *et al.*, 1996), nanospheres and nanotapes (Matsuura *et al.*, 2005). The diversity of the types of structures that can be created, their intrinsic biocompatibility and biodegradability, and the ability to synthesise them in large quantities have made them the subject of major interest (Mandal *et al.*, 2014).

Particularly relevant to dental hard tissue engineering and this project are anti-parallel β -sheet forming peptides which can undergo hierarchical self-assembly to form 3-dimensional fibrillar networks (Aggeli *et al.*, 2001). The hierarchical self-assembly of antiparallel β -sheet forming peptides has been extensively studied with respect to the aggregates formed and the thermodynamic parameters which drive the aggregate formation (Aggeli *et al.*, 1997; Aggeli *et al.*, 2003a; Davies *et al.*, 2006; Carrick *et al.*, 2007; Kyle *et al.*, 2010). The principle forces which drive peptide self-assembly are the hydrogen bonding between the peptide backbone and the non-covalent interactions of the side chains (Kirkham *et al.*, 2007).

The hierarchical self-assembly process of the SAPs developed at the University of Leeds begins when the concentration of peptide monomer (solvated peptide molecule) reaches the critical monomer concentration (C^*). This is the concentration at which the peptides can form stable aggregates (Davies *et al.*, 2006). At concentrations larger than the C^* value, aggregates will form, although there is always a background concentration of monomer which is equal to the C^* . This is a consequence of the reversible nature of peptide self-assembly which follows Le Chatelier's principle of equilibrium. The size and structure of the peptide aggregates are dependent on the concentration of monomer present and follow the hierarchical sequence described in Figure 2-10.

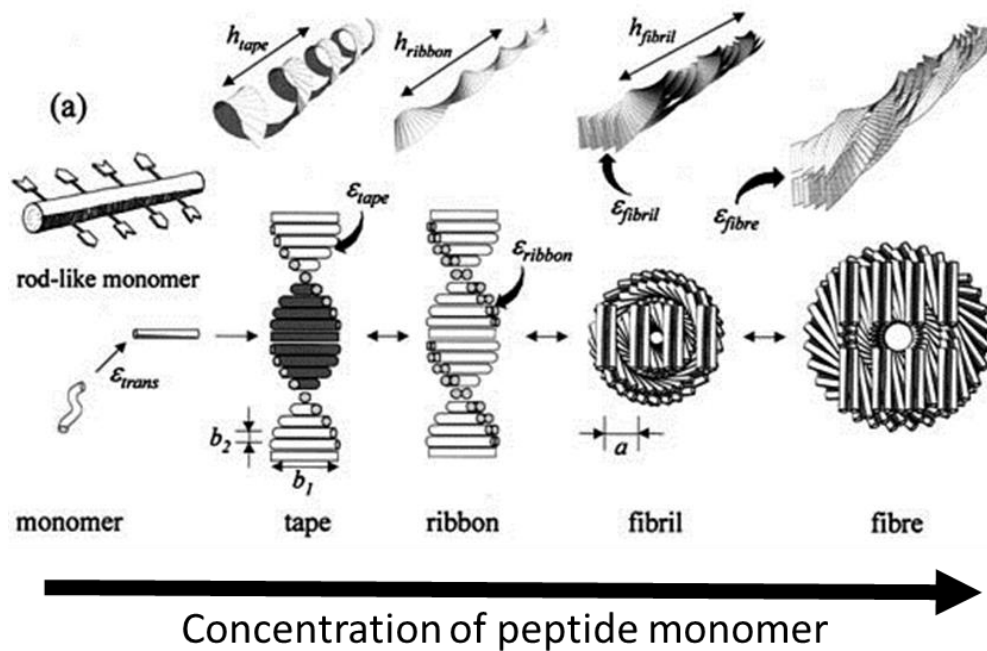


Figure 2-10 Schematic of the hierarchical self-assembly of anti-parallel β -sheet forming peptides as a function of peptide monomer concentration. At low concentrations below the critical concentration (C^*) peptide monomers exist in solution. As the concentration increases above C^* the monomers interact to form β -sheet tapes which can then go on to interact to form ribbons, then fibrils and finally fibres with respect to increasing peptide monomer concentration. Image modified from Aggeli *et al.* (2001) Copyright (2001) National Academy of Sciences.

An anti-parallel β -sheet forming self-assembling peptide has been developed at the University of Leeds and was reported as safe for use and associated with significant enamel regeneration in the treatment of early caries lesions in a clinical safety trial (Brunton *et al.*, 2013). The peptide P₁₁₋₄ has been previously shown to produce fibrillar networks that mimic the biological macromolecules found in the extracellular matrices of the mammalian skeleton which are known to control the mineralisation of hard tissues (Kirkham *et al.*, 2007). The 11 amino acid long P₁₁₋₄ (amino acid sequence AcQQRFEWFEQQNH₂) was designed to self-assemble at $\text{pH} \leq 2$ in deionised H₂O (Davies *et al.*, 2006). The design principles used to drive self-assembly were principally the complementary hydrogen bonding between the glutamic residues at positions 1,2,10,11 combined with hydrogen bonding of the peptide backbone between peptide molecules. The hydrophobic amino acids phenylalanine, at positions 4 and 6,

and tryptophan at position 8, can interact through π - π stacking and stabilise the ribbon level of the β -sheet self-assembly hierarchy (Kyle *et al.*, 2010). The 3 glutamic acid residues, at $\text{pH} \leq 2$, would be protonated (neutral charge) due to the negative charge stabilising effects of the aromatic residues resulting in a $\text{pK}_a < 4.25$. The arginine residue would be protonated (positive charge) producing an overall positive peptide charge of +1. When dissolved in deionised H_2O at a $\text{pH} > 2$, no self-assembly occurs due to the negatively charged glutamic acid residues which produce repulsive forces between peptide molecules (Davies *et al.*, 2006). Interestingly when the P_{11-4} peptide was investigated under physiological conditions of $\text{pH} 7.4$ and $\text{NaCl} 130 \text{ mM}$, the repulsive forces of the negatively charged amino acid groups were shielded by the salt ions present in solution coupled with the ionic interaction between the positively charged arginine and the negatively charged glutamic acid, resulting in the self-assembly of P_{11-4} at a $\text{pH} \leq 7.5$ (Carrick *et al.*, 2007). A schematic of the amino acid sequence, with corresponding protonation state at physiological pH is shown in Figure 2-11. The surface formed by the self-assembled P_{11-4} produces sites of negative charge (4 deprotonated Glu-residues) which, through molecular dynamics simulations, have been shown to be approximately 0.94 nm apart which would match the columnar Ca^{2+} ions in the hydroxyapatite crystal (Thomson *et al.*, 2014). The negative charge domains on the self-assembled surface are thought to act as a heterogeneous nucleating template, dehydrating the calcium ion producing a nucleating centre.

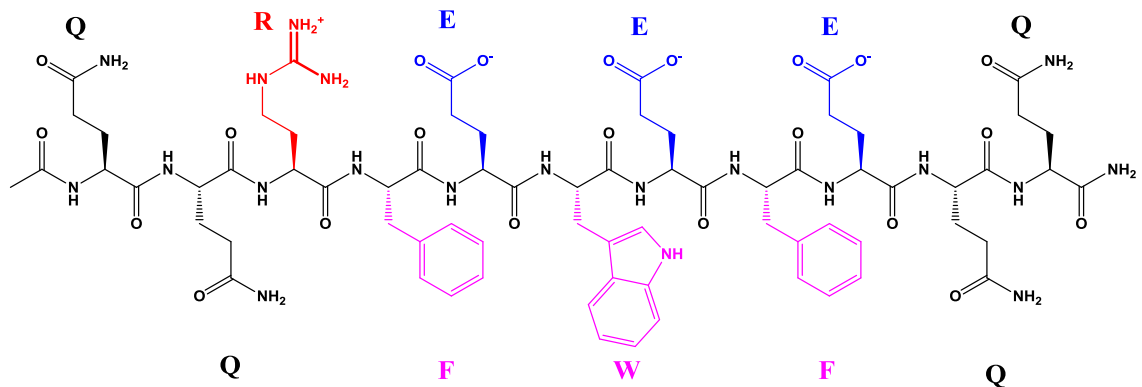


Figure 2-11 P₁₁₋₄ amino acid sequence protonation states at physiological pH (7.4). The glutamic acid residues are deprotonated (blue) producing a negative charge (-3) and the arginine side chain is protonated (red) producing a positive charged (+1) resulting in an overall charge per molecule of P₁₁₋₄ of -2. Hydrophobic side chains tryptophan and phenylalanine (lilac) provide sites for π - π interactions for stabilisation of the tape-tape interaction present in the ribbon level of β -sheet hierarchy. The peptide backbone and glutamine residues (black) form complementary hydrogen bonding between peptide molecules.

2.11 Concluding Remarks

In conclusion, the lack of a “gold standard” treatment for dentine sensitivity has produced a plethora of treatments with no one treatment being able to conclusively prove its effectiveness when compared to others. The occlusion of dentine tubules seems to be the superior strategy as it could provide a permanent alleviation of dentine sensitivity if a suitable material can be developed. Nerve stabilisation treatments seem to be the inferior choice due to their need for frequent re-application and relatively long time to take effect. The biomimetic self-assembling peptide treatment based on P₁₁₋₄, now CE-labelled for clinical use illustrates the strategy of biomimetics in the regeneration of enamel (Brunton *et al.*, 2013). If the mineralisation ability of the self-assembling peptide P₁₁₋₄ could be translated into the treatment of dentine sensitivity, it could have the potential to provide a superior treatment option. The rationale of using nano-hydroxyapatite crystals in tandem with the peptide treatment is supported by the energetic considerations of mineral formation. By providing a crystal seed

the energetically unfavourable formation of a nucleus in solution is avoided which should increase mineralisation and decrease the time for the treatment to take effect. The work carried out by Wang *et al.* (2014) although promising does contain some issues, such as the lack of mineral penetration into the tubules, which would need to be improved if the treatment is to provide a permanent solution. This issue may be resolved through the use of optimisation of the treatment with regards to nano-hydroxyapatite crystal size or type and concentration of peptide used.

2.12 Project aim

To investigate a combination of rationally designed self-assembling peptides (SAPs) and nano-apatite as novel hybrid biomaterials for the infiltration and occlusion of dentinal tubules as a possible future treatment option for dentine hypersensitivity.

Project Objectives:

- 1) Synthesise and characterise nanoHA crystals with optimum chemistries and sizes to act as seed crystals using hydrothermal and chemical synthesis, electron microscopy, X ray diffraction, scanning electron microscopy and dynamic light scattering;
- 2) Using nanoHA seed crystals produced and characterised in (1) above, determine the efficacy of a rationally designed self-assembling peptide/nanoHA hybrid material to nucleate and support the growth of hydroxyapatite mineral *in vitro* under steady state conditions;
- 3) Develop quantitative and qualitative methodologies to determine the effect(s) of the SAP-nanoHA hybrid material on dentine permeability and dentine tubule occlusion in extracted human teeth using dentine fluid filtration and scanning electron microscopy.

Chapter 3 – Synthesis and Characterisation of Nano-sized Hydroxyapatite Seed Crystals.

This chapter will describe the synthesis of hydroxyapatite nanorod powders using a hydrothermal synthesis method. The characterisation of the synthesised powders by x-ray diffraction, scanning electron microscopy, dynamic light scattering, transmission electron microscopy and energy-dispersive x-ray spectroscopy will also be described. These characterisation techniques enabled crystal structure, morphology, size and atomic composition to be confirmed. The powder analysis confirmed the formation of nanohydroxyapatite nanorods with a median long axis length of 45 nm. In total, 3 batches of crystals were synthesised with batch 2 suspected of being a calcium deficient hydroxyapatite and was not used in subsequent experiments. The nanohydroxyapatite powders produced in batches 1 and 3 were later combined with a self-assembling peptide material to produce the hybrid material investigated in this thesis.

3.1 Introduction

Nano-sized hydroxyapatite (nanoHA) crystals are seen as an attractive method to promote the growth of mineral deposits in oral healthcare due to their favourable biocompatibility and bioactive properties and have been used in a number of dental applications (Huang et al., 2009; Sadat-Shojai et al., 2010; Najibfard et al., 2011; Hillet al., 2015a). The advantage of using nanoHA compared to micron sized and above HA crystals as seed crystals is primarily due to the increased specific surface area to seeding density ratio. In nanoHA, the total surface area for a given weight is significantly larger than for micron sized particles, providing a larger surface for heterogeneous crystal nucleation.

There are a number of different techniques that are used to produce nanoHA, with a range of sizes, crystallinity and morphologies possible (Sadat-Shojai et al., 2013). Chemical precipitation reactions have been shown to produce nanoHA powders with the morphology and size controlled by the conditions used, for example pH, reaction time, stirring speed and atmospheric conditions (Afshar et al., 2003). The methodology commonly involves the addition of an ionic calcium solution to an ionic phosphate solution under string while maintaining a pH of between 8-10 and constant temperature. The advantage of chemical precipitation is that it can produce nanoHA at a low cost and with a variety of morphologies. Potential disadvantages are that often the nanoHA is not stoichiometric with respect to hydroxyapatite and can contain other calcium phosphate mineral phases (Abidi and Murtaza, 2014).

Hydrothermal synthesis can be considered a chemical precipitation reaction followed by a thermal treatment at high temperature and pressure. The hydrothermal method provides a highly crystalline sample with excellent control of crystal size and distribution through control of pH, temperature, pressure and treatment time (Suchanek and Riman, 2006). Hydrothermal synthesis of nanoHA often results in a small size distribution, rod/needle morphology, highly crystalline and single phase powders. The disadvantages of hydrothermal synthesis of nanoHA is that the reactor cost is very high and due to its tendency to produce nanoHA with rod like morphology is not useful if other morphologies (for example spheres) are required.

There were a number of considerations which were taken into account when the method of nanoHA synthesis used in this work was chosen. The hydroxyapatite crystallites in dentine have been reported as having a rod shaped morphology, 2-3 nm in diameter and up to 60 nm in length (Goldberg *et al.*, 2011). The production of a nanoHA particle that not only enabled the infiltration of the dentine tubule but also provided a crystal morphology similar to that of the already present biological apatite crystals was desired. A second criterion was that the nanoHA particles were single phase and highly crystalline. The use of a nanoHA seed crystal that was highly crystalline and single phase hydroxyapatite would support the growth of crystalline hydroxyapatite. The improved mechanical properties and insolubility of crystalline hydroxyapatite compared to other biologically relevant calcium phosphate phases supports the desired growth of hydroxyapatite within the dentine tubule (Goldberg *et al.*, 2011).

The use of a method to produce a small size distribution was desired to ensure that the majority of the nanoHA would be of a small enough size to penetrate down into the dentine tubule. Previous work by Earl *et al.* (2006a) and Sayed *et al.* (2013). have shown that hydrothermal synthesis can provide nanoHA which is highly crystalline, single phase, stoichiometric HA, with a small size distribution that is capable of penetrating dentine tubules and providing crystal nuclei to promote crystal growth. For these reasons the hydrothermal method of nanoHA synthesis was chosen.

3.2 Methods

3.2.1 Hydrothermal Synthesis of Nanohydroxyapatite

The hydrothermal method used in this thesis was initially developed by Earl *et al.* (2006b). Stock solutions of 1 M calcium nitrate tetrahydrate ($\text{Ca}(\text{NO}_3)_2 \cdot 4\text{H}_2\text{O}$, Acros Organics ACS grade, Geel, Belgium) and di-ammonium hydrogen phosphate ($(\text{NH}_4)_2\text{HPO}_4$, VWR Chemicals, Radnor, PA, USA) were prepared in distilled water. These were then further diluted to 0.1 M before the drop wise addition, via an addition funnel, of di-ammonium phosphate solution to calcium nitrate solution to produce a suspension with a Ca/P molar ratio of 1.67. The suspension was then pH adjusted to 10 (Hanna Instruments HI2211-02 pH meter Woonsocket, RI, USA, fitted with a VWR pH electrode DJ 113, Radnor, PA, USA) through the addition of 28-30% ammonium hydroxide solution (Sigma-Aldrich ACS Grade St. Louis, MO, USA), then transferred to a 2 L stainless steel hydrothermal reactor vessel (Parr instruments model 4524 Moline, IL, USA). The suspension was then heated with stirring at approximately 500 rpm, and once the target temperature of 200°C was reached, left for 24 hours. Once the 24-hour heating period was complete, the heater was switched off, the heating jacket removed and the reactor was left to cool under stirring for a further 24 hours. The suspension was poured into 50 mL falcon tubes and underwent a washing cycle of centrifugation (Thermo Fisher Scientific Heraeus Megafuge 16R, Waltham, MA, USA) at 16500 g, supernatant removal and resuspension in distilled H_2O aided by ultrasonic agitation (Ultrawave Ltd, 120W, 4L, UK) and vortexing (Vortex Genie 2 Scientific Industries, Bohemia, NY, USA). This process was repeated 6 times with ethanol replacing H_2O in the last 2 washes and a centrifugal speed of 30000 g. The particles were suspended a final time in ethanol before being poured into a foil lined tray and placed in a fume hood overnight. To ensure all the ethanol had evaporated, the tray was then transferred to a heated cabinet at 50°C overnight. Once dry, the powder was collected and stored in 50 mL falcon tubes under vacuum. The synthesis was completed 3 times producing 3 batches of nanoHA powders.

3.2.2 Powder Characterisation

The 3 synthesised powder batches were characterised using the methods outlined below. A commercially available nanoHA sample was also characterised to provide a control sample (Sigma-Aldrich, nanopowder, <200 nm particle size (BET), ≥97%, synthetic St. Louis, MO, USA).

3.2.2.1 X-Ray Diffraction

Powders were loaded into the spinner type sample holder using the back fill method to ensure a flat homogenous test surface. The sample was then loaded into the x-ray diffraction instrument (XRD Phillips X'pert, Amsterdam, Netherlands) and scanned over a 2θ range of $10-60^\circ$ using a scan speed of $0.027^\circ \text{ s}^{-1}$. The resulting spectrum was processed using the Highscore software (Phillips, Amsterdam, Netherlands) by performing a baseline correction followed by automatic peak fitting. These selected peaks were then compared to the ICDD reference database to confirm the crystal structures present.

3.2.2.2 Dynamic Light Scattering

Powder suspensions were produced in ethanol at a concentration of 0.2 mg/mL. All samples were thoroughly vortexed and sonicated (Ultrawave Ltd, 120W, 4L, UK) to ensure dispersion and limit aggregation during measurement. A small volume (approx. 1 mL) of sample was placed into a disposable cuvette and placed into the Malvern Zetasizer ZS device (Malvern Instruments Ltd, UK) and analysed with the average of 3 runs per sample being produced.

3.2.2.3 Scanning Electron Microscopy

Carbon adhesive disks were attached to 15 mm SEM stubs (Agar Scientific Ltd, UK) and then coated with a small amount of each batch of nanoHA powder. The samples were then sprayed with compressed air to remove any loose particles and coated in carbon (Agar Automatic Carbon Coater, Stansted, UK). Samples were then loaded and imaged in turn with a Hitachi SU8230 scanning electron microscope (Hitachi, Tokyo, Japan) 20 kV accelerating voltage, 21.1 μA emission current with secondary electron emission detection. EDS spectra of each batch were obtained (Oxford Instruments Aztec Energy EDX system with 80mm X-Max SDD detector, Abingdon, UK) to allow for the atomic composition

and therefore the Ca/P molar ratio to be calculated and compared to the theoretical HA ratio of 1.67 (He *et al.*, 2003).

3.2.2.4 TEM

A small amount of each powder was suspended in ethanol at a concentration of 50 µg/mL. All suspensions were vortexed and sonicated to ensure dispersion. A small amount of each suspension was dropped onto copper TEM grids and left to dry. Each sample was then imaged by TEM (Thermo Fisher Scientific FEI Tecnai TF20: FEGTEM, Waltham, MA, USA) using 200 kV accelerating voltage and emission current 1 µA. Size distributions were then produced through the measurement of the longest axes of 200 particles from each batch using ImageJ. The data was then statistically analysed using SPSS 21 (IBM, NY, USA) using the non-parametric tests independent samples median test, Mann-Whitney U test and Kolmogorov Smirnov test.

3.3 Results

3.3.1 Hydrothermal Synthesis of NanoHA Batches

To synthesise the nanoHA which would later be used to infiltrate human dentine tubules as part of the hybrid material, the hydrothermal method was chosen due to its ability to produce hydroxyapatite crystals with nanorod morphology which are capable of penetrating dentine tubules (Earl et al., 2006b). Synthesis of nanoHA was completed as described in section 3.2.1. The powders produced in the 3 hydrothermal experiments were white in colour with no visible differences between the 3 batches. The powder produced was visibly finer than the Sigma powder, which was more granular. All samples were stored in a vacuum desiccator when not in use. Yields for batches 1, 2 and 3 were 7.64 g, 6.89 g and 7.25 g respectively.

3.3.2 X-Ray Diffraction of NanoHA Batches

To determine the crystal structure and confirm the formation of hydroxyapatite samples in the synthesised powders obtained in batch 1, 2, 3 and in the powder purchased from Sigma, samples were loaded into the XRD powder sample holder, scanned and processed as described in section 3.2.2.1. The resulting spectra, see Figure 3-1, were stack plotted together and the selected peaks labelled with a dotted line. The list of peaks for each sample was then submitted to the ICDD database and compared. When compared to the reference database, all powders used here had the same hexagonal crystal system with $P6_3/M$ point group (LeGeros, 1994). Batch 2 was the only batch which did not confirm the presence of hydroxyapatite, see Table 3-1. Instead it matched to a hydrated form of hydroxyapatite called calcium phosphate hydroxide hydrate with the formula $Ca_{4.65}(PO_4)_3(OH)_{0.3}(H_2O)$.

Powder sample	Matched reference	Ref Code ICDD
Batch 1	Hydroxyapatite	04-016-2958
Batch 2	Calcium Phosphate Hydroxide Hydrate	04-012-1119
Batch 3	Hydroxyapatite	01-074-0565
Sigma sample	Hydroxyapatite	01-080-6199

Table 3-1 Table showing which reference samples matched the synthesised and Sigma powder samples. Batches 1, 3 and Sigma matched hydroxyapatite references while batch 2 matched a calcium deficient hydroxyapatite

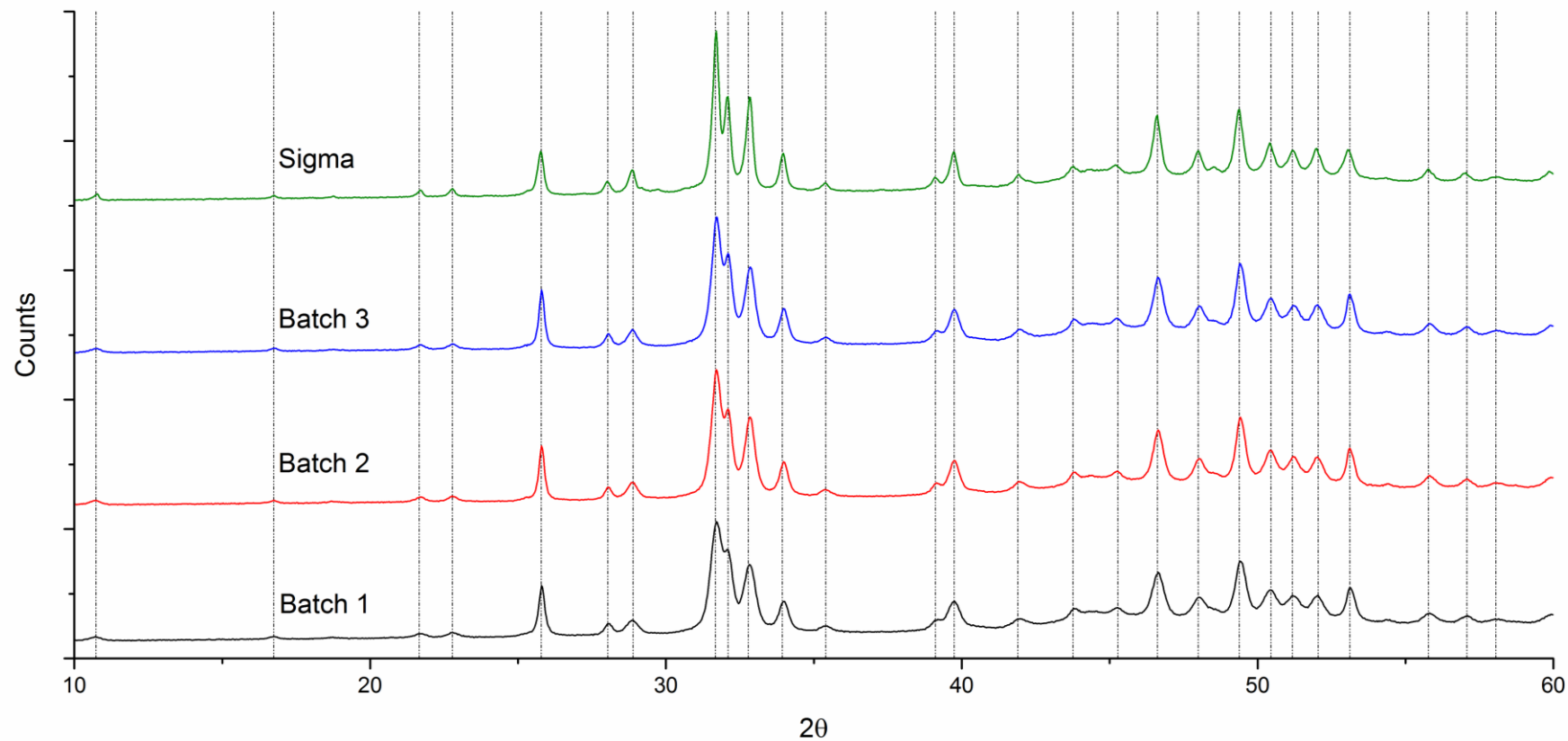


Figure 3-1 Graph showing XRD patterns produced from batch 1, 2, 3 and Sigma nanoparticles. Dashed line represent common peaks between samples (average standard deviation between peaks 0.02 2θ). Batch 1, 3 and Sigma all confirmed a hydroxyapatite crystal structure while batch 2 confirmed a hydrated form of hydroxyapatite.

3.3.3 Scanning Electron Microscopy of NanoHA Batches

To confirm the morphology of the crystals within the powders produced as described in section 3.2.1, samples were prepared as described in section 3.2.2.3 and analysed using SEM. SEM analysis confirmed the presence of rod shaped particles in all of the synthesised batches and spherical shaped particles in the Sigma sample, see Figure 3-1. It was not possible to provide a size distribution as the density of particles prevented accurate measurement.

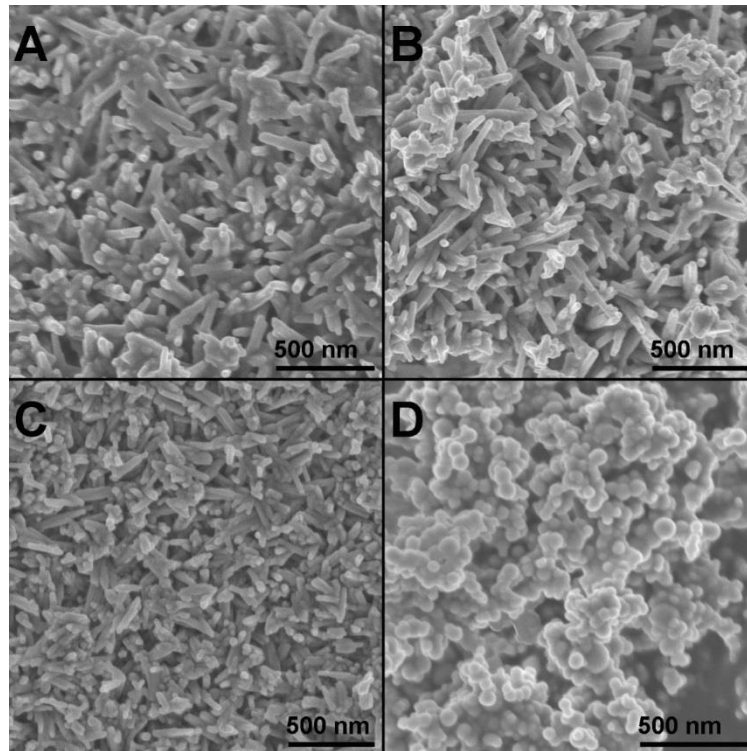


Figure 3-2 SEM images of powders from A) batch 1, B) batch 2 and C) batch 3 all showing densely packed rod shaped particles. In contrast, D) Sigma powder showed spherical particles. Density of particles prevented measurement although morphology was clearly visible.

EDS measurements of the powder material were also taken, with the molar Ca/P ratios for each sample presented in Table 3-2. The Ca/P ratios present in Table 3-2 show that the batches 1 and 3 confirmed a close value compared to the theoretical ratio of 1.67 when the $\pm 3\%$ error in EDS measurements was taken into account (MyScope™, 2014). Batch 2, with the EDS measurement error taken into account, produced a calcium deficient Ca/P ratio of 1.60 ± 0.05 . The Sigma nanoHA produced a Ca/P of 1.73

Powder Sample	Ca/P molar ratio
Theoretical molar ratio	1.67
Batch 1	1.63
Batch 2	1.60
Batch 3	1.70
Sigma	1.72

Table 3-2 Calculated Ca/P molar ratios obtained from EDS data. Powders from synthesised batches 1, 3 and Sigma produced Ca/P molar ratios characteristic of stoichiometric hydroxyapatite (1.67) when the $\pm 3\%$ error in EDS measurements was taken into account (Ca/P error = ± 0.05). The synthesised batch 2 produced a calcium deficient Ca/P ratio.

3.3.4 Dynamic Light Scattering Analysis of NanoHA Batches

To provide a bulk measurement of the particle size distribution, each of the powder batches was analysed using DLS, as described in section 3.2.2.2. The resulting size distributions confirmed the presence of nanoHA particles in each of the powders although the size distributions were different across the 4 batches. The plot shown in Figure 3-3 confirms that as a function of the number of particles, the majority of the particles in all the samples were between 25-130 nm. Figure 3-3 B provides a more detailed view of the distributions, with batches 2, 3 and Sigma powders all showing a large peak around 68 nm, while batch 1 had a large peak at 38 nm. Both batches 1 and 2 had a bimodal peak distribution with batch 1 also producing a small peak at 91 nm while batch 2 had a smaller peak at 38 nm.

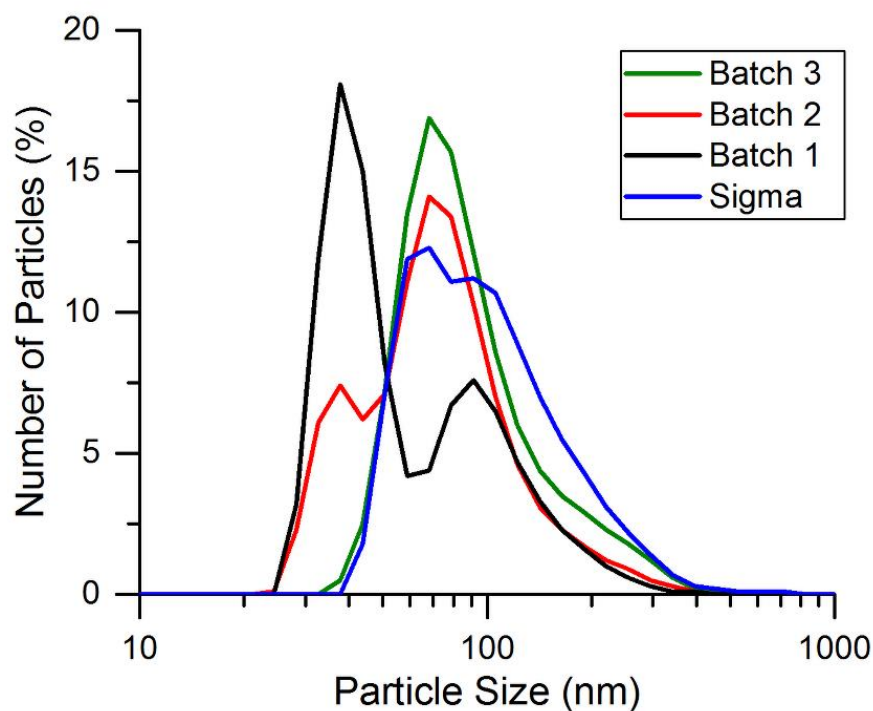


Figure 3-3 Dynamic light scattering (DLS) data showing size distribution of particles as a function of the % of total particle number for batches 1, 2, 3 and Sigma powders. DLS measurements confirmed the bulk of the particles were in the 30-130 nm size range.

3.3.5 Transmission Electron Microscopy of NanoHA Batches

TEM analysis was undertaken to provide a direct measurement of the particle sizes and allow for comparisons with the DLS distribution measurements. The TEM images of particles in each of the powders were produced as described in section 3.2.2.4. The TEM images confirmed the presence of nano-sized rod shaped particles in batches 1, 2 and 3, see figures Figure 3-4, Figure 3-5, and Figure 3-6 respectively. The Sigma particles were confirmed as spheres, see Figure 3-7.

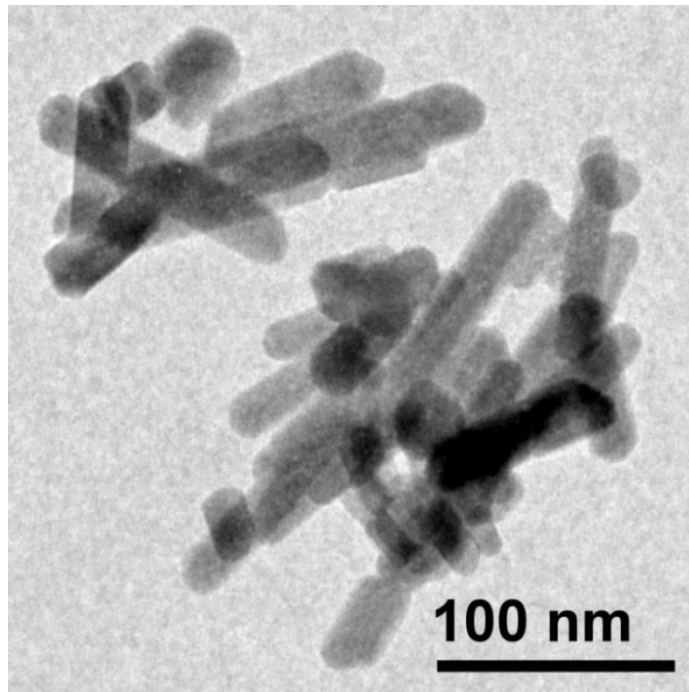


Figure 3-4 TEM image showing rod shaped particles present in batch 1 powder. Images confirmed a range of particle sizes present within the sample, with the majority below 100 nm in length with respect to the longest axis. Scale bar 100 nm.

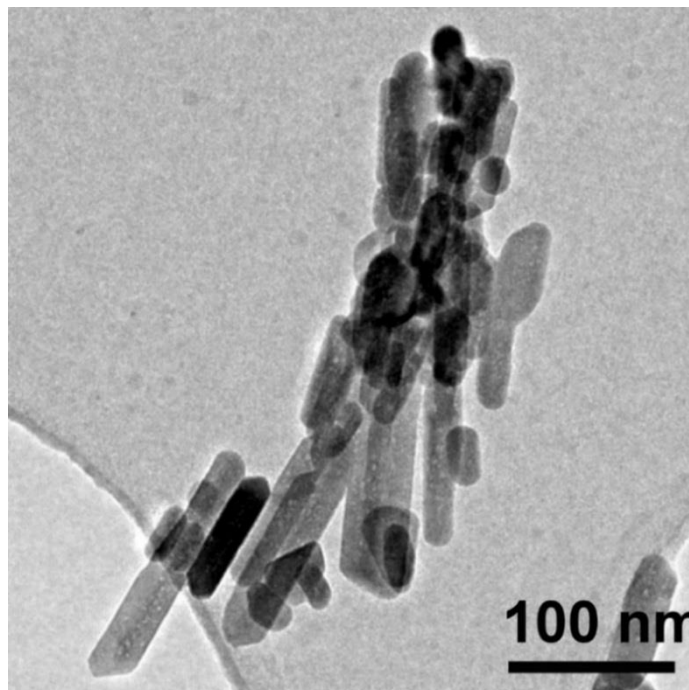


Figure 3-5 TEM image showing rod shaped particles present in batch 2 powder. Images confirmed a range of particle sizes present within the sample with the majority below 100 nm in length with respect to the longest axis. Scale bar 100 nm.

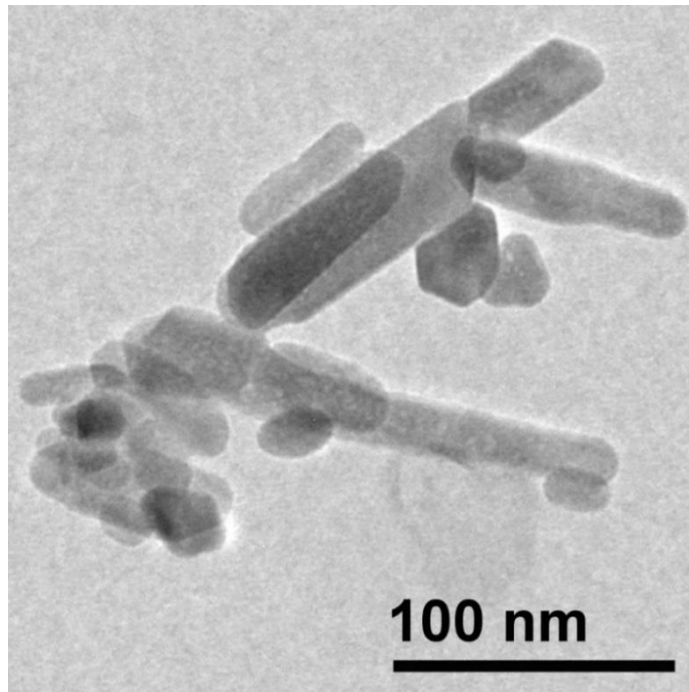


Figure 3-6 TEM image showing rod shaped particles present in batch 3 powder. Images confirmed a range of particle sizes present within the sample with the majority below 100 nm in length with respect to the longest axis. Scale bar 100 nm.

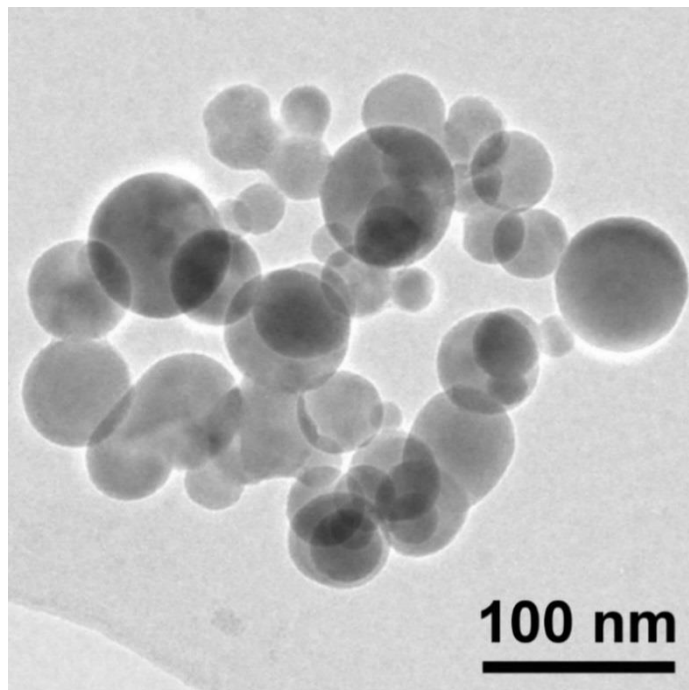


Figure 3-7 TEM image showing spherical shaped particles present in the Sigma powder. Images confirmed a range of particle sizes present within the sample with the majority below 100 nm in length with respect to the spherical particle diameter. Scale bar 100 nm.

Particles were then analysed using ImageJ by measuring the longest axis of the rods, or the diameter of the spheres. This data was then used to produce size distributions, see Figure 3-8. A Kolmogorov-Smirnov test of normality was carried out on the measurements which determined that particles from all batches and the Sigma particles were not normally distributed. Due to the non-normal distribution, non-parametric tests were undertaken to determine any statistical differences. The Kruskal-Wallis statistical test was performed on particles from all synthesised batches and confirmed that the distributions were the same across the 3 data sets (significance level $p < 0.05$) and a median test confirmed that the median values, see Table 3-3, of batches 1, 2 and 3 were not statistically different (significance level $p < 0.05$). The interquartile range for all batches was relatively large compared to the median value which suggests that the spread of particle size was large.

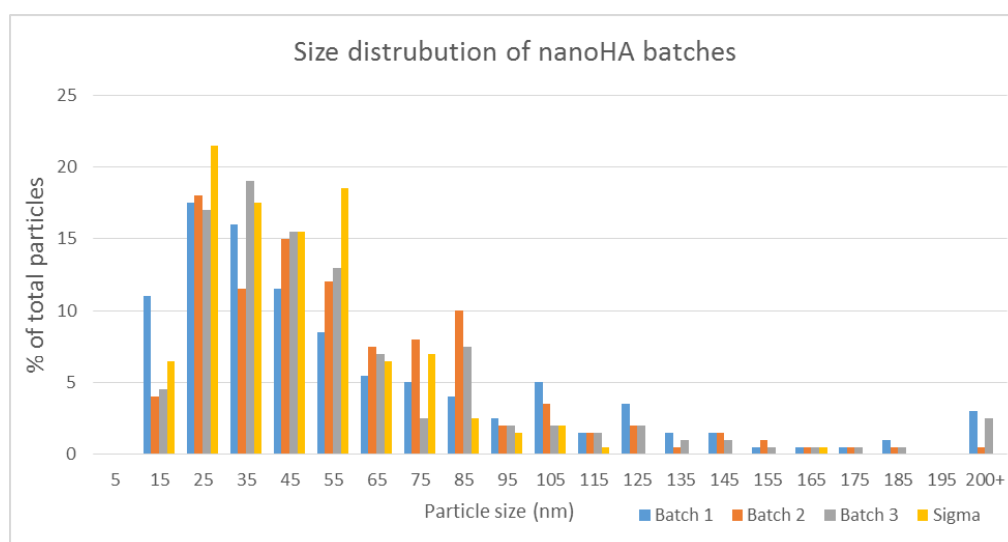


Figure 3-8 Size distributions produced from TEM measurement data for batches 1, 2, 3 and Sigma particles. Measured length was of the longest axis for rods, or diameter for spheres. All synthesised batches and Sigma particles produced a similar particle size distribution.

Sample	Median (nm)	Interquartile range (nm)
Batch 1	45	54
Batch 2	51	47
Batch 3	45	36
Sigma	42	29

Table 3-3 Table summarising median and interquartile range calculated from TEM measurement data for particles from batches 1, 2, 3 and Sigma samples.

3.4 Discussion

The hydrothermal synthesis method described in section 3.2.1 produced nanoHA particles of similar crystal structure, size and morphology as those previously reported by Earl *et al.* (2006b) and Sayed (2013). The XRD data confirmed the presence of a hexagonal crystal system with P6₃/M point group, which is characteristic of apatite (LeGeros, 1994) for batches 1, 2, 3 and Sigma samples through comparison with the ICDD reference database. Batch 2 was matched to a calcium deficient HA reference sample, see Table 3-1. The formation of the calcium deficient HA phase calcium phosphate hydroxide hydrate $\text{Ca}_{4.65}(\text{PO}_4)_3(\text{OH})_{0.3}(\text{H}_2\text{O})$ in batch 2 was not confirmed but could have been due to an error in the precipitation reaction step that resulted in the initial Ca/P ratio being below the predicted value of 1.67. The Ca/P ratio determined by the EDS analysis for batch 2 was the lowest of all the Ca/P ratios for the powders synthesised, see Table 3-2, and it was also outside the EDS error boundaries ($\pm 3\%$) but not as low as the Ca/P ratio of 1.55 generated by the Wilson *et al.* (2005) which produced the calcium deficient XRD data used in the reference file. The XRD spectra can be used to distinguish between stoichiometric HA and calcium deficient HA through analysis of the peaks around approximately $32^\circ 2\theta$, with the peaks resolution becoming less defined in calcium deficient HA (Liou *et al.*, 2004). The XRD spectra determined for batches 1, 2 and 3, Figure 3-1, did not appear to be different with regards to the resolution of the large peak around $32^\circ 2\theta$ and would seem to be less resolved in batch 1 although this was confirmed as stoichiometric HA.

Another factor which could explain the assignment of batch 2 as calcium deficient HA is the peak broadening effects associated with nano-sized particles. As particles decrease in size, the effect of the surface atoms, which have a slightly different coordination, cause peak broadening to occur (Scardi *et al.*, 2011). When comparing the sizes of particles produced in batches 1, 2 and 3 it was found that there was not a significant difference in particle size suggesting that the particle size effect was not the cause of the batch 2 being identified as calcium deficient. The combination of the peak broadening effects associated with nanoparticles and calcium deficient HA made confirmation of the batch 2

composition difficult. To determine if the HA sample batch 2 was calcium deficient further experiments would need to be carried out which are more sensitive to calcium deficiency, for example x-ray absorption which can be used to determine the fine structural changes that occur with calcium deficient HA (Liou *et al.*, 2004). With regards to this work, it was deemed unnecessary to further explore the reason for the failure of batch 2 to match to stoichiometric HA and this batch was simply excluded from future use with batches 1 and 3 taken forward.

The images produced using the SEM clearly confirmed the presence of rod shaped particles in batches 1, 2 and 3, with no obvious differences between the samples, while the Sigma particles had a profoundly different, spherical morphology, Figure 3-2. The measurement of the particles as imaged in the SEM was not possible due to the quantity of particles and aggregated nature of the samples, which was caused by the method of sample preparation. The SEM images did, however, provide a bulk sample view of the powders and confirmed a seemingly homogenous sample morphology of rod shaped particles across all batches with spherical particles for the Sigma particles.

The confirmation of nanoparticle size was determined using a combination of DLS and TEM (Earl, 2007; Murdock *et al.*, 2008; Cengiz *et al.*, 2008; Sayed, 2013). These 2 techniques were combined to ensure that the known disadvantages of each individual method were eliminated by the other. The main weakness with regards to the DLS technique is that it does not directly measure particle size and relies on the assumption of a spherical morphology for the particles, which, for the rod-like particles of batches 1, 2 and 3 could generate inaccurate values (Cengiz *et al.*, 2008). DLS is also obviously affected by sample aggregation which is an issue when measuring HA nanoparticles. The DLS technique is never the less useful for its bulk measurement approach which allows for the measurement of the entire sample. TEM enables the direct measurement of particles along with information on particle morphology. The disadvantage of using TEM is that the particle distributions produced only rely on a small proportion of the whole sample, which may not be representative of the bulk. When these 2 techniques are combined, a more complete analysis of the

size distributions of the particles can be obtained. The DLS data confirmed the presence of particles below 100 nm in all samples, see Figure 3-3. The TEM measurements broadly agreed with the DLS data but with some exceptions. In the DLS analysis, all samples appeared to contain a small percentage of particles with sizes above 200 nm. When compared to the TEM measurements, some particles of 200 nm or over were seen but not to the extent seen in the DLS. This apparent discrepancy is most likely due to aggregation effects in the DLS samples caused by incomplete sonication or aggregation of particles during the testing period. A bimodal distribution was seen in batches 1 and 2 with the peak intensities seeming to mirror each other. The cause of this bimodal distribution in the DLS data is unclear and it was not present in batch 3 or the Sigma sample. It was also unconfirmed by the TEM data. The intensity of the DLS readings around 100 nm (approximately 10% for batches 2, 3 and Sigma) was not confirmed by the TEM measurements, see Figure 3-8. This discrepancy could have been caused by aggregation as it seems to have affected all particles equally, independent of particle shape. Another cause for this discrepancy could be due to the DLS measurement itself, which measures the hydrated particle radius, resulting in a larger particle reading than the actual particle size (Kaasalainen *et al.*, 2017), this may be the cause of the disagreement between the 2 measurement techniques. For a summary of the information provided and limitations of the characterisation techniques used in this work see Table 3-4.

Characterisation Method	Information Provided	Limitations
Dynamic light scattering (DLS)	Size distribution of HA particles	Resulting distribution affected by aggregation. Assumes spherical particles.
X-ray diffraction (XRD)	Crystal structure of HA crystals, can be matched to sample database. Degree of crystallinity measurements based on peak broadening.	Crystallinity determination affected by nano-sized HA particles which results in broadening of peaks. No size or morphology information
Scanning electron microcopy (SEM)	Morphology and size measurements	Values obtained are limited by sample size measured. Does not provide bulk sample size/morphology values.
Transmission electron microscopy (TEM)	Morphology and size measurements	Values obtained are limited by sample size measured. Does not provide bulk sample values. Provides better resolution at nm scale than SEM
Energy-dispersive X-ray spectroscopy (EDS)	Atomic composition of HA particles	No size or morphology information

Table 3-4 Table summarising information provided by HA characterisation techniques used in this work with the limitations of each method.

When comparing the results produced by Earl (2007) and Sayed (2013), see Table 3-5, there were some pronounced differences between the resulting particle sizes and distributions with those found in this work, despite using the same methodology. Earl produced a nanoHA powder with mean particle size of

112 nm, almost double the particle size produced in this work, with a well-defined single peak in the TEM data. It is not possible to compare the size distributions *per se* as Earl (2007) did not provide any further information other than the mean size for the hydrothermal synthesis at pH 10. In contrast Sayed (2013) did not provide a mean particle size and only provided a particle size range of 50 – 475nm. The reason for this was most likely due to the complexity of the TEM derived particle distribution which would not be sufficiently described through a mean or median particle size. When comparing the DLS data of batches 1, 2 and 3 generated in this thesis to Sayed’s DLS distribution, the particle range was slightly smaller, with the larger particles reported by Sayed possibly attributable to aggregation effects.

Sample	TEM (nm)	DLS range (nm)
Batch 1	45 (median) 62 (mean)	28 - 400
Batch 2	51 (median) 60 (mean)	24 - 400
Batch 3	45 (median) 58 (mean)	38 - 460
Sigma	42 (median) 46 (mean)	44 - 712
Sayed (Sayed, 2013)	50 – 475 (range)	56-550
Earl (Earl, 2007)	112 (mean)	No data

Table 3-5 Table showing TEM and DLS nanoparticle size distribution compared with previously reported nanoparticle size following synthesis using the Earl *et al.* (2007) hydrothermal method.

The cause of the differing particle size distributions reported using the same method by 3 different operators is most likely due to the different types of hydrothermal reactor and stirring used. Earl (2007) used a small 125 mL Teflon lined reactor with no stirring capability while Sayed (2013) used a larger 1.6 L capacity vessel (Model 4570, Parr Instrument) and a stirring rate of approximately 500 rpm. The reactor used in this work was a 2 L reactor vessel (Parr instruments model 4524) with approximately 500 rpm stirring speed.

Although the stirring speeds in this work and that of Sayed (2013) are approximately the same, the forces experienced by the growing crystals due to stirring in the 2 different models are likely to be different from each other due to the different shaped reactor vessels and the resulting agitation flows within the reactor during the hydrothermal process. Once the first stage of crystal nucleation has occurred in the reactor, resulting in the formation of many small crystals, secondary crystal growth will depend on the mixing process which can affect crystal size and morphology through Oswald ripening and aggregation effects (Cushing *et al.*, 2004). A study by Riman *et al.* (2002) was able to control the size of hydrothermally synthesised HA from 44 nm with no stirring to 38 nm with stirring at 1500 rpm at 200°C for 15 hours. The measurements were carried out using DLS although no statistical comparisons between the distributions were provided (Riman *et al.*, 2002). The difference in agitation may be the cause of the difference in particle size distributions between batches 1, 2, 3 reported here and those described by Earl (2007) and Sayed (2013), although further work would be required to confirm this hypothesis.

3.5 Conclusion

The hydrothermal synthesis of 3 batches of hydroxyapatite nanoparticles were completed and characterised using XRD, SEM, EDS, DLS and TEM. SEM and TEM of synthesised powder batches confirmed nanoHA rods present in all batches with a median size of 45, 51, 45 nm in batches 1, 2, and 3 respectively. XRD analysis confirmed that batches 1 and 3 powder had hydroxyapatite crystal structure through comparisons with reference files. EDS analysis confirmed a stoichiometric Ca/P molar ratio for both batches 1 and 3. XRD analysis of batch 2 produced a calcium deficient hydroxyapatite match to the reference files which was supported by EDS analysis. Further analysis would be required to confirm the composition of batch 2, for example FTIR or X-ray absorption. Batches 1 and 3 were therefore taken forward and used to optimise the concentration of nanoparticles in the IVNCG and for use as part of the hybrid self-assembling peptide/nanoHA material.

Chapter 4 - *In Vitro* Nucleation and Crystal Growth Assay

Validation with Assessment of the Effect of Nanohydroxyapatite Seeding.

The following chapter describes the validation of an *in vitro* nucleation and crystal growth assay (IVNCG). The validated assay was then used to determine the minimum concentration of nanohydroxyapatite required to produce increased mineralisation compared to the poly-L-glutamic acid positive control to inform subsequent formulations in combination with self-assembling peptides. Crystals produced in the IVNCG were isolated and imaged using SEM. It was found that at low nanohydroxyapatite seeding densities the seeds dissolved due to undersaturation with respect to hydroxyapatite prior to the diffusion of the buffer solutions into the sample wells. Nanohydroxyapatite crystals produced by Sayed were then compared with the nanohydroxyapatite crystals produced in this thesis. The minimal nanohydroxyapatite seeding density required to produce a significant difference compared to the glutamic acid positive control was found to be 3 times greater than the value obtained by Sayed using the same system (Sayed, 2013) .

4.1 Introduction

To enable the optimisation of a nanohydroxyapatite/self-assembling peptide hybrid material with regards to its ability to support the growth of hydroxyapatite seed crystals, a validated, reliable and quantitative *in vitro* assay was needed. The assay used throughout this thesis to optimise the hybrid material prior to its application to dentine was the so-called *in vitro* nucleation (IVN) assay developed and described by Sayed (2013) in his thesis. Although named the *in vitro* nucleation assay, the assay was not capable of differentiating between nucleation and subsequent crystal growth, with the resulting mineral recovered being the product of both crystal nucleation and growth. The IVN assay was developed from diffusion assay work by De Jong and co-workers (1978; 1980), Boskey (1989) and Hunter and Goldberg (1993; 1994).

All of the previous methods described in the papers cited above can be divided into either static or dynamic diffusion, depending on the experimental design (Dorvee *et al.*, 2012). Static systems assume that a steady state is quickly achieved with regards to the ions of interest within the sample well when compared to the length of the experiment. Dynamic systems are based on the assumption that the concentration of the ions of interest is always changing within the sample well and that a steady state is not achieved within the time frame of the experiment. In a stirred flow reactor, a steady state system is a system in which the concentration of constituent ions present within the solution are independent of time (Muller, 1994). In a precipitate-forming system this means that the concentrations of constituent ions present within the solution are constant and independent of any mineral formation. The use of a steady state system provides a method which better reflects the biological processes involved in biomineralisation and allows for the study of biological nucleation and crystal growth.

The origins of the IVN assay developed by Sayed can be traced back to work carried out by Cornelisse and van Duijn (1973) which aimed to study the kinetics of the capture reaction in phosphatase enzyme cytochemistry. The method used a polyacrylamide film containing inorganic phosphate ions which were then placed into an incubation medium containing lead ions. Precipitation of lead

phosphate in polyacrylamide films dosed with phosphate was measured to determine the trapping efficiency of lead ions by phosphate ions. Later, De Jong *et al.* identified issues with the method and developed an improved system (De Jong *et al.*, 1978). The Cornelisse and van Duijn (1973) system only allowed a short time, 5 – 60 seconds, for precipitation to occur and during this short time the concentration of phosphate was falling due to the formation of the lead phosphate precipitates. The system was not representative of the cytochemical reaction in tissues where enzymes produce phosphate continuously, resulting in a steady state of phosphate at the enzymes' catalytic sites. De Jong *et al.* (1978) developed a system whereby a solution containing lead was pumped along one side of the polyacrylamide film and a phosphate-containing solution was pumped along the opposite side, Figure 4-1. This arrangement allowed for the diffusion of lead and phosphate ions into the film, resulting in lead phosphate precipitation once the solubility limit of lead phosphate had been exceeded. The constant flow of fresh solutions containing lead and phosphate allowed the lead phosphate precipitation to occur under steady state conditions as the continued pumping of fresh solutions ensured that the concentration of ions was constant and independent of the amount of precipitation. The films were then either processed for quantitative measurements of phosphate, light microscopy or electron microscopy studies.

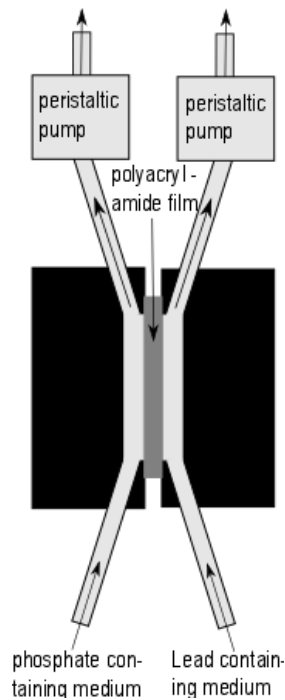


Figure 4-1 – Schematic of sample chamber described by De Jong *et al.* (1978), comprising of a polyacrylamide film with lead-containing solution on one side and phosphate-containing solution on the opposite side. The lead and phosphate ions would diffuse into the polyacrylamide film sample. Precipitation formed within the polyacrylamide film once the saturation limit with respect to lead phosphate was reached. Image modified from De Jong *et al.* (1978).

De Jong *et al.* (1980) then used the system to study calcium phosphate mineral precipitation and how the addition of collagen and chondroitin sulphate to the polyacrylamide matrix affected resulting nucleation and crystal growth in the system. The effect of the addition of 25 μM pyrophosphate (a known inhibitor of crystal growth) to the pumped solutions was also studied (De Jong *et al.*, 1980). The calcium and phosphate solutions were buffered using 0.15 M Tris-HCl buffer (pH 7.4) which produced a more physiologically relevant system compared to the previous lead phosphate system. The method was able to determine differences in nucleation abilities between the chondroitin sulphate-doped polyacrylamide films and the polyacrylamide control. It was shown that the addition of chondroitin sulphate lowered the calcium phosphate solubility product required to initiate the nucleation of calcium phosphate mineral. The addition of 25 μM pyrophosphate to the calcium-containing buffer and phosphate-containing buffer resulted in a decrease in calcium phosphate solubility product for the onset of calcium phosphate mineralisation compared to the polyacrylamide control. It

also had an inhibitory effect on the growth of the mineralised phase during the crystal growth phase compared to the polyacrylamide control. However, it was unable to determine any differences in the nucleation abilities between the collagen sample and polyacrylamide film control, permitting conclusions to be drawn in respect of the relative nucleating abilities of chondroitin sulphate and collagen. The ability to quantitatively determine differences between macromolecules of interest with respect to their nucleation and crystal growth abilities at physiological pH provided a means to test biologically relevant macromolecules for their ability to nucleate and support calcium phosphate crystal growth. It was also shown to be capable of assessing a material's ability to inhibit crystal growth. However, the system still relied on a polyacrylamide sheet, which did not provide a biologically relevant matrix, such as collagen, which would be analogous to that in calcifying tissues. The method also used multiple sample holders in series which could result in each sample being exposed to progressively lower concentrations of the ions of interest due to their removal through precipitation in the previous sample holder.

Crystal growth within gels has been frequently used to study the growth of biological minerals in matrices such as gelatine and silicates. These systems involved the formation of a gel containing the material under investigation with the constituent ions of the mineral phase being supplied by either adding to the surface or including into the gels. Alternatively, the ions were trapped in a separate gel and placed either side of the gel containing the material under investigation (Hunter *et al.*, 1987). These systems shared similar issues with the Cornelisse and van Duijn (1973) system discussed previously, as the concentrations of ions were not in steady state. In addition, the respective ions of the mineral being studied were often of supra physiological concentration to allow mineralisation to occur within a reasonable time frame.

Boskey (1989) identified these issues and produced a hybrid system based on these gel-based systems and De Jong's steady state system. Her method required the production of gelatine slabs which were then mounted into sample holders. The gels were dosed with macromolecules of interest and separate

buffers containing calcium and phosphate were pumped around the system diffusing into the gels from opposite sides.

This system did not provide a steady state within the time frame of the experiment due to the use of 6 cm long samples which precluded the reaching steady state across the full length of the gel. The long sample length allowed the analysis of sample across the hydroxyapatite supersaturation threshold from sub-threshold to super-threshold (Dorvee *et al.*, 2012) within a single sample. To ensure mineralisation occurred within an acceptable time frame, the concentration of calcium and phosphate-containing buffers was optimised at 100 mM (Boskey, 1989). The system also allowed the measurement of multiple samples within one experiment which increased the throughput. One issue that was not resolved however was the non-physiological (20-25°C) temperature used in the method, due to the fact that the gelatine would melt if incubated at 37°C. Nevertheless, this system was used to investigate a variety of proteins to determine their mineralisation promotion/inhibition properties. For example, it was shown that complexed acidic phospholipids were promoters of mineralisation, decreasing the time required for mineralisation to occur and that proteoglycans inhibited the formation of mineral within the system (Boskey, 1989).

The De Jong *et al.* (1978) system was also adapted by Hunter and Goldberg (1993), who opted to change the original polyacrylamide matrix to agarose, which was stable at physiological temperature and allowed for the study of nucleation and crystal growth under more physiologically relevant conditions. The Hunter and Goldberg method used separate chambers, similar to the De Jong *et al.* method, to contain the agarose gel. Agarose gels (2% agarose, 150 mM NaCl, 10 mM Tris-HCl at pH 7.4) were poured into each chamber and a piece of dialysis membrane placed over each side, Figure 4-2 (Hunter and Goldberg, 1993). The chambers were added in series with a total number of 12 being used per experiment. Calcium-containing buffer was pumped in one direction and phosphate-containing buffer was pumped in the opposite direction. Once the buffers had travelled the 12 holders, the buffer was collected as waste while fresh buffer continued to circulate.

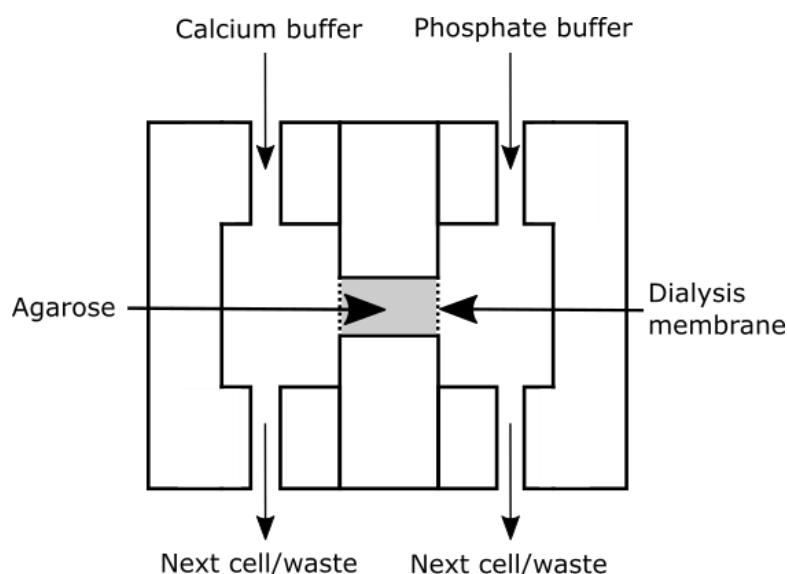


Figure 4-2 – Schematic of sample holder used by Hunter and Goldberg (1993). Calcium-containing buffer would flow past one side of the agarose sample and phosphate-containing buffer would flow past the opposite side. The calcium and phosphate ions would diffuse into the agarose sample with the mass of mineral formed dependent on the macromolecules seeded within the agarose samples. Image modified from Hunter & Goldberg (1993) Copyright (1993) National Academy of Sciences.

The system was used to study the roles of different phosphoproteins in the nucleation of hydroxyapatite and demonstrated that bone sialoprotein was capable of nucleating hydroxyapatite under steady state conditions at sub threshold supersaturation (Hunter and Goldberg, 1993).

The Hunter and Goldberg (1993) system was later adapted by Sayed (2013) who developed an *in vitro* nucleation assay (IVN) with high throughput that was capable of consistent results. The IVN system replaced the flow of fresh buffers used in both the Hunter and Goldberg (1993) system and the Boskey (1989) experimental set-up with a large buffer reservoir which approximated constant buffer composition over the course of the experiment. The IVN assay comprised of a large container, 10 L capacity, with a 36 well sample holder separating 2.5 L compartments, see Figure 4-3. The sample wells were filled with agarose gel (controls) each containing one of the materials of interest and each compartment was filled with either calcium-containing buffer (6.5 mM $\text{Ca}(\text{NO}_3)_2 \cdot 4\text{H}_2\text{O}$, 20 mM HEPES, 150 mM NaCl) or phosphate-containing buffer (3.9 mM $\text{Na}_2\text{HPO}_4 \cdot 2\text{H}_2\text{O}$, 20 mM HEPES, 150 mM NaCl). The buffers were then incubated at 37 °C for 4

days with stirring. The samples were then removed from the sample wells and analysed for their phosphate content (Sayed, 2013). The advantage of this method compared to the Hunter and Goldberg (1993) method was that the ionic concentrations of calcium and phosphate experienced by all the samples were the same, whereas in the latter method, the concentration of buffer ions in successive sample cells could be affected by mineralisation in the preceding cells.

The use of agarose in Sayed's (2013) IVN system allowed the system to test materials under physiological temperature. The large 5 L compartments which housed the buffers ensured that an approximate steady state was maintained in the sample wells within the time frame of the experiment and the ion concentrations were maintained throughout the 5-day run time. The system was used to determine the minimum nanohydroxyapatite (nanoHA) seeding density required to produce an increased phosphate reading compared to the positive control of 10 µg/mL poly-L-glutamic acid in agarose. This was found to be 10 µg/mL. The assay was later used to determine the effectiveness of a number of self-assembling peptides combined with nanoHA with respect to their potential use as a hybrid material for bone and enamel repair. The self-assembling peptides P₁₁₋₄, P₁₁₋₈ and the complementary peptides P₁₁₋₁₃ and P₁₁₋₁₄ were analysed using the IVN to determine their nucleating and crystal growth supporting properties with and without the addition of 10 µg/mL nanoHA (Sayed, 2013). It was shown that P₁₁₋₄ and P₁₁₋₈ were excellent nucleators of the calcium and phosphate containing mineral, hydroxyapatite, (HA) although both were unaffected by the addition of nanoHA. The complementary peptide P_{11-13/14} showed poor nucleating properties with respect to hydroxyapatite when tested alone but provided good crystal growth capability with the addition of nanoHA (Sayed, 2013).

This system, referred to by Sayed (2013) as the *in vitro* nucleation (IVN) assay, not only allowed the study of the nucleating potential of a material but also its ability to sustain the growth of the crystal nuclei over a 4-day testing period. The system allowed for the use of calcium-containing buffer and phosphate-containing buffer at sub threshold concentrations with respect to hydroxyapatite.

The majority of the experiments carried out in this thesis using the IVN assay had seed crystals present within the samples themselves and so were primarily focussing on crystal growth. The IVN assay is not able to distinguish between the calcium-phosphate containing mineral precipitate formed through nucleation or crystal growth and will most likely reflect a combination of both. For this reason, from this point on, the *in vitro* nucleation assay will be referred to as the *in vitro* nucleation and crystal growth (IVNCG) assay as this better reflects the capability of the assay.

The following chapter will describe the validation of the experimental IVNCG assay through statistical analysis of positive (10 µg/mL poly-L-glutamic acid in agarose) and negative (agarose) controls. The validation results will be compared to previous work carried out by Sayed (2013) and Hunter and Goldberg (1993). The nanoHA synthesised as part of this thesis, see Chapter 3, will then be optimised with regards to the minimal seeding density of nanoHA in agarose required to provide a statistically significant difference compared to the positive control. The crystals grown within the IVNCG will then be isolated and studied using SEM and EDS.

4.2 Methods

4.2.1 *In Vitro* Nucleation and Crystal Growth Assay (IVNCG)

Validation

The IVNCG apparatus was first described by Sayed in his thesis (Sayed, 2013). To validate the assay in this study, the apparatus, see Figure 4-3, was first soaked overnight in 0.1M HCl (Sigma-Aldrich St. Louis, MO, USA) to remove any mineral present within the sample wells from previous experiments. Calcium-containing buffer at pH 7.4 was prepared with calcium nitrate tetrahydrate ($\text{Ca}(\text{NO}_3)_2 \cdot 4\text{H}_2\text{O}$, Acros Organics ACS grade, Waltham, MA, USA) 6.5 mM, in 20 mM HEPES (Sigma-Aldrich St. Louis, MO, USA) and 150 mM NaCl (Sigma-Aldrich St. Louis, MO, USA) in distilled H_2O . Phosphate-containing buffer at pH 7.4 was prepared using 3.9 mM sodium phosphate dibasic dihydrate ($\text{Na}_2\text{HPO}_4 \cdot 2\text{H}_2\text{O}$ 99%+ for analysis Acros Organics) with HEPES 20 mM (Sigma-Aldrich St. Louis, MO, USA) and 150 mM NaCl (Sigma-Aldrich St. Louis, MO, USA) in distilled H_2O . All buffers were pH adjusted using 5 M NaOH (Sigma-Aldrich St. Louis, MO, USA) to pH 7.4 and filtered using a 22 μm bottle top vacuum filtration system (Corning 1L filtration system Corning, NY, USA, 431098). Two agarose (BIO-RAD low melt agarose, Hercules, CA, USA, 1613111) samples were produced from 2% agarose in distilled H_2O and kept at 50°C. All samples tested using the IVNCG were prepared in steady state buffer at pH 7.4 (20 mM HEPES and 150 mM NaCl) to maintain physiological pH and salt concentration throughout the experiment. The positive control was made by adding an equal volume of 2x concentrated steady state buffer at pH 7.4 (40 mM HEPES and 300 mM NaCl) to agarose producing 1% agarose in steady state buffer at pH 7.4 (20 mM HEPES 150 mM NaCl) with 10 $\mu\text{g}/\text{mL}$ poly-L-glutamic acid (Sigma-Aldrich St. Louis, MO, USA, P4886) added. The negative control was made by adding an equal volume of 2x steady state buffer to agarose producing a 1% agarose sample in steady state buffer. Both positive and negative controls were pipetted into the sample wells (0.85 mL, 10 mm long, diameter 5.2 mm), see Figure 4-3 C, with dialysis membrane (SpectraPor-3 MWCO 3.5kD, Hoeksteen Netherlands, 132724) covering both sides (n=16 positive, n=20 negative). Once cooled, the sample holder was screwed into place

within the system and 5 L of calcium-containing buffer was added to one compartment and 5 L of phosphate-containing buffer to the other compartment. The IVNCG apparatus with samples *in situ* was then incubated at 37°C, with stirring, for 5 days. The agarose gels were then removed from the sample holder and stored in 14 mL glass vials.

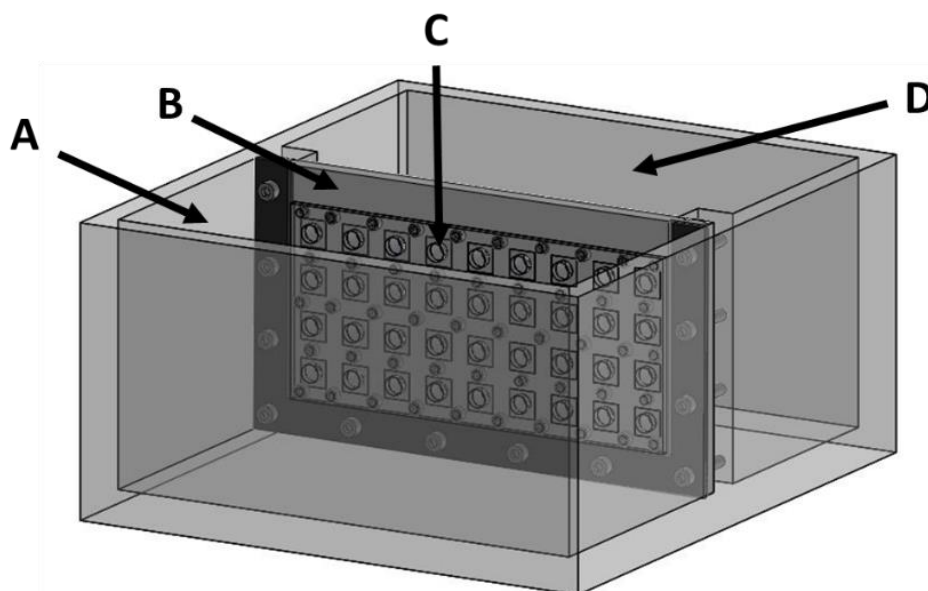


Figure 4-3 – Schematic representation of the IVNCG assay showing the position of the buffer compartments, A and D, Sample holder, B, and sample wells, C. Image modified from Sayed (2013).

4.2.2 Determination of Phosphate Content in Agarose Controls Recovered from IVNCG After 5 Days.

Agarose samples were recovered from the sample wells of the IVNCG after the 5-day test period and were ashed in 10 mL sealable glass vials following the method of Chen *et al.* (1956). Concentrated nitric acid, 2 mL (Sigma-Aldrich St. Louis, MO, USA) was added to each gel and to each of 4 additional empty 10 mL glass vials (to act as blanks). The solution was then boiled until the volume had reduced to 1 mL. The solutions were then made up to 10 mL using de-ionised H₂O. The solutions were then further diluted 10 times through the addition of de-ionised H₂O prior to analysis. Phosphate standards were produced (10.5 mM phosphate standard, Fisher Chemicals, Loughborough, UK) across a range of concentrations from 0-100 µM phosphate in 10 µM intervals. Each sample and standard (300 µL) was added to individual 1 mL Eppendorf tubes.

To each sample or standard, 700 μL of a mixture of 10% ascorbic acid (Sigma-Aldrich St. Louis, MO, USA; solution A) and 0.42% ammonium molybdate.4H₂O (VWR chemicals Lutterworth UK) in 0.5M H₂SO₄ (Sigma-Aldrich St. Louis, MO, USA; solution B) was added in a ratio of 1 part A to 6 parts B. Each sample (300 μL) was then pipetted into wells of a 96 well plate. The phosphate calibration standards (also 300 μL) were added to the 96 well plate in triplicate. The plate was incubated at 37° for 1 hour 30 minutes. The absorbance was then read using a plate reader (Thermo Fisher Scientific, VarioSkan Flash, software SkanIt RE, Waltham, MA, USA) at 820 nm. The absorbance readings from the 4 blanks were averaged and subtracted from each calibration reading. Once the blank reading was subtracted, average absorbance against standard concentration was plotted and a line of best fit generated. R² analysis of the fit was calculated to determine linearity with 0.999 being used as the minimal acceptable level. The gradient of the line of best fit was used to calculate the mass of phosphate in each sample chamber assuming a IVNCG sample volume of 0.85 mL, resulting in a total sample dilution factor of 117.65 (0.85 mL sample diluted to 10 mL followed by an additional 10 times dilution prior to analysis). The resulting phosphate concentration was then used to calculate hydroxyapatite (HA) present in each sample, presuming that the mineral deposited in the samples was wholly HA and that all of the phosphate derived from the HA. The experiment was repeated 4 times to allow analysis of inter run variability.

4.2.3 IVNCG Statistical Analysis

The phosphate mass data produced from the IVNCG experiments were imported into SPSS and the Kolmogorov-Smirnov statistical test of normality and the independent t-test were used to confirm a normal distribution and determine statistical differences between sample groups. When IVNCG experiments were undertaken with more than 2 sample groups, a one-way ANOVA *post hoc* Bonferroni test was run to determine differences between runs. A power test was also undertaken using the validation data to determine the number of controls which would be required for future testing (Rosner, 2011). A significance level of $p < 0.05$ was used for all statistical analysis.

4.2.4 Effect of IVNCG Run Time on Buffer Calcium and Phosphate Content

The buffer compartments of the IVNCG were designed to be large enough to ensure that the concentration of calcium in the calcium-containing buffer and the concentration of phosphate in the phosphate-containing buffer approximated steady state conditions throughout the 5-day testing period, such that the concentrations of the ions did not change as a function of time or as a function of calcium phosphate mineral formation within the sample wells. To test this assumption, the IVNCG experiment was run as previously described in section 4.2.7 using samples with nanoHA at seeding densities of 10, 20 and 30 $\mu\text{g}/\text{mL}$ in agarose (n=10), and including positive and negative controls (n=3). For each day of the 5-day run period, a 10 mL sample of the calcium-containing buffer and the phosphate-containing buffer was taken from the IVNCG assay buffer compartments and stored in sealed vials under refrigeration prior to analysis.

4.2.5 Determination of Buffer Phosphate Concentration

A phosphate assay was then carried out on both the phosphate-containing buffer and calcium-containing buffer. The samples taken from the calcium-containing buffer on days 0-5 were diluted 10 times while the samples taken from the phosphate-containing buffer on days 0-5 were diluted 100 times. A solution of 10% ascorbic acid (Sigma-Aldrich St. Louis, MO, USA) (solution A) and 0.42% ammonium molybdate.4H₂O (VWR chemicals Lutterworth UK) in 0.5M H₂SO₄ (Sigma-Aldrich St. Louis, MO, USA) (solution B) in a ratio of 1 part A to 6 parts B was prepared and 210 μL aliquoted into the wells of a 96 well plate. The diluted calcium-containing buffer samples, the diluted phosphate-containing buffer samples and phosphate standards as described previously were then added, 90 μL to each well, in triplicate to the solutions of AB. The plate was left to incubate at 37 °C for 1 hour and 30 minutes before absorbance was read at 820 nm as described in section 4.2.2.

4.2.6 Determination of Buffer Calcium Concentration

The calcium concentration within each of the buffer reservoirs was determined using a Arsenazo III method previously described by Smith and Bauer (Smith Jr. and Bauer, 1979). A solution of 0.932 g Arsenazo III (Sigma-Aldrich St. Louis, MO, USA) and 6.808 g of Imadazol buffer (Sigma-Aldrich St. Louis, MO, USA) diluted to 500 mL with DI H₂O and the pH adjusted to 6.5) was prepared and 50 μ L added to all the wells of a 96 well plate. The samples taken from the calcium-containing buffer on days 0-5 were diluted 50 times; samples taken from the phosphate-containing buffer on days 0-5 were used undiluted. Samples (50 μ L) were then added in triplicate to the 96 well plate wells containing 50 μ L of Arsenazo III solution described above. Calcium standards (1 M calcium chloride, BDH laboratory supplies Poole, UK) were produced by dilution with DI H₂O to produce a 1 mM calcium chloride stock solution. The 1 mM calcium chloride stock solution was then further diluted using DI H₂O to produce concentrations between 0 and 0.6 mM in 0.1 mM increments in 1.5 mL Eppendorf tubes. Each calibration standard (50 μ L) was then pipetted, in triplicate into the 96 well plate wells already containing 50 μ L of previously added Arsenazo III solution described above. After 10 minutes the absorbance was read using a plate reader (Thermo Fisher Scientific, VarioSkan Flash, software SkanIt RE, Waltham, MA, USA) at 640 nm.

4.2.7 Determination of Minimum NanoHA Seeding Density Required to Produce Increased HA Formation Compared to Controls Using IVNCG

To minimise the possibility of any potential cytotoxic effect arising from using nanoHA in the treatment of dentine sensitivity, the minimum amount of nanoHA required to produce a statistically significant difference in mineral precipitation compared to the positive control was determined using the IVNCG. The preparation method for the IVNCG was carried out as described in section 4.2.1 except that the number of control samples was reduced to n=3 for both positive and negative controls, following the power test analysis carried out during the validation. A 1 mg/mL suspension of nanoHA batch 1, see Chapter 3, was

produced by weighing out 25 mg of nanoHA into a 50 mL falcon tube and adding 25 mL of 2x steady state buffer. A second 1 mg/mL suspension of the nanoHA batch 3, see Chapter 3, was produced by weighing out 25 mg of batch 3 nanoHA into a 50 mL falcon tube and adding 25 mL of 2x steady state buffer. Both suspensions were vortexed for 30 seconds followed by 2 x 20 second periods of sonic probe agitation (MISONIX model XL2010 model XL2010 Farmingdale, NY, USA , with micro probe output 20 KHz). The 2 suspensions of nanoHA were then combined together in equal volumes to produce a 1 mg/mL nanoHA stock suspension combined from batches 1 and 3. The combined suspension was then further diluted and added to an equal volume of 2% agarose in DI H₂O to produce 1% agarose samples with nanoHA seeding concentrations of between 10 and 100 µg/mL with an interval of 10 µg/mL in 1% agarose steady state buffer. Samples were then placed in a sonic bath at 37 °C until required (no longer than 20 minutes) to ensure the nanoHA remained suspended and the agarose remained molten. Each agarose sample was then pipetted in triplicate into the IVNCG sample holder and the calcium-containing buffer added to one buffer compartment and the phosphate-containing buffer added to the other. The IVNCG system was then placed in the incubator at 37°C with stirring for 5 days. After 5 days the samples were removed from the sample wells and their phosphate concentration determined as previously described in section 4.2.2. Due to the high phosphate values obtained in the agarose samples containing nanoHA, see section 4.3.3, a calibration curve with a greater range was produced, using standards of between 0 and 160 µM phosphate. The experiment to determine minimal nanoHA seeding density was carried out in triplicate, using nanoHA seeding densities of 10, 20 and 30 µg/mL in agarose, n=10. This experiment was then repeated 3 times to confirm the minimum concentration of nanoHA which could produce a statistically significant increase in phosphate concentration compared with the positive control.

4.2.8 Isolation and Analysis of Mineral Formed in NanoHA Seeded Agarose After 5 Days in IVNCG

To enable the elemental composition and morphological analysis of the mineral formed during the IVNCG experiment to be investigated, the agarose control samples and nanoHA seeded agarose samples used in the IVNCG buffer experiment described in section 4.2.4 were processed to enable the isolation of any crystals present. After the 5-day IVNCG test period was completed, the agarose gel samples were removed from the IVNCG sample wells and placed into a 24 well plate. Images of the gels were taken using a Bio-Rad ChemiDoc™ MP Imaging System from both above, and perpendicular to, the buffer contact surface with respect to their positions when in the IVNCG assay. Images were taken using the Coomassie Blue Bio-Rad ChemiDoc™ standard protocol selected from the ChemiDoc™ software, using a white light screen, standard filter, automatic exposure time and white light transillumination. Once imaged, the agarose gels were combined into sample groups of positive control, negative control, 10 µg/mL nanoHA seeding density, 20 µg/mL nanoHA seeding density, 30 µg/mL nanoHA seeding density in separate 50 mL falcon tubes. Milton Sterilising Fluid (2 % w/v sodium hypochlorite) was then added, 40 mL, to each sample falcon tube and left overnight. The resulting suspensions were then centrifuged (Thermo Sci Heraeus Megafuge 16R) at 16,500 g for 10 minutes, then washed with DI H₂O pH adjusted to 10 using ammonium hydroxide (Sigma) 3 times to ensure the Milton Sterilising Fluid was removed. A pH of 10 was used as hydroxyapatite is sparingly soluble at high pH limiting any change in crystal size or morphology. Suspensions were finally washed 3 times in ethanol and stored in ethanol. Samples were then pipetted onto SEM stubs and left to dry. Once dry the samples were sputter coated in gold (Agar Auto Sputter Coater B3743, Stansted, UK) and analysed using SEM (Hitachi S-3400N VP, Tokyo, Japan) with accelerating voltage 10 kV and current 84 µA to determine particle size and morphology. EDS analysis was also undertaken (Bruker XFlash 129 ev, Billerica, MA, US) to determine atomic composition.

4.2.9 Effect of Shortening the IVNCG Run Duration with Respect to Crystal Growth

To enable direct comparisons to the work of Sayed, a repeat of the experiment described in section 4.2.7 was carried out but with the experimental duration decreased from 5 days to 4 days (Sayed, 2013). The IVNCG experiment was repeated using a sample size of $n=3$ for the positive and negative controls and a sample size of $n=10$ for the 10, 20 and 30 $\mu\text{g/mL}$ nanoHA combined batches 1 and 3 seeded in agarose samples.

4.2.10 Comparison of NanoHA Synthesised in this Work to Other Synthetic NanoHA with Respect to Crystal Growth in IVNCG

The IVNCG assay was run over a 4-day period using nanoHA synthesised by Sayed (2013) ("small-HA"), nanoHA obtained from Sigma-Aldrich (Sigma-Aldrich, nanopowder, < 200 nm particle size (BET), $\geq 97\%$, synthetic St. Louis, MO, USA) and the nanoHA synthesised in this work to determine if the nanoHA produced in this work differed with respect to its ability to seed crystal growth. The experiment was run in the same manner as described previously in section 4.2.7 using samples of 5, 10 and 30 $\mu\text{g/mL}$ of each nanoHA sample, along with the usual positive and negative controls (10 $\mu\text{g/mL}$ poly-L-glutamic acid in 1% agarose and 1% agarose only respectively). All samples were tested in triplicate.

4.3 Results

4.3.1 Validation of *In Vitro* Nucleation and Crystal Growth Assay (IVNCG)

To enable the comparison of materials with respect to their ability to nucleate/support the growth of hydroxyapatite, the IVNCG was validated using a positive control of 10 µg/mL poly-L-glutamic acid in 1 % agarose and a negative control of 1% agarose. For the experiment to be considered valid, the positive control had to have produced a statistically significant increase in phosphate mass compared to the negative control. The IVNCG validation experiment was run on 4 separate occasions as described in section 4.2.1, using multiple samples of poly-L-glutamate in agarose (positive controls) or agarose alone (negative controls) in each run. Following a 5-day incubation, the samples were retrieved and phosphate analysis completed as described in section 4.2.2. A typical calibration curve for the phosphate standards used for these experiments is shown in Figure 4-4. This produced a linear line of best fit with an R^2 value of 0.999 that was used to calculate the concentration of phosphate in the positive and negative controls. A calibration curve for phosphate was produced for each of the IVNCG validation runs.

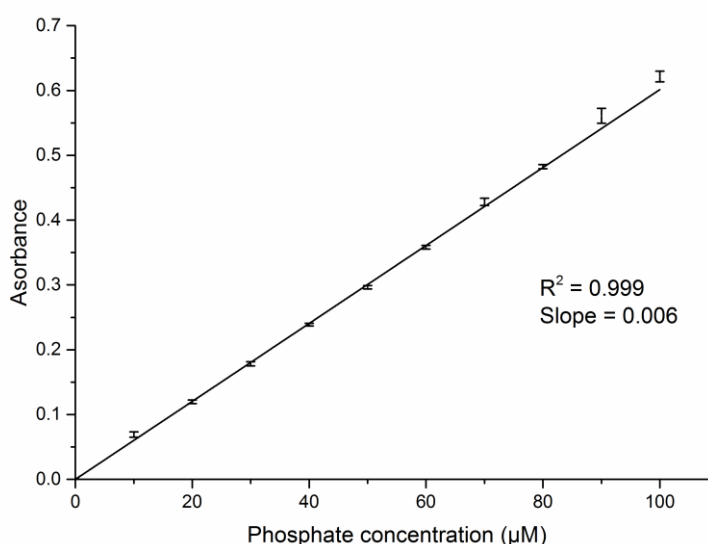


Figure 4-4 Typical calibration curve showing absorbance at 820 nm against phosphate concentration. The line of best fit showed a linear response with a R^2 value of 0.999. Error bars show 2x standard deviation, n=3.

Statistical analysis of the distributions of the phosphate mass produced in both positive and negative controls using the Kolmogorov-Smirnov statistical test confirmed a normal distribution which enabled the use of the independent t-test to test for significance between the positive and negative controls. This showed a statistically significant difference between the positive and negative controls in each individual experimental run, with a significance level of at least $p < 0.05$.

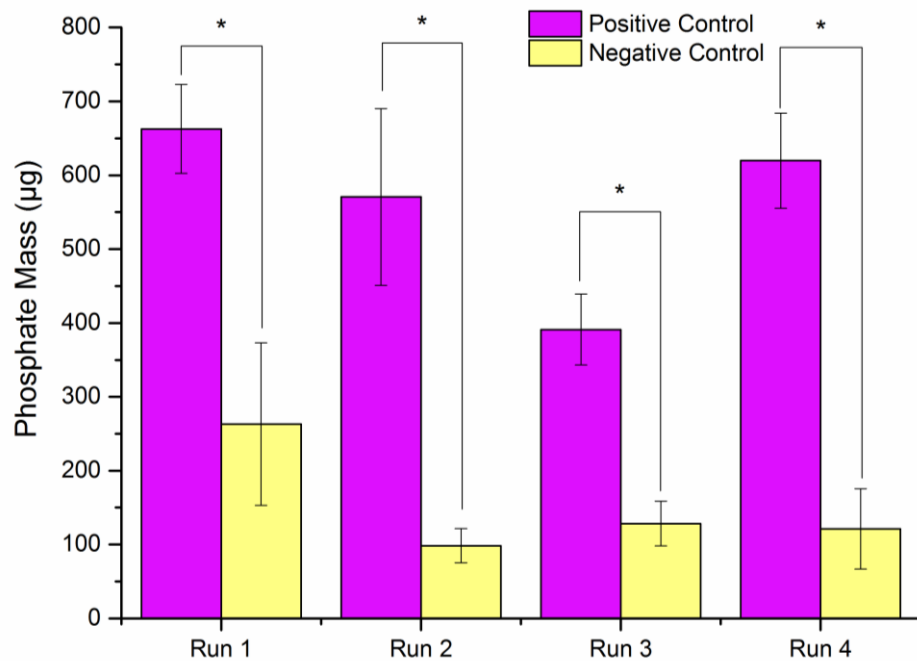


Figure 4-5 Bar histograms showing amounts of phosphate determined in positive (poly-L-glutamate in agarose, $n=16$) and negative (agarose, $n=20$) controls after 4 separate 5-day runs in the IVNCG. Greater amounts of phosphate were present in the positive controls compared with the negative controls on each occasion. Error bars show 2x standard deviation. * confirms statistically significant difference using independent t-test significance level of at least $p < 0.05$.

To determine the reproducibility of the assay with regards to the quantity of phosphate produced in the positive and negative controls between IVNCG experimental runs, a *post hoc* Bonferroni test was undertaken, with the results shown in Table 4-1. To directly compare the phosphate quantities produced between individual experimental runs, the quantity of phosphate produced in the positive controls and negative controls must not be statistically different with respect to its corresponding control over the 4 individual runs. The *post hoc* analysis confirmed that this was not the case. The positive controls produced

similar mean phosphate masses over the 4 individual IVNCG runs but the run 3 positive control had a statistically significant lower mean phosphate mass compared to the phosphate masses of run 1, run 2 and run 4 ($p < 0.05$). Similarly, the run 1 negative control produced a statistically significant larger mean phosphate mass compared to phosphate masses produced in run 2, run 3 and run 4.

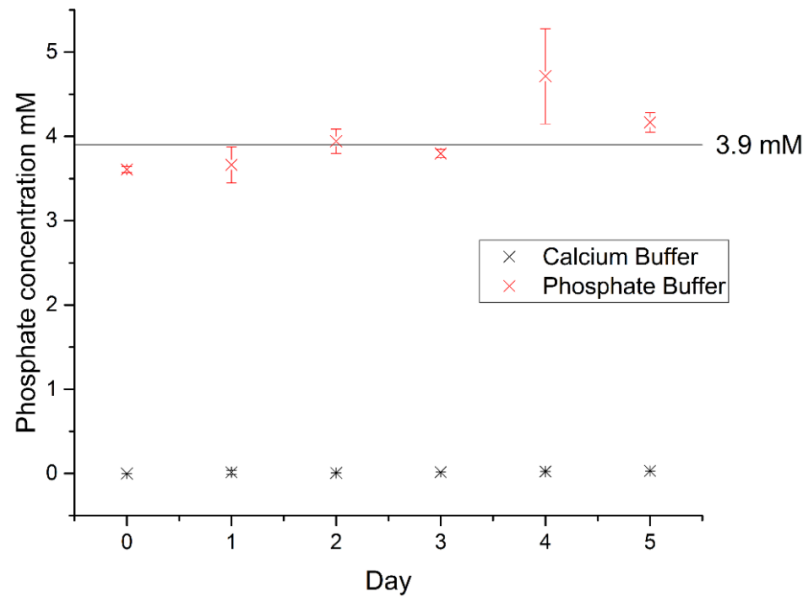
	Run 1 Positive Control	Run 1 Negative Control	Run 2 Positive Control	Run 2 Negative Control	Run 3 Positive Control	Run 3 Negative Control	Run 4 Positive Control	Run 4 Negative Control
Run 1 Positive Control		SD	SD	SD	SD	SD	N/A	SD
Run 1 Negative Control	SD		SD	SD	SD	SD	SD	SD
Run 2 Positive Control	SD	SD		SD	SD	SD	N/A	SD
Run 2 Negative Control	SD	SD	SD		SD	N/A	SD	N/A
Run 3 Positive Control	SD	SD	SD	SD		SD	SD	SD
Run 3 Negative Control	SD	SD	SD	N/A	SD		SD	N/A
Run 4 Positive Control	N/A	SD	N/A	SD	SD	SD		SD
Run 4 Negative Control	SD	SD	SD	N/A	SD	N/A	SD	

Table 4-1 Output from Bonferroni statistical test carried out on the 4 separate IVNCG validation runs comparing the positive and negative controls. Statistically significant differences were found between the amounts of phosphate measured in the positive controls across the 4 runs. Statistically significant differences were also found between the amounts of phosphate measured across the negative control runs. SD shows significant difference while N/A shows no significant difference, significance level = 0.05.

4.3.2 Effect of IVNCG Run Time on the Calcium and Phosphate Concentrations of the Reservoir Buffers

To determine if the IVNCG reservoir buffers (calcium-containing buffer on one side of the sample holder and phosphate-containing buffer on the other) maintain a steady state with respect to ionic calcium and ionic phosphate concentrations throughout the 5-day testing period, 10 mL of each of the reservoir buffers were removed each day from the respective buffer compartments and analysed for calcium and phosphate concentrations. The analyses were carried out as described in section 4.2.4 and the results are shown in Figure 4-3. The theoretical concentration of ions in each buffer is shown by the solid black line present on each graph. There was very little change with respect to the concentration of ionic calcium and phosphate in the buffers over time.

A



B

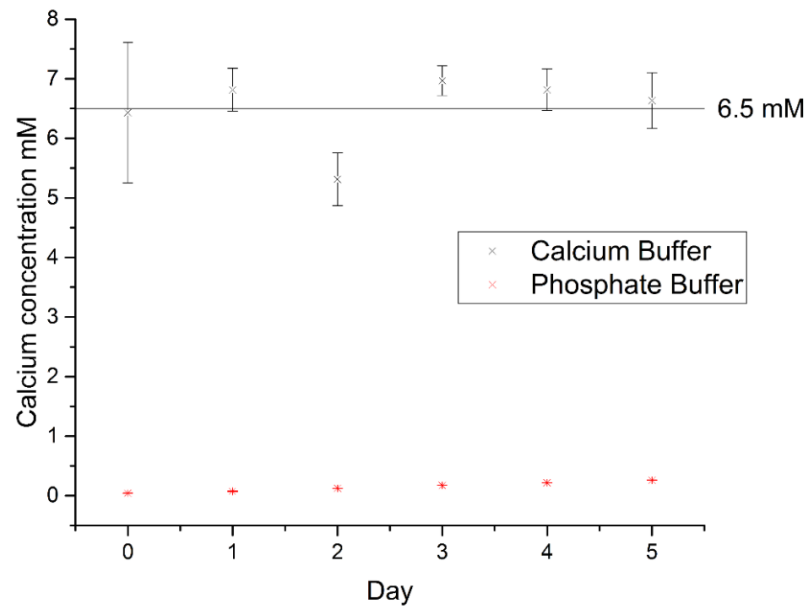


Figure 4-6 A) Scatter graph showing the phosphate concentration in phosphate-containing reservoir buffer (red) and calcium-containing reservoir buffer (black) during the IVNCG 5-day run period. B) Scatter graph showing the calcium concentration in the phosphate-containing reservoir buffer (red) and calcium-containing reservoir buffer (black) during the 5-day run period. Error bars show standard deviation. The concentration of phosphate in the phosphate-containing buffer and the concentration of calcium in the calcium-containing buffer remained reasonably constant over time, confirming the IVNCG system was in steady state over 5 days (n=3).

4.3.3 Determination of Minimum NanoHA Seeding Density in Agarose Required to Produce Increased HA Formation Compared to Controls Using IVNCG.

To minimise any potential cytotoxic effect caused by the use of nanoHA within a dentine occlusion material, the minimum nanoHA seeding density required to outperform the positive control with respect to increased total phosphate mass was determined. The IVNCG was run as described in section 4.2.7 with phosphate analysis determined as described in section 4.2.2. In order to accommodate the higher amounts of phosphate present in the sample gels following seeding with nanoHA, the calibration curve for phosphate was re-run to check for linearity at higher phosphate values. The resulting line of best fit was linear with an R^2 value of 0.999, confirming the linearity of the response at concentrations higher than the 100 μM phosphate standard previously used. All absorbance readings from the samples containing nanoHA seed crystals in the IVNCG experiments were within the absorbance value limits of the new calibration curve.

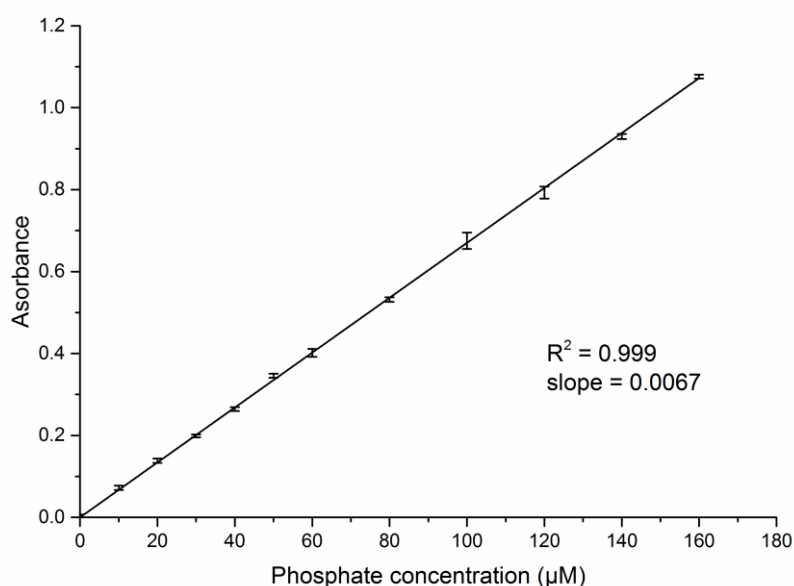


Figure 4-7 Calibration curve showing absorbance at 820 nm against phosphate concentration up to 160 μM . The line of best fit shows a linear response with a R^2 value of 0.999 confirming linearity. Error bars show 2x standard deviation, $n=3$.

The experiment to determine the minimum nanoHA seeding density required to significantly increase the phosphate mass showed a significant difference between the positive and negative controls ($p < 0.05$), Figure 4-8, which confirmed that the run was valid. The results suggested a linear increase in phosphate mass within the samples seeded with 10 to 50 $\mu\text{g/mL}$ nanoHA with any seeding density above 50 $\mu\text{g/mL}$ producing a similar phosphate mass up to the maximum seeding density tested at 100 $\mu\text{g/mL}$ nanoHA. The minimum nanoHA seeding density required to produce a statistically significant increase in phosphate mass compared to the positive control was found to be 30 $\mu\text{g/mL}$ ($p < 0.05$).

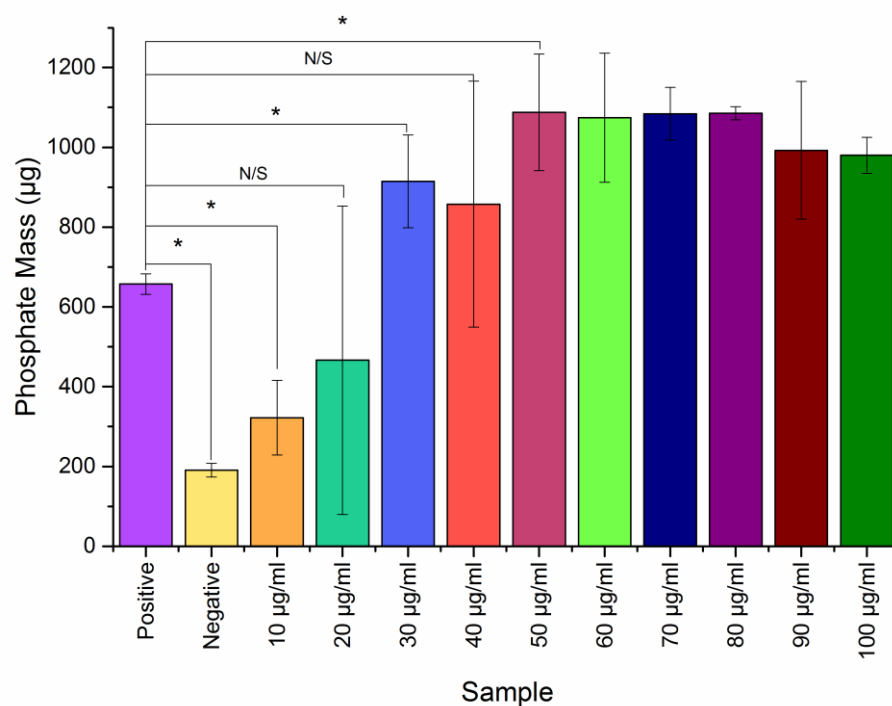


Figure 4-8 Bar chart showing phosphate mass in samples of increasing nanoHA seeding density ($n=3$) after 5 days in IVNCG compared with positive and negative controls. Positive control was agarose with 10 $\mu\text{g/mL}$ poly-L-glutamic acid, negative control was agarose alone. Error bars show 2x standard deviation, N/S= no significant difference, *= significant difference ($p < 0.05$). The minimum seeding density of nanoHA required to produce a statistically significant increase in phosphate mass compared to the positive control was 30 $\mu\text{g/mL}$. Added phosphate in form of nanoHA 5.66 μg of phosphate per 10 μg of nanoHA added.

To confirm the results from the IVNCG assay using a range of different seeding densities (10-100 $\mu\text{g/mL}$ nanoHA seeded 1% agarose, see Figure 4-8), the experiment was repeated using the lower concentrations of 10, 20 and 30 $\mu\text{g/mL}$

of nanoHA seeded in 1% agarose with $n=10$ per concentration. This experiment was repeated 3 times to determine reliability. The results of the IVNCG experiments using samples containing 10, 20 and 30 $\mu\text{g/mL}$ nanoHA seeded in 1% agarose confirmed that a minimum nanoHA seeding density of 30 $\mu\text{g/mL}$ was required to produce a significant increase in phosphate mass over the 5-day IVNCG experiment when compared to the positive control ($p<0.05$), Figure 4-9. Each of these repeats showed statistically significant differences between the positive and negative controls ($p<0.05$). Runs 1 and 2 produced similar results for samples containing 10 and 20 $\mu\text{g/mL}$ nanoHA which were both significantly below the phosphate values for the positive control. However, in contrast, the 10 and 20 $\mu\text{g/mL}$ nanoHA samples in run 3 produced larger phosphate masses, with both the mean phosphate mass for the 10 and 20 $\mu\text{g/mL}$ nanoHA seeding density samples not statistically different to the positive control.

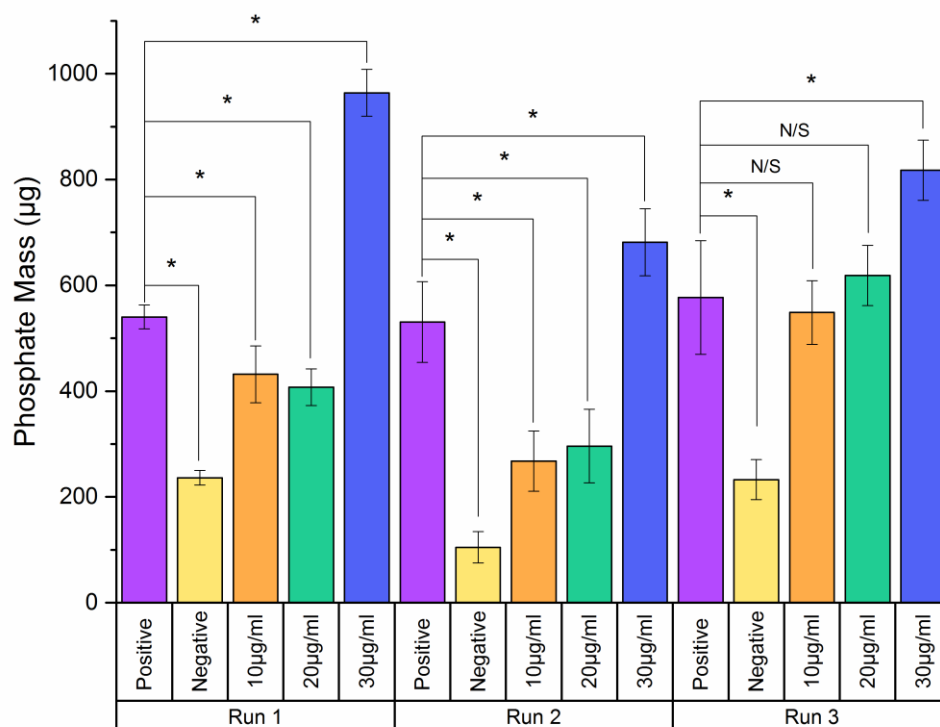


Figure 4-9 Bar chart showing quantity of phosphate produced as a function of nanoHA seeding density after 5 days in the IVNCG. All 3 runs showed that a 30 µg/mL nanoHA seeding density was the minimal seeding density required to produce statistically significant increase in phosphate mass compared to the 10 µg/mL poly-L-glutamic in 1% agarose positive control (*= $p < 0.05$). Added Phosphate in form of nanoHA 5.66 µg of phosphate per 10 µg/mL of nanoHA added. Error bars show 2x standard deviation. Samples $n=10$, controls $n=3$.

4.3.4 Isolation and Analysis of Mineral Formed in NanoHA Seeded Agarose after 5 Days in IVNCG

To investigate the mineral formed during the IVNCG 5-day run, the deposits were isolated and then analysed using SEM and EDS to determine morphology and elemental composition. Following the 5-day IVNCG experiment described above using increasing amounts of seed crystals in each of the sample wells, the Bio-Rad ChemiDoc™ MP Imaging system was used to image the precipitated mineral in each recovered sample gel at the end of the run. Figure 4-10 shows clearly the band-like precipitation of mineral present in the positive (poly-L-glutamate) control and in the sample seeded with 30 µg/mL nanoHA. The samples seeded with 10 µg/mL and 20 µg/mL nanoHA showed not only an

apparently less dense mineral precipitation but also a wider spread of mineralisation foci throughout the gel. The negative control showed only very sparse formation of mineral.

The precipitated material was then recovered from the agarose gels using the method described in 4.2.8. Both the positive controls and the samples containing 30 $\mu\text{g}/\text{mL}$ of nanoHA formed a cloudy suspension after the agarose had been dissolved by the sodium citrate, with no large aggregates visible. In contrast the negative control and samples seeded with 10 $\mu\text{g}/\text{mL}$ and 20 $\mu\text{g}/\text{mL}$ nanoHA all maintained the large “particle-like” morphology visible in the Bio-Rad ChemDoc™ images, see Figure 4-10. In order to determine crystal morphology and composition in the samples, SEM and EDS analyses were completed as described in section 4.2.8.

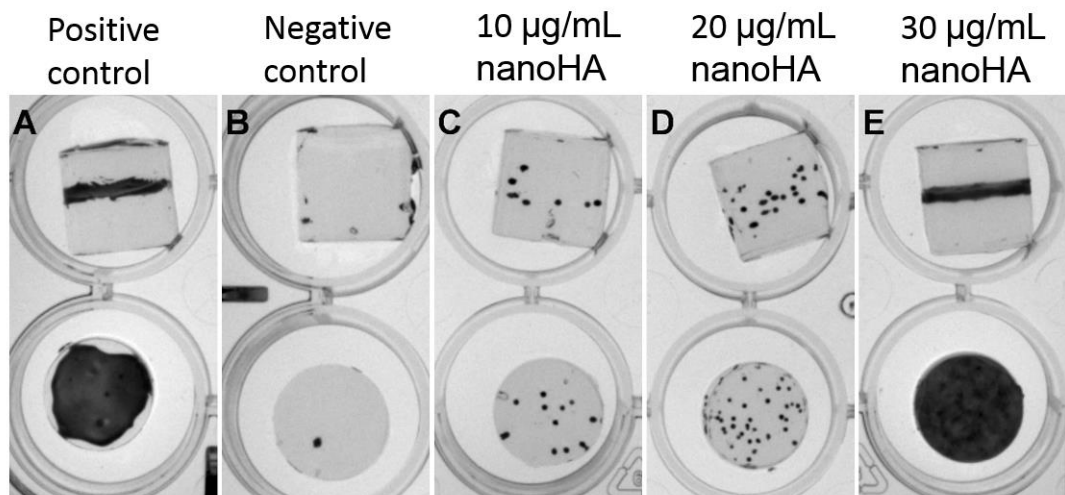


Figure 4-10 Images of mineral precipitate formed within agarose gels and retrieved after 5 days in the IVNCG assay. A) Positive control (1% agarose with poly-L-glutamate at 10 $\mu\text{g}/\text{mL}$); B) Negative control (1% agarose only); C) 10 $\mu\text{g}/\text{mL}$ nanoHA in 1% agarose; D) 20 $\mu\text{g}/\text{mL}$ nanoHA in 1% agarose; E) 30 $\mu\text{g}/\text{mL}$ nanoHA in 1% agarose. Images taken on the Bio-Rad ChemDoc™ MP imaging system using the Coomassie Blue standard protocol available on the ChemDoc™ software. Top row images show side-on view of the samples, bottom row shows gel from the perspective of the buffer interface with respect to position in the IVNCG assay. A change in precipitate appearance is visible when nanoHA seeding density increased from 20 $\mu\text{g}/\text{mL}$ nanoHA (sparse regions of precipitate) to 30 $\mu\text{g}/\text{mL}$ nanoHA (dense band of precipitate was visible).

The negative control and samples seeded with 10 $\mu\text{g}/\text{mL}$ and 20 $\mu\text{g}/\text{mL}$ nanoHA revealed the presence of large micron sized spherical particles which increased in number from the negative control to the 20 $\mu\text{g}/\text{mL}$ nanoHA seeded sample, see Figure 4-11 C, E and G. The particles were, however, all of similar size with diameters between 300 – 600 μm and had a similar surface morphology, see Figure 4-11 D, F and H. Material obtained from the poly-L-glutamate positive control sample had a sparse covering of what appeared to be small rod and needle shaped crystals with the longest axis having a size of 3 – 5 μm , see Figure 4-11 A and B.

Finally, crystals recovered from the 30 $\mu\text{g}/\text{mL}$ nanoHA seeded sample produced material more similar in morphology to the positive control than the lower concentrations of nanoHA seeded gels, with a dense coverage of needle and plate-like crystals, although these appeared larger than those crystals present in the positive control with the longest axis having a size of 7 – 20 μm , see Figure 4-11 I and J.

EDS analysis of the particles produced, shown in Table 4-2, indicated that the crystals produced in the negative control, 10 and 20 $\mu\text{g}/\text{mL}$ nanoHA samples had Ca/P molar ratios of 1.36, 1.38 and 1.42 respectively, suggesting the presence of octacalcium phosphate. The Ca/P ratios for the positive control at 1.51 and the 30 $\mu\text{g}/\text{mL}$ nanoHA seeded sample at 1.65 suggest a calcium deficient HA and stoichiometric HA respectively.

EDS Sample	Ca/P ratio	Standard deviation
Negative	1.36	0.04
10 µg/mL	1.38	0.20
20 µg/mL	1.42	0.12
Positive	1.51	0.01
30 µg/mL	1.65	0.05
Stoichiometric HA	1.67	
OCP	1.33	

Table 4-2 Table showing Ca/P molar ratio of isolated crystals produced in different samples in the IVNCG after 5 days, determined through EDS analysis. The analyses suggest that crystals produced in the negative control, 10 and 20 µg/mL nanoHA seeded samples were of similar Ca and P composition to OCP. The 30 µg/mL nanoHA sample produced a Ca/P ratio similar to hydroxyapatite while the positive control Ca/P ratio suggested a calcium deficient hydroxyapatite.

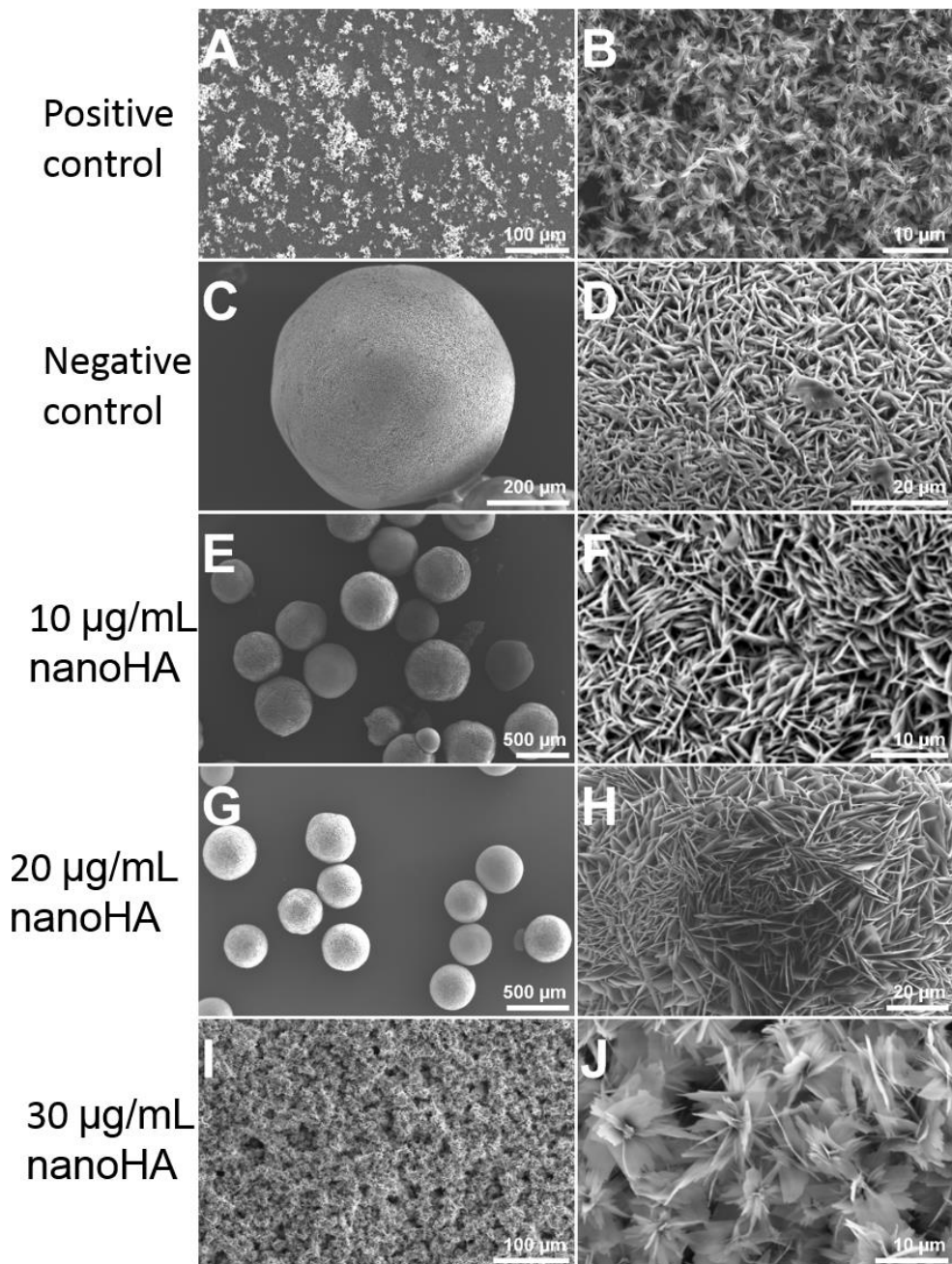


Figure 4-11 SEM images of mineral recovered from samples retrieved from the IVNCG assay after a 5-day run. A) and B) Positive control 10 µg/mL poly-L-glutamic acid in 1% agarose C) and D) negative control 1% agarose, E) and F) 10 µg/mL nanoHA G) and H) 20 µg/mL nanoHA, I) and J) 30 µg/mL nanoHA seeded agarose. Changes in crystal morphology were seen when nanoHA seeding density was increased from 20 µg/mL to 30 µg/mL, from large (300-600 µm), single spherical aggregates to smaller (7-20 µm) plate-shaped individual crystals (arrowed) respectively. The crystals retrieved from samples containing 30 µg/mL nanoHA had a similar appearance to the positive control while the crystals retrieved from samples containing 10 and 20 µg/mL nanoHA looked similar to those seen in the negative control.

4.3.5 Effect of Shortening the Duration of the IVNCG Run with Respect to Crystal Growth

To determine the effect of decreasing the length of the IVNCG experiment on the amount of phosphate produced after 4 days, the IVNCG experiment was repeated using agarose seeded with nanoHA at 10, 20 and 30 $\mu\text{g}/\text{mL}$ using nanoHA from a combination of batches 1 and 3, as described in section 4.2.7. This was undertaken to determine the effect of decreased run duration on the quantity of phosphate produced as well as enabling comparisons with the data described by Sayed (2013), who used a 4-day incubation.

After 4 days, the samples were removed from the IVNCG assay sample wells, ashed and analysed before determining phosphate mass as previously described in section 4.2.2. The phosphate masses produced in samples during the 4-day IVNCG assay run confirmed statistically significant differences between the positive (poly-L-glutamate in 1% agarose at 10 $\mu\text{g}/\text{mL}$) and negative (1% agarose) controls for all 3 individual runs ($p < 0.05$), see Figure 4-12 Bar chart showing phosphate mass produced in samples with different nanoHA seeding density after 4 days in the IVNCG assay, error bars show 2x standard deviation. All phosphate amounts detected in nanoHA seeded agarose samples were significantly lower compared to the positive control ($p < 0.05$) except for the sample seeded at 30 $\mu\text{g}/\text{mL}$ nanoHA in run 2 which contained a significantly increased level of phosphate ($p < 0.05$). Samples seeded with 30 $\mu\text{g}/\text{mL}$ nanoHA (produced by combining nanoHA batches 1 and 3) was the only sample to produce a statistically significant increase in recovered phosphate mass compared to the positive control ($p < 0.05$) and this was only apparent in run 2. The phosphate masses produced for samples seeded with nanoHA at 10 and 20 $\mu\text{g}/\text{mL}$ were significantly lower compared to the positive control in all 3 experimental runs ($p < 0.05$).

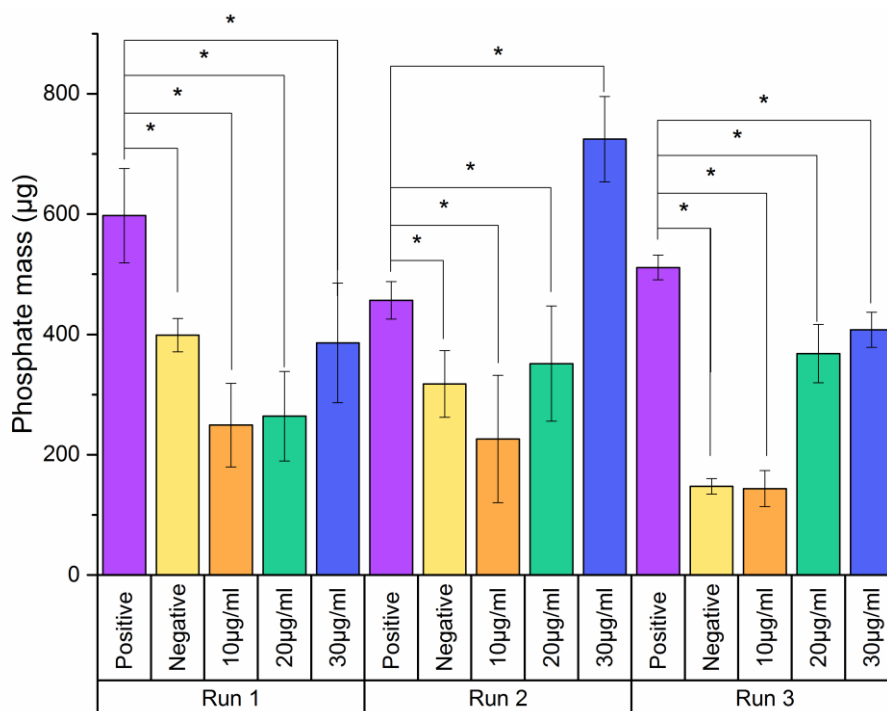


Figure 4-12 Bar chart showing phosphate mass produced in samples with different nanoHA seeding density after 4 days in the IVNCG assay, error bars show 2x standard deviation. All phosphate amounts detected in nanoHA seeded agarose samples were significantly lower compared to the positive control ($p < 0.05$) except for the sample seeded at 30 µg/mL nanoHA in run 2 which contained a significantly increased level of phosphate ($p < 0.05$). Added phosphate in form of nanoHA 5.66 µg of phosphate per 10 µg of nanoHA added.

4.3.6 Comparison of Synthesised NanoHA Produced in this Work to Other Synthetic NanoHA Using the IVNCG over a 4-Day Test Period.

To investigate if the source of nanoHA had any effect on the amount of phosphate produced during a 4-day IVNCG run, an experiment was designed using 3 different nanoHA samples (nanoHA produced in this thesis, combining batches 1 and 3), nanoHA of <200nm purchased from Sigma and “small-HA” produced by Sayed). The experiment would therefore enable comparisons to be made to the work of Sayed (2013) using the same IVNCG assay run length and the actual nanoHA sample that he used to produce his results. The IVNCG was run as described in sections 4.2.1 and 4.2.10.

After 4 days, there was a statistical difference in the amount of phosphate recovered from the positive and negative controls ($p < 0.05$). Only samples

seeded with 30 µg/mL nanoHA produced in this thesis produced a phosphate mass that was insignificantly different to the positive control ($p>0.05$). All other samples produced phosphate levels similar to the negative control, see Figure 4-13.

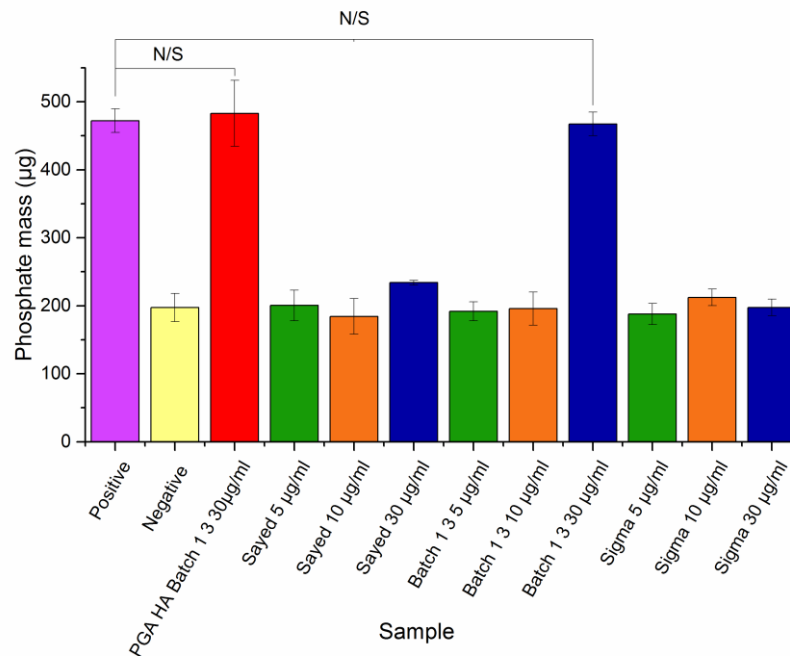


Figure 4-13 Bar chart showing effect of nanoparticle source (“small HA” from Sayed’s work, combined batches 1 and 3 nanoHA produced in this thesis and nanoHA purchased from Sigma) at varying seeding densities against phosphate mass in the samples after 4-day IVNCG assay runs (n=3). Red shows Poly-glutamic acid in agarose seeded with 30 µg/mL batch 1 3 nanoHA seeding density. Green bars show phosphate in samples with a 5 µg/mL nanoHA seeding density, orange bars show 10 µg/mL seeding density and blue bars show 30 µg/mL seeding density. Almost all samples contained significantly lower amounts of phosphate compared with the positive control. The exceptions were samples containing 30 µg/mL nanoHA produced in this thesis by combining batches 1 and 3. No significant differences were seen between these and the positive control (significance value $p<0.05$). Added phosphate in form of nanoHA 5.66 µg of phosphate per 10 µg of nanoHA added. Error bars show 2x standard deviation.

4.4 Discussion

The ultimate aim of this thesis was to generate a hybrid material containing nanoHA and self-assembling peptides for use in the treatment of dentine sensitivity. To enable the optimisation and assessment of the hybrid material with respect to its ability to support nanoHA crystal growth, a validated, quantitative assay was needed. The assay used in this work was developed from previous steady state assays as described in section 4.1.

Poly-L-glutamic acid was selected as the positive control for the IVNCG assay developed here as it has been used as a positive control in hydroxyapatite crystal nucleation and growth studies previously (Hunter *et al.*, 1996; Sayed, 2013) and has also been investigated as a potential material to promote the nucleation and growth of hydroxyapatite in demineralised dentine collagen (Sun *et al.*, 2014). Poly-L-glutamic acid is a peptide polymer composed of L-glutamic acid residues. Glutamic acid residues have been reported to be associated with the nucleating domains of a number of non-collagenous proteins implicated in biological HA nucleation (Deshpande *et al.*, 2011). The mechanism by which poly-L-glutamic acid promotes the nucleation of HA under biological conditions is presumed to be a function of the negative charge that the amino acid carries at pH 7.4 due to deprotonation of the carboxylic acid R group. The negative charge on the carboxyl group is thought to attract calcium ions, increasing the local saturation of ions with respect to HA, favouring the formation of stable crystal nuclei which can then undergo crystal growth (Jahromi *et al.*, 2013). Poly-L-glutamic acid has not only been shown to promote HA nucleation, it has also been shown to interact with growing HA crystals through bonding preferentially to specific crystal planes during crystal growth. The interaction of poly-L-glutamic acid at concentrations of 20 – 80 mg/mL with HA surfaces in an environment saturated with respect to HA has also been investigated (Wang *et al.*, 2015). The results confirmed a change in the morphology of the crystals formed through limiting growth along the crystal axis to which the poly-L-glutamate was bound, resulting in plate like crystals, in contrast to the chemical precipitation method which resulted in needle-like crystal morphology.

A number of macromolecules thought to be potential nucleators of HA in the formation of bone have been shown to contain domains of negative charge due to glutamic acid rich sequences. Bone sialoprotein, which contains a significant amount of glutamic acid residues, was shown by Hunter and Goldberg (1994) to promote the nucleation of HA *in vitro*. A follow up paper also confirmed the effectiveness of bone sialoprotein and phosphophoryn as nucleators of HA when compared to the negative control of 1% agarose. Both bone sialoprotein and phosphophoryn produced an increase in calcium and phosphate mass as a function of the concentration of protein added, with bone sialoprotein producing a larger calcium phosphate mass than phosphophoryn when equal masses of the protein were used. Interestingly, when osteopontin was used in the same experiments, it was found to have no calcium phosphate nucleating properties. The structure of osteopontin is very similar to that of bone sialoprotein except for the glutamic acid rich motif, which is absent from the osteopontin protein (Hunter *et al.*, 1996). This suggested that the presence of the glutamic acid rich region of bone sialoprotein is important to the calcium phosphate nucleation properties of the bone sialoprotein protein.

The effectiveness of poly-L-glutamate as nucleator of HA makes it an ideal choice as a positive control within the IVNCG due to its proven ability as a nucleator of HA. This not only enables the validation of the system through comparisons with other established *in vitro* nucleation methods but also provides a means to assess how effective other materials are with regards to their nucleation and support of crystal growth.

To validate the IVNCG assay with respect to its ability to determine the nucleation and crystal growth supporting properties of a given sample, a statistical comparison between the positive control, 10 µg/mL poly-L-glutamic acid in 1% agarose and the negative control, 1% agarose, was used. The results from the 4 individual experiments carried out in order to validate the IVNCG system produced significant differences between the positive and negative controls on each occasion ($p < 0.05$; Figure 4-5). These data confirmed the work initially carried out by Sayed (2013) and showed that the IVNCG assay is a reliable assay capable of providing reproducible differences between the positive and

negative controls. However, each individual run resulted in different amounts of mineral being deposited in both the positive and negative control samples, underlining the individuality of each run and the necessity to run controls for each experiment when testing unknown samples. The optimisation and assessment of material with respect to their nucleation and crystal growth supporting properties would require the materials of interest to be tested within one experimental run if their properties are to be compared and statistically analysed. Measurement of the concentrations of phosphate and calcium in the calcium-containing buffer and the phosphate-containing buffer in the respective reservoir tanks of the IVNCG assay confirmed the approximate steady state nature of the system, see Figure 4-6.

When comparing the quantity of phosphate measured in each of the controls in the experiments carried out in this thesis to the work of Sayed (2013), there was a significantly increased level of phosphate in both the negative and positive controls in the current work. Amounts of phosphate were also significantly different from those reported by Hunter and Goldberg (1994), using a different system but the same controls. Table 4-3 summarises these differences. Sayed (2013) used the same system as that described in the current work so it is perhaps surprising to see significant differences between his previous work and that carried out in the course of this thesis. The most simple and straightforward explanation for the significant difference between the values of phosphate precipitated in the Sayed (2013) experiments and those obtained here, is a possible error made in the mathematical calculation of phosphate mass. Sayed (2013) present's images showing significant precipitation within the retrieved agarose gels after his IVNCG assay runs which would be expected to correspond to a significantly larger phosphate mass than the levels quoted. The negative controls obtained in this thesis after the IVNG runs contained very little or no visible mineral deposits, yet apparently yielded phosphate masses that were larger than those quoted for the positive controls in the work by Sayed (2013). The method by which the data was processed by Sayed (2013) states that the amount of phosphate measured in a background sample that had not been in contact with the reservoirs buffers was subtracted from each sample's phosphate mass at the end of the IVNCG assay experiment. The contribution of phosphate

to the final sample arising from the reservoir buffer itself was not accounted for. Given that the phosphate-containing reservoir buffer has a concentration of approximately 315 µg/mL, the quoted value of 15 -25 µg/mL quoted by Sayed (2013) as the amount of phosphate present in the agarose negative control at the end of the IVNCG run is very low.

	Negative control (µg of phosphate/mL)	Positive control (µg of phosphate/mL)
IVNCG assay: This work	120 - 300	470 – 770
IVNCG assay Sayed 2013	15-25	120-170
Hunter and Goldberg 1994	440 (70 % = 310)	1000 (70 % = 700)

Table 4-3 Table showing comparison of approximate phosphate masses produced during *in vitro* mineralisation studies normalised to µg/mL. The 70% values in brackets show expected phosphate concentrations when the decrease in surface area of sample in contact with calcium-containing and phosphate-containing buffer is taken into account due to the smaller sample wells used in the IVNCG assay.

Comparison of the phosphate values obtained in IVNCG assay control samples in this work and those presented by Hunter and Goldberg suggests that the phosphate mass values obtained using the IVNCG assay were slightly lower, see Table 4-3. The ion concentrations of the buffer solutions used by Hunter and Goldberg (1994), (6 mM CaCl₂ and 6 mM NaPO₄ compared with 6.5 mM Ca(NO₃)₂.4H₂O and 3.9 mM Na₂HPO₄.2H₂O used here) may be one reason for the elevated phosphate masses produced in their agarose controls. A further experimental parameter which is different between the IVNCG assay used here and the Hunter and Goldberg (1994) system is the surface area of each sample that is in contact with the calcium-containing and phosphate-containing buffers. The surface area of the sample in contact with the buffer in the IVNCG used here is approximately 70% of the area in contact with the buffers in the Hunter and Goldberg (1994) method (0.785 cm² and 1.12cm² respectively). On inspection of

the positive controls after the 5-day IVNCG testing period, it can be seen that a band of mineral had formed in the middle of the gel with no mineral formed at either end. The presence of this mineralising band has been reported previously using other *in vitro* mineralisation assay techniques (De Jong *et al.*, 1980; Boskey, 1989; Hunter and Goldberg, 1993). If we consider that the band volume near the centre of the gel has the potential to mineralise because the concentrations of calcium and phosphate have reached the required concentration to support the nucleation and growth of crystals, see Figure 4-14, a decrease in the area of the surface area of sample in contact with the calcium-containing and the phosphate-containing reservoir buffers would be expected to have a significant effect on the amount of mineralisation that can occur. The smaller diameter of the sample wells (thus the surface area in contact with the calcium containing and phosphate-containing buffers) in the IVNCG system used here is thus likely to result in a smaller phosphate reading, 30% lower, than the values obtained using the Hunter and Goldberg system (1994), assuming the thickness of the mineralised band is the same in both methods. When this is taken into account, the values displayed in Table 4-3 seem reasonably close when using the higher end of the range produced in this work.

The formation of a small amount of precipitate in the negative controls is most likely caused by heterogeneous nucleation of mineral on the surface of impurities within the agarose samples, which in effect act as crystal seeds. The presence of solid particles (e.g. dust) provides a liquid/solid interface which acts to lower the free energy of crystal formation, as part of the energy barrier to crystal nucleation is the creation of a new phase which would no longer have to occur due to the solid phase present in the form of dust. The concentrations of calcium and phosphate ions present in the IVNCG system are below that expected to result in spontaneous homogenous nucleation but are high enough to promote crystal growth once stable nuclei are present. The effect of the solid phase with respect to its ability to support the growth of a mineral precipitate will depend on how well the surface of the solid particle mimics the crystal structure of the calcium phosphate phase growing on its surface. The minimal amount of phosphate mass present in the negative controls confirms that the steps taken

to limit the solid impurities through thorough cleaning of the IVNCG assay equipment and filtration of the buffer solutions, is effective.

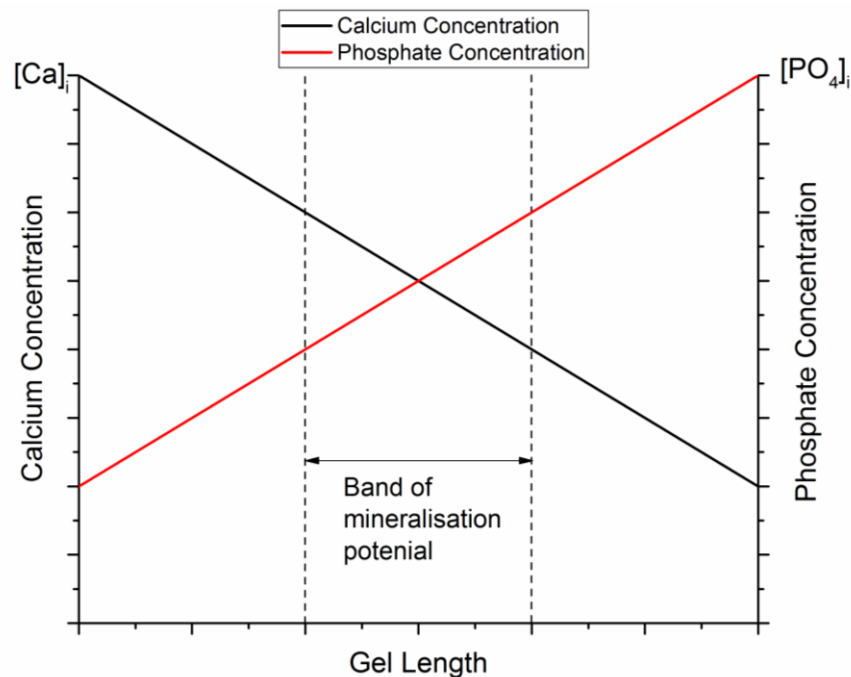


Figure 4-14 – Graph showing the model diffusion properties of the IVNCG system assuming a static system. The model holds only prior to the formation of mineral. Dashed lines indicate region where mineralisation is possible.

The phosphate masses recovered from control samples reported in this work are considerably closer to those obtained by Hunter and Goldberg (1994) than those previously reported by Sayed (2013) despite the fact that Sayed used the same experimental set-up as that used here and are even closer when the smaller sample surface area in contact with the calcium-containing and phosphate-containing buffers is considered. The reliability of the IVNCG assay data produced during this study coupled with the similar phosphate masses produced when compared to the work of Hunter and Goldberg (1994) confirms the validation of the IVNCG assay with regards to the outcomes produced using positive and negative agarose controls.

Having validated the IVNCG with respect to its ability to demonstrate statistically significant differences between the abilities of materials to nucleate and support the growth of HA under physiological conditions, the assay was then used to determine the minimum seeding density of nanoHA required to increase the

quantity of phosphate mass produced during the 5-day test period compared to the positive control.

The use of nanoHA as a material for bone tissue engineering and as a material for use in dental applications is seen as an effective means to provide the materials required to form new bone and enamel tissues (Zhou and Lee, 2011). NanoHA is seen as a potentially useful source of HA as the small size of the crystals are similar to those of the native tissues themselves and they are able to penetrate into small spaces, for example into dentine tubules. However, one important issue regarding the clinical use of nanoHA in medical applications is potential toxicity and changing of cellular function. This currently is a matter of debate due to the variable effects of the particle size (Shi *et al.*, 2009), seeding density (Motskin *et al.*, 2009) and morphology (Xu *et al.*, 2009) of the nanoHA used. There are a number of authors who have investigated the effect of nanoHA on a range of cells but with the results seemingly inconclusive (Xu *et al.*, 2009; Remya *et al.*, 2014; Shi *et al.*, 2017).

One factor which was explored by Xu *et al.* (2009) was how different nanoHA crystal morphologies (spherical versus needle), at a seeding density of 10 mg/mL affected protein expression in osteoblasts (Xu *et al.*, 2009). They showed that nanoHA needle morphology resulted in significantly reduced osteoblast cell numbers compared to the nanoHA spherical morphology over a 4-day period in culture. Both spherical and needle nanoHA crystal morphologies produced significantly lower osteoblast cell density compared to the controls, suggesting that nanoHA was toxic to osteoblast cells. The concentration of nanoHA used in the Xu *et al.* (2009) study was 10 mg/mL which was considerably greater than the concentrations used in this work (<100 µg/mL) but the mechanism of the toxicity was hypothesised to be a function of local calcium concentration due to the dissolution of nanoHA crystals (Liu *et al.*, 2009). This then could be an issue even at lower concentrations, depending on how the nanoHA and the cells interact (Shi *et al.*, 2017). However, a study by Remya *et al.* (2014) concluded that the use of nanoHA crystals with a needle morphology at a seeding concentration of up to 800 µg/mL had no significant effect on bone marrow mesenchymal stem cells isolated from mouse bone marrow.

The literature is inconclusive with respect to the toxicity of nanoHA and its effects on cellular function and so to limit the effect of any potential toxicity or interaction with cellular processes when using the proposed hybrid material, which contains nanoHA with needle morphology, the minimum concentration of nanoHA required to provide a statistically significant increase compared to the positive control was undertaken using the IVNCG assay. The IVNCG experiment would also provide an overview of the effect of the addition of increasing the sample nanoHA seeding density.

The testing of agarose samples seeded with nanoHA at concentrations above 40 µg/mL was carried out to determine what levels of phosphate mass could be achieved using concentrations that were higher than the previous work carried out by Sayed (2013), which analysed samples with a maximum nanoHA seeding density of 40 µg/mL. The results from the current study showed that there was a direct relationship between phosphate mass in precipitates recovered from samples containing 10 to 50 µg/mL nanoHA seeds after incubation in the IVNCG system. This was in agreement with the work of Sayed (2013). Above 50 µg/mL, it appeared that the addition of more seed crystals had no effect on the resulting phosphate mass of the precipitated mineral after 5 days in the IVNCG system. The reason for this plateau in recovered phosphate mass in precipitates as seeding density increased over and above 50 µg/mL is unclear but one possible cause is disruption to the diffusion pathway within the gels caused by significant mineral accumulation within the sample gel, which would act to impede further mineralisation on either side of the central mineralised band. Further work to confirm this hypothesis would be required, via measurement of phosphate and calcium ion concentrations in areas of the sample gel either side of the mineralisation band, in a similar manner to the work of Boskey (1989). However, this would be difficult to achieve in the IVNCG system which uses sample gels that are only 1 cm long compared to the 6 cm gels used in the Boskey method.

Further repeats of the seeding density experiments described previously confirmed that a minimal seeding density of 30 µg/mL nanoHA was required to provide a positive statistically significant difference compared to the positive control ($p < 0.05$, Figure 4-9). The minimal seeding density of 30 µg/mL nanoHA

was different to that identified by Sayed (2013), who reported a minimal seeding density value of 10 µg/mL nanoHA using the same IVNCG system. Further work was therefore carried out to explore the reasons behind this difference.

There are no works in the literature that explore the effect of nanoHA seeding density on the rate or quantity of phosphate/mineral produced in gel-based systems. Seeding density studies have, however, been undertaken in dilute aqueous systems. For example Moreno *et al.* (1977) studied the crystal growth kinetics of hydroxyapatite seeds added to a stirred 250 mL vessel through pH and calcium and phosphate analysis. Using starting seeding densities equating to 80 µg/mL- 200 µg/mL HA (particle size of 44 -53 µm), Moreno *et al.* (1977) determined an initial linear relationship between precipitation rate and seeding density up to 160 µg/mL HA, at which point the rate decreased away from linear. The system employed by Moreno *et al.* (1977) provided a quantitative means for measuring the effect of seed crystals on initial precipitation rates but due to the non-steady state of the method, determination of the quantity of phosphate as a function of seeding density mass was not possible.

The use of nanoHA should have the effect of decreasing the seeding density required to increase the total mass of phosphate mineral produced compared to micron sized particles due to the large increase in surface area of nanoHA compared to micron sized HA when using equal seeding masses. The increased surface area would be expected to increase the potential for crystal growth as there would be a larger surface for calcium and phosphate ions to interact with. To determine the possible cause of the discrepancy between the results of this work and that of Sayed (2013), the variables of experimental run time, see section 4.3.5, and source of synthesised nanoHA used, see section 4.3.6, including a sample of small-HA produced by Sayed (2013), were investigated.

The use of a shorter, 4-day IVNCG experimental run did not affect the resulting minimum nanoHA seeding density of 30 µg/mL nanoHA required to significantly increase recovered phosphate mass in samples compared to the positive control. However, the decrease in run time did result in 2 of the 3 experimental runs returning a non-significant difference between the positive control and the 30 µg/mL nanoHA seeding density, see Figure 4-12. The decrease in IVNCG

assay run time had the effect of making the IVNCG assay less reliable. The use of different nanoHA samples (nanoHA produced in this thesis combined from batches 1 and 3, nanoHA purchased from Sigma and Sayed's "small-HA") over a 4-day time period did not produce any significant increases in phosphate mass compared to any sample. The combined batches 1 and 3 was the only sample to produce a phosphate mass that was similar when compared to the positive control with all other samples producing a significantly lower phosphate mass compared to the positive control ($p < 0.05$), see Figure 4-13. The variables of IVNCG assay run time and nanoHA sample source were investigated although neither variable could be proven to have caused the differences in the minimum nanoHA seeding densities required to significantly increase phosphate compared to the control between this work and the work of Sayed (2013).

To investigate the morphology and composition of the mineral produced in the nanoHA seeded agarose samples, the IVNCG was repeated using nanoHA seeding densities of 10, 20 and 30 $\mu\text{g/mL}$ in 1% agarose, along with the positive and negative controls. The resulting precipitate was isolated from the agarose gels and analysed using SEM and EDS using the method described in section 4.2.8. SEM images of the crystals isolated from each sample at the end of the IVNCG assay run suggested that increasing the crystal seeding density from 20 $\mu\text{g/mL}$ to 30 $\mu\text{g/mL}$ nanoHA resulted in a profound change in the resulting morphology of the mineral deposited within the gels, see Figure 4-11. The mineral formed below a 30 $\mu\text{g/mL}$ nanoHA seeding density appeared in the form of large spherical crystal aggregates of approximately 400 μm in diameter after 5 days in the IVNCG assay. These large crystals were also seen in the negative controls but increased in number from between 1 and 3 in the negative control up to 30-40 in the 20 $\mu\text{g/mL}$ nanoHA seeded samples. No smaller crystals were seen which suggested that either the smaller crystals were lost during the isolation process or the initial seed crystals dissolved during the initial diffusion period when the sample gels were undersaturated with respect to HA. In contrast, the mineral recovered from the samples seeded initially with 30 $\mu\text{g/mL}$ nanoHA was comprised of many small plate and rod-like crystals, see Figure 4-10 I and J. These were more similar, although larger, to those obtained from the positive controls, see Figure 4-10 A and B.

The reason for this change in crystal morphology above the 30 µg/mL nanoHA seed crystal concentration could be that lower concentrations of seeds are dissolving due to initial conditions of undersaturation with respect to HA at the beginning of the IVNCG experiment. This in turn would be expected to increase the local calcium and phosphate ion concentrations in the sample gels and would eventually result in re-precipitation of mineral with chemistry and morphology different to that of the initial crystal seeds. When seeding density is at 30 µg/mL nanoHA, the initial dissolution of seed crystals would still be expected to occur but crucially a significant number would endure, which could then undergo secondary crystal growth once the buffer calcium and phosphate ions had diffused into the samples. The resulting crystals would then be expected to be more similar in morphology to hydroxyapatite, such as was seen in the SEM.

This theory is also partly supported through the comparison of the crystals recovered from the 30 µg/mL nanoHA with the crystals recovered from the positive control. In both cases, a mineral precipitant was produced which comprised of many small crystals, with crystals in the positive control samples being smaller than those recovered from the seeded samples. The positive control, poly-L-glutamic acid, contained no crystal seeds and formed mineral purely through the nucleation and subsequent crystal growth of HA (Hunter *et al.*, 1996; Tye *et al.*, 2003). The formation of crystal nuclei by the positive control is a consequence of the saturation level with respect to HA. Once the saturation threshold is reached, HA nucleation initiates and is then overtaken by seeded crystal growth resulting in the large number of small crystals seen in the SEM images, see Figure 4-11. In the case of the samples seeded with 30 µg/mL nanoHA, the local saturation levels ultimately reached would prevent the further dissolution of seed crystals and would also be expected to favour the growth of crystals through Ostwald ripening (Iggländ and Mazzotti, 2012).

The EDS analysis also supported the theory of seed crystal dissolution at lower seeding densities as indicated by a change in the Ca/P ratio that accompanied the change in crystal morphology when the nanoHA seeding density was increased from 20 µg/mL to 30 µg/mL. The Ca/P ratio of crystals formed within the negative controls, 10 µg/mL and 20 µg/mL nanoHA samples suggested that

the calcium phosphate phase present was OCP-like and this was supported by the comparisons of the SEM image presented in Figure 4-1 D,F and G which look nearly identical to published SEM images of OCP coatings, see Figure 4-15 produced in the literature (Lin *et al.*, 2015). The complete initial loss of nanoHA seed crystals in the 10 $\mu\text{g/mL}$ and 20 $\mu\text{g/mL}$ nanoHA seeded samples would result in the formation of OCP which is kinetically favoured over HA at $\text{pH} < 9$ due to its lower activation energy (Hill and Gillam, 2015). The formation of HA mineral at 30 $\mu\text{g/mL}$ nanoHA seeding density would occur only if the nanoHA seeds were still present due to the template effect of having HA mineral already present within the solution. The increased number of seed crystals still available prior to the diffusion of ions into the gels from the buffers compared to the lower seeding density samples results in significant crystal growth once steady state is achieved. The remaining seeds crystals then grow under the steady state saturated system present in the agarose gels producing the increased mineral density and increased number of crystals compared to the lower nanoHA seeded samples.

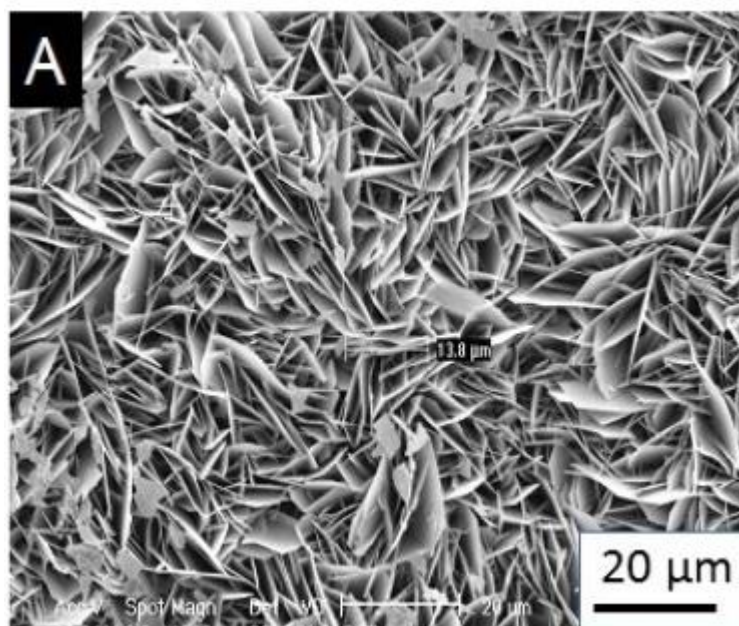


Figure 4-15 SEM micrographs of OCP coating reproduced from Lin *et al* (2015)

4.5 Conclusion

The work undertaken in this chapter has validated the IVNCG assay with respect to its ability to provide reproducible, statistically significant differences between phosphate levels recovered from positive and negative gel controls over a 5-day period. Analysis of the calcium and phosphate concentrations in the reservoir buffer solutions demonstrated the steady state principle of the assay. The IVNCG assay was also able to identify a minimal nanoHA seeding concentration of 30 $\mu\text{g/mL}$, defined as providing a statistically significant increase in phosphate mass compared to the poly-L-glutamate positive control, indicating that this amount of crystal seed would be useful in further experiments to minimise any potential toxic effects associated with the use of nanoHA. Differences between the work here and that presented previously by Sayed (2013) were investigated by changing the IVNCG run length and nanoHA source with no sample other than 30 $\mu\text{g/mL}$ (or above) nanoHA seeds produced in this study being able to provide a statistically significant positive difference or statistically similar result when compared to the positive control. Analysis of crystals formed in the agarose gels provided an insight into the mineralisation mechanisms operating within the samples, suggesting that initial conditions of undersaturation influence the resulting mineral formed. This should be taken in to account when using samples which can be affected by the initial undersaturated conditions.

Chapter 5 – IVNCG Assay Assessment and Optimisation of Self-Assembling Peptide/Nano-Apatite Hybrid Material With Respect to its Mineral Forming Potential.

The following chapter will introduce the self-assembling peptide/nanoHA hybrid material (“hybrid material”) and describe the combination and assessment of the material with regards to its mineral forming ability using the IVNCG assay. Issues arose with respect to the solubility of the hybrid material when used in the IVNCG assay which resulted in hybrid material precipitation. Novel precipitation studies were undertaken to determine the cause of the precipitation in high ionic strength media i.e. the conditions found in the IVNCG assay and in artificial saliva. It was determined that the hybrid material was unstable with respect to its solubility when testing with the calcium and phosphate-containing buffers used in the IVNCG assay. Conversely it was found to be soluble when using calcium and phosphate concentrations associated with artificial saliva solutions.

5.1 Introduction

The use of self-assembled peptides is a vast research area with a wide variety of potential applications including tissue engineering (Kyle *et al.*, 2009), drug delivery (Fan *et al.*, 2017), active therapeutics (Tsomaia, 2015) and cell culture scaffolds (Worthington *et al.*, 2015). The ease of peptide synthesis and limitless sequences that can be synthesised make them attractive alternatives to natural products for use in medical applications (Vlieghe *et al.*, 2010). Peptide self-assembly is a strategy used to make functional materials and relies on the reversible association of molecules through a multiplicity of weak (compared to thermal energy) non-covalent interactions (typically Van der Waals, electrostatic, hydrophobic, hydrogen bonds, π - π stacking) to produce large (nanoscale to macroscopic) highly ordered structures (Whitesides and Boncheva, 2002). The reversible nature of the interactions between the individual peptide molecules is key to the self-assembly process and results in the thermodynamic minimum energy configuration being produced negating the effect of any kinetic intermediates which may form (Marini *et al.*, 2002). There are many different structures which can be formed using peptide self-assembly including but not limited to nanotubes (Hatip Koc *et al.*, 2017), spherical micelles (Hatip Koc *et al.*, 2017), cylindrical micelles (Hartgerink *et al.*, 2001) monolayers (Leo *et al.*, 2017) and 3D fibrillar networks (Davies *et al.*, 2006). The driving force for self-assembly of molecules is a combination of the formation of non-covalent molecular interactions between molecules (listed above) which lower the Gibbs free energy, and the release of the structured array of solvent molecules which increases the entropy of the system. When considering H₂O as a solvent this effect is called the hydrophobic effect and is a significant driving force in self-assembling systems containing hydrophobic domains in an aqueous environment. The energy of interaction between the H₂O and self-assembling molecules is smaller than for the interaction between self-assembling molecules, therefore providing an enthalpic force to the self-assembly process in addition to the entropic driving force (Beer *et al.*, 2003).

The self-assembling peptide (SAP) component of the hybrid material under investigation in the following chapter has been developed from the active

ingredient in the commercially available “Curodont” dental product range. The active ingredient present in the Curodont products is based upon the P₁₁₋₄ self-assembling peptide developed at the University of Leeds (Aggeli *et al.*, 2003b; Davies *et al.*, 2006; Kirkham *et al.*, 2007; Carrick *et al.*, 2007). P₁₁₋₄ with the amino acid sequence AcQQRFWOFOQQNH₂ structure, shown in Figure 5-1, belongs to a class of SAPs that is designed to undergo a well characterised and understood 1 dimensional self-assembly into nano-tapes through the formation of the β -sheet conformation (Davies *et al.*, 2006). The β -sheet tapes then undergo further self-assembly in a hierarchical manner to produce ribbons, fibrils and finally fibres, see section 2.10. P₁₁₋₄ was assessed alongside the hybrid material to determine its potential effectiveness when added to the dentine surface.

P₁₁₋₄ Amino acid sequence

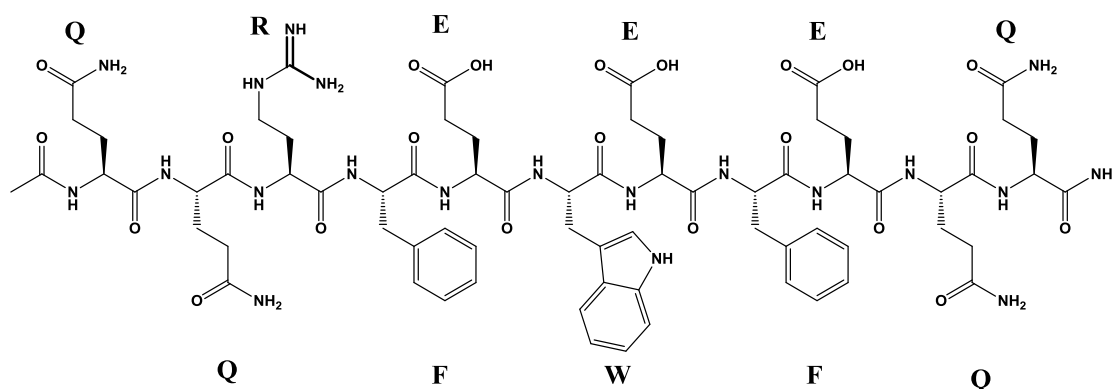
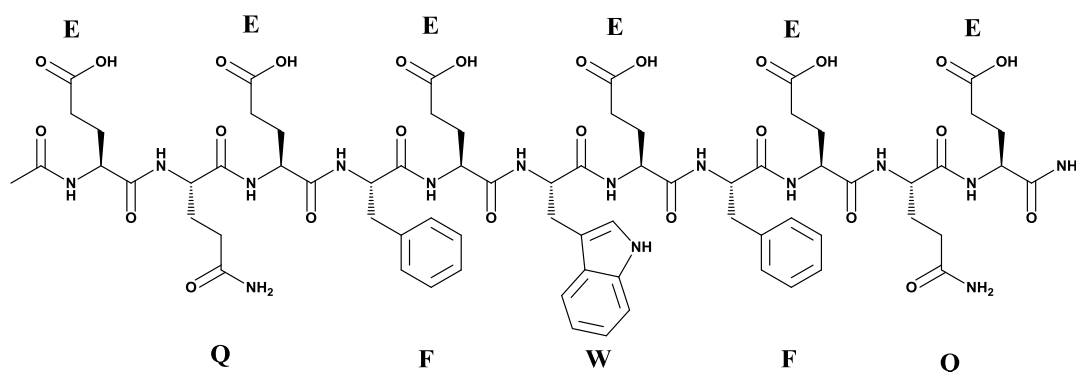


Figure 5-1 Amino acid sequence of peptide P₁₁₋₄ with one letter amino acid code labels. At pH 7.4 the 3 glutamic acid residues (E) of P₁₁₋₄ are deprotonated (pK_a<4.25, see section 2.10) and the Arginine (R) is protonated (pK_a= 12.5) producing an overall negative charge of 2-. Stereochemistry shown through dashed line representing behind the peptide backbone while thick black line represents in front of the peptide backbone.

Through appropriate design and consideration of the chemistry behind the monomer interactions, it is possible to control or trigger self-assembly; examples include but are not limited to temperature, pH, solvent polarity and presence of metal ions (Zou *et al.*, 2015). The peptides that were used as the primary target for development of the hybrid material described in this work are triggered to assemble through the addition of 2 different monomer units which, when dissolved individually at pH 6-8 and in physiological salt concentrations, remain

in an unassembled monomer state, but when added together in equal molar concentrations, the monomers self-assemble producing a self-supporting gel system. This class of SAPs are termed peptide electrolyte complexes or commonly referred to as ‘complementary’ peptides due to the need for both to be added for self-assembly to be triggered (Kyle *et al.*, 2012). The complementary peptides P₁₁₋₁₃ and P₁₁₋₁₄ are 21 amino acid long peptides with the amino acid sequence AcEQEFWEFEQENH₂ and AcQQOFOWFOQQNH₂ respectively, see Figure 5-2.

P₁₁₋₁₃ Amino acid Sequence



P₁₁₋₁₄ Amino acid Sequence

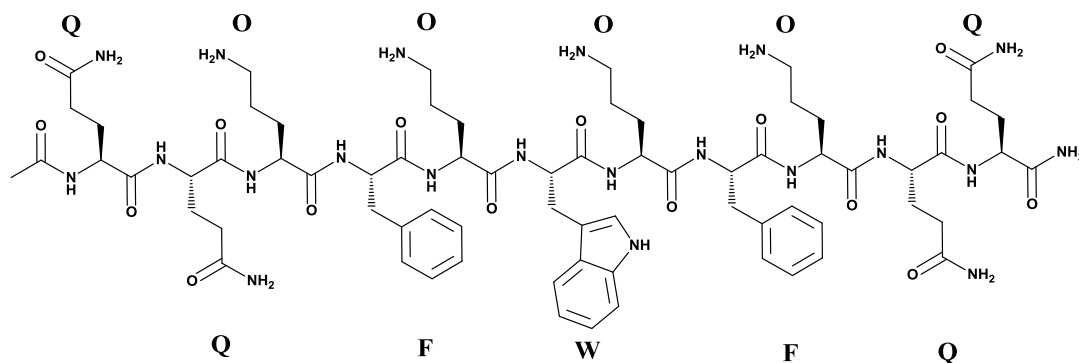


Figure 5-2 – Amino acid sequence of complementary peptides P₁₁₋₁₃ and P₁₁₋₁₄ with one letter amino acid code labels. At pH 7.4 the glutamic acid residues (E) of P₁₁₋₁₃ are deprotonated (pK_a<4.25 see section 2.10) producing an overall negative charge of 6-. At pH 7.4 the ornithine residues (O) are protonated (pK_a=10.76) producing an overall positive charge of 4+. Stereochemistry shown through dashed line representing behind the peptide backbone while thick black line represents in front of the peptide backbone.

Both P₁₁₋₁₃ and P₁₁₋₁₄ were designed so that when dissolved individually at physiological pH and salt concentration (pH 7.4, 120 mM NaCl), no self-

assembly would occur due to the 4+ charge on P₁₁₋₁₄ (protonation of the ornithine residues pK_a = 10.76) and 6- charge on P₁₁₋₁₃ (deprotonation of the glutamic acid residues pK_a < 4.25 see section 2.10). When the peptide powders are dissolved, they are in monomeric form which is in an un-assembled and unordered conformation and exist as a non-Newtonian liquid. When the monomers are added together in equal molar ratios, with respect to peptide concentration, the peptide monomers self-assemble into an anti-parallel β -sheet conformation resulting in β -sheet tapes. The β -sheet tapes then interact in a hierarchical manner to form a 3-dimensional fibrillar network. There are a number of interactions which occur between the P₁₁₋₁₃ and P₁₁₋₁₄ β -strands which, when combined, result in the formation of anti-parallel β -sheets. The hydrophobic residues on both P₁₁₋₁₃ and P₁₁₋₁₄ can interact through the hydrophobic effect, and these interactions are further stabilised through π - π stacking due to the respective positions of the tryptophan and phenylalanine residues on both the P₁₁₋₁₃ and P₁₁₋₁₄ monomer units. The peptide backbone of the peptide monomers interact with one another through hydrogen bonding of the double bonded oxygen to the hydrogen of the nitrogen on the peptide backbone either side with respect to the β -sheet. The hydrogen bonds act like a “zip” and the monomer units will position themselves to maximise the number of corresponding hydrogen bonds between each monomer unit to minimise the free energy. Finally, the negatively charged glutamic acid residues (6 in total) form ionic interactions with the positively charged ornithine residues (4 in total), see Figure 5-3. The cumulative result of these non-covalent interactions is the formation of the anti-parallel β -sheet configuration as this produces the minimal energy state.

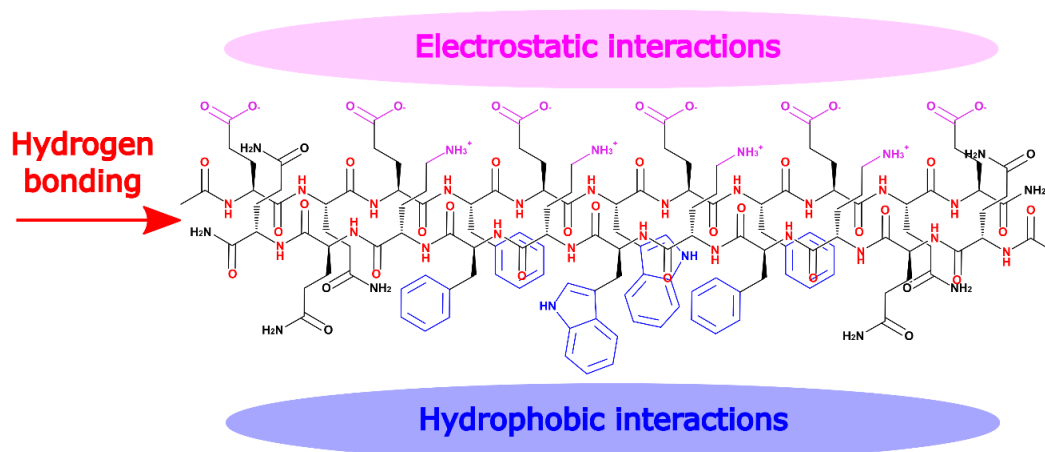


Figure 5-3 - Schematic of the non-covalent interactions between one molecule of P₁₁₋₁₃ and one molecule of P₁₁₋₁₄ when in anti-parallel β -sheet formation under physiological conditions (pH 7.4, 150 mM NaCl). Lilac residues show position of charged groups present at pH 7.4. Blue residues show positions of hydrophobic residues at pH 7.4. Red atoms show position where hydrogen bonding occurs between peptide backbones. For simplicity only 2 units are shown although in reality a continuous repeating dimeric unit of P₁₁₋₁₃ and P₁₁₋₁₄ is present when critical concentration is reached.

The combination of one unit of P₁₁₋₁₃ and one unit of P₁₁₋₁₄ results in an overall charge of -2 per repeating unit. This overall charge aids the self-assembled peptide with respect to its solubility (Pace *et al.*, 2004). The odd number of peptide residues ensures that the anti-parallel configuration occurs as this ensures that the hydrogen bonding between partnering peptides is maximised in contrast to the parallel configuration, which would result in 1 set of unsatisfied hydrogen bonds on each individual monomer unit. The reversible nature of self-assembly ensures that the lowest energy conformation is produced. The self-assembled tapes can then interact due to the attraction of the hydrophobic sides of the tapes resulting in the formation of fibrils. The fibrils formed by P_{11-13/14} have been investigated by Kyle *et al.* (2012).using TEM. The maximum length was found to be 2 μ m long with a fibrillar diameter of 10-20 nm

The hybrid material used through this work was produced through combining the P_{11-13/14} complementary peptide pair with nanoHA seed crystals. The resulting peptide hydrogel is highly charged due to the -2 charge per repeating dimeric unit which results in dense overall negative charge domains across the fibril surface. The peptides were designed as such in the hope that the negative

charge domains would replicate the negatively charged domains present in extracellular matrix proteins responsible for the nucleation and crystal growth of biological hydroxyapatite during biological mineral growth (Boskey, 2003).

Previous studies carried out by Sayed have shown that the complementary peptides P₁₁₋₁₃ and P₁₁₋₁₄ were poor nucleators of hydroxyapatite but when combined with nanoHA were excellent at supporting the growth of hydroxyapatite seed crystals when tested using the IVNCG assay described here in Chapter 4 (Sayed, 2013). The following chapter will investigate the mineral supporting properties of the hybrid material with respect to its ability to support the growth of the previously synthesised nanohydroxyapatite crystals, (Chapter 3), through using the previously validated IVNCG assay (Chapter 4).

5.2 Methods

5.2.1 Assessment of Mineralisation Potential of P_{11-13/14} SAP Seeded with 30 µg/mL NanoHA Using the IVNCG Assay

To assess and optimise the hybrid material with respect to its ability to promote and support the growth of hydroxyapatite, the hybrid material was tested in the previously validated IVNCG assay (Chapter 4). The IVNCG assay was cleaned and prepared as described in section 4.2.1. A 1 mg/mL suspension of the synthesised nanoHA batch 1 was produced by weighing out 25 mg of batch 1 nanoHA, (Chapter 3), into a 50 mL falcon tube and adding 25 mL of steady state solution (20 mM HEPES, 150 mM NaCl in DI H₂O). A second 1 mg/mL suspension of the synthesised nanoHA batch 3, (Chapter 3), was produced by weighing out 25 mg of batch 3 nanoHA into a 50 mL falcon tube and adding 25 mL of steady state solution. Both suspensions were vortexed (Vortex Genie 2 Scientific Industries, Bohemia, NY, USA) for 30 seconds followed by 2 times 20 second periods of sonic probe agitation (MISONIX model XL2010 Farmingdale, NY, USA with micro probe output 20 KHz). The 2 suspensions were then combined together in equal volumes to produce a 1 mg/mL nanoHA stock suspension of combined batches 1 and 3 nanoHA which was further diluted through the addition of steady state solution to produce a final concentration of 30 µg/mL nanoHA in steady state buffer. Peptide powders of P₁₁₋₁₃ and P₁₁₋₁₄ were weighed out into 2 mL glass vials (1 sample per concentration) and diluted using the combined nanoHA at 30 µg/mL in steady state solution, creating P₁₁₋₁₃ and P₁₁₋₁₄ peptide solutions at concentrations of 10 mM, 13 mM, 16 mM and 20 mM seeded with 30 µg/mL nanoHA (1.8 mL of each concentration). A small amount of base (5 M NaOH) was added dropwise to P₁₁₋₁₃ suspensions to fully dissolve the peptide and reach a pH of 8.0. A small amount of acid (1 M HCl) was added dropwise to P₁₁₋₁₄ samples to lower the pH to 7.0. Peptide solutions were then sonicated before 425 µL of P₁₁₋₁₃ solution of each concentration was added in triplicate into separate IVNCG assay sample wells. The corresponding P₁₁₋₁₄ peptide solution was then added in to each well, which resulted in the formation of a self-supporting gel of P_{11-13/14} in steady state buffer seeded with 30 µg/mL nanoHA. Controls containing 10 µg/mL poly-L-glutamic acid in 1 %

agarose and 1 % agarose in triplicate were included as positive and negative controls respectively as described in Chapter 3. A P_{11-13/14} sample at a peptide concentration of 20 mM was also included without any addition of nanoHA seeding. A P₁₁₋₄, known to nucleate HA, was also included as a control at a concentration of 20 mM. This was prepared by dissolving a small amount of P₁₁₋₄ in steady state solution producing a final concentration of 20 mM. The P₁₁₋₄ solution was then pH adjusted to pH 7.4 and heated (50 °C) to prevent gelation before pipetting into sample holder and cooling to form a gel. Calcium-containing buffer and phosphate-containing buffer were added to the IVNCG assay buffer compartments and the whole equipment, including the samples, was incubated at 37°C, with stirring, for 5 days. After the 5-day test period the samples were removed from the sample wells and analysed for phosphate content as previously described in Chapter 3.

5.2.2 Effect of Decreasing the NanoHA Seeding Density and IVNCG Assay Run Length on Quantity of Mineral Formed by the Hybrid Material

The effect of decreasing the nanoHA seeding density added to the peptide gels from 30 µg/mL to 10 µg/mL and of decreasing the length of the IVNCG testing period from 5 to 4 days, with respect to the phosphate mass produced in the hybrid material using the IVNCG assay, was investigated. This experiment was undertaken to determine the effect of decreased nanoHA seeding density and IVNCG run length on the hybrid material's ability to promote mineral growth and to allow for comparisons to the work of Sayed (2013). The IVNCG assay experiment described in section 5.2.1 was repeated using a lower concentration of nanoHA seeds of 10 µg/mL and an IVNCG test duration of 4 days.

5.2.3 Effect of Using a Benzoylated Dialysis Membrane on Quantity of Mineral Formed In The Presence of the Hybrid Material Using the IVNCG Assay

To determine if the self-assembling P_{11-13/14} aggregates were disassembling due to monomer diffusion through the dialysis membrane, the membrane was changed to a 2000 kD benzoylated membrane which decreased the molecular

weight cut off (MWCO) to 57% of the original. The precipitation of the hybrid material after 5 days in the IVNCG could have been caused by the disassembly of the hybrid material due to diffusion of peptide through the dialysis membrane. To determine if a decrease in pore size of the dialysis membrane used to cover the hybrid material samples in the IVNCG assay sample wells had any effect on the resulting mass of phosphate formed, the IVNCG experiment was repeated as described in section 5.2.1, with the replacement of the membrane (SpectraPor-3 MWCO 3.5kD, Hoeksteen Netherlands, 132724) with a benzoylated membrane (Dialysis tubing, benzoylated 2000 kD, Sigma-Aldrich, St. Louis, MO, USA).

5.2.4 Investigation of Peptide Precipitation

During IVNCG experiments using the hybrid material, precipitation was seen to occur in the sample wells. A novel experiment was therefore designed to investigate the cause of the peptide precipitation. Peptide samples (200 μ L total volume) were placed into the well of a 96 well plate and buffer solutions pipetted onto the surface (100 μ L). The plate was then incubated at 37 °C for 5 days with any precipitation being monitored visually and recorded photographically daily. When recording the daily observations of the sample appearance, each sample was assessed and assigned to one of 3 categories depending on the severity of the precipitation present. If the sample was clear with no precipitation evident, it was assigned as “clear”. If a small amount of precipitation was present but it was still possible to see through the sample, then it was assigned as “slightly opaque”. If it was not possible to see through the sample, it was assigned as “opaque”.

5.2.4.1 Effect of Addition of IVNCG Calcium and Phosphate-Containing Buffers on Solubility of the Hybrid Material at Varying P_{11-13/14} Concentrations

The novel precipitation assay was first used to investigate the effect of P_{11-13/14} concentration (10, 13, 16, 20 mM) with a seeding density of 30 μ g/mL nanoHA when calcium-containing buffer, phosphate-containing buffer or calcium/phosphate-containing buffer was added. Control samples of 20 mM P_{11-13/14} (no nanoHA), 20 mM P₁₁₋₄ (no nanoHA), 20 mM P₁₁₋₄ (30 μ g/mL nanoHA) were also analysed. The peptide solutions were produced as previously

described, see section 5.2.1., and each sample and control (200 μ L) was pipetted into a 96 well plate sample well in triplicate. To each of the sample triplicates, 100 μ L of either IVNCG assay calcium-containing buffer (6.5 mM CaNO_3 , 20 mM HEPES 150 mM NaCl), phosphate-containing buffer (3.9 mM $\text{NaHPO}_4 \cdot 2\text{H}_2\text{O}$ 20 mM HEPES 150 mM NaCl) or a combination of IVNCG assay calcium and phosphate-containing buffer (6.5 mM CaNO_3 , $\text{NaHPO}_4 \cdot 2\text{H}_2\text{O}$ 20 mM, HEPES 150 mM NaCl) was added. The plate was then incubated at 37 °C for 5 days with any precipitation being monitored visually and recorded photographically daily.

5.2.4.2 Effect of Decreasing Calcium and Phosphate Concentrations on Hybrid Material Stability at 37°C

To investigate the effect of changing the calcium and phosphate concentrations on the precipitation of 20 mM peptide hybrid material samples, a second precipitation assay was carried out. Samples of hybrid material (20 mM P11-13/14 seeded with 30 μ g/mL nanoHA) were added (200 μ L) to 9 of the 96 well plate as described in section 5.2.4.1. IVNCG assay buffers were prepared at varying concentrations to produce 9 different buffers, all containing 20 mM HEPES and 150 mM NaCl but with varying levels of calcium and phosphate corresponding to 100 %, 75 % or 50 % of the concentrations present in the original IVNCG assay buffers ; [Ca] 6.5 mM (100 %), [Ca] 4.875 mM (75 %), [Ca] 3.75 mM (50 %)[PO_4] 3.9 mM (100 %), [PO_4] 2.925 mM (75 %), [PO_4] 1.95 mM (50 %) [Ca+ PO_4] 6.5 mM + 3.9 mM (100 %), [Ca] 4.875 mM + 2.925 mM (75 %), [Ca] 3.75 mM + [PO_4] 1.95 mM (50 %). Each buffer was added to one sample of P_{11-13/14} at 20mM concentration seeded with 30 μ g/mL of nanoHA. Control samples of 20 mM P_{11-13/14} (no nanoHA), 20 mM P₁₁₋₄ (no nanoHA), 20 mM P₁₁₋₄ (30 μ g/mL nanoHA) were exposed to IVNCG assay buffer at 100 % concentration only. The plate was then treated and monitored using the same method as described previously.

5.2.5 Quantitative Precipitation Study Comparing IVNCG to Artificial Saliva Calcium and Phosphate-Containing Buffers with Respect to Hybrid Material Precipitation.

The novel precipitation assay developed in section 5.2.4 was further adapted to provide better quality images and a quantitative measurement of the degree of hybrid material precipitation. The improvement in image quality was achieved through the use of the Bio-Rad ChemiDoc™ MP Imaging system using the Coomassie Blue standard protocol available on the Bio-Rad Chemidoc™ software, using a white light screen, standard filter, automatic exposure time and white transillumination. The quantitative improvement was achieved through the measurement of turbidity using the plate reader at wavelength 860 nm. Turbidity standards were produced using concentrations of 0-2000 NTU in 1000 NTU intervals (VWR Chemicals, standard turbidity formazin 4000 NTU, Lutterworth, UK). To determine if the hybrid material precipitated when in the presence of artificial saliva (AS) solution, a precipitation assay plate was prepared. The AS used throughout this work was first developed by Eisenburger *et al.* (2001) and is composed of CaCl₂ 0.7 mM (Sigma), MgCl₂ 0.2 mM (Sigma-Aldrich St. Louis, MO, USA) KH₂PO₄ 4 mM (BDH AnalaR, Poole, UK), KCl 30 mM (Sigma-Aldrich St. Louis, MO, USA) and HEPES 20 mM (Sigma-Aldrich St. Louis, MO, USA) with the pH adjusted to 7 using KOH (Eisenburger *et al.*, 2001). For the precipitation assay, 3 solutions of AS were prepared using the above method, one containing all of the listed constituents, the second containing all except the CaCl₂ and MgCl₂ and the final solution containing all with the exception of KH₂PO₄. The 3 IVNCG assay buffers being calcium-containing buffer (6.5 mM CaNO₃, 20 mM HEPES 150 mM NaCl), phosphate-containing buffer (3.9 mM NaHPO₄.2H₂O 20 mM HEPES 150 mM NaCl) and a combination of IVNCG assay calcium and phosphate-containing buffer (6.5 mM CaNO₃, NaHPO₄.2H₂O 20 mM, HEPES 150 mM NaCl), were also produced creating a total number of 6 buffers (3 AS solution buffers and 3 IVNCG buffers). Peptide solutions of 20mM P_{11-13/14} seed with 30 µg/mL nanoHA, 20 mM P_{11-13/14} (no nanoHA), 20 mM P₁₁₋₄ and 20 mM P₁₁₋₄ seeded with 30 µg/mL nanoHA were prepared as described in section 5.2.1. Each peptide sample (200 µL) was pipetted into 6 wells of a 96 well plate and had one of the 6 buffers (100 µL) described previously

(3 AS solution buffers and 3 IVNCG buffers) added. The plate was then incubated at 37 °C for 7 days with daily observations, turbidity measurement and imaging as described above.

5.2.6 The Use of ^1H NMR Analysis to Probe Peptide Aggregation with Respect to IVNCG NanoHA, Ionic Calcium and Ionic Phosphate Concentrations.

^1H NMR was used to investigate the potential interaction of P₁₁₋₁₃ and P₁₁₋₁₄ monomers with the added nanoHA particles in an environment containing ionic calcium at concentrations equal to those found in the calcium-containing buffer used in the IVNCG experiment (6.5 mM). A solution of D₂O steady state solution (20 mM HEPES, 150 mM NaCl in D₂O) was prepared and doped with 0.125 mM 3-(trimethylsilyl) propionic acid sodium salt (TMSP, Sigma-Aldrich St. Louis, MO, USA). The TMSP was added as an internal standard during the ^1H NMR experiments for the integration of the peaks, allowing comparisons between samples to be made. For both P₁₁₋₁₃ and P₁₁₋₁₄, 4 samples were prepared as described in the table below. D₂O steady state solution was used to dilute the peptide powders at a concentration of 20 mM producing a 0.8mL total sample volume. Samples were pD adjusted using DCI (Alfa Aesar, 20% w/w in D₂O, 99.96+%, Haverhill, MA, USA), and NaOD (Sigma Aldric, 40 wt. % in D₂O, 99.5 atom % D, St. Louis, MI, USA) to pD 6 for the P₁₁₋₁₄ samples, and pD 8 for the P₁₁₋₁₃ samples.

Samples were placed into a Bruker av500lc 500MHz NMR device using a H₂O pre-saturation programme with 1024 scans per spectrum. Once the spectrums were produced, they were analysed using the ACD/Spectrum Processor Academic addition (Advanced Chemistry Development, Inc., Toronto, On, Canada, www.acdlabs.com, 2015) software and the integral of the peaks in the 6.9-7.8 ppm region was measured and normalized to the TMSP peak. When the peptide is in a monomeric state, the free induction decay of the aromatic region hydrogen atoms proceeds at the same rate, producing sharp peaks in the signal. When the peptide is in an assembled state, the free induction decay is limited due to the close proximity of other hydrogen atoms resulting in a broadening of the signal. By comparing the integrals of the aromatic region, it was possible to

determine if the peptide was in a monomeric form, which would produce sharp peaks, or in an assembled state, which would produce broad peaks (Miles, 2012).

Sample number	Starting solution: 20 mM P ₁₁ -13 D ₂ O, 150 mM HEPES, 150 mM NaCl	Starting solution 20 mM P ₁₁ -14 D ₂ O, 150 mM HEPES, 150 mM NaCl
1	Control (as above)	Control (as above)
2	30 µg/mL nanoHA added	30 µg/mL nanoHA added
3	6.5 mM Ca(NO ₃) ₂ added	6.5 mM Ca(NO ₃) ₂ added
4	30 µg/mL nanoHA, 6.5 mM Ca(NO ₃) ₂ both added	30 µg/mL nanoHA, 6.5 mM Ca(NO ₃) ₂ both added

Table 5-1 Composition of samples investigated using ¹H NMR analysis to determine if peptide material was assembling on the nanoHA crystals.

5.3 Results

5.3.1 Assessment of Mineralisation Potential of P_{11-13/14} SAP Seeded with 30 µg/mL NanoHA (the “Hybrid Material”) Using the IVNCG Assay

To confirm the work of Sayed (2013) with respect to the hybrid material’s ability to support the growth of nanoHA crystals, the hybrid material was tested in the IVNCG assay. The concentration of P_{11-13/14} within the hybrid material was varied, while maintaining a constant nanoHA seeding density of 30 µg/mL, to investigate the effect of peptide concentration on the mass of phosphate produced. The experiment was completed as described in section 5.2.1.

After the 5-day testing period, the gels were removed from the sample holder onto the bench. The agarose samples (controls) had all retained their gel-like appearance as seen during the validation experiments previously. The P₁₁₋₄ gels retained a gel-like structure and were easily transferred to the glass vials. None of the P_{11-13/14} samples had maintained a gel-like appearance and were mainly liquid when removed from the sample wells. The samples had an opaque appearance indicative of mineral formation, though no band was visible prior to removal from the holder. The samples were grainy in appearance with small amounts of gel-like material surrounded by liquid. It was extremely difficult to transfer the samples to the glass vials due to the complete loss of gel structure. The samples were collected from the IVNCG sample wells using a Pasteur pipette and transferred to individual 10 mL glass vials. Phosphate analysis was determined as described in Chapter 3 and statistical analysis completed using one-way ANOVA with a *post hoc* Bonferroni test at the significance level 0.05.

The control sample of 1 % agarose seeded with 30 µg/mL nanoHA produced a significant increase in phosphate mass compared to the positive control (poly-L-glutamate, no nanoHA seeds, $p < 0.05$) which supported previous results, see Chapter 3. Statistical analysis confirmed a statistically significant increase in the phosphate mass produced in the positive control (poly-L-glutamate in agarose) compared to the negative control (agarose only), confirming that the run was valid, see Chapter 4. The 20 mM P_{11-13/14} control containing no nanoHA and

the 20 mM P_{11-13/14} sample with 30 µg/mL nanoHA were statistically insignificant compared to the positive (p>0.05). There was no statistical difference in recovered phosphate mass between the 20 mM P_{11-13/14} with or without the additional 30 µg/mL nanoHA seeds (p>0.05). The P_{11-13/14} nanoHA seeded samples and the P₁₁₋₄ sample all produced a phosphate reading statistically similar to the negative control (p>0.05).

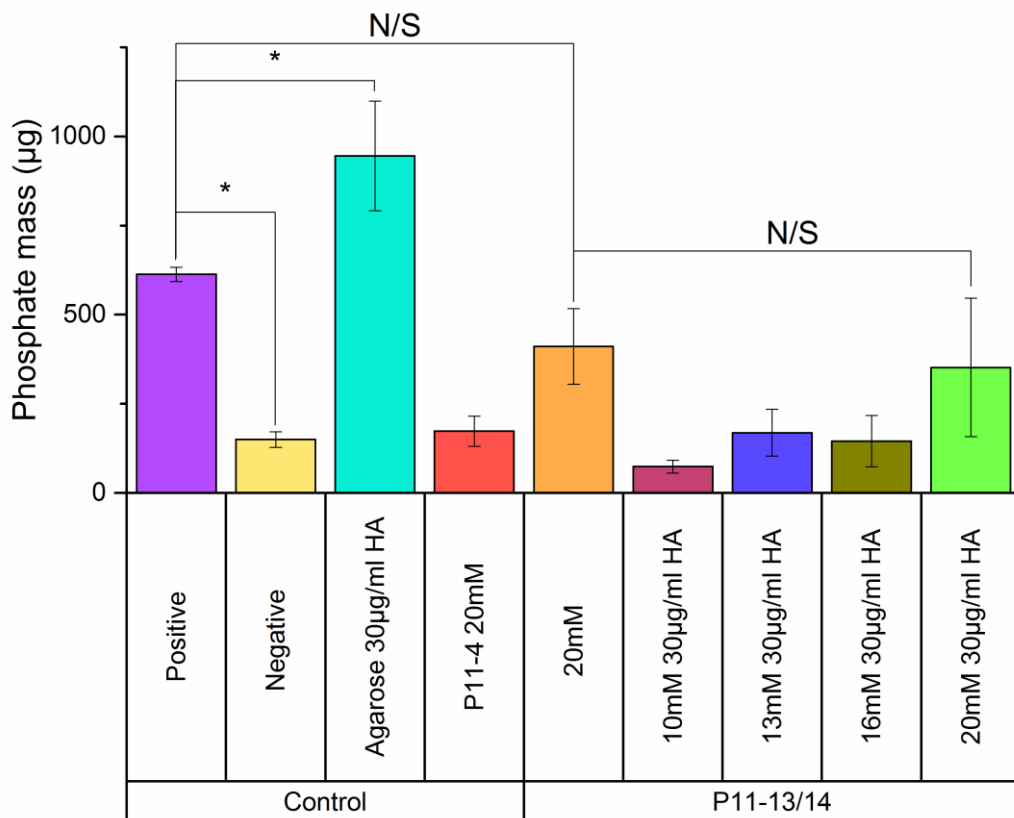


Figure 5-4 Bar chart showing the effect of changing SAP concentration on the amount of phosphate produced in the IVNCG assay. P_{11-13/14} samples were seeded with 30 µg/mL nanoHA. One sample at 20 mM was not seeded with 30 µg/mL nanoHA to act as a control. Control samples were 1 % agarose with 10 µg/mL poly-L-glutamic acid (positive), 1% agarose (negative), 1 % agarose seeded with 30 µg/mL nanoHA (nanoHA positive control) and 20 mM P₁₁₋₄ (peptide positive control). * = p < 0.05 . Error bars show 2x standard deviation.

5.3.2 Effect of Decreasing the NanoHA Seeding Density of P_{11-13/14} and Experiment Duration on Quantity of Mineral Formed Using the IVNCG Assay

To investigate the effect of decreasing the nanoHA seeding density from 30 µg/mL to 10 µg/mL in the hybrid material on the resulting phosphate mass formed in the IVNCG experiment, experiments were completed as described in section 5.2.2. The objective of this experiment was to not only study the effect of decreasing nanoHA seeding density but to also allow comparisons to the work of Sayed (2013).

At the end of the experiment, the P_{11-13/14} samples retrieved from the IVNCG assay had the same partially liquid/ broken gel structure as seen in the previous experiment, with the decreased nanoHA seeding density having had no discernible effect on the appearance of the samples. Again, the agarose controls and the P₁₁₋₄ samples all retained their self-supporting gel appearance. The masses of phosphate recovered from the samples after the IVNCG run were statistically analysed using one-way ANOVA with *post hoc* Bonferroni test at the significance level of 0.05, see Figure 5-5. The analysis confirmed a statistically significant difference between the positive and negative controls, validating the run. The negative control (1% agarose) seeded with 10 µg/mL nanoHA resulted in a low phosphate content which was not statistically different compared to the negative control itself, confirming the previous experiments undertaken in nanoHA seeding density determination. The P₁₁₋₄ sample (no nanoHA seeds) resulted in a phosphate recovery that was statistically similar to the positive control. The P_{11-13/14} samples however, had all produced low phosphate mass with all being statistically different to the positive control, except for the 10 mM P_{11-13/14} seeded with 10 µg/mL nanoHA sample which was statistically similar to the positive control ($p < 0.05$).

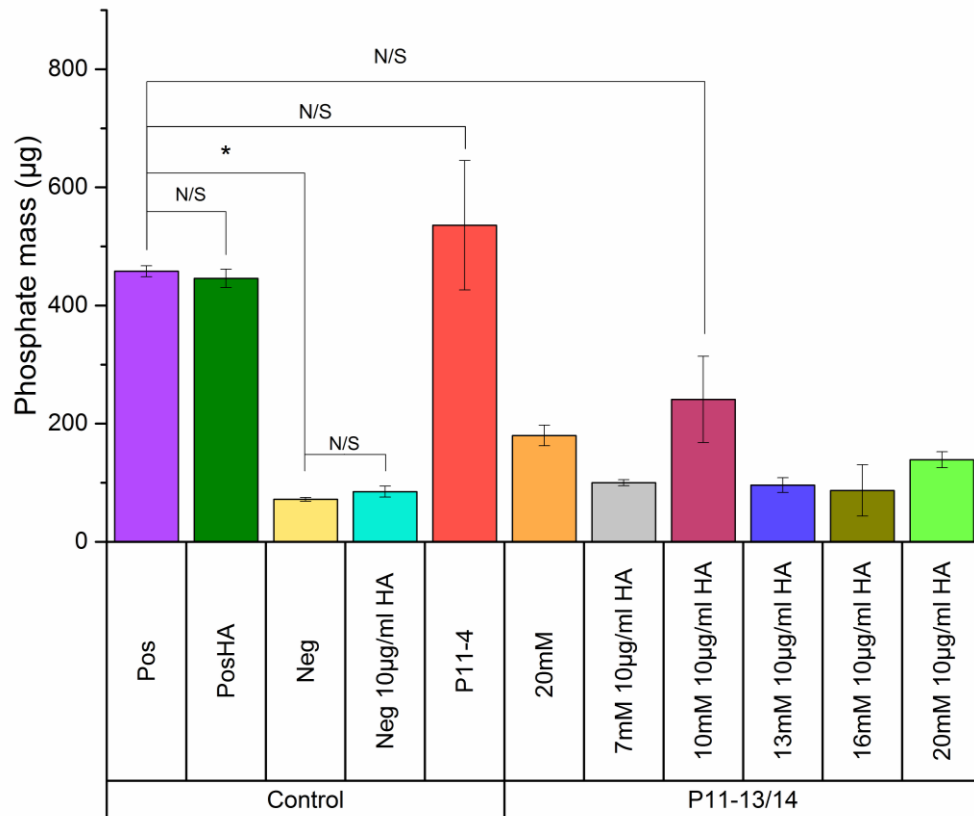


Figure 5-5 Bar chart showing effect of varying peptide concentration in hybrid material on phosphate mass produced in IVNCG assay when seeded with 10 µg/mL nanoHA over 4 days. The phosphate masses produced confirmed a statistically significant lack of phosphate mass accumulation for all the P_{11-13/14} samples compared with the positive control (poly-L-glutamic acid). Error bars show 2x standard deviation.

5.3.3 Effect of Using a Benzoylated Membrane on P_{11-13/14} on Quantity of Mineral Formed Using the IVNCG Assay

To determine if the use of a dialysis membrane with a smaller pore size would affect the quantity of mineral formed and prevent the breakdown of the gels when using the SAP/nanoHA hybrid material, the IVNCG experimental run was completed as described in section 5.2.3 using a benzoylated membrane to replace the standard membrane used previously. The benzoylated membrane reduced the molecular weight cut off by 57%. Unfortunately, at the end of the IVNCG run, there was no statistical difference in recovered phosphate mass between the negative and positive controls, which invalidated the run although the gels did maintain a gel structure.

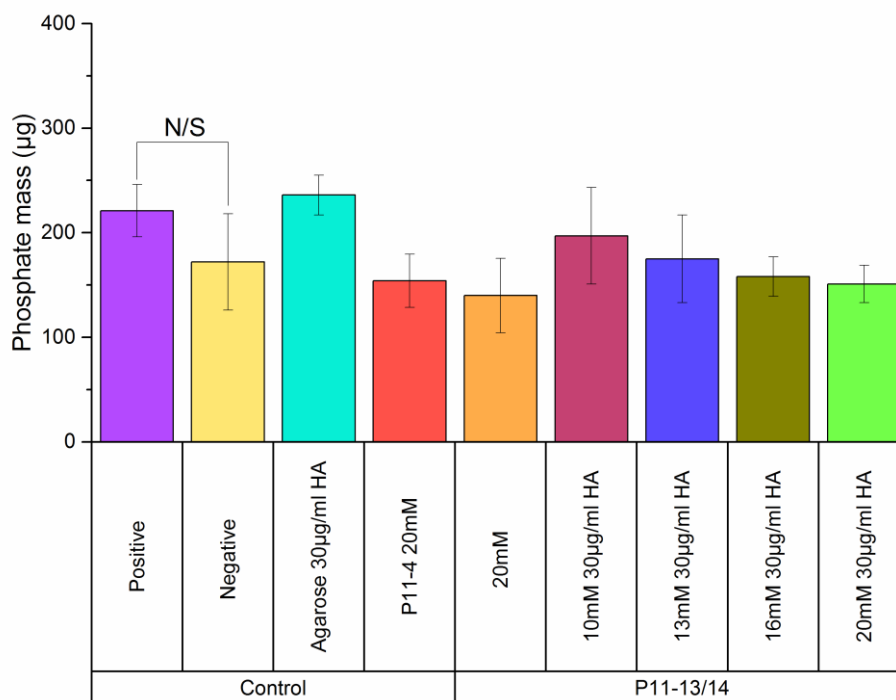


Figure 5-6 Bar chart showing varying hybrid material concentration IVNCG assay using benzoylated dialysis membrane. Hybrid material was seeded with 10 µg/mL nanoHA. Error bars show 2x standard deviation.

5.3.4 Precipitation Studies

5.3.4.1 Effect of Peptide Concentration, IVNCG Calcium and IVNCG Phosphate Buffers on Hybrid Material Precipitation.

To investigate if the addition of calcium-containing buffer, phosphate-containing buffer and a calcium/phosphate containing combination buffer (at calcium and phosphate concentrations used in the IVNCG assay) had any effect on the precipitation behaviour of the hybrid material, the precipitation assay was used over a 5-day testing period and observations were taken as previously described. Samples were loaded into the precipitation assay 96 well plate and the IVNCG assay calcium-containing buffer, phosphate-containing buffer and calcium/phosphate containing combination buffer added as described in section 5.2.4.1.

Initially, all P_{11-13/14} seeded with 30 µg/mL nanoHA samples, including the P_{11-13/14} control (no nanoHA), were clear. P₁₁₋₄ samples were slightly opaque which is consistent with the appearance of P₁₁₋₄ gels at a concentration of 20 mM, see Figure 5-7 day 0. On day 2, the samples of 10 mM P_{11-13/14} seeded

with 30 µg/mL nanoHA in calcium-containing buffer were slightly opaque, with all other peptide gels remaining unchanged. On day 3, precipitation was apparent in the samples containing 10 mM, 13 mM and 16 mM P_{11-13/14} with 30 µg/mL nanoHA that were exposed to calcium-containing buffer. The severity of the precipitation decreased with increasing peptide concentration. The sample containing 10 mM P_{11-13/14} seeded with 30 µg/mL nanoHA in calcium and phosphate combination buffer also turned slightly opaque. All other samples remained clear, see Figure 5-7 day 3.

On day 4, all the nanoHA seeded P_{11-13/14} samples with no calcium-containing buffer had precipitation present, increasing in severity with decreasing peptide concentration. In addition, precipitation was visible in the samples containing 10 mM P_{11-13/14} seeded with 30 µg/mL nanoHA in phosphate-containing buffer, which appeared slightly opaque. The P_{11-13/14} control sample (no added nanoHA) with calcium-containing buffer had a slightly opaque appearance. Precipitation in the nanoHA seeded P_{11-13/14} samples with calcium and phosphate combination buffer was visible in the 10 mM P_{11-13/14} sample and, to a lesser extent, in the 13 mM P_{11-13/14} sample. All the other samples remained unchanged.

On day 5, see Figure 5-7, the severity of the precipitation in the nanoHA seeded P_{11-13/14} samples with calcium-containing buffer had increased so that there was no observable difference between the samples, all containing a significant amount of precipitation and assigned as opaque. The sample containing 20 mM P_{11-13/14} (no nanoHA) with calcium-containing buffer control looked slightly opaque with a small amount of precipitation present. The sample containing 10 mM P_{11-13/14} seeded with nanoHA in phosphate-containing buffer was opaque with precipitation visible and the sample containing 13 mM P_{11-13/14} seeded with nanoHA was slightly opaque in appearance indicating a small amount of precipitation. All other samples incubated in the phosphate-containing buffer solutions remained unchanged from initial observations.

To summarise, the addition of calcium-containing buffer resulted in the most severe precipitation of P_{11-13/14} peptide gels with the effect increasing with decreasing peptide concentration. The addition of phosphate-containing buffer

had only a small effect on peptide precipitation which was again most noticeable in the samples with lower peptide concentrations. The results, obtained when using the calcium/phosphate containing combination buffer, were similar to those obtained using the calcium-containing buffer alone, although the rate and severity of precipitation formed in the samples were lower.

Sample Day 0	P ₁₁ -13/14 + 30µg/ml HA				P ₁₁ -13/14	P ₁₁ -4 30µg/ml HA	P ₁₁ -4 control	Sample Day 3	P ₁₁ -13/14 + 30µg/ml HA				P ₁₁ -13/14	P ₁₁ -4 30µg/ml HA	P ₁₁ -4 control
Peptide conc mM	10	13	16	20	20	20	20	Peptide conc mM	10	13	16	20	20	20	20
Calcium Buffer								Calcium Buffer							
Phosphate Buffer								Phosphate Buffer							
Calcium Phosphate Buffer								Calcium Phosphate Buffer							
Sample Day 1	P ₁₁ -13/14 + 30µg/ml HA				P ₁₁ -13/14	P ₁₁ -4 30µg/ml HA	P ₁₁ -4 control	Sample Day 4	P ₁₁ -13/14 + 30µg/ml HA				P ₁₁ -13/14	P ₁₁ -4 30µg/ml HA	P ₁₁ -4 control
Peptide conc mM	10	13	16	20	20	20	20	Peptide conc mM	10	13	16	20	20	20	20
Calcium Buffer								Calcium Buffer							
Phosphate Buffer								Phosphate Buffer							
Calcium Phosphate Buffer								Calcium Phosphate Buffer							
Sample Day 2	P ₁₁ -13/14 + 30µg/ml HA				P ₁₁ -13/14	P ₁₁ -4 30µg/ml HA	P ₁₁ -4 control	Sample Day 5	P ₁₁ -13/14 + 30µg/ml HA				P ₁₁ -13/14	P ₁₁ -4 30µg/ml HA	P ₁₁ -4 control
Peptide conc mM	10	13	16	20	20	20	20	Peptide conc mM	10	13	16	20	20	20	20
Calcium Buffer								Calcium Buffer							
Phosphate Buffer								Phosphate Buffer							
Calcium Phosphate Buffer								Calcium Phosphate Buffer							

Figure 5-7 – Daily photographs taken during precipitation assay showing effect of peptide concentration on rate and severity of precipitation under different buffer conditions. The white opaque appearance was indicative of peptide precipitation. Addition of calcium-containing buffer caused precipitation to occur at the fastest rate with samples containing the lower concentrations of peptide precipitating first. Addition of phosphate-containing buffer also resulted in precipitation but this was slower and less severe compared to the effects of the calcium-containing buffer. The addition of nanoHA also increased the severity and rate of precipitation compared to the unseeded P₁₁-13/14 20 mM control samples.

5.3.4.2 Effect of Calcium and Phosphate-Containing Buffer Concentration on Hybrid Material Precipitation

To investigate any relationship between the observed precipitation in the hybrid material and calcium and phosphate concentration in the incubation buffer, a repeat of the precipitation assay was undertaken using a fixed peptide concentration of 20 mM. The concentration of calcium and phosphate in the calcium-containing, phosphate-containing and calcium/phosphate-containing buffers was decreased to 75 % and 50 % of the initial concentrations used during the IVNCG experiment. The precipitation assay was prepared as described in section 5.2.4.2. When initially loaded into the wells, all of the P₁₁-13/14 samples were clear and the P₁₁-4 samples were slightly opaque, as expected from previous experiments, see Figure 5-8 day 0. After 24 hours, there was no change in appearance for any of the samples, with no opaque precipitation present with no opaque precipitation present until day 4.

On day 4, the samples containing P₁₁-13/14 with 30 µg/mL nanoHA and 100% concentration IVNCG calcium-containing buffer developed a slightly opaque appearance, as did the samples being incubated with the same buffer at 75 % concentration. A small amount of precipitation was also visible in the P₁₁-13/14 control (no added nanoHA) that was exposed to calcium-containing buffer, although not to the same extent as the samples containing nanoHA seeds. All other samples were unchanged.

On day 5, the samples that had been incubated with calcium-containing buffer had an opaque appearance that was severe in the case of the sample containing P₁₁-13/14 with 30 µg/mL nanoHA seeds at 100% IVNCG calcium concentration. Decreasing severity of precipitation was seen as the calcium concentration of the added buffer decreased. P₁₁-13/14 (no nanoHA) that was exposed to calcium-containing buffer also contained a small amount of precipitation and was considered slightly opaque. All other samples remained unchanged over the test period.

Sample Day 0	P11-13/14 + 30µg/ml HA			P11-13/14 no HA	P11-4 30µg/ml HA	P11-4 No HA	Sample Day 3	P11-13/14 + 30µg/ml HA			P11-13/14 no HA	P11-4 30µg/ml HA	P11-4 No HA
Conc buffer %	100	75	50	30	30	30	Conc buffer %	100	75	50	100	100	100
Calcium buffer							Calcium buffer						
Phosphate Buffer							Phosphate Buffer						
Calcium Phosphate buffer							Calcium Phosphate buffer						
Sample Day 1	P11-13/14 + 30µg/ml HA			P11-13/14 no HA	P11-4 30µg/ml HA	P11-4 No HA	Sample Day 4	P11-13/14 + 30µg/ml HA			P11-13/14 no HA	P11-4 30µg/ml HA	P11-4 No HA
Conc buffer %	100	75	50	30	30	30	Conc buffer %	100	75	50	100	100	100
Calcium buffer							Calcium buffer						
Phosphate Buffer							Phosphate Buffer						
Calcium Phosphate buffer							Calcium Phosphate buffer						
Sample Day 2	P11-13/14 + 30µg/ml HA			P11-13/14 no HA	P11-4 30µg/ml HA	P11-4 No HA	Sample Day 5	P11-13/14 + 30µg/ml HA			P11-13/14 no HA	P11-4 30µg/ml HA	P11-4 No HA
Conc buffer %	100	75	50	100	100	100	Conc buffer %	100	75	50	100	100	100
Calcium buffer							Calcium buffer						
Phosphate Buffer							Phosphate Buffer						
Calcium Phosphate buffer							Calcium Phosphate buffer						

Figure 5-8 Daily photographs taken during precipitation assay showing effect of IVNCG buffer concentration on rate and severity of precipitation in the hybrid material. White opaque appearance due to precipitation of peptide was visible in the calcium-containing buffer samples on day 5. Decrease in buffer calcium concentration resulted in a decrease in the rate and severity of precipitation over the 5-day test period.

5.3.5 Quantitative Precipitation Study Comparing IVNCG to Artificial Saliva (AS) Calcium and Phosphate Concentrations with Respect to Hybrid Material Precipitation.

To determine if the hybrid material displayed similar precipitation properties when exposed to AS solution (lower ionic calcium and phosphate concentrations) compared to the IVNCG buffer conditions, the enhanced quantitative precipitation assay was used. The previous novel precipitation assay was enhanced through the use of turbidity standards to enable measurement of

the precipitation while imaging was improved through the use of a Bio-Rad ChemiDoc™ MP Imaging system. The precipitation assay samples were loaded and measured as described in section 5.2.5. Initial observations agreed with the previous work with regards to clear P_{11-13/14} samples and the slightly opaque P₁₁₋₄ samples prior to the incubation period. Between days 1 to 4, all samples remained unchanged apart from the formation of bubbles, which occurred in a number of samples on day 1, see Figure 5-9. On day 5, the IVNCG calcium-containing buffered samples P_{11-13/14} seeded with 30 µg/mL nanoHA produced an opaque precipitate while the P_{11-13/14} control had a small amount of precipitate present. On day 6, the precipitate present in the IVNCG calcium-containing buffered samples had increased, with the P_{11-13/14} 30 µg/mL nanoHA sample having a severe amount of precipitation present. Both the IVNCG phosphate-containing buffered samples produced a small amount of white precipitate with the nanoHA seeded sample having slightly more white precipitate. The IVNCG calcium/phosphate combination buffer P_{11-13/14} 30 µg/mL nanoHA samples also had a small amount of precipitation present. On day 7, the precipitation in the IVNCG calcium buffered P_{11-13/14} samples had increased with the nanoHA seeded sample having a large amount of white precipitate present and the unseeded sample having a slightly opaque appearance. The precipitate present in the IVNCG phosphate-containing buffer had maintained a similar small amount of precipitate as visible on day 6. The IVNCG calcium/phosphate combination buffer also maintained the slightly opaque precipitate seen on day 6, with the nanoHA seeded sample being the most affected. The P_{11-13/14} sample under artificial saliva conditions maintained a clear appearance through the 7-day experiment with no precipitation visible. The P₁₁₋₁₄ samples under both IVNCG and AS buffer conditions maintained their appearance over the course of the 7-day experiment with the cloudiness attributed to the P₁₁₋₄ sample at 20 mM concentration seeming to spread evenly over the entire sample as a function of time.

Sample Day 0	P _{11-13/14} AS concentrations		P ₁₁₋₄ AS saliva concentrations		P _{11-13/14} IVNCG concentrations		P ₁₁₋₄ IVNCG concentrations		Sample Day 4	P _{11-13/14} AS concentrations		P ₁₁₋₄ AS saliva concentrations		P _{11-13/14} IVNCG concentrations		P ₁₁₋₄ IVNCG concentrations	
HA seeding density	0	30µg/ml	0	30µg/ml	30µg/ml	0	0	30µg/ml	HA seeding density	0	30µg/ml	0	30µg/ml	30µg/ml	0	0	30µg/ml
Calcium Buffer									Calcium Buffer								
Phosphate Buffer									Phosphate Buffer								
Calcium Phosphate Buffer									Calcium Phosphate Buffer								
Sample Day 1	P _{11-13/14} AS concentrations		P ₁₁₋₄ AS saliva concentrations		P _{11-13/14} IVNCG concentrations		P ₁₁₋₄ IVNCG concentrations		Sample Day 5	P _{11-13/14} AS concentrations		P ₁₁₋₄ AS saliva concentrations		P _{11-13/14} IVNCG concentrations		P ₁₁₋₄ IVNCG concentrations	
HA seeding density	0	30µg/ml	0	30µg/ml	30µg/ml	0	0	30µg/ml	HA seeding density	0	30µg/ml	0	30µg/ml	30µg/ml	0	0	30µg/ml
Calcium Buffer									Calcium Buffer								
Phosphate Buffer									Phosphate Buffer								
Calcium Phosphate Buffer									Calcium Phosphate Buffer								
Sample Day 2	P _{11-13/14} AS concentrations		P ₁₁₋₄ AS saliva concentrations		P _{11-13/14} IVNCG concentrations		P ₁₁₋₄ IVNCG concentrations		Sample Day 6	P _{11-13/14} AS concentrations		P ₁₁₋₄ AS saliva concentrations		P _{11-13/14} IVNCG concentrations		P ₁₁₋₄ IVNCG concentrations	
HA seeding density	0	30µg/ml	0	30µg/ml	30µg/ml	0	0	30µg/ml	HA seeding density	0	30µg/ml	0	30µg/ml	30µg/ml	0	0	30µg/ml
Calcium Buffer									Calcium Buffer								
Phosphate Buffer									Phosphate Buffer								
Calcium Phosphate Buffer									Calcium Phosphate Buffer								
Sample Day 3	P _{11-13/14} AS concentrations		P ₁₁₋₄ AS saliva concentrations		P _{11-13/14} IVNCG concentrations		P ₁₁₋₄ IVNCG concentrations		Sample Day 7	P _{11-13/14} AS concentrations		P ₁₁₋₄ AS saliva concentrations		P _{11-13/14} IVNCG concentrations		P ₁₁₋₄ IVNCG concentrations	
HA seeding density	0	30µg/ml	0	30µg/ml	30µg/ml	0	0	30µg/ml	HA seeding density	0	30µg/ml	0	30µg/ml	30µg/ml	0	0	30µg/ml
Calcium Buffer									Calcium Buffer								
Phosphate Buffer									Phosphate Buffer								
Calcium Phosphate Buffer									Calcium Phosphate Buffer								

Figure 5-9 Daily photographs showing severity of peptide precipitation under IVNCG and AS buffer conditions. Dark grey areas indicate peptide precipitation. All the P₁₁₋₄ samples maintain a slightly opaque grey throughout the 7-day experiment. The P_{11-13/14} samples under AS buffer conditions remained unchanged over the 7-day test period. The P_{11-13/14} under IVNCG calcium-containing buffer conditions increase in grey value as the experiment progresses with the nanoHA seeded sample producing the darkest grey due to the significant precipitation produced. Full 7-day results see appendix 1.3.

Each day the turbidity of each sample well was measured using the plate reader to determine whether precipitation had occurred over the preceding 24-hour period. The turbidity analysis results provided a complex picture of the change in turbidity over time, see Figure 5-10, Figure 5-11 and Figure 5-12. The readings for the P₁₁₋₄ samples are generally higher than for the P_{11-13/14} samples, irrespective of the conditions used, which is as expected due to the opaque appearance of the P₁₁₋₄ gels when used at 20 mM concentrations.

The turbidity analysis of the peptide samples incubated in the presence of calcium-containing buffer confirmed the visual observations with regards to the precipitating effect of adding the calcium-containing buffer at calcium concentrations used in the IVNCG assay. The addition of the IVNCG calcium-containing buffer to the 20 mM P_{11-13/14} (no nanoHA) control was associated with an increase in turbidity from below 200 NTU on day 4 to over 1600 NTU on day 7, see Figure 5-10. A similar effect was seen in the samples containing P_{11-13/14} seeded with 30 µg/mL nanoHA, although to a lesser extent, with an increase from 110 NTU on day 4 to 1000 NTU on day 7. The P_{11-13/14} samples and controls exposed to the AS calcium-containing buffer showed no visible change in turbidity over the 7-day testing period.

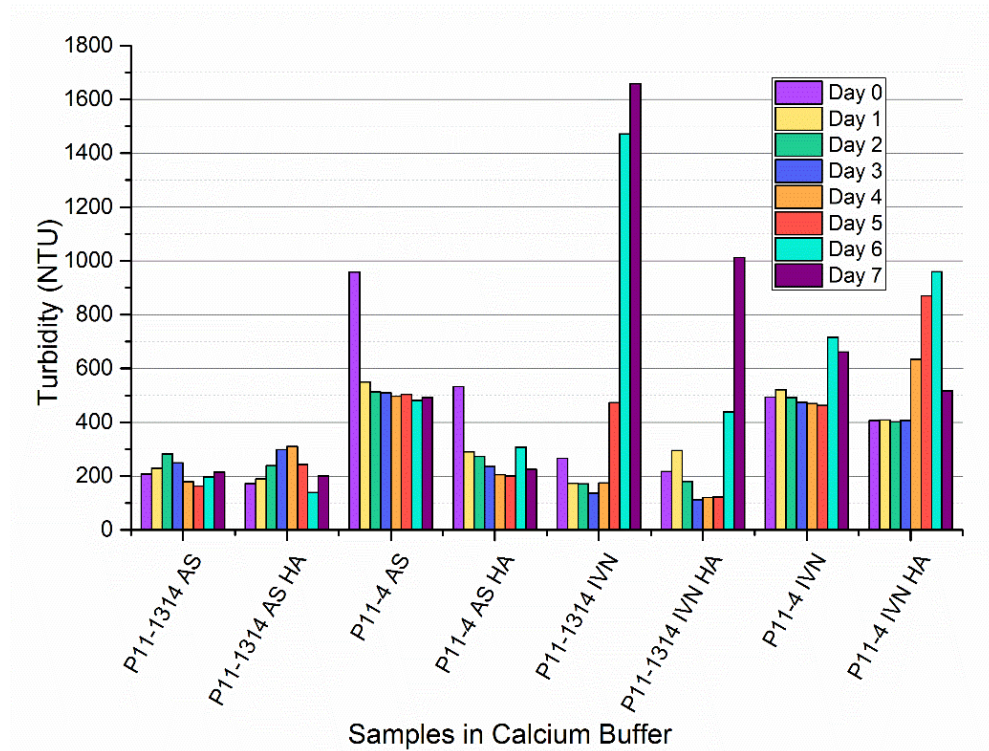


Figure 5-10 Bar chart showing turbidity measurements of precipitation assay using 860 nm absorbance over the 7-day test period with buffer containing IVNCG and AS calcium ion concentrations. AS calcium-containing buffer samples remain nearly constant over time. The P_{11-13/14} samples with IVNCG calcium-containing buffer show a large increase in turbidity around day 6/7 corresponding to the development of opaque samples observed.

The turbidity analysis of the peptide samples under phosphate-containing buffer conditions produced less well-defined results with respect to visual observations.

The addition of the IVNCG phosphate-containing buffer to the 20 mM P₁₁-13/14 control caused an increase from below 200 NTU on day 4 to 500 NTU on day 7, see Figure 5-11. A similar effect was seen in the P₁₁-13/14 seeded with 30 µg/mL nanoHA which increased from below 200 NTU on day 4 to 500 NTU on day 7. The P₁₁-13/14 samples and controls exposed to the AS calcium-containing buffer showed a large turbidity reading (over 1000 NTU) throughout the testing period. When considering the P₁₁-13/14 nanoHA seeded sample, the cause of the large turbidity measurements is most likely down to an uneven surface or small bubbles as the measured values did not confirm the visual observations. The results of the phosphate-containing buffer experiments with regards to the AS buffer samples are inconclusive. The analysis of IVNCG buffered samples suggests that the addition of phosphate has a limited effect with regards to the solubility of the hybrid material with and without the addition of nanoHA due to the small variation in turbidity over the course of the experiment.

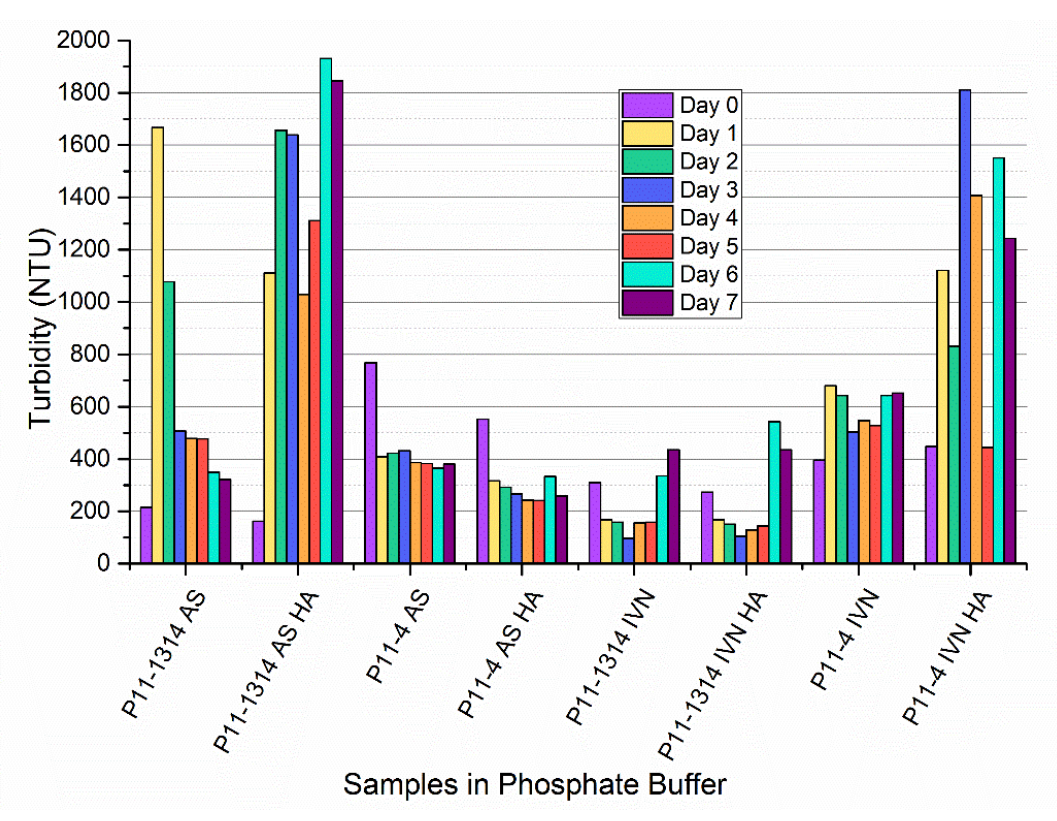


Figure 5-11 Bar Chart showing the turbidity measurements of precipitation assay using 860 nm absorbance over the 7-day test period with buffer containing IVNCG and AS phosphate ion concentrations.

The AS calcium and phosphate-containing combination buffer samples, see Figure 5-12, showed that once the initial turbidity subsided on day 1, the readings for all the P₁₁₋₄ samples are reasonably constant across the 7-day test period. The comparison of the readings and the observations would suggest that any large changes in turbidity shown in the absorbance readings, for example P₁₁₋₄ IVNCG nanoHA day 4, are most likely due to bubbles present within the sample or an uneven surface. The P_{11-13/14} samples (no nanoHA and 30µg/mL nanoHA) in IVNCG buffer showed that, after day 1, the turbidity was comparable, and that, on day 6, both samples experienced an increase in turbidity, with the nanoHA seeded sample increasing significantly from 125 NTU up to 450 NTU which corresponds to the increase in precipitation seen in the images taken. The P_{11-13/14} sample in AS showed an extremely large increase on day 2 and day 3 which does not correspond with the observations taken. These large values could be due to the formation of bubbles or an uneven gel surface which could diffract the light away from the sensor and result in the recording of a larger absorbance. As the experiment progressed the turbidity slowly increased from day 4 to day 7 although the increases are small from 190 NTU to 225 NTU respectively. The P_{11-13/14} nanoHA sample in AS buffer had a large increase in turbidity on day 1 and day 2 of 700 NTU and 800 NTU respectively, compared to an initial day 0 value of 165 NTU. The reason for this initial large turbidity value, followed by a decrease to below 200 NTU on day 3, is not clear as no bubbles are visible in the sample photos but could be caused by an uneven gel surface.

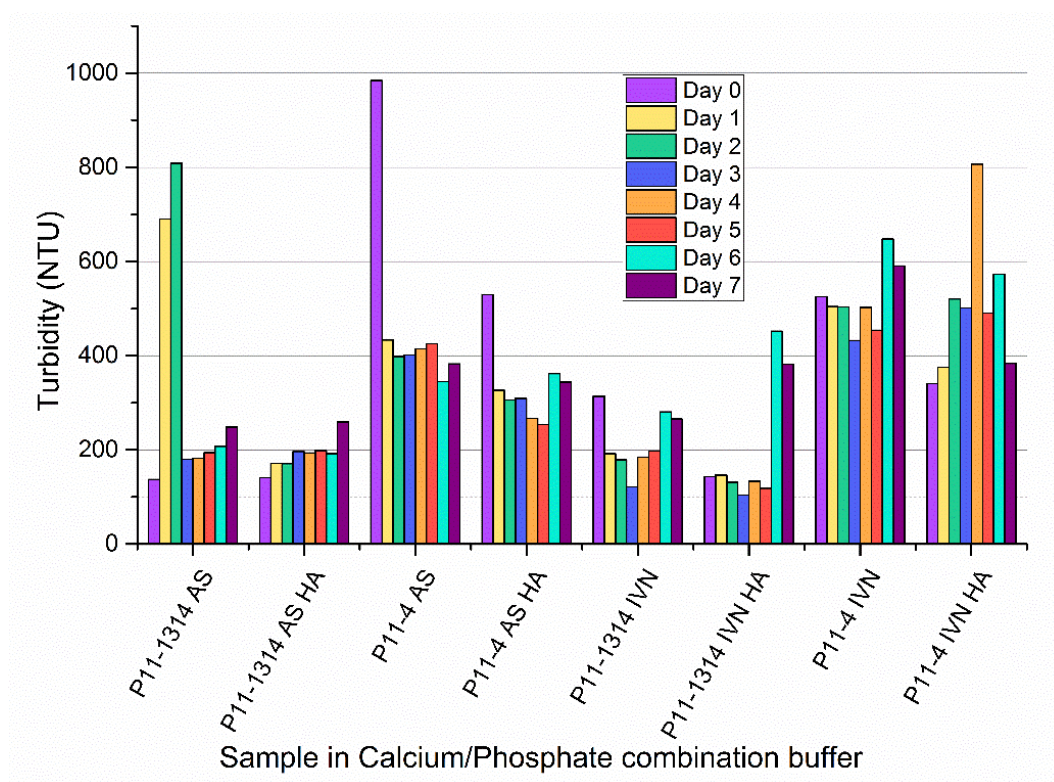


Figure 5-12 Bar chart showing turbidity measurements of precipitation assay using 860 nm absorbance over the 7-day test period buffer containing IVNCG and AS phosphate/calcium ion concentrations.

5.3.6 ^1H NMR Analysis of Peptide Monomers Interaction with NanoHA Particles in Ionic Calcium Environment.

To investigate any co-operative precipitation between the hybrid material, ionic calcium and the nanoHA particles, indicated in the previous studies, a series of ^1H NMR experiments was undertaken. Peptide monomer samples were produced and ^1H NMR analysis completed as described in section 5.2.6. The results of this experiment are summarised in Table 5-2. The line width broadening present in the P₁₁₋₁₃ nanoHA sample in the presence of ionic calcium produced a larger peak integral in the 7-8 ppm region which indicated the loss of the free induction decay of the aromatic region due to the assembled state of the P₁₁₋₁₃ peptide.

Sample	Total integral 7-8 ppm	Sample	Total integral 7-8 ppm
P ₁₁ -13	578	P ₁₁ -14	669
P ₁₁ -13 nanoHA	565	P ₁₁ -14 nanoHA	654
P ₁₁ -13 Ca	600	P ₁₁ -14 Ca	678
P ₁₁ -13 nanoHA Ca	813	P ₁₁ -14 nanoHA Ca	660

Table 5-2 Integral of the 7-8 ppm region of the ¹H NMR spectra when normalised to the TMSP reference peak. Results suggest that the P₁₁-13 monomer, when in the presence of ionic calcium at a concentration of 6.5 mM, could enter in to surface mediated self-assembly on the surface of the nanoHA particles.

5.4 Discussion

The use of self-assembling peptides P_{11-13/14} as a means of promoting and supporting the growth of hydroxyapatite crystals is a strategy which has been shown to be potentially applicable in the treatment of dentine sensitivity (Sayed, 2013). To further assess and optimise the self-assembling peptide nanoHA hybrid material with respect to its ability to support the growth of the nanoHA crystals, the IVNCG assay was utilised (see Chapter 4). However, when used in the IVNCG assay, the hybrid material changed from a strong gel to white opaque liquid samples containing small amounts of gel like material. This observation was true for P_{11-13/14} samples with and without nanoHA seeding. The result was unexpected, as previous work by Sayed described the hybrid material as being capable of maintaining its self-supporting gel appearance after 4 days in the IVNCG assay (Sayed, 2013). The phosphate analysis of the P_{11-13/14} samples following incubation in the IVNCG assay did not reveal sufficiently large amounts of phosphate to be present that would have accounted for the large amount of white precipitate, as the concentrations were below that of the positive control. The failure of the P_{11-13/14} samples to maintain their gel structure coupled with the formation of a white precipitate suggested that under the conditions experienced by the hybrid material samples in the IVNCG, the stability of the peptide material was compromised with respect to its solubility and that the white precipitate seen was the peptide material precipitating out of solution.

Repeats of the experiment were undertaken using a 4-day test period to determine if the hybrid material was soluble at the shorter test period and the nanoHA seeding density was also decreased to 10 µg/mL to replicate the work carried out by Sayed (2013). The results produced similar white precipitation and loss of gel-like appearance as that seen in the 5-day test period. The phosphate concentrations of all the P_{11-13/14} samples following IVNCG were significantly low compared to the positive control in almost all cases, see Figure 5-5.

One possible explanation for the failure of the gel to maintain its structure was the loss of monomer peptide from the sample well which could have caused the peptide fibrils to disassemble (though this would not explain the precipitate). To test this hypothesis, the dialysis membrane separating the sample from the

buffer reservoir in the IVNCG assay was changed for a benzoylated membrane which provides a smaller pore size and would theoretically limit the amount of peptide monomer which could diffuse away from the sample well. Although the SAP gels maintained a gel like structure, the introduction of benzoylated membrane proved to be unsatisfactory as the IVNCG assay was then unable to demonstrate a statistical difference between the positive and negative control ($p > 0.05$), see Figure 5-6. The concentrations of phosphate in all samples, including the controls, were very low, approximately 200 ug/mL, suggesting that the benzoylated membrane was impeding the diffusion of buffer ions into the sample wells.

To determine the cause of what was assumed to be precipitation of the peptide, further studies were therefore undertaken using a novel precipitation assay. The novel precipitation assay was developed to systematically analyse the precipitation behaviour of the hybrid material at varying peptide concentrations and under a variety of conditions (effect of adding IVNCG buffer solutions and the effect of calcium and phosphate concentration), see section 5.2.4. The effect of adding calcium-containing buffer or phosphate-containing buffer solutions, at the concentrations used in the IVNCG assay, was analysed. Decreased peptide concentration in the gel resulted in an increase in the rate and quantity of precipitation with a calcium-rich environment producing the most severe precipitation, see Figure 5-7. Interestingly, the P_{11-13/14} control sample (without the addition of nanoHA) also formed a small amount of precipitate after 5 days in a calcium-rich environment at IVNCG buffer concentration. Overall, the results showed that a decrease in peptide concentration resulted in an increase in the rate of peptide precipitation over the 5-day test period when in the presence of calcium-containing and phosphate-containing buffer solutions.

The effect of decreasing the calcium and phosphate concentration in the buffers was also investigated using the precipitation assay and confirmed the findings above. The experiment also confirmed that as the concentration of calcium and phosphate decreased, the rate and quantity of precipitation also decreased. The calcium-containing buffer samples again produced the most severe amount and rate of precipitation with the calcium/phosphate-containing buffer producing less

severe precipitation. The cause of the precipitation in the presence of calcium ions with and without the addition of nanoHA can be explained through considering the surface chemistry of the self-assembled peptide hydrogel and nanoHA in a calcium ion rich environment. When considering the P_{11-13/14} self-assembling material there is a background concentration of peptide in the monomer state. This concentration is equal to the critical SAP concentration called c^* and is the concentration of peptide required to start the hierarchical self-assembly process (Davies *et al.*, 2006). Peptide monomer can be considered as a colloidal dispersion within the buffer solution. A potential cause of the precipitation when the system is changed through the addition of IVNCG calcium-containing buffer is that the solubility of the peptide is compromised due to the strong “salting out” efficacy of the calcium ion (Shaw, 1991) which competes with the peptide for its H₂O hydration sphere. This competition for H₂O results in the precipitation of the peptide monomer which in turn could result in the disassembly of the peptide-based fibrils due to the lack of monomer present in the surrounding solution. This would explain the liquid/broken gel appearance of the SAP samples after 5 days in the IVNCG assay. This would also explain the relationship between the peptide concentration and rate of precipitation if the difference in stability of the self-assembled fibrils within the lower peptide concentration and higher concentration is considered. The thickness of the SAP fibrils increases as peptide concentration increases which in turn increases the thermodynamic stability of the aggregates formed. When the smaller fibrils in the lower peptide concentration samples are exposed to an environment that is lacking in peptide monomer, they will disassemble more quickly compared to the thicker fibrils of the higher peptide concentration samples.

The addition of nanoHA also caused an increase in the quantity and rate of precipitation, as can be seen in both the peptide concentration and IVNCG buffer concentration precipitation studies. The nanoHA has a similar effect to the addition of calcium ions as the particles are also a colloid suspension. The nanoHA particles will compete for solvation by H₂O resulting in the same peptide precipitation described before. A further issue with the addition of nanoHA is that the addition of electrolyte, calcium ions, will result in the compression of the Stern

layer formed around the nanoHA particles, thereby increasing their tendency to aggregate (Shaw, 1991).

To determine if the hybrid material was capable of maintaining stability at the lower calcium and phosphate concentrations experienced in the oral environment, the improved quantitative precipitation assay was developed using an artificial saliva (Eisenburger *et al.*, 2001) as the added buffer, see section 5.2.5. To quantify the precipitation behaviour of the hybrid material under IVNCG and artificial saliva concentrations, the precipitation assay was altered to include formazin standards which were used to provide a measurement of the turbidity of the samples through the measurement of absorbance. The use of formazin standards is common in the turbidity analysis of H₂O sample to determine the H₂O quality (Klein *et al.*, 2012). The results of the assay provided a quantitative determination of precipitation, although 2 factors associated with the gels made the turbidity measurements complex and potentially inaccurate. One factor was the formation of bubbles within the samples, which had a large effect on the absorbance readings. The cause of the bubbles is unknown as they were not present on application and then developed on day 1 or 2 before slowly disappearing as the experiment progressed. One possible cause of bubble formation could be the peptide solution preparation during which the solutions were lightly shaken to aid dissolution of peptide, this may have resulted in small amounts of air being added into the samples which during the incubation period resulted in the formation of small bubbles seen during the initial stages of the experiment. The presence of bubbles made the comparisons to visual observations key to ensure large turbidity readings were not correlated to precipitation when no precipitation was present. The second factor which seemed to have an effect on the absorbance readings was the surface of the samples. Some of the samples developed a slightly uneven surface which could have been caused by the knocking of the assay while in the incubator or the removal of the coverslip prior to imaging and absorbance measurement. The effects associated with an uneven surface were most pronounced in the P_{11-13/14} AS nanoHA sample with phosphate-containing buffer, Figure 5-11, which had extremely high turbidity readings, all above 1000 NTU, even though no precipitation or bubbles were visible in the images, Figure 5-9. Again, through

comparisons with the visible observations and images, it was possible to determine that the turbidity reading was not a result of the precipitation or bubbles within the sample and must be due to an uneven surface which could have resulted in diffraction of the light produced by the plate reader. The quantitative assay proved useful in the assessment of the hybrid material under various conditions but to improve the assay further, some simple developments would need to be undertaken. The first would be to ensure that repeats of each condition are undertaken to minimise the effect of bubbles and uneven sample surfaces if they occur. This would also permit the use of statistical testing to confirm significance. The assay plate should be kept in an incubator with minimal communal use to prevent the knocking of the plate and also the potential shaking due to the repeated opening and closing of the door. Finally, investigation into the cause of the formation of bubbles would be useful and, potentially, the use of degassed buffers and peptide solutions could address this issue. Taking the limitations of the quantitative precipitation assay into account, it can be concluded that the use of calcium-containing buffer and phosphate-containing buffer at AS concentrations appears to have very little effect, with regards to the precipitation of the hybrid material, with and without the addition of nanoHA, see Figure 5-9. The lower calcium and phosphate concentrations seem to be compatible with the P_{11-13/14} material which suggests that it may still be suitable as a material for the occlusion of dentine tubules through the growth of nanoHA crystals.

To determine if the peptide monomers P₁₁₋₁₃ and P₁₁₋₁₄ interact with the nanoHA particles, a series of ¹H NMR experiments was undertaken as described in section 5.2.6. Each of the peptide monomers was tested in 4 different dilution media at a fixed peptide concentration of 20 mM. The first medium used was a control of 150 mM HEPES, 150 mM NaCl, 0.125 mM TMSP. The integrals produced by the control samples in the ¹H NMR spectra were used to produce a background value for the aromatic peak integral. The 3 conditions tested against the controls were 30 µg/mL nanoHA, 6.5 mM Ca(NO₃)₂ and 30 µg/mL nanoHA with 6.5 mM Ca(NO₃)₂. The only sample to produce a large increased integral in the aromatic region was the 20 mM P₁₁₋₁₃ D₂O, 150 mM HEPES, 150 mM NaCl, 30 µg/mL nanoHA with 6.5 mM Ca(NO₃)₂. The increased aromatic region integral

of the P₁₁₋₁₃ sample when in the presence of 30 µg/mL nanoHA and 6.5 mM ionic calcium suggested that the peptide molecules are in an assembled state. The lack of any large increased integral for any of the other samples suggests that the peptide molecules remain in a monomer state within the solution. The reason for the assembly of the P₁₁₋₁₃ molecules in the presence of ionic calcium and nanoHA particles is not clear although a working hypothesis is that the addition of the calcium results in the assembly of the P₁₁₋₁₃ monomer on the surface of the nanoHA particles, perhaps through ion bridging. The results of the ¹H NMR experiments suggest that the P₁₁₋₁₃ assembly seems to occur only when both the nanoHA and 6.5 mM ionic calcium are present and does not occur when in the presence of either in isolation. A hypothesis to explain this result is that the P₁₁₋₁₃ is binding with the surface cationic calcium of the nanoHA seed crystals. The widely accepted calcium bridging could then be occurring, similar to the effect seen in pellicle formation on enamel (Ash *et al.*, 2014), whereby ionic calcium could promote further peptide aggregation resulting in layers of peptide covering the nanoHA seed crystal surface. This would not only explain the P₁₁₋₁₃ aggregation inferred in the ¹H NMR results but also why the positively charged P₁₁₋₁₄ does not exhibit the same behaviour. The results of the ¹H NMR experiments suggest that the P₁₁₋₁₃ monomer, when in the presence of nanoHA and 6.5 mM ionic calcium, produces a self-assembled aggregate and a working hypothesis is that the peptide is undergoing a nanoHA surface mediated calcium bridging self-assembly producing multiple layers of P₁₁₋₁₃ on the nanoHA surface. Further work would be required to test this hypothesis, although in relation to this work the interaction of the P₁₁₋₁₃ molecule with the surface of the nanoHA crystals could be the cause of the failure of the IVNCG to produce increased mineral deposition within the sample wells. If the peptide is assembling on the surface of the nanoHA crystals, it may be preventing the diffusion of calcium and phosphate to the crystal surface, preventing mineralisation.

5.5 Conclusion

The hybrid material, composed of P_{11-13/14} seeded with nanoHA crystals, was assessed with regards to its hydroxyapatite crystal growth supporting properties using the IVNCG. It was shown that the hybrid material was unstable with regards to its solubility when used in the IVNCG system. To determine the cause of the precipitation a novel precipitation assay was developed which enabled the variables of temperature, addition of calcium and phosphate-containing buffers and calcium/phosphate-containing buffer to be investigated. The results suggest that the hybrid material is not soluble when in the presence of calcium and phosphate ions at the concentrations used in the IVNCG system with the precipitation occurring at a faster rate when lower concentrations of peptide are used. The novel precipitation assay was further developed through a quantitative measurement of the precipitation using turbidity analysis. It was confirmed that the calcium and phosphate-containing buffers used in the IVNCG system resulted in the precipitation of the hybrid material, while the use of the lower calcium and phosphate concentrations in artificial saliva seem to have no effect on the precipitation of the hybrid material. The ¹H NMR analysis seems to suggest that the P₁₁₋₁₃ component of the hybrid material interacts with the nanoHA seed crystals which could be preventing their growth.

Chapter 6 – Application of Self-Assembling Peptide/Nano-Apatite Hybrid Material to Dentine

This chapter describes the addition of the self-assembling peptide/nano-apatite (hybrid) material to human dentine and the subsequent determination of dentine tubule occlusion through the measurement of dentine permeability using a fluid filtration system. A fluid filtration system was designed, developed and validated to industrial standards for this purpose. Dentine disk samples were produced from human 3rd molars and the hybrid material applied. Fluid filtration measurements were taken to measure the change in fluid flow across the dentine disks before and after treatment and then after 7 days incubation in artificial saliva at physiological temperature. Scanning electron microscopy of the dentine surface was then undertaken along with imaging of the penetration of mineral into the dentine tubules. The hybrid material proved ineffective in promoting the growth of mineral within the dentine tubules and resulted in an increase in dentine permeability with respect to fluid flow through the dentine. In contrast, P₁₁-4 treated samples produced a reduction in fluid flow with mineral deposits observed 20 µm into the dentine tubules. We hypothesise that the P₁₁-13 monomer component of the hybrid material interacts with the dentine tubule wall, resulting in an increased wettability of the surface, increasing fluid flow. The hybrid material was found to be unsuitable for the use in the treatment of dentine sensitivity although the P₁₁-4 self-assembling peptide produced encouraging results with respect to its ability to reduce fluid movement in dentine tubules.

6.1 Introduction

The *in vitro* determination of a material's ability to promote mineral deposition within the dentine tubules is an essential step in the development of new dentine sensitivity treatments. The current *in vitro* gold standard method used to determine a material's potential to block the fluid flow in dentine is the fluid filtration method first developed by Reeder *et al.* (1978). This involved measuring fluid flow through the dentine before and after the application of citric acid (50 % w/v) (Reeder *et al.*, 1978) . The method used the dentine disk model (Gillam *et al.*, 1997) where a dentine disk sample is sandwiched between 2 rubber "O" rings to provide the test surface, see Figure 6-1. H₂O held in a reservoir a minimum of 20 cm above the sample was then used to provide a positive pressure of fluid which could produce fluid flow through the dentine samples. The fluid flow was measured by fluid displacement in a micropipette attached to the outlet of the chamber. The fluid flow was then measured and converted into hydraulic conductance units. This early study using the fluid filtration technique was able to demonstrate that as dentine disk thickness increased, the hydraulic conductance decreased, that as surface area increased so did hydraulic conductance and that etching the disks with 50% (w/v) citric acid produced a 32 fold increase in hydraulic conductance (Reeder *et al.*, 1978). This method provided a much improved system compared to others in development at the time (Polhagen and Brännström, 1971; Johnson and Brännström, 1974) as the standardised nature of the dentine disk model, although variations from donor to donor do occur, provided a controllable thickness of sample and a control test surface area.

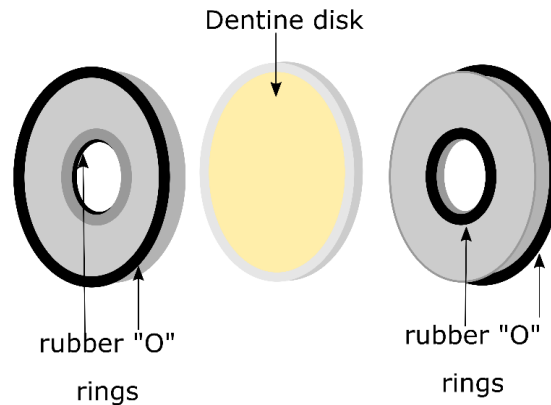


Figure 6-1 Pashley (1984) dentine disk split chamber device, test area determined by rubber “O” rings (black) are forced against dentine disk through tightening of external sample holder (not pictured).

The system was then used to assess the effectiveness of a variety of commercially available desensitising dentifrices to assess and compare their ability to reduce the fluid flow through dentine samples (Pashley *et al.*, 1984). The dentifrices tested were “Promise” and “Denquel” which both contained 5% potassium nitrate as the active ingredient, “Sensodyne” and “Thermodent” which both contained 10% strontium chloride as the active ingredient, “Crest” which contained 0.2% sodium fluoride as the active ingredient and an experimental oxalate treatment which contained 2% potassium oxalate as the active ingredient. These treatments were applied in PBS at ratios of 1:3, 1:1 and 3:1. The active ingredients present in each dentifrice were also analysed independently at the same concentration as the commercial treatments to determine their effectiveness in reducing the fluid flow without the other dentifrice ingredients. The medium in which these controls were made was not stated although they were prepared fresh each day. A placebo for each commercial treatment was also tested which contained all of the treatment ingredients, except the stated active ingredient. The results of the study found that only the experimental oxalate-containing dentifrice was able to produce a statistically significant ($p < 0.01$) decrease in fluid flow compared to the corresponding placebo dentifrices. The oxalate dentifrice was also found to produce larger reductions in fluid flow through dentine at all dilutions when compared to the other commercial treatments. This was explained through reference to previous

work which had shown ionic calcium within the dentine tubules reacting with the oxalate, resulting in the precipitation of calcium oxalate crystals (Greenhill and Pashley, 1981).

The fluid filtration system was further developed by the replacement of the 20 cm high H₂O reservoir with a pressure vessel which could be used to provide much higher pressures to enable the measurement of hydraulic conductance post-treatment (Pashley and Galloway, 1985), Figure 6-2. The micropipette was also moved from the outlet of the split chamber to the inlet side with the movement of a trapped air bubble used to measure the flow. This modified method was used to measure the effect of oxalate treatments on hydraulic conductance of dentine before and after an acid challenge. The results showed that a 2-minute addition of (30% w/v) neutral di-potassium oxalate, (3% w/v) monopotassium-monohydrogen oxalate or (30% w/v) dipotassium oxalate, followed by (3% w/v) monopotassium –monohydrogen oxalate produced a significant decrease in fluid flow compared to treatment with the KCl negative control ($p < 0.001$). The study also explored the effect of acid etching after the application of oxalate treatments and found that the oxalate treated dentine was less permeable (20-30% increase in fluid flow depending on oxalate treatment) than the untreated dentine (400% increase in fluid flow).

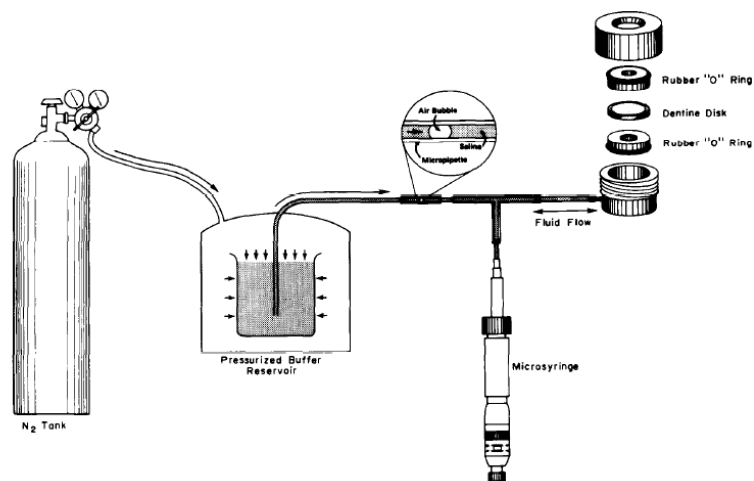


Figure 6-2 Schematic of the fluid filtration device developed with pressurised vessel to allow post-treatment fluid filtration measurements. Image reproduced with permission from Pashley & Galloway (1985)

The objectives of the following chapter were to develop and validate a fluid filtration system based on the Pashley and Galloway (1985) system shown in Figure 6-2. Once validated, the system would be used to assess the self-assembling peptide/nanoHA hybrid material with respect to its ability to reduce fluid flow in dentine after treatment application and after 7 days in an artificial saliva (AS) solution.

6.2 Methods

6.2.1 Dentine Disk Production

All human teeth selected for preparation of dentine disks were obtained from the Leeds University School of Dentistry Skeletal Tissues Research Tissue Bank following full ethical approval (DREC ref: 010714/SW/137) and informed donor consent. The teeth were required to meet the following criteria:

- Donor was healthy with no known systemic illnesses at time of extraction – prevent confounding factors which may affect dentine permeability.
- Donor must be aged 20-50 years when teeth were removed – age range when dentine sensitivity is commonly observed in the clinic (Rees, 2000)
- Teeth must be 3rd molars – ensured large dentine disks were produced.
- Teeth must be caries free – prevents any dentine disks being produced which contain damaged dentine which could affect permeability measurement.

Selected teeth were hydrated in PBS (Lonza Bio Whittaker, Basel, Switzerland) containing 0.05% thymol (BDH Laboratory Supplies, Poole, UK) in a 7 mL plastic bijou tube. After 24 hours, the PBS was replaced and the teeth left to hydrate for at least 6 more days. Each tooth was then removed from solution and dried with lab towel. A small plastic cuvette was then cut approximately 1 cm from the base producing a 1 cm deep container which would hold the tooth during cutting. A small amount of Kemdent® simplex rapid powder (Swindon, England) was placed into a 7 mL bijou and approximately 1 mL of Kemdent® simplex rapid liquid (Swindon, England) was added and thoroughly mixed producing a viscous resin just capable of pouring. The resin was poured into the holder and the tooth added. While the resin was setting, the tooth was positioned to ensure that during cutting, the saw would cut perpendicular to the tubule direction. The initial cut position was determined by ensuring the widest parts of the tooth were in line, taking into account that parts of the tooth may well be worn through use, see Figure 6-3. If the roots of the tooth prevented its appropriate positioning, they were removed using files. Once the resin had set, the tooth was left for 15 minutes to ensure the curing process was complete. The tooth was then mounted into the Accutom cutter (Struers Accutom-5, Ballerup, Denmark) fitted with a

diamond coated blade with settings of 3000 rpm, 0.05 mm per second feed rate. An initial transverse cut was made just below the widest part of the tooth. This was done to ensure that all the enamel from the fissures was removed producing an enamel-free dentine surface. This cutting procedure was continued until the pulpal horns were visible on the dentine surface. This section of dentine was chosen as it provides a dentine surface without enamel or pulpal horn holes/indentations which could produce a dentine like fluid flow. A total of 120 dried teeth were sectioned to produce dentine disks, each with a thickness of 0.5 mm. It was not uncommon for the disks to break during cutting but as long as the fragments were large enough to cover the 4 mm diameter sample holder used in the fluid filtration sample holder, they were deemed to be acceptable for use. All dentine samples were stored in PBS containing 0.05% thymol. At all times patient numbers were labelled on all samples in accordance with tissue bank guidelines.



Figure 6-3 Picture of a molar tooth cast into holder prior to cutting. Tooth was positioned to ensure cut was as perpendicular to the long axis of the tooth (root to crown) as possible.

6.2.2 Fluid Filtration Device

A dentine fluid filtration device was constructed based on the system used at GSK (Weybridge, UK) and Intertek (Hooton, UK) and used during a collaborative industrial placement aimed at transferring the knowledge to Leeds. The device is not commercially available and was assembled using components from a

number of suppliers. An image of the device is shown in Figure 6-4 along with a schematic in Figure 6-5.

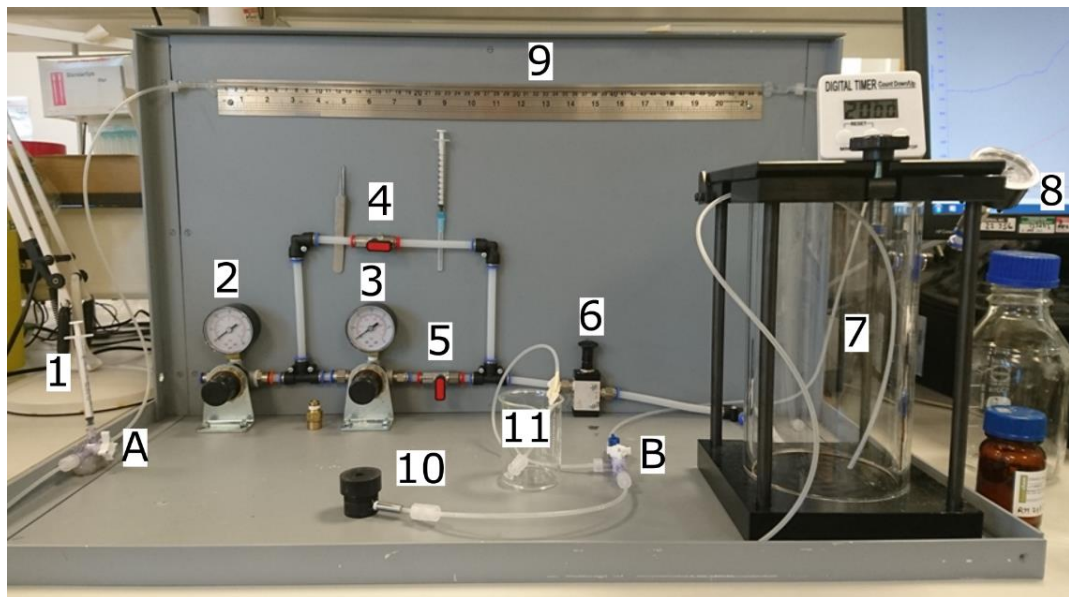


Figure 6-4 Photograph of dentine fluid filtration device based on the work of Pashley (1984). 1) Micro syringe 2) Inlet pressure regulator 3) Test pressure regulator 4) Purge pressure tap 5) Test pressure tap 6) Pressure evacuation tap 7) Pressure vessel 8) Pressure vessel pressure gauge 9) Glass capillary 10) Sample holder 11) Buffer reservoir A) 3 way tap B) 3 way tap with on/off tap.

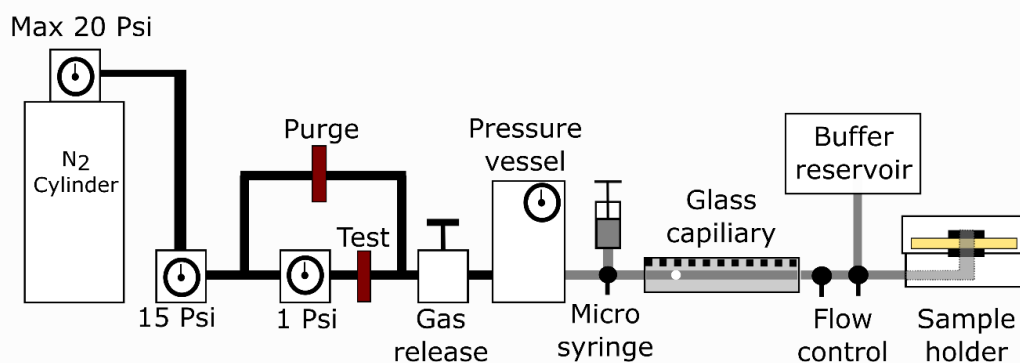


Figure 6-5 Schematic of dentine fluid filtration device illustrated above. Black lines indicate gas system while grey lines indicate fluid system. Pressure is produced using nitrogen and regulated down to a purge pressure of 15 PSI or test pressure of 1 PSI. PBS is stored in pressure vessel and travels through the system and exits through the dentine sample (yellow rectangle in sample holder). The movement of the bubble within the glass capillary is used to record the fluid flow over the 5-minute test period.

The fluid filtration device was developed using the following materials: Pneumatic plastic push fittings and tubing (KELM, UK), Nitrogen cylinder (Boc gasses, UK), Hydraulic tubing and Luer fittings (Cole-Parmer Instrument Co Ltd, Eaton Socon, UK), Pressure Vessel and Pressure gauges (Fisnar, Ellsworth adhesives, EU) and Glass capillary (CM Scientific Ltd, 600 mm 0.5 mm internal diameter). The frame was produced in-house by the School of Dentistry workshop team. The sample holders were based on the design shown in Figure 6-2 and were custom-made (Kirkstall precision, Leeds, UK). A cross-section of the sample holder assembly is shown in Figure 6-6. Once the system was assembled, a small piece of plastic was placed in a sample holder to determine if the system was watertight by ensuring that there was no movement in the bubble under test conditions. This system check was carried out daily when the system was in use to ensure that there were no leaks in the fluid part of the system.

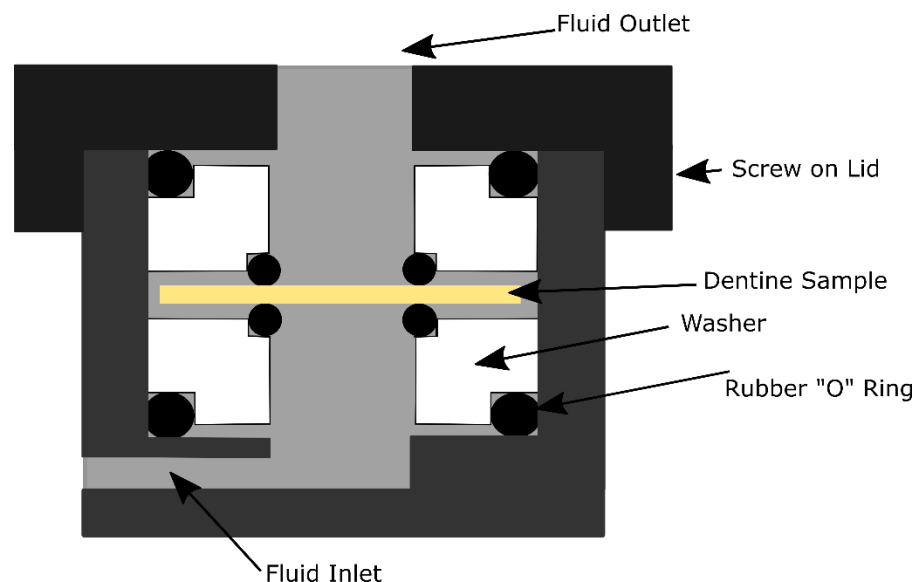


Figure 6-6 Schematic of sample holder assembly cross-section showing the dentine disk “sandwiched” between the 2 PTFE washers via the rubber “O” rings. Fluid flows through the inlet, through the dentine disk and then out of the outlet. Speed of fluid flow is dependent on the permeability of dentine disk and pressure of fluid (of which pressure is held constant).

6.2.3 Fluid Filtration Validation

Dentine disks produced previously, see section 6.2.1, were polished using 1200 carbide paper followed by 2500 carbide paper to ensure that the surface was flat. Each sample was acid-etched in 10% citric acid for 2 minutes under shaking to

remove any smear layer producing during the cutting/polishing procedures. The disks were then rinsed thoroughly in DI H₂O and mounted into a sample holder. An air bubble approximately 3 mm long was introduced into the capillary tube and positioned towards the capillary opening using the microsyringe. The test pressure (1psi) was applied and the flow controls opened to the sample holder. The initial position relative to the ruler was recorded in mm and the movement of the bubble measured over a 5-minute period. After the 5-minute test period, the bubble's position relative to the ruler was recorded and the flow controls closed. The same bubble was then moved back to the capillary opening ready for the second measurement. The validation method used a negative control treatment of brushing the dentine surface with PBS and a positive control treatment of brushing with oxalic acid, 5% w/v, dissolved in DI H₂O (98% Sigma-Aldrich St. Louis, MO, USA). Oxalic acid has been previously shown to be effective in the occlusion of dentine tubules (Pashley and Galloway, 1985) and is often used as a positive control in dentine permeability studies (Sauro *et al.*, 2010). Each treatment was brushed on the dentine surface for 1 minute followed by a DI H₂O rinse. After the application of a treatment, the permeability was measured again as described previously. The second measurement was then subtracted from the first measurement and then divided by the first measurement to produce a % reduction in flow. Each control treatment was tested on 10 dentine disk samples and a mean % reduction in fluid flow produced. The % reduction in fluid flow data was then imported into SPSS and a statistical test for normality followed by an independent t-test to determine statistical differences between the positive and negative control were carried out.

6.2.4 Fluid Filtration Assessment of the Hybrid Material's Tubule Occlusion Ability After 7 Days in Artificial Saliva.

To determine the effectiveness of the addition of the hybrid material to dentine with respect to its ability to occlude dentine tubules through presumed promotion of nanoHA crystal growth, a series of fluid filtration experiments was undertaken. Each treatment group was assigned 10 dentine disks produced earlier, see section 6.2.1, with each dentine disk checked to ensure no visible cracks or pulpal horn indentations were present. Each dentine disk was then polished

using 1200 and 2500 carbide paper respectively. The disks were then placed in a 7 mL bijou with 5 mL of 10% citric acid added and then shaken for 2 minutes. The disk was then removed from the bijou and rinsed in copious amounts of DI H₂O. The dentine disk was then mounted into the sample holder and connected to the fluid filtration system. The initial permeability of the dentine disk was measured by recording the initial position of the bubble at the beginning of exposure to the test pressure. A second measurement was taken after 5 minutes, producing a measurement of fluid flow in mm per 5 minutes for each dentine disk. The sample area of exposed dentine was then dabbed with a paper towel, to remove any fluid present on the surface, and a treatment applied as described in Table 3-1. After treatment application, the test surface was rinsed in DI H₂O and the fluid flow was measured using the same method as that described for determination of the initial permeability. The initial permeability measurement (dentine disk permeability before treatment application) was then subtracted from the measurement after the treatment was applied and then divided by the initial measurement to produce a % reduction in flow. Once the test was complete, the dentine sample (including the holder to ensure the test area of the dentine disk remained the same) was placed in a 60 mL plastic beaker with screw lid and 40 mL of artificial saliva (AS) solution composition CaCl₂ 0.7 mM (Sigma), MgCl₂ 0.2 mM (Sigma-Aldrich St. Louis, MO, USA) KH₂PO₄ 4 mM (BDH AnalaR, Poole, UK), KCl 30 mM (Sigma-Aldrich St. Louis, MO, USA) and HEPES 20 mM (Sigma-Aldrich St. Louis, MO, USA) with the pH adjusted to 7 using KOH (Eisenburger *et al.*, 2001) added. The sample was then placed into the incubator at 37°C. Every 24 hours, the AS solution was removed and fresh AS solution added. After 7 days, the samples were removed from the incubator, attached to the fluid filtration system and the fluid flow was measured a final time as previously described. Once the measurement was completed, the sample was removed from the holder and left to dry overnight, covered. Once dry, the dentine sample was stored in a labelled 24 well plate.

The treatments used, together with their corresponding method of application are summarised in Table 6-1. The negative treatment control for these experiments was a solution of 20 mM HEPES and 30 mM KCl. The negative control treatment acted as a control both for brushing and to ensure that the solution (which was

used to dissolve the test treatment materials) had no effect on dentine tubule permeability. The negative control was applied to the test surface using a Pasteur pipette (4 drops) and then brushed using a micro applicator brush (3M, Maplewood, Minnesota, USA) for 30 seconds followed by a 90-second pause to allow for the treatment solution to settle and permeate down into the dentine tubules. The sample was then lightly washed with DI H₂O before taking the measurement. A nanoHA treatment of 30 µg/mL nanoHA in 20 mM HEPES, 30 mM KCl was produced by weighing out 25 mg of batch 1 nanoHA, see Chapter 3, into a 50 mL falcon tube and adding 25 mL of 20 mM HEPES 30 mM KCl in DI H₂O. A second 1 mg/mL suspension of the previously synthesised nanoHA batch 3, see Chapter 3, was produced by weighing out 25 mg of batch 3 nanoHA into a 50 mL falcon tube and adding 25 mL of 20 mM HEPES 30 mM KCl in DI H₂O. Both suspensions were vortexed for 30 seconds followed by 2 times 20-second periods of sonic probe agitation (MISONIX model XL2010 with micro probe output 20 KHz). The 2 suspensions were then combined together in equal volumes to produce a 1 mg/mL nanoHA stock suspension of combined batches 1 and 3. The suspension was then further diluted through addition of 20 mM HEPES, 30 mM KCl in DI H₂O to produce a final solution of 30 µg/mL nanoHA combined batches 1 and 3 in 20 mM HEPES 30 mM KCl. The 30 µg/mL nanoHA combined batches 1 and 3 in 20 mM HEPES 30 mM KCl treatment was applied to the test surface using a Gilson pipette (50 µL) and then brushed using a micro applicator brush (3M, Maplewood, Minnesota, USA) for 30 seconds followed by a 90-second pause to allow for the effect of treatment to settle. The sample was then lightly washed with DI H₂O before taking the measurement.

A treatment solution of 20 mM P_{11-13/14} was produced by weighing P₁₁₋₁₃ and P₁₁₋₁₄ into separate 2 mL glass vials. A solution of 20 mM HEPES, 30 mM KCl in DI H₂O was then added to the P₁₁₋₁₃ and P₁₁₋₁₄ powders producing individual solutions of 20 mM P₁₁₋₁₃ and P₁₁₋₁₄ in 20 mM HEPES KCl DI H₂O. A small volume of 5M NaOH was added to the P₁₁₋₁₃ solution to reach dissolution. Both suspensions were pH adjusted, P₁₁₋₁₄ solution to pH 7 and P₁₁₋₁₃ solution to pH 8, using 2 M HCl and 5 M NaOH respectively. Both peptide solutions were sonicated for 5 minutes prior to use. The P_{11-13/14} treatment was applied to the test surface by adding 25 µL of the P₁₁₋₁₄ solution which was then brushed using

a micro applicator brush for 15 seconds, followed by a 90-second pause to allow for the effect of treatment to settle. The 20 mM P₁₁₋₁₃ was then added in equal volume and brushed for 15 seconds followed by a 90-second time to settle. The sample was then lightly washed with DI H₂O before taking the measurement.

A treatment of 20 mM P_{11-13/14} seeded with 30 µg/mL nanoHA was produced by weighing P₁₁₋₁₃ and P₁₁₋₁₄ into separate 2 mL glass vials. The peptide powders were then diluted with 20 mM HEPES, 150 mM NaCl seeded with 30 µg/mL nanoHA of combined batches 1 and 3 to produce individual samples of 20 mM P₁₁₋₁₃ seeded with 30 µg/mL nanoHA and 20 mM P₁₁₋₁₄ seeded with 30 µg/mL nanoHA. A small volume of 5M NaOH was added to the P₁₁₋₁₃ solution to reach dissolution. Both suspensions were pH adjusted, P₁₁₋₁₄ solution to pH 7 and P₁₁₋₁₃ solution to pH 8, using 2 M HCl and 5 M NaOH respectively. Both peptide solutions were sonicated for 5 minutes prior to use. The P_{11-13/14} seeded with 30 µg/mL nanoHA treatment was applied to the test surface by adding 25 µL of the 20 mM P₁₁₋₁₄ seeded with 30 µg/mL nanoHA solution which was then brushed using a micro applicator brush for 15 seconds followed by a 90-second pause to allow for the effect of treatment to settle. The 20 mM P₁₁₋₁₃ seeded with 30 µg/mL nanoHA was then added in equal volume and brushed for 15 seconds followed by a 90 second-time to settle. The sample was then lightly washed with DI H₂O before taking the measurement.

A treatment of 20 mM P₁₁₋₄ was prepared by dissolving a small amount of P₁₁₋₄ in 20 mM HEPES, 30 mM KCl. The P₁₁₋₄ solution was then pH adjusted to pH 7.4 and heated at 50 °C to prevent gelation. The 20 mM P₁₁₋₄ treatment was then applied to the test surface using a Gilson pipette (50 µL) and then brushed using a micro applicator brush for 30 seconds followed by a 90-second pause to allow for the effect of treatment to settle. The sample was then lightly washed with DI H₂O before taking the measurement.

A control treatment of iBond[®] universal (Kulzer, Basingstoke, UK), was applied as per the manufacturer's instructions. The iBond dentine bonding resin treatment was chosen to act as a positive control as the formation of a polymer resin on the surface of the dentine disk would prevent fluid flow. A micro applicator brush was placed into the iBond[®] resin and brushed on the surface of

the dentine for 30 seconds. An Elipar DeepCure-S dental curing light (3M, Maplewood, MN, USA) was then applied for 20 seconds to cure the resin after which it was allowed to settle for 90 seconds. The sample was then lightly washed with DI H₂O before taking the measurement.

Each treatment was applied to 10 dentine disks prepared and analysed as described above. The measurements were then imported into SPSS and statistically analysed using a one-way Anova Bonferroni test to determine statistical significance between treatment groups ($p < 0.05$).

Treatment (dilution medium)	Application – all brushing was completed using micro applicator brush (3M ESPE Disposable Micro applicators Brushes, USA)
Negative control (20 mM HEPES 30 mM KCl)	4 drops of solution were applied to dentine surface from a Pasteur pipette and brushed for 30 seconds, then left for a further 90 seconds.
Positive control iBond Universal dentine bonding system	Brush was dipped into resin and applied to dentine surface by brushing for 30 seconds then cured with blue light for 20 seconds (as per manufacturer's instructions). After curing left for 90 seconds.
20 mM P ₁₁ -4 (20 mM HEPES 30 mM KCl)	50 µL of treatment solution added to dentine surface and brushed for 30 seconds then left for 90 seconds.
NanoHA 30 µg/mL (20 mM HEPES 30 mM KCl)	50 µL of treatment solution added to dentine surface and brushed for 30 seconds then left for 90 seconds.
20 mM P ₁₁ -13/14 (20 mM HEPES 30 mM KCl)	P ₁₁ -14 solution (25 µL) added to dentine surface and brushed for 15 seconds then left for 90 seconds. Then, P ₁₁ -13 solution (25 µL) added to dentine surface and brushed for 15 seconds then left for 90 seconds.
20 mM P ₁₁ -13/14 seeded with 30 µg/mL nanoHA (20 mM HEPES 30 mM KCl)	P ₁₁ -14 nanoHA solution (25 µL) added to dentine surface and brushed for 15 seconds then left for 90 seconds. Then, P ₁₁ -13 nanoHA solution (25 µL) added to dentine surface and brushed for 15 seconds then left for 90 seconds.

Table 6-1 Table detailing application procedure for each treatment tested using the fluid filtration device to determine any effect on dentine permeability. After application procedure, the test surface was rinsed with DI H₂O and the test pressure applied. Each treatment was applied to 10 dentine disk samples with 3 fluid filtration measurements taken. The first measurement was taken before treatment application, the second directly after application and the final taken after 7 days in artificial saliva solution at 37 °C.

6.2.5 Scanning Electron Microscopy Imaging Assessment of 7-Day Fluid Filtration Study Treatment Groups

To analyse the effect of adding the treatments to the surface of the dentine and the penetration of any mineral formed in the dentine tubules, a SEM study was undertaken. For the dentine surface analysis, 3 samples from each treatment group from the 7-day AS study were selected randomly, mounted onto SEM stubs using a carbon-coated disk and then sputter-coated in gold (Agar Auto Sputter Coater B3743, Stansted, UK). The dentine disk samples were then loaded into the SU8230 scanning electron microscope (Hitachi, Tokyo, Japan) and the test area was analysed (20 kV accelerating voltage, 113 μ A emission current, secondary electron emission). For the dentine tubule penetration analysis, 3 dentine samples from each treatment group were chosen at random, placed in liquid nitrogen for 1 minute and then removed, snapped in half across the test area and mounted onto a SEM stub using Blu Tack (Bostik, Paris, France). The Blu Tack supporting the sample was then painted with conductive silver paint (Agar conductive silver paint AGG3790) ensuring the paint was brushed from the Blu Tack to the side of the sample to allow for proper conductivity. No silver paint was brushed onto the part of the dentine under investigation. Once the paint was dry the samples were sputter-coated in gold and then analysed using the SEM.

6.3 Results

6.3.1 Dentine Disk Production

A total of 120 human 3rd molars were sectioned to produce 500 µm thick dentine disks as described in section 6.2.1. The cutting resulted in only 58 of the total 120 teeth successfully producing dentine samples of sufficient size for use in the fluid filtration experiments. On average, just under 3 dentine disk samples per tooth were produced from the 58 teeth resulting in 147 dentine disks produced in total.

6.3.2 Fluid Filtration System Validation

To validate the fluid filtration system, a validation experiment was run to ensure that the system was capable of determining differences in fluid flow when using a negative control (brushing the dentine surface with PBS) and a positive control (brushing with 5% oxalic acid). The fluid flow was measured before and after the application of negative and positive controls. The experiment was carried out as described in section 6.2.3. The results confirmed a statistically significant difference in fluid flow between the positive and negative controls ($p < 0.05$) as can be seen in Figure 6-7. Application of the positive control of 5% oxalate produced a 98 ± 3 % reduction in flow while the negative control produced a -11 ± 19.0 % reduction in flow (negative reduction being an increase in flow) using the same application procedure.

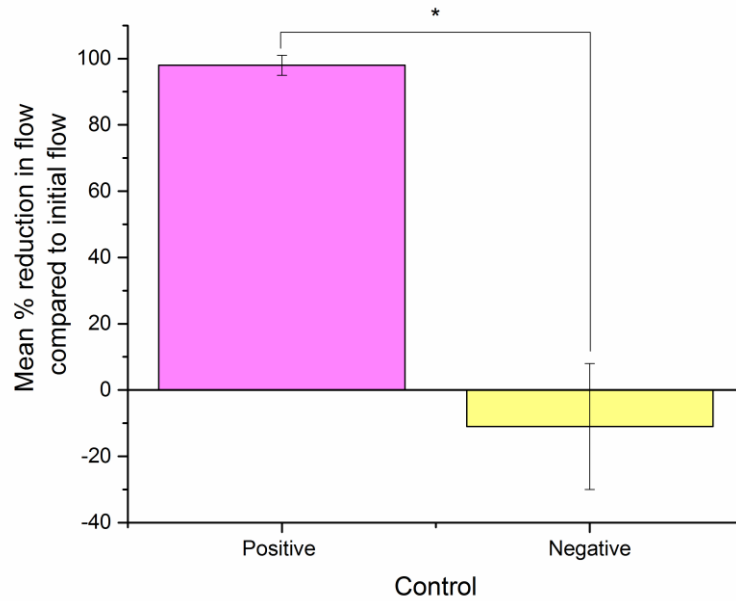


Figure 6-7 Validation of fluid filtration device. Graph shows mean % reduction in fluid flow through dentine after application of positive control treatment (oxalic acid 5%) and negative control treatment (PBS) compared to the initial measurement (n=10). Statistical analysis using an independent t-test confirmed significant decrease in fluid flow in positive control compared to negative control. Error bars show 2x standard deviation. * Statistically significant at least $p < 0.05$.

6.3.3 Effect of Application of Hybrid Material to Dentine Disks on Dentine Permeability After Initial Application and after 7 Days Incubation in Artificial Saliva Solution.

To assess the hybrid material's ability to occlude the dentine tubules and so reduce dentine permeability as measured by fluid flow, the study described in section 6.2.4 was undertaken. In brief, a dentine disk's initial permeability was measured using the fluid filtration method, described in section 6.2.3, to produce an initial base line fluid flow measurement. A test treatment was then applied and the fluid flow was measured again, providing an initial % reduction in fluid flow value after treatment application. The treated disks were then stored in AS solution for 7 days, with the AS solution replaced every 24 hours. After 7 days the fluid flow was measured again, producing a % reduction in fluid flow after 7 days in AS with respect to the initial baseline fluid flow measurement. The results of the change in fluid flow after the initial application of the treatments are shown

in Figure 6-8. On initial treatment application, the 20 mM P₁₁-13/14 solution, 20 mM P₁₁-13/14 seeded with 30 µg/mL nanoHA and the iBond treatment groups all produced a statistically significant decrease in fluid flow compared to the positive control (p<0.05), with mean % reduction values of 69 ± 25%, 74 ± 20% and 60 ± 27% respectively. The 20 mM P₁₁-4 solution treatment (no added nanoHA) resulted in a small mean decrease in flow of 12 ± 14%. Treatment with 30 µg/mL nanoHA also produced a small increase in fluid flow of -22 ± 21 %, with neither treatment being statistically different to the negative control (p>0.05).

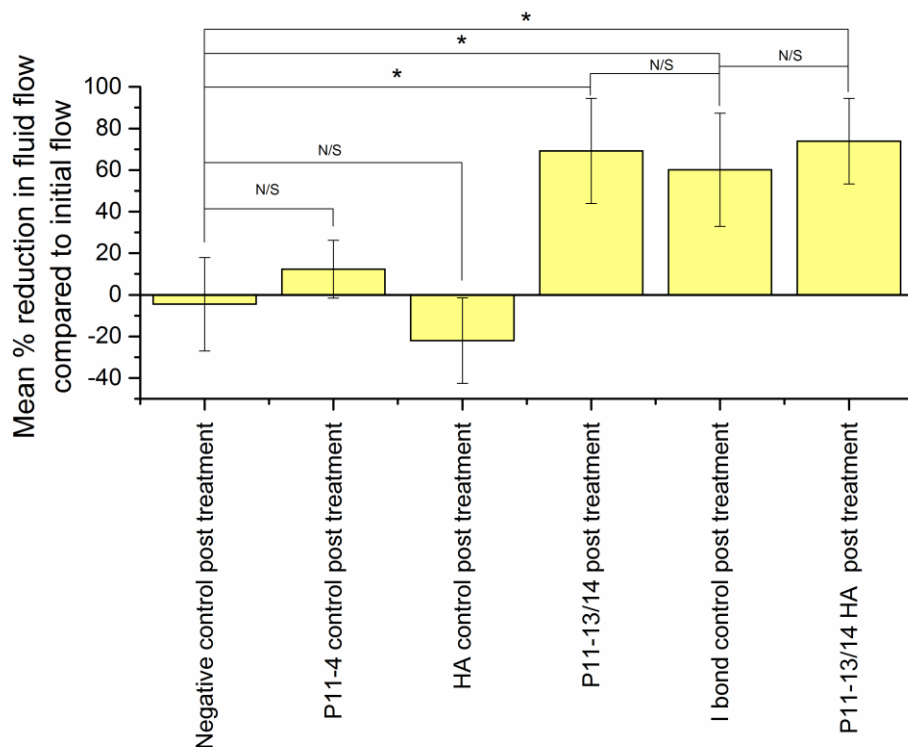


Figure 6-8 Bar chart showing mean % reduction in fluid flow (dentine permeability) compared to fluid flow immediately after treatment application. A one-way Anova Test with *post hoc* Bonferroni correction showed that after initial application, there was no significant difference between the negative control (20 mM HEPES and 30 mM KCl), 20 mM P₁₁-4 and 30 µg/mL nanoHA treatment groups. The P₁₁-13/14, P₁₁-13/14 seeded with 30 µg/mL nanoHA and iBond treatments were significantly more effective at decreasing fluid flow after initial application compared with the negative control and there was no significant difference between these 3 groups. Error bars show 2x standard deviation. * confirms statistically significant difference using one-way ANOVA Bonferroni test significance level of at least p<0.05 (n=10).

The fluid filtration experiment was then repeated on the treated dentine samples after 7 days incubation in AS solution (AS replaced daily). The results are shown in Figure 6-9. For statistical analysis, the results for the 20 mM P_{11-13/14} solution (no nanoHA), 20 mM P_{11-13/14} seeded with 30 µg/mL nanoHA and the 30 µg/mL nanoHA treatments were excluded due to the large standard deviations associated with these treatment groups, indicating very large variability of response. The 20 mM P_{11-13/14} seeded with 30 µg/mL nanoHA and the 30 µg/mL nanoHA treatments produced such large increases in flow after 7 days in AS solution that only 6 and 8 samples respectively were able to provide usable readings before the end of the 5-minute measuring period, due to the bubble reaching the end of the capillary before this time.

The dentine permeability produced after 7 days in AS by the treatments 20 mM P_{11-13/14} solution (no nanoHA), 20 mM P_{11-13/14} seeded with 30 µg/mL nanoHA and the 30 µg/mL nanoHA produced an increase in flow of $-62 \pm 100\%$, $-70 \pm 130\%$ (n=8) and $-162 \pm 161\%$ (n=6) respectively (a negative % reduction is an increase in flow). The negative control treatment (buffer solution only) produced a small mean increase in fluid flow ($-13 \pm 150\%$) after 7 days in AS. In the 20 mM P₁₁₋₄ (no nanoHA) treatment group, 2 of the dentine samples from the group produced extremely large increases in fluid flow (data not shown). When one of these samples was removed from the sample holder it fell apart, while the other sample, on closer inspection, had a crack running through the test surface. These 2 readings were therefore removed from the statistical analysis as such defects would clearly have affected the results. Treatment of dentine with 20 mM P₁₁₋₄ and subsequent incubation in AS resulted in a large decrease in fluid flow ($57 \pm 35\%$) which was smaller but not statistically different to the iBond control treatment ($78 \pm 13\%$) ($p>0.05$).

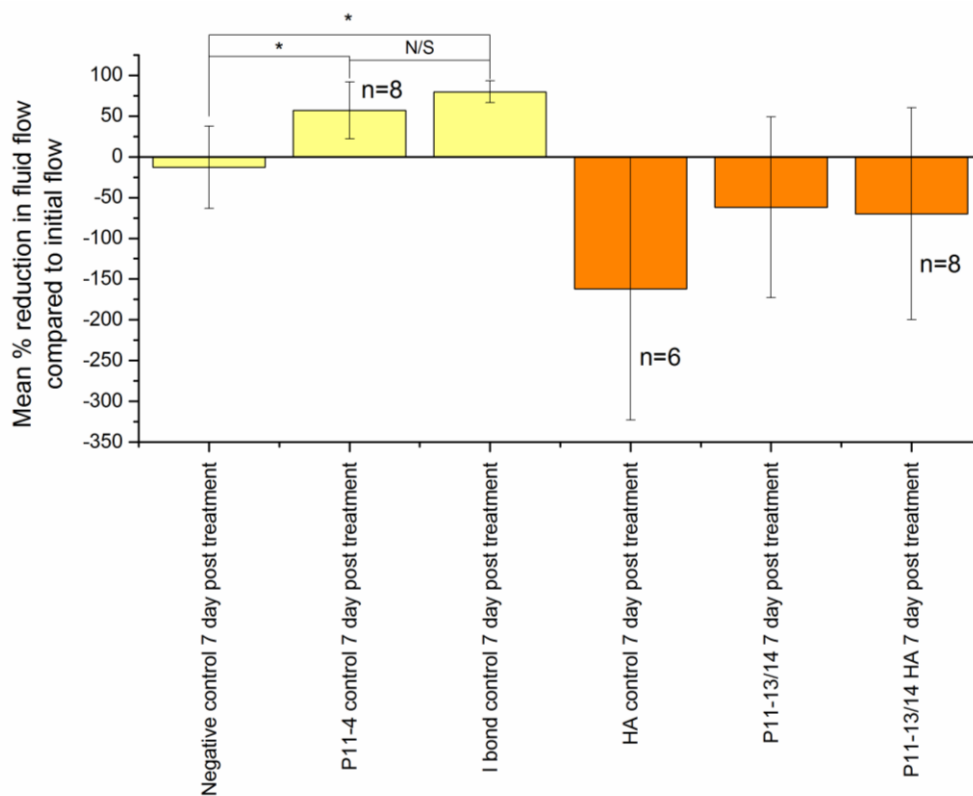


Figure 6-9 Bar chart showing mean % reduction in fluid flow (dentine permeability) and standard deviation following a range of treatments and after 7 days incubation in artificial saliva. The 20 mM P_{11-13/14}, 20 mM P_{11-13/14} seeded with 30 µg/mL nanoHA and the 30 µg/mL nanoHA treatments (orange) were not considered due to their very high variability. After 7 days in AS solution there was a significant difference between the negative control and the 20 mM P₁₁₋₄ and iBond treatment groups. There was no significant difference between the P₁₁₋₄ and iBond treatments after 7 days in AS solution. Error bars show 2x standard deviation. * confirms statistically significant difference using one-way ANOVA Bonferroni test significance level of at least p<0.05 (n=10 unless stated different on graph).

The initial post-treatment fluid filtration measurements and the measurements after 7 days in AS were then compared using an independent t-test to determine the effect of 7 days in AS solution on the treatments ability to occlude dentine tubules, see Figure 6-10. Both the 20 mM P_{11-13/14} solution (no nanoHA) and treatment with 20 mM P_{11-13/14} seeded with 30 µg/mL nanoHA resulted in a statistically significant increase in fluid flow after 7 days in AS compared to the fluid flow immediately after post treatment application (p<0.05). The 30 µg/mL nanoHA treatment produced an initial post-treatment increase in fluid flow and, after 7 days in the AS solution, there was a statistically significant increase in

fluid flow compared to the initial application ($p < 0.05$). The 20 mM P₁₁₋₄ treatment produced a statistically significant decrease in fluid flow after 7 days in AS solution compared to the initial post treatment fluid flow ($p < 0.05$).

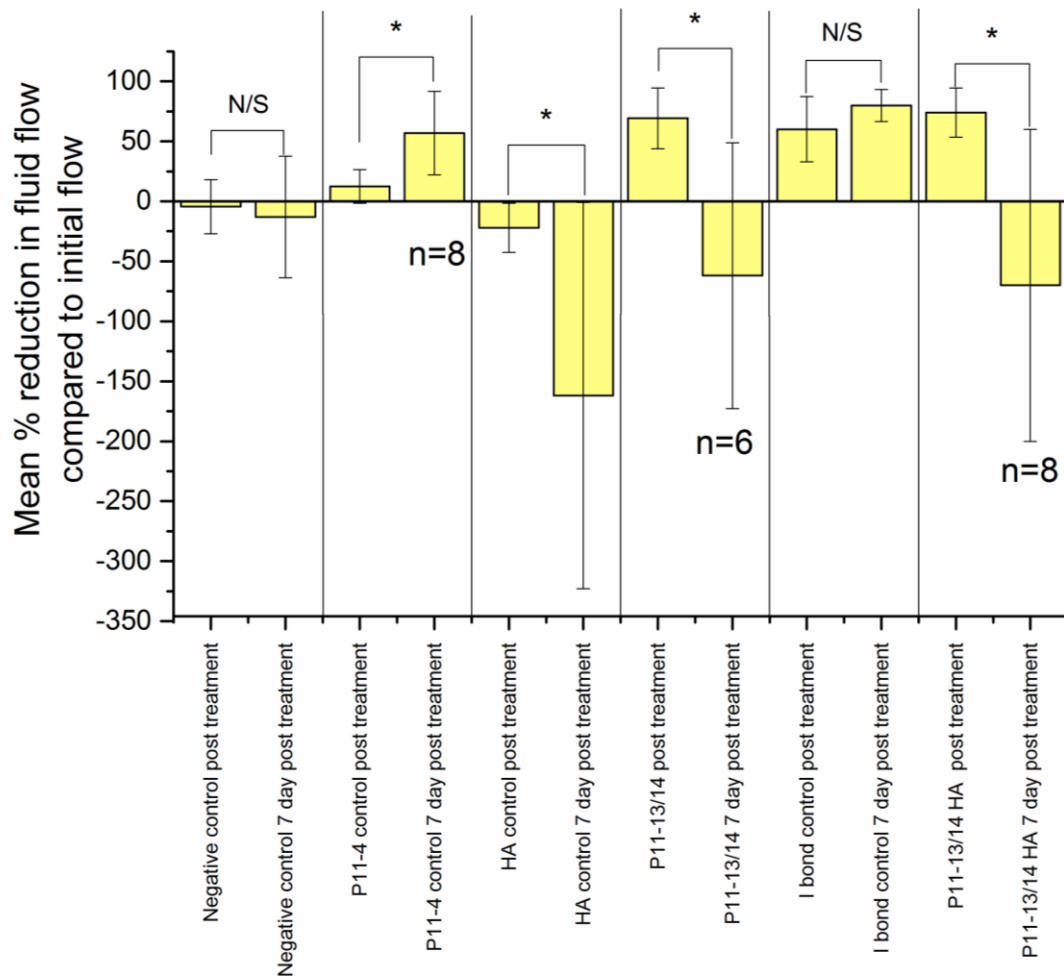


Figure 6-10 Bar chart showing mean % reduction in fluid flow (dentine permeability) immediately after treatment application and after 7 days in AS solution. The 20 mM P_{11-13/14}, 20 mM P_{11-13/14} seeded with 30 $\mu\text{g/mL}$ nanoHA and the 30 $\mu\text{g/mL}$ treatment groups all produced significant increase in mean % fluid flow after 7 days in AS solution. The 20 mM P₁₁₋₄ treatment group resulted in a significantly greater reduction in mean % fluid flow after 7 days in AS solution while the negative control and iBond treatments produced no significant change after incubation in AS solution. Error bars show 2x standard deviation. * confirms statistically significant difference using one-way ANOVA Bonferroni test significance level of at least $p < 0.05$. (n=10 unless stated different on graph).

6.3.4 Effect of Various Treatments on the Ultrastructural Appearance of Dentine

To assess the effectiveness of the test treatments to not only reduce fluid flow but to also achieve tubule occlusion, a SEM study was undertaken. To assess for both the surface effects and tubule penetration, samples from each of the treatment groups in the study described above were used and split into 2 assessment groups. The first group was used to examine the dentine surface via direct imaging of the surface onto which the treatment had been applied. The second group was used to image inside the dentine tubules to assess penetration. This was done by imaging treated dentine disks which had been placed into liquid nitrogen for 30 seconds and snapped in half across the test area providing access to the interior of the tubules.

Imaging of the dentine surface of samples after 7 days incubation from the 6 different treatment groups resulted in only the iBond treatment producing any apparent difference in appearance compared with the negative PBS control. It can be seen in Figure 6-11 D that only image D, which corresponds to the iBond treatment group appeared different, with the polymer-based resin seemingly filling the dentine tubules. All the other treatment groups show the same open dentine tubules with no evidence of mineral formation on the surface or within the dentine tubule openings themselves.

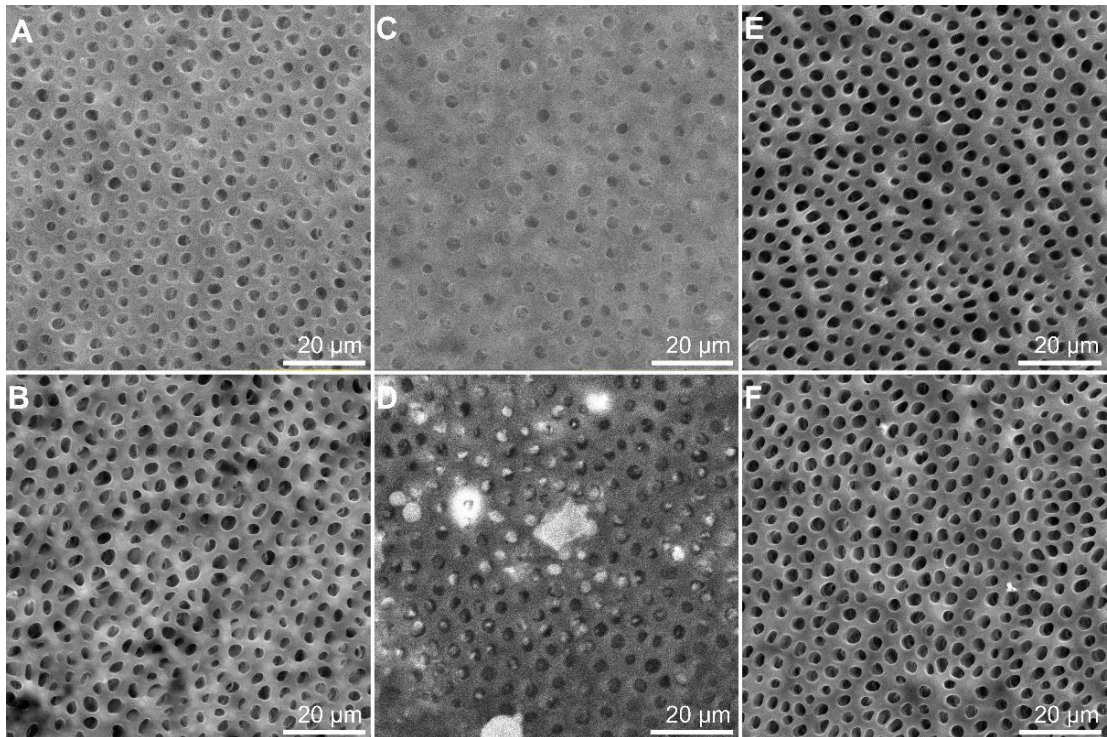


Figure 6-11 Scanning electron micrographs of dentine surfaces of samples taken from different treatment groups after 7 days in AS solution. A) Negative control (PBS) showed no deposits with open tubules. B) nanoHA control showed no differences compared to negative control. C) P₁₁-4 produced no differences compared to negative control. D) iBond control produced a thick layer on the surface of the dentine with other areas showing resin filled tubules. E) P₁₁-13/14 showed no differences compared to negative control. F) P₁₁-13/14 with 30 µg/mL nanoHA showed no differences compared to negative control.

The analysis of micrographs, taken from within the dentine using the fractured surfaces, confirmed the absence of any mineral deposits in the tubules of the negative control and samples from the 20 mM P₁₁-13/14, 20 mM P₁₁-13/14 seeded with 30 µg/mL nanoHA and the 30 µg/mL nanoHA treatment groups. Samples treated with iBond showed a clear surface layer of resin but no evidence of tubule penetration, see Figure 6-12 D. The samples treated with 20 mM P₁₁-4 showed a layer of what looks like mineral approximately 20 µm from the dentine surface, with a thickness of 20 µm penetrating further down the dentine tubule. This layer was present across the test area only and was not seen in dentine proximal to the test area, see Figure 6-12 C. A higher magnification image, see Figure 6-12, clearly showed material which was apparently dislodged from inside the tubule spreading when splitting the disk.

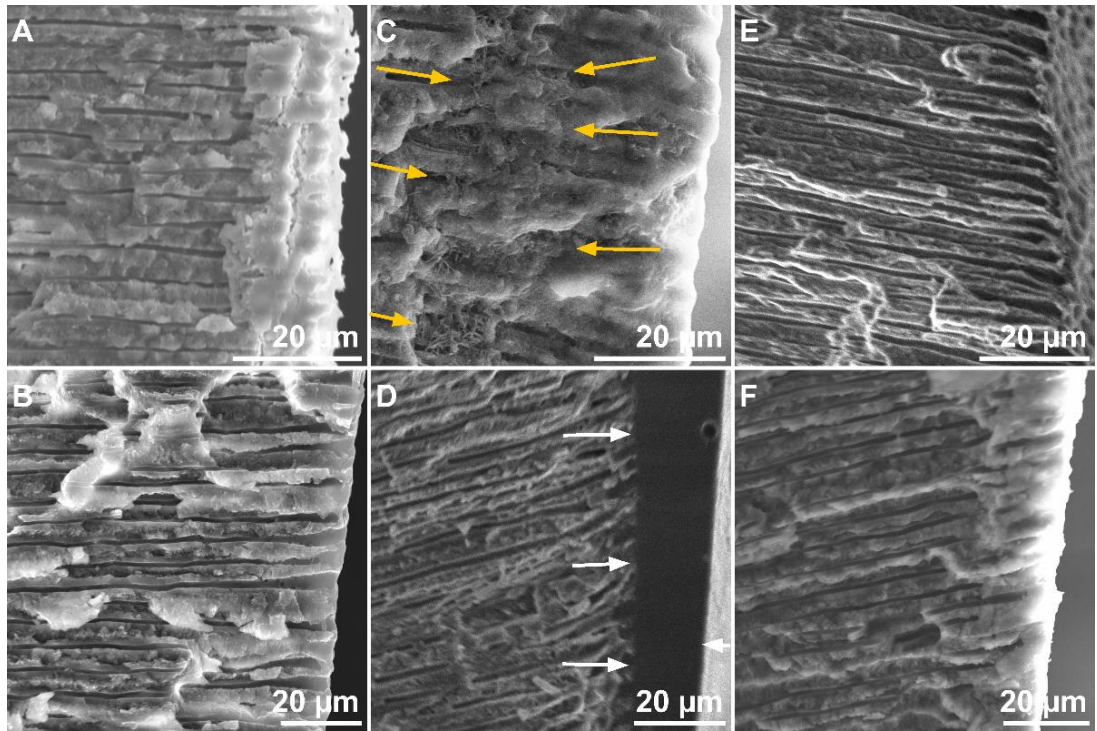


Figure 6-12 Scanning electron microscopy images of dentine tubules in samples from different treatment groups after 7 days in AS solution. A) Negative control of PBS treated dentine showed no deposits with open tubules. B) nanoHA treated dentine showed no obvious differences compared to negative control. C) P₁₁₋₄ treated dentine showed deposits 20 μm down the tubules with a deposit thickness of 20 μm, see orange arrows. D) iBond treated samples showed a thick layer of material on the surface of the dentine, see white arrows, although very little penetration is visible down the tubules. E) P_{11-13/14} treated samples showed no differences compared to negative control. F) P_{11-13/14} with 30 μg/mL nanoHA treated samples showed no differences compared to negative control.

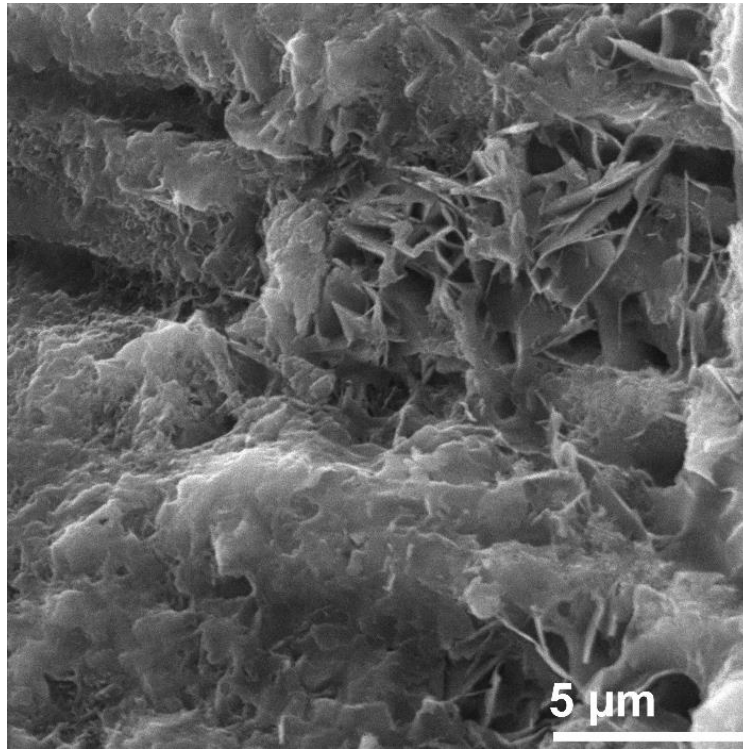


Figure 6-13 High magnification SEM micrograph showing the deposits associated with P₁₁₋₄ treatment of dentine disks after 7 days in artificial saliva. These deposits may have been the cause of the observed reduction in dentine permeability. These deposits localised to the test area approximately 20 μm away from the surface and were approximately 20 μm in thickness (deposit depth approximately 40 μm into dentine tubule at deepest point).

6.4 Discussion

To test the hypothesis that the SAP/nanoHA hybrid material would occlude dentine tubules via its ability to promote/support the growth of nanoHA seed crystals, a quantitative means of measuring the change in dentine permeability was required. The use of a fluid filtration device is a common method to assess the potential of dentine tubule occlusion products (Pashley and Galloway, 1985; Ayad *et al.*, 2009; Sauro *et al.*, 2010; Wang *et al.*, 2011; Thanatvarakorn *et al.*, 2013; Zhong *et al.*, 2015).

A study by Wang *et al.* (2010) used the fluid filtration method to assess the effectiveness of 3 commercially available treatments with respect to their fluid flow reducing properties (indicating decreased permeability and increased tubule occlusion) in a dentine disk model (Wang *et al.*, 2010). The treatments assessed were all toothpaste formulations, including Novamin, Sensodyne, Freshmint and Colgate Sensitive. Controls of no treatment and distilled H₂O were also tested. Initial dentine disk permeability was measured after etching with EDTA to provide a baseline reading and then a treatment was applied. Each treatment (1g) was applied using a toothbrush under constant loading of 150 g for 300 strokes per minute for 2 minutes after which the dentine permeability was measured again. Half of the samples from each treatment group then underwent an acid challenge (6% citric acid for 1 minute) with the permeability measured again. The remaining samples from each treatment group were then left in artificial saliva (1.5 mmol/L CaCl₂, 50 mmol/L KCl, 0.9 mmol/L KH₂PO₄, 20 mmol/L Tris, pH 7.4) for 24 hours after which the permeability was measured. The results showed that the use of all treatments, including the distilled H₂O control, resulted in a significant decrease in permeability compared to the no treatment control ($p < 0.001$). The Novamin and Sensodyne treatments lowered the permeability significantly compared to distilled H₂O ($p < 0.001$) while Colgate Sensitive was not significantly different to the distilled H₂O group. The ineffectiveness of the Colgate Sensitive treatment was perhaps not unexpected as this was developed as a nerve stabilisation treatment as opposed to a material that occludes tubules.

Recently the fluid filtration system has been further developed to provide not only fluid flow measurements but also real time imaging using laser scanning confocal

microscopy (Williams *et al.*, 2008). The new device used a modification of the Pashley methodology by employing a syringe pump which was configured to ensure a flow rate of 3 mL/h and measuring the pressure required to maintain this flow pre- and post-treatment. The fluid used to infiltrate into the dentine was 10 μ M rhodamine B, 20 mM HEPES buffer and 1 mM CaCl₂. The dentine samples were placed under a confocal microscope during the fluid flow measurement and the fluid was then imaged within the dentine tubules due to the presence of the fluorescent dye, rhodamine B. The technique was used to test a commercial dentine resin, Cervitec® (Ivoclar Vivadent, Schaan, Liechtenstein) and an experimental alginate gel toothpaste (n=4) to simultaneously determine both their effectiveness in reducing fluid flow and to image the dentine surface during testing. The study concluded that the use of Cervitec resin produced a significant reduction in visible fluid flow which was supported by a linear increase in pressure, with a maximum of 13 kPa (1.88 psi) required to maintain the flow rate of 3 mL/h over the 120-second test period. The alginate gel toothpaste treatment produced a similar initial reduction in fluid flow but as the pressure increased to 6 kPa (0.87 psi), the fluid flow increased.

The ability to image and measure fluid flow through dentine is a desirable combination as it could be used to determine the mode of failure, allow for imaging in its hydrated state minimising drying artefacts and also allow for increased understanding of the fluid flow through the tissue itself. With regards to its use as a measurement tool for dentine permeability to aid the development and assessment of dentine occlusion treatments however, it has a number of potential issues. The use of a constant flow rate which results in a varying test pressure is not ideal for all materials and, in effect, acts to provide a measurement of the failure pressure required to prevent the treatment working. The imaging of the fluid flow, although impressive with regards to it showing the increasing areas of fluorescence as the fluid leaves the tubules, does not have the required resolution to image the morphology of the dentine tubules or dentine surface. As such the use of traditional imaging, for example SEM or TEM, would still be required to assess the effect of the treatments at the ultrastructural level. No publications could be found which have used this technique to assess dentine

sensitivity treatments, which is most likely due to the lack of improvement in the data produced compared to the established fluid filtration technique.

Another development which has been made to the fluid filtration experiment is the use of a Flodec device (De Marco Engineering, Geneva, Switzerland) which replaces the manual measurement of the bubble movement with the use of an infrared light to measure the bubble displacement (Pashley *et al.*, 1996). This development removes the need for visual measurements as the Flodec device can be connected to a computer increasing the precision of each measurement. There have been a number of studies utilising the Flodec development to investigate a range of dentine permeability-related topics including, but not limited to, hydroxyapatite-containing toothpaste (Hiller *et al.*, 2018), nanostructured bioactive glass treatment (Mitchell *et al.*, 2011), and arginine-containing toothpaste (Ayad *et al.*, 2009) with the advantages of using the Flodec device not being discussed. To determine if there was any advantage of using the Flodec device, a study was undertaken by De La Macorra and Escribano (2002) to investigate if the Flodec device produced different results to the traditional visual measurements. The method measured fluid flow using both Flodec and visual measurement methods simultaneously. In total, 6 dentine samples were used with each sample being tested at fluid pressures of 0, 5, 10, 15, 20, 25, and 29 cm H₂O in sequence. The results of the study concluded that the use of a Flodec device did not produce results which were statistically different to the traditional method when compared using Passing and Bablok regression ($p > 0.1$). The accuracy of the Flodec device, with its change in fluid volume detection limit of 10 to 20 nL (De La Macorra and Escribano, 2002), is much more accurate than the human eye but when we consider the experimental method, the main source of sample to sample variation is not caused by the visual measurement of the fluid flow but is a product of the inherent variability between dentine samples. Due to the lack of any real improvement in measurement or imaging quality, the fluid filtration device used in this thesis was based on the work of (Pashley and Galloway, 1985). There are currently no commercially available dentine disk fluid filtration instruments and so one was

developed as described in section 6.2.2 and was built to similar specifications as the devices used by GSK (Weybridge, UK) and Intertek (Hooton, UK).

Validation of the fluid filtration device used here was undertaken using 5% oxalic acid as a positive control and PBS as a negative control (n=10). Oxalic acid was chosen as the positive control because desensitisers based on oxalic and/or potassium oxalate are considered the gold standard in the occlusion of dentine tubules due to the formation of acid resistant calcium oxalate crystals on the surface and within the dentine tubules, although the applications are limited due to potential toxicity (Sauro *et al.*, 2010). The results of the validation experiments demonstrated unequivocally that the fluid filtration device developed for use in this thesis was capable of producing a statistically significant difference in the mean reduction in fluid flow through dentine between 5% oxalic acid and PBS ($p < 0.05$), see Figure 6-7. The relatively small standard deviations produced by the negative and positive control treatments, $\pm 19\%$ and $\pm 3\%$ respectively also supports the validity of the system.

The fluid filtration study where treatments were followed by 7 days incubation in AS solution involved 2 measurements of fluid flow reduction. The first measurement was taken directly after the treatment was applied and is referred to as the treatments' initial application. The second measurement was taken after a 7-day incubation period in AS solution to determine the effect of the treatments in a biologically relevant environment and to allow the mineralisation process to occur within the dentine tubules.

The data resulting from treatment with 20 mM P_{11-13/14} (no nanoHA) and 20 mM P_{11-13/14} seeded with 30 $\mu\text{g}/\text{mL}$ nanoHA might be explained as follows. These treatments resulted in an initial reduction in fluid flow of $74 \pm 21\%$ and $69 \pm 25\%$ respectively, immediately after application when compared to the initial fluid flow through the same untreated disks. This may be due to the formation of a SAP gel over the surface of the dentine or within the dentine tubules as per the hypothesis. After 7 days in AS solution, the 20 mM P_{11-13/14} (no nanoHA) and 20 mM P_{11-13/14} seeded with 30 $\mu\text{g}/\text{mL}$ nanoHA treatments produced very large increases in fluid flow ($-62 \pm 110\%$ and $-70 \pm 130\%$ respectively). The cause of this increase in fluid flow cannot be simply explained by the hybrid material

disassembling and diffusing out of the dentine tubules or off the dentine surface. In the case of the negative controls, there was no significant difference in fluid flow after the initial application of the PBS or after 7 days incubation in AS, suggesting that the hybrid material had actively increased the flow after 7 days in AS solution. A large increase in fluid flow measured following application of the hybrid material treatment and after 7 days in AS could potentially be explained by considering the fluid dynamics of the system.

In Chapter 5 of this thesis, where the hybrid material was investigated using ^1H NMR analysis, the data indicated that the P_{11-13} monomer was assembling on the surface of the nanoHA. It may therefore be that the P_{11-13} monomer interacts with the interior walls of the dentine tubule producing a monolayer covering in a similar manner. The interaction of the P_{11-13} monomer with the surface of the dentine tubule wall would result in the hydrophobic face of the monomer facing towards the fluid within the tubules, effectively producing a hydrophobic layer on the tubules' surface. If we consider a single tubule as a channel with fluid running through it, we can then apply the widely accepted "non-slip" condition which concerns the fluid in contact with the surface of the channel. The non-slip condition is a condition which states that there is no relative motion between the wall and the fluid in contact with it (Day, 1990). The depth of the layer with respect to the distance between the tubule wall and the fluid which is immobilised by the non-slip condition is called the slip length (Priezjev *et al.*, 2005). The non-slip condition has an insignificant effect when considering macroscale tubule fluid flow as it only affects a small proportion of the total fluid volume (the fluid in contact with the walls of the tube). However it has been recently shown that when we examine micro/nano tubes, the effect needs to be considered and may be significant (Nagayama *et al.*, 2017).

The formation of a self-assembled monolayer on the surface of the dentine tubule would produce a hydrophobic coating which would decrease the slip length. This is the distance of the fluid from the wall which is under the non-slip condition (Tretheway and Meinhart, 2002). The decrease in the slip length has a minimal effect on large channels as the channels already have a large area that is not affected by the non-slip region but when we consider dentine tubules, these are

very small channels (1-2 μm). It is therefore probable that a significant amount of intra-tubular fluid would be affected by the non-slip conditions resulting in an inhibition to fluid flow. Even a small reduction in the slip length could have a significant effect on the fluid flow dynamics, increasing the flow when under laminar pressure. Although this theory helps explain the increase in fluid flow produced in this work, a recent review considering fluid dynamics in micro channels and its deviation from macroscopic models was produced by Celata (2004) and concluded that due to the relatively large errors of the measurements, there was currently no consensus as to the fluid flow within micro channels. We were unable to determine the mechanism by which treatment with the SAP/nanoHA hybrid material resulted in an increase in fluid flow through dentine after 7 days in AS solution but compression of the slip length causing an effective increase in tubule diameter is a possible cause despite the theory being still debated.

To summarise, the hypothesis is that the formation of a monolayer of P₁₁₋₁₃ on the interior of the dentine tubules' surfaces produces a hydrophobic layer. This hydrophobic layer decreases the slip length resulting in an increase in fluid flow under laminar pressure compared to the natural dentine tubule internal surface. However, the lack of agreed understanding of such fluid flow behaviour in the literature means that this remains a hypothesis only.

NanoHA particles are increasingly being seen as a material with significant potential to increase the effectiveness of a range of dental and bone restoration treatments (Huang et al., 2009; Zhou and Lee, 2011; Hill et al., 2015b; Vano et al., 2018). These experimental treatments often use relatively large seeding densities compared to the 30 $\mu\text{g}/\text{mL}$ used in this work. For example, an experimental treatment developed by Li *et al.* (2008) used a nanoHA seeding density of 10 mg/mL to promote the repair of tooth enamel (Li *et al.*, 2008). This strategy of using nanoHA relies upon a relatively large concentration of nanoHA particles to produce a layer of nanoHA across the tooth surface to promote enamel repair. The use of nanoHA in this work was undertaken to provide seed crystals which would hopefully grow, supported by the SAP component, blocking the dentine tubules and reducing fluid flow (permeability) within the dentine

samples. The results of the investigation into the use of nanoHA in this way did not produce the desired effect and resulted in an *increase* in fluid flow within the treated dentine samples after 7 days in AS solution, see Figure 6-9. The increase in fluid flow suggests that not only are the nanoHA seed crystals not blocking the dentine tubules but they are also causing the dentine tubules to become more efficient at allowing the flow of fluid through them. The cause of this is unclear and was not explored further within this work although one hypothesis is that the low concentration of nanoHA present could result in the highly crystalline seed crystals growing at the expense of the natural mineral of the dentine tubules resulting in the increasing diameter. The dentine tubules walls are composed of peritubular dentine which is composed of 25 nm diameter crystals (Goldberg *et al.*, 2011) while the nanoHA seed crystals are approximately 45 nm with respect to the longest axis, see Chapter 3. The aforementioned potential cause of the increase in dentine permeability after the application of the nanoHA seed crystal treatment could be due to the Ostwald ripening process which would result in the smaller, less thermodynamically stable dentine crystals dissolving and the larger, more thermodynamically stable nanoHA seed crystals growing (Vetter *et al.*, 2013). As previously discussed a small increase in diameter could result in a large increase in flow. There were no examples in the literature of nanoHA-based treatments which utilise $\mu\text{g/mL}$ seeding densities of nanoHA but this work suggests that they may have a negative effect on dentine tubule mineralisation.

The P₁₁₋₄ SAP is a proven nucleator of hydroxyapatite (Kirkham *et al.*, 2007) and has been developed into 3 clinical products of which it is the active ingredient, Curodont™ Repair, Curodont™ Protect and Curodont™ D'senz (Credentis, Windisch, Switzerland). The use of Curodont™ Repair has been shown to be effective in the remineralisation of early caries lesions (Brunton *et al.*, 2013). The commercially available P₁₁₋₄ Curodont™ D'senz treatment is applied with the peptide in the assembled state within a gel formulation, which means that there is little opportunity for the peptide to diffuse down into the dentine tubules. In this work P₁₁₋₄ was used in its monomer state to act as a known nucleating agent which could be compared against the experimental hybrid material, in addition to exploring the use of P₁₁₋₄ in its monomer state as a desensitising treatment. After initial application, the P₁₁₋₄ treatment did not produce any significant mean %

reduction in fluid flow compared to the negative control ($p>0.05$), see Figure 6-8. The lack of any change in the fluid flow within the dentine is not unexpected due to the short length of time which had occurred before the testing of the fluid flow. The P₁₁₋₄ treatment required exposure to the AS solution which would provide the ions required for mineralisation to occur and time for the mineral to grow. The large reduction in fluid flow (dentine permeability) measured after 7 days in AS solution in dentine samples treated with P₁₁₋₄, see Figure 6-9, supports the nucleation and crystal growth supporting properties of P₁₁₋₄. Further evidence of this mechanism was seen in the SEM images, see Figure 6-13, where small crystals can be seen forming a layer some 20 μm from the surface of the dentine tubules in samples treated with P₁₁₋₄ and then incubated in AS solution. It is possible that these crystals represent some form of hydroxyapatite as predicted by previous studies showing the formation of hydroxyapatite by P₁₁₋₄ (Kirkham *et al.*, 2007). The shape of the crystals is also indicative of hydroxyapatite (Sadat-Shojai *et al.*, 2013).

6.5 Conclusion

Apparatus for the measurement of fluid flow through dentine samples was developed and validated for these studies. Treatment of dentine surfaces using the P₁₁-13/14 nanoHA hybrid material was shown to be ineffective in reducing dentine permeability as evidenced by the increased fluid flow in these experiments. The cause of this increase in fluid flow/dentine permeability associated with treatment with the hybrid materials is not known but appears to be related to the SAP component. A working hypothesis to explain the observations is that the P₁₁-13 monomer interacts with the dentine tubule surface resulting in a decrease in the slip length, effectively increasing the diameter of the dentine tubule. The use of nanoHA at a seeding density of 30 µg/mL also resulted in an increase in fluid flow compared to the negative control. Again, the cause of this is unknown though the growth of the seeded nanocrystals at the expense of the dentine tubules may be a potential cause. Treatment of dentine surfaces with the SAP P₁₁-4 proved to be an effective tubule occlusion agent after incubating samples in AS for 7 days, producing intra-tubular crystalline material 20 µm down the dentine tubule which acted to reduce the fluid flow significantly and was statistically comparable to the use of iBond resin. This may be attributed to the known nucleation properties of P₁₁-4.

Chapter 7 - General Discussion

The aim of this thesis was to develop, characterise and optimise a novel self-assembling peptide/nanoHA hybrid material and assess its ability to support the occlusion of dentine tubules with a view to its potential use in the treatment of dentine sensitivity.

The prevalence rate of dentine sensitivity varies depending on the population studied, with between 3.8% to 35% of people being affected by dentine sensitivity in the general population (Beddis *et al.*, 2013). The large variation in reported rates of dentine sensitivity, as high as 74% (Rees and Addy, 2002), is often due to studies being based on populations seeking dental work or referred to university dental hospitals which can result in highly biased samples (Rees, 2000). There are a number of factors which can increase the reported rates of dentine sensitivity. These include, but are not limited to, periodontal disease (Chabanski, 1996), gender (Splieth and Tachou, 2013), age (Rees and Addy, 2002), higher social class (Chrysanthakopoulos, 2011) and consumption of dietary acids (O'Toole and Bartlett, 2017).

A dentine sensitivity study produced by Clayton *et al.* (2002) investigated the prevalence and distribution of dentine sensitivity in a population of 17-58 year-old serving personnel (228 participants) on an RAF base in the Midlands, UK. This population was chosen to remove the confounding factors associated with patients seeking clinical treatment or through referral to a university teaching hospital, with the study being completed through a self-assessment questionnaire.

The results of the study revealed a prevalence rate of 50%, which was considered high compared to previous dentine sensitivity prevalence rates. The cause of this relatively high prevalence rate compared to other studies (Rees and Addy, 2002) was unclear, although a number of potential factors were discussed. A high percentage (26%) of study participants reported only brushing their teeth once or less per day which could suggest that other forms of dental pain, for example untreated caries, could be the cause. A second factor identified by the authors was a relatively large intake of dietary acid (through consumption

of fizzy drink or fruit juice) combined with twice daily tooth brushing. The intake of dietary acid has been shown to increase dentine sensitivity with the contact time between the dietary acid and tooth being reported as the main risk factor with respect to enamel erosion (O'Toole and Bartlett, 2017). The authors suggested that clinical assessment of the study participants would be required to establish if untreated caries was the cause of the high prevalence rate reported.

No comparisons between gender were analysed due to the small number of females (Clayton *et al.*, 2002) in the sample population. Dentine sensitivity is often reported to be more prevalent in the female population (Flynn *et al.*, 1985; Chrysanthakopoulos, 2011) although a number of studies have reported no statistical difference when comparing males to females (Chabanski *et al.*, 1997; West *et al.*, 2013). One potential factor which has been cited as a reason for the reported difference is that women are more likely to seek treatment compared to males (Rees and Addy, 2002).

The incidence of dentine sensitivity with respect to age can also vary depending on the population studied, although the range is often quoted as 20-49 years of age peaking at the 30-39 age bracket (Orchardson and Gillam, 2006).

The increase in prevalence within the higher social classes (often defined as having a university education), who have been shown to maintain a high standard of oral health (Rees, 2000), suggests that a more varied diet containing increased dietary acids is causing increased levels of dentine sensitivity (Rees and Addy, 2002; Chrysanthakopoulos, 2011; Liang *et al.*, 2017). The increase in relatively wealthy individuals reporting dentine sensitivity could result in a larger market for dentine sensitivity treatments and may lead to more expensive treatments, if they can produce a comparable reduction in painful symptoms to current treatments but provide a near permanent effect, more economically viable.

Although the measurement of prevalence rates can vary depending on the study, dietary acid is a common factor reported in the literature which could pose issues in the future and make the development of new effective dentine sensitivity treatments essential. Dentine sensitivity prevalence studies on populations in

developing countries, for example China, are reporting dentine sensitivity as a result of a more varied diet containing higher amounts of dietary acid (Liang *et al.*, 2017). The link between economic growth and a more acid rich diet could result in an increased number of potential dentine sensitivity sufferers world-wide.

The accurate measurement of the prevalence of dentine sensitivity is difficult to achieve and can depend on the country or population studied (West *et al.*, 2013). When assessment is undertaken in a clinical environment, confounding factors, such as distorted population, can affect the resulting value. When using a self-reported questionnaire, as described in the Clayton *et al.* (2002) study, the need for clinical evaluation is required to allow confirmation that dentine sensitivity is the true cause and not a symptom of untreated dental issues, for example untreated caries.

There is a real clinical need for new dentine sensitivity treatments (Schmidlin and Sahrman, 2013) as those currently available do not provide a satisfactory outcome as defined by the criteria of a gold standard sensitivity treatment. An ideal treatment should be: easily applied, rapid in action, non-irritant to the pulp, long-lasting, have no staining effects, be consistently effective and be relatively painless on application (Kimura *et al.*, 2000). A further consideration, which is important with regards to the expensive peptide-based treatment investigated in this work, is that any treatment must be economically viable. The current range of available treatments, described in section 2.5, have at least one common characteristic which prevents them from being considered as a gold standard as defined above. This is that they are unable to provide a permanent relief from the painful symptoms of dentine sensitivity and so require repeated/frequent application. One reason for the lack of permanency of current treatments is the lack of tubule penetration achieved. To provide a permanent/more enduring solution, the P_{11-13/14} nanoHA hybrid material was developed in this thesis. The advent of a new generation of biomimetic materials with bioactive properties offers new potential avenues of research with regards to the treatment of dentine sensitivity.

The use of peptides in the treatment and prevention of dental diseases is a growing field of research with applications in tubule occlusion (Wang *et al.*, 2010; Cao *et al.*, 2014; Schlee *et al.*, 2017) and caries repair (Kosoric *et al.*, 2007; Kirkham *et al.*, 2007; Melcher *et al.*, 2016; Dogan *et al.*, 2018). The use of peptides which can mimic the natural mineralisation process is desirable as they are able to effectively repair or replace the tissue which has been damaged or removed and can prevent further tissue damage or loss. The properties of the assembled peptides developed at the University of Leeds can be controlled through rational design of the monomer peptide amino acid sequence to provide optimal interaction with the enamel surface and sites for HA nucleation as well as prevent further demineralisation (Kirkham *et al.*, 2007).

The rationale behind combining the self-assembling peptides used in this thesis with nanoHA seed crystals in the hybrid material under investigation is that although the HA nucleation properties of the P₁₁-13/14 self-assembled material *per se* are poor, it has been shown that it is effective in supporting the growth of embedded nanoHA seed crystals (Sayed, 2013). The complementary self-assembling peptides P₁₁-13 and P₁₁-14 were developed at The University of Leeds as part of a portfolio of peptides offering a range of properties and so have similar design principles to P₁₁-4, see section 5.1.

P₁₁-4 is a self-assembling peptide that is already commercially available and is the active ingredient in Curolox® technology which is the basis of the Curodont remineralisation, regeneration and demineralisation protection product range (www.curodont.com). P₁₁-4 has been shown to be effective in the nucleation and support of HA crystal growth and in the repair of early caries lesions (Brunton *et al.*, 2013).

Unlike P₁₁-4, which is designed to self-assemble in conditions of pH<8 and/or high ionic strength (Carrick *et al.*, 2007), P₁₁-13 and P₁₁-14 were designed so that when dissolved separately in solutions at physiological pH and ionic strength, no self-assembly occurs. When P₁₁-13 and P₁₁-14 are combined in equimolar concentrations of above 10 mg/mL, self-assembly occurs spontaneously due to the complementary ionic bonding between the negatively charged P₁₁-13 and positively charged P₁₁-14 (Kyle *et al.*, 2012), see section

5.1. The P_{11-13/14} self-assembled peptides have been investigated as potential scaffolds for tissue engineering and have shown excellent cytocompatibility when tested with primary human dermal fibroblast (Kyle *et al.*, 2010).

The hypothesised method of treatment application was that nanoHA would be incorporated into the individual P₁₁₋₁₃ and P₁₁₋₁₄ solutions and, when added to the surface of exposed and open dentine tubules, the monomeric non-Newtonian liquid would travel down into the tubules with the first solution and then the addition of the second peptide solution would trigger self-assembly. Due to the peptide acting as a carrier surfactant for the nanoHA, this would result in the nanoHA being present on the dentine surface and within the dentine tubules. NanoHA crystal growth would be supported by the SAP hydrogel. The hybrid material would then, in the presence of sufficient ionic calcium and phosphate, provide a source of mineral to occlude the dentine tubules from within.

The novel feature of this treatment is that the trigger for self-assembly would occur only after the application of the second nanoHA seeded peptide solution. This would allow enough time for the first nanoHA seeded peptide solution to travel down into the tubule. On subsequent application of the second peptide, self-assembly would be triggered to provide a gel containing the nanoHA seed crystals within the dentine tubule. This is important as the growth of the seed crystals within the tubule would be difficult to remove via abrasive and attrition means, due to its position below the dentine surface, producing a long-lasting or permanent relief to the painful symptoms of dentine sensitivity as long as the crystals remain within the tubule. The ability to control self-assembly within the tubule itself through addition of the second complementary peptide solution is a key design feature to address what was suggested to be a potential disadvantage of using P₁₁₋₄ in the treatment of dentine sensitivity as it would avoid premature assembly of the peptide at the tooth surface, prior to infiltration.

To test this hypothesised SAP/nanoHA hybrid material treatment it was first assessed and optimised using the *in vitro* nucleation and crystal growth assay (IVNCG) developed by Sayed (2013) with respect to its ability to promote mineral formation under steady state conditions. The hybrid material and P₁₁₋₄ peptide were then applied to the dentine disk model with the effect on dentine

permeability measured using a fluid filtration device after initial application and after 7 days incubation in artificial saliva (AS) followed by SEM analysis above and below the dentine surface.

7.1 Development of an Optimised Hybrid Material for Dentine Tubule Occlusion

To optimise the self-assembling peptide/nanoHA hybrid material, and provide a means to develop future potential treatments which rely upon the growth of hydroxyapatite mineral to produce dentine occlusion, a high throughput *in vitro* mineralisation method was required.

The IVNCG method used in this work was first developed by Sayed (2013) and was based on work by Hunter and Goldberg (1993, 1994), see section 4.1. Once validated, see section 4.3.1, the IVNCG was used to optimise the seeding density of nanoHA with respect to its ability to produce a significant repeatable mineralisation-promoting effect while limiting the initial seeding density to reduce possible toxicity. This was of interest due to the poorly understood toxicity of nanoHA and to enable the use of the smallest seeding density of nanoHA in the hybrid material to mitigate this (Xu *et al.*, 2009; Shi *et al.*, 2009; Remya *et al.*, 2014).

A nanoHA toxicity study produced by Xu *et al.* (2009) using a nanoHA seeding density of 10 mg/mL showed that on addition to osteoblast cells, their growth was significantly reduced. The nanoHA particles used were rod-shaped with a mean length of 80 nm. The effect on osteoblast growth was hypothesised to be caused by nanoHA dissolution resulting in elevated ionic calcium (Xu *et al.*, 2009). The seeding density used in the Xu *et al.* study (2009) is significantly larger (10 mg/mL) than the seeding density used in the hybrid material (0.03 mg/mL).

We have hypothesised that the nanoHA in the hybrid material could undergo a similar dissolution behaviour before crystal growth could occur, see section 4.4, producing an increase in localised ionic calcium which could result in the same effect. An additional study which analysed the effect of nanoHA (20-30 nm) at a range of seeding densities (10 µg/mL, 100 µg/mL, 1 mg/mL and 10 mg/mL) on

apoptosis in MC3T3-E1 cells confirmed that cell death was dose dependent even at 10 µg/mL (Wang *et al.*, 2012). In contrast a study produced by Remya *et al.* (2014) investigated the effect of 800 µg/mL (below 50 nm) nanoHA on mouse mesenchymal stem cells isolated from bone marrow. The results showed that the nanoHA was compatible with mouse bone marrow mesenchymal stem cells. The conflicting results with regards to the toxicity of nanoHA depending on the cell line used, concentration of nanoHA used and size of nanoHA used, suggest that further research is required with respect to the clinical use of nanoHA.

However, nanoHA is already used in dental products. The seeding densities of the currently available nanoHA based dental treatments are considerably larger than the densities used in this work. In a clinical trial investigating the remineralisation potential of a nanoHA toothpaste produced by Sangi Co (Apagard® nHAP toothpaste) containing 5% nanoHA (crystal size 30–84 nm) (Huang *et al.*, 2009), the toothpaste was shown to have the same remineralising capacity as a fluoride dentifrice (Najibfard *et al.*, 2011). Another clinical trial was reported by Vano *et al.* (2014) which used a 15% nanoHA toothpaste to treat dentine sensitivity but the size of the nanoHA was not reported. The study concluded that the use of paste containing 15% nanoHA provided relief from dentine sensitivity after 2 – 4 weeks (Vano *et al.*, 2018). Both of these studies used significantly larger nanoHA seeding densities than what was used in this work. Published clinical trials therefore suggest that the use of nanoHA at significantly higher seeding densities than 30 µg/mL are acceptable despite published literature on *in vitro* data which suggests that this might not be the case, as described previously.

To ensure that any toxicity due to the use of nanoHA was minimised, the minimum seeding density of the nanoHA seed crystals for further testing in this thesis was identified as described in section 4.3.3, with respect to mineral growth (measured as phosphate mass) in the IVNCG compared to the 10 µg/mL poly-L-glutamic acid positive control. The results of this study produced a repeatable (n=3) minimal nanoHA seeding density of 30 µg/mL to increase the HA mineral mass present compared to the positive control (p<0.05). Interestingly, it was shown, through the use of TEM analysis on mineral recovered from the IVNCG

system, that when using a seeding concentration of below 30 µg/mL the morphology and composition of the mineral deposits formed within the agarose gels changed, see section 4.3.4. The mineral deposits formed when using a seeding density of 20 µg/mL or lower produced a small number of large spherical crystals, 400 µm diameter which had a Ca/P ratio and crystal morphology characteristic of OCP. In contrast, when using a seeding density above 30 µg/mL, a much larger mass of mineral was formed, composed of a much larger quantity of smaller (2-5 µm) crystals with a Ca/P ratio and crystal morphology characteristic of hydroxyapatite.

It is hypothesised that the cause of this transition in mineral morphology and composition was due to the seed crystals dissolving within the gels when lower concentrations of nanoHA were used and then recrystallising once the calcium and phosphate ions had diffused into the agarose gels from the buffers. The addition of 30 µg/mL nanoHA would also be expected to result in some nanoHA crystal dissolution but, significantly, not all would be dissolved. Once the calcium and phosphate buffers diffused into the agarose, it was hypothesised that the remaining nanoHA crystals underwent crystal growth producing a large quantity of small needle crystals (2-5 µm), see Figure 7-1.

To my knowledge there are no publications which have observed this transitional behaviour with respect to the use of nanoHA crystal seeds and, although dependent on the salts and buffer composition, this behaviour may well be occurring in other nanoHA seeded systems and treatments which rely on nanoHA as a component and so could be of interest to this field of research. This result could also have implications for the formulation of future treatments which rely on concentrations of nanoHA similar to that used here (30 µg/mL and below) as maintaining nanoHA crystal seed stability with respect to dissolution must be considered.

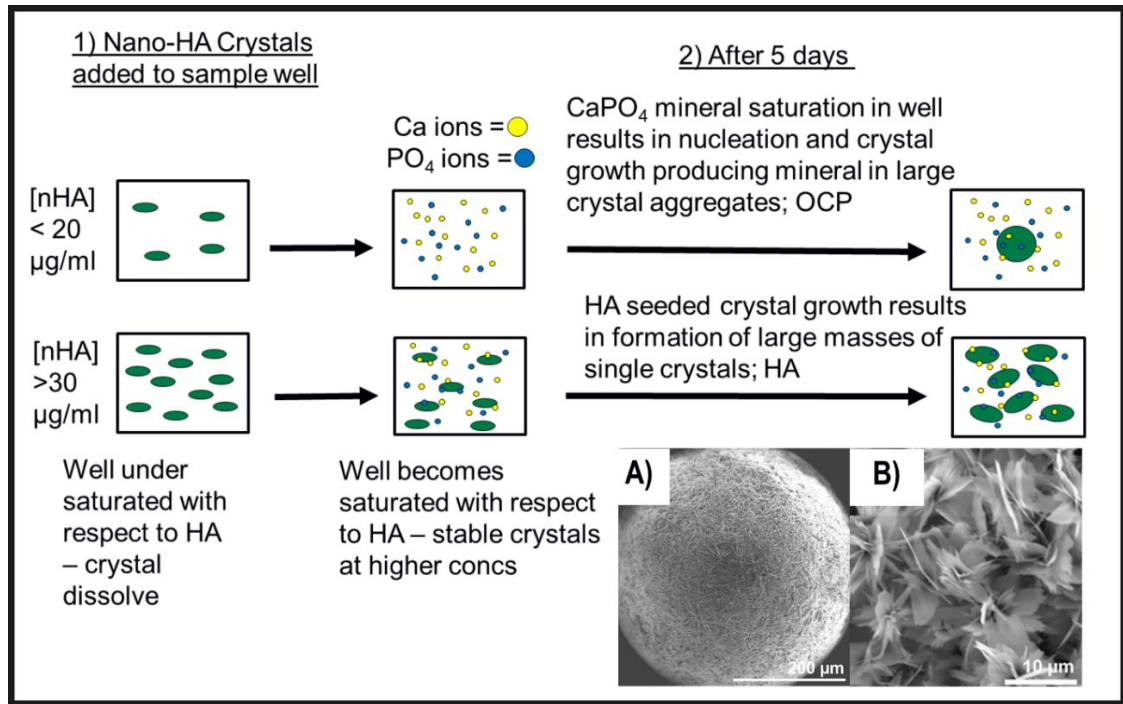


Figure 7-1 Schematic describing the hypothesised nanoHA seeding density dependent transition from what is believed to be OCP (this could be tested using XRD), at 20 µg/mL or below nanoHA seeding density to HA, when seeded at 30 µg/mL or above after 5 days in IVNCG assay. At both nanoHA seeding densities the sample well is undersaturated with respect to HA causing crystal seed dissolution. When nanoHA seeding is below 20 µg/mL, all the seed crystals dissolve and then recrystallise when calcium and phosphate ions from buffer reservoir diffuse into the sample well forming large crystal aggregates of what we believe to be OCP, see SEM image A) (scale bar 200 µm). When nanoHA seeding is 30 µg/mL or above, nanoHA seeds dissolve but some remain which then go on to grow, producing a large number of what we believe to be small HA crystals as seen in the SEM image, (scale bar 10 µm). Schematic not to scale.

The results of the IVNCG optimisation and assessment of the self-assembling peptide/nanoHA material proved disappointing with regards to its ability to support nanoHA crystal growth; this was due to the hybrid material precipitating out of solution within the hydrogel. The use of a novel precipitation assay, see section 5.3.4, confirmed that the rate of hybrid material precipitation increased as the concentration of ionic calcium increased. The cause of this relationship was hypothesised to be due to the strong salting out efficacy of the calcium ion (Shaw, 1991) which competes with the peptide assemblies for the sphere of hydration resulting in their precipitation. A similar result was produced when samples of nanoHA were added to the peptide gels although to a lesser extent

than addition of calcium ions. This was attributed to the same salting out process hypothesised for the calcium ions.

A final series of experiments was undertaken using ^1H NMR to identify if the peptide monomers were interacting with the nanoHA with or without the presence of ionic calcium, see section 5.2.6. The results showed that the P₁₁₋₁₃ monomer, when in the presence of 6.5 mM of ionic calcium and 30 $\mu\text{g}/\text{mL}$ nanoHA, was subject to aggregation. When in the presence of 6.5 mM of ionic calcium or 30 $\mu\text{g}/\text{mL}$ nanoHA in isolation, no peptide aggregation was detected. A working hypothesis to explain this observation is that P₁₁₋₁₃ was assembling on the surface of the nanoHA through the widely accepted calcium bridging process, similar to the effect seen in pellicle formation on enamel (Ash *et al.*, 2014). The interaction of ionic calcium with the P₁₁₋₁₃ peptides assembled on the surface of the nanoHA could promote further peptide aggregation resulting in layers of peptide covering the nanoHA seed crystal surface. Further experiments would be required to confirm this hypothesis which could include further ^1H NMR experiments to investigate the P₁₁₋₁₃ and ionic calcium concentration effect on P₁₁₋₁₃ aggregation.

The IVNCG assessment and optimisation of the hybrid material proved unsuccessful as none of the IVNCG assay experiments resulted in the hybrid material exhibiting any efficacy with respect to supporting the growth of the seed crystals as evidenced by a significant increase in phosphate mass compared to the positive control. Further analysis of the hybrid material with respect to its precipitation under the IVNCG conditions, through the use of a novel precipitation assay, suggested that it is unsuitable for testing the SAP component of the material, see section 5.3.4. Although the hybrid material was unsuitable for testing in the IVNCG, this did not exclude it from being tested using the dentine disk model as the conditions used in the fluid filtration study were of lower ionic calcium concentration (0.7 mM) which could prevent or reduce the surface-mediated SAP aggregation hypothesised above. Comparisons with the published literature are difficult due to the lack of publications that use self-assembled peptides or other materials combined with sub 100 $\mu\text{g}/\text{mL}$ nanoHA used in this work, in the field of dentine sensitivity or caries repair.

7.2 Suitability of SAPs for Use as Dentine Occlusion Treatments

The *in vitro* assessment of the hybrid material provided a more detailed understanding of the material's behaviour, including its unsuitability for use in IVNCG system. The next step was to apply the hybrid material to its intended substrate – human dentine. The hybrid material was compared throughout the human dentine studies with P₁₁₋₄ without the addition of nanoHA as this peptide has already been brought through to clinical use, albeit not yet for infiltration of dentine tubules. In order to evaluate efficacy of tubular occlusion experimentally, both the hybrid material and P₁₁₋₄ were applied to human dentine and fluid flow reduction assessed using the fluid filtration device first developed by Reeder *et al.* (1978), see Chapter 6. The fluid filtration device is the gold standard method for the measurement of dentine tubule permeability *in vitro* (Al-Jadaa *et al.*, 2014) and is used extensively for the assessment of dentine sensitivity treatments (Pashley *et al.*, 1984; Sauro *et al.*, 2006; Wang *et al.*, 2011; Hiller *et al.*, 2018), including the development of new formulations for commercial use.

The application of the P_{11-13/14} to human dentine with and without the addition of nanoHA produced a surprising result. Instead of reducing fluid flow as hypothesised, the application of P_{11-13/14} to human dentine resulted in an *increase* in dentine permeability with or without the nanoHA seed crystals after 7 days incubation in AS solution.

A hypothesis for this result is that the large increase in fluid flow was due to the interaction of the charged face of P₁₁₋₁₃ with the dentine tubule wall, producing an effectively hydrophobic dentine tubule surface. The previous results using ¹H NMR that led to the suggestion of calcium bridging of P₁₁₋₁₃ peptide to nanoHA crystals, described in section 5.4, support the hypothesis explaining the observed increase in fluid flow. In the dentine permeability study, the interaction of the peptide with the dentine tubule wall would reduce the non-slip length, causing an effective increase in the circumference of the tubule with respect to the area of fluid which could flow (Day, 1990). If this hypothesis is correct, then the application of the hybrid material to dentine would cause the tubule to

become more permeable to fluid movement. This is exactly what was observed in the fluid filtration study, see Figure 7-2.

Further experimental work would be required to confirm this hypothesis. This could include a fluid filtration study using varying concentrations of SAP which could provide a dose-response with respect to fluid flow and confirm the SAPs active role in affecting fluid flow in dentine. Further analysis could be undertaken using P₁₁₋₁₄ (positively charged) as a negative control as this would not be expected to interact with the dentine tubule wall. P₁₁₋₈ (negatively charged at physiological pH) could also be assessed which would be expected to interact in a similar manner to P₁₁₋₁₃ with respect to the P₁₁₋₈ interaction with the tubule wall (Maude *et al.*, 2011). Comparisons with the literature are not possible due to the lack of published work relating to this behaviour in dentine studies or more generally in micron size channels. As previously discussed, see section 6.4, the effect of hydrophobic coating on the non-slip condition within microchannel is a poorly understood phenomena and further analysis was not within the scope of this thesis.

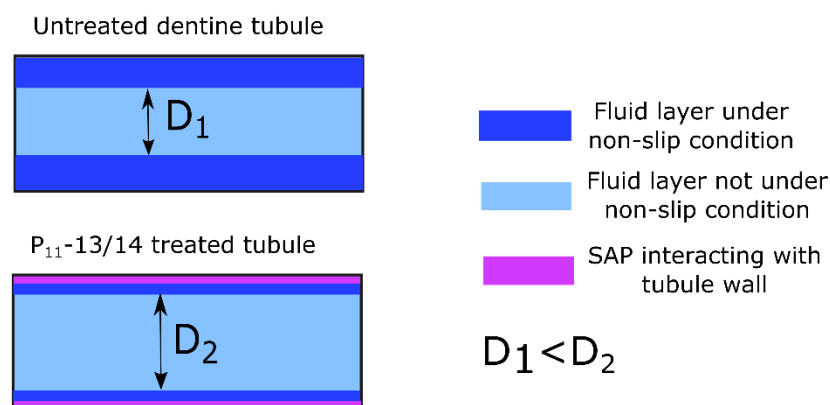


Figure 7-2 Schematic cross section of dentine tubule (not to scale) depicting the hypothesised decrease in non-slip length (dark blue) when hydrophobic SAP layer (magenta) assembles on tubule wall. The increase in diameter of D1 to D2 results in an increase in fluid not under non-slip condition (light blue) which, when under laminar pressure, would result in increased fluid flow.

In contrast to the increase in fluid flow reported for the hybrid material, P₁₁₋₄ proved to be the most effective SAP material in reducing fluid flow through dentine after treatment, producing a statistically significant reduction in fluid flow ($57 \pm 34\%$, n=8) compared to the negative control ($p < 0.05$) after 7 days

incubation in AS solution. SEM examination of the treated dentine samples revealed a lack of any obvious surface deposits and the presence of small needle-like crystals (5 μm) within the dentine tubules some 20 μm from the surface. This observation suggested that the fluid flow reducing properties associated with P₁₁₋₄ treatment were produced by nucleation of crystals *de novo* by the P₁₁₋₄ peptide within the dentine tubule, see Figure 6-13. The formation of these crystals within the dentine tubules suggests that application of P₁₁₋₄ as a monomeric (solution) could be investigated further as a treatment for dentine sensitivity as the deposits could be difficult to remove due to their location within the dentine tubule. The nature of the crystals formed within the dentine tubules by P₁₁₋₄ would need further analysis to be able to draw conclusion with regards to their permanency. The reduction in fluid flow after 7 days incubation in AS is a positive result with regards to the effectiveness of the P₁₁₋₄ treatment but does not confirm its ability over a longer timescale of more than 7 days.

Additionally, the fluid filtration study undertaken in this work does not fully replicate the conditions present in the clinic. One major issue which was not investigated was the positive pressure exerted by open dentine tubules in a “living” tooth. In a “living tooth”, there is a positive pressure exerted by the pulp which results, when the dentine tubules are open, in a constant flow through the dentine tubules in the pulp to dentine surface direction. The treatments in this study were applied to a dentine surface with no fluid pressure applied to the dentine disk model through the tubules, which might have enabled a more efficient diffusion of the P₁₁₋₄ into the dentine tubule when compared to a “living tooth” as the peptide would not have to diffuse against a positive flow of fluid. Application of the P₁₁₋₄ in a clinical trial would be required to determine if the P₁₁₋₄ peptide could diffuse into a dentine tubule, and once there, if it could promote the formation of the crystals seen in the SEM dentine study.

When the fluid filtration results are compared to a similar study presented in the literature, the results of P₁₁₋₄ seem promising. A dentine fluid filtration study reported by Zhong *et al.* (2015) investigated the effect of using novel bioactive glass-ceramic HX-BGC (SiO₂-P₂O₅-CaO-Na₂O-SrO), to reduce dentine tubule permeability after initial application, 1-day submersion in AS solution and after 7

days of daily treatment applications with submersion in AS between treatments. The effectiveness of HX-BCG was assessed, in both its powder form and also as part of a toothpaste formulation, and compared to a control treatment of distilled water and Sensodyne Repair toothpaste which contained the bioglass NovaMin®. The fluid filtration device used was based on the original device produced by Reeder *et al.* (1978) utilising a reservoir of H₂O held at 20 cm above the dentine sample holder to provide a constant pressure.

There are similarities between the study produced by Zhong *et al.* (2015) and the fluid filtration study presented in this thesis which make a comparison between the studies relevant. Both used the fluid filtration method to assess dentine tubule occlusion after initial application and after 7 days incubation at 37 °C in AS solution. Both studies also used 10 dentine disks per treatment group. Although similar, there are some differences in the study methodology used that need to be taken into consideration. The AS solution in the study by Zhong *et al.* was 1.5 mM CaCl₂, 0.9 mM KH₂PO₄, 130 mM KCl, 5 mM NaN₃ and 20 mM HEPES with pH 7.4 (stabilised with NaOH) compared to the AS solution used in this study which was CaCl₂ 0.7 mM, MgCl₂ 0.2 mM, KH₂PO₄ 4 mM, KCl 30 mM and HEPES 20 mM with the pH adjusted to 7 using KOH (Eisenburger *et al.*, 2001). The effect of different AS solutions could have a significant effect on the performance of the test materials due to the availability of ionic calcium and phosphate for HA mineralisation. Another difference was the measurement after 1 day in AS solution which may have had an effect on the resulting dentine permeability measurement at day 7 although this cannot be confirmed without further measurements. Although differences between the 2 study methodologies exist, a comparison of the results seems reasonable. The original results of this study were presented as a percentage of the original flow compared to the initial reading (initial reading being 100%); this has been converted to % reduction to enable comparisons with the fluid filtration study produced in this work and is shown in Table 7-1.

Time point	Distilled H ₂ O control	Sensodyne Repair [®] (Bioglass)	HX-BGC Toothpaste (Bioglass)	HX-BGC Powder (Bioglass)	P₁₁₋₄ monomer treatment
After treatment	12 ± 11.8 %	43.4 ± 10.1 %	51 ± 8.8 %	20.3 ± 11.9 %	12 ± 14%
1 day of AS immersion	27.6 ± 14.1 %	53.9 ± 20.1 %	58.3 ± 16.1 %	59.7 ± 15.8 %	no data
7 days of daily treatment	28 ± 10.7 %	71.7 ± 14 %	78.7 ± 10.1 %	79 ± 9.3 %	57 ± 34 %*

Table 7-1 Dentine fluid filtration measurements (converted into % reduction ± SD) after application of a novel bioglass HX-BGC formulated into a toothpaste and as a powder compared to Sensodyne repair (Novamin[®]) and distilled H₂O control. Treatments were assessed after initial application, 1 day of submersion in AS solution and after 7 days of daily treatment application followed by AS submersion (Zhong *et al.*, 2015). The fluid filtration % reduction for the P₁₁₋₄ monomer treatment produced in this work is shown in bold. * No repeated daily application of P₁₁₋₄ was done after initial application.

When comparing the % reduction in fluid flow for the P₁₁₋₄ treated dentine samples after initial application (12 ± 14 %) to the treatments used in the Zhong *et al.* study (2015), the performance of the bioglass treatments (all above 70%, see Table 7-1) is more effective with respect to their ability to reduce fluid flow. This P₁₁₋₄ treatment was found not to be statistically different to the negative control (20 mM HEPES and 30 mM KCl) in the dentine fluid filtration study in this thesis ($p > 0.05$), and when statistically compared to the bioglass treatments produced significantly lower reductions in fluid flow ($p < 0.05$) which confirms the poor performance of the P₁₁₋₄ monomer treatment after initial application with respect to the reduction of fluid flow through dentine. The limited effectiveness of monomer P₁₁₋₄ on application is not surprising considering it requires time and the availability of ionic calcium and phosphate to allow the mineral nucleating properties of P₁₁₋₄ to promote crystal formation, and so tubule occlusion. When the reduction in fluid flow after 7 days incubation in AS solution of the HX-BGC

toothpaste ($78.7 \pm 10.1\%$), HX-BGC powder ($79 \pm 9.3\%$), and Sensodyne Repair ($71.7 \pm 14\%$) was statistically compared to the P₁₁₋₄ treatment ($57 \pm 34\%$) using an independent t-test it was found that there was no statistical difference between the P₁₁₋₄ treatment and any of the treatment groups listed above ($p < 0.05$). When one considers that the P₁₁₋₄ treatment was applied only once, compared to the daily repeated treatments of the bioglass material over 7 days, then the single application of P₁₁₋₄ treatment produces an impressive decrease in fluid flow after 7 days incubation in AS. The repeated application of the P₁₁₋₄ treatment would be required to determine if any further fluid flow reducing effect could be achieved.

A recent clinical trial compared the assembled P₁₁₋₄ gel formulation Curodont D'Senz (concentration and dispersion medium not stated) to a 8% arginine and calcium carbonate [ACC] toothpaste. Patients in the P₁₁₋₄ gel treatment group were instructed to rub a small amount of P₁₁₋₄ gel treatment on the affected teeth twice a day for 1 week only. The ACC treatment group were instructed to use the ACC toothpaste for the duration of the 90-day trial twice a day. The patients were then assessed using Visual Analogue pain Score (VAS) and Verbal Rating Scale (VRS) pain scores which were recorded over the 90-day study at time points of day 3,7,30,90 (Schlee *et al.*, 2017). Interestingly, no data was collected after the initial treatment application; this could have been an important piece of data as it would have determined if relief from the symptoms of dentine sensitivity was decreased instantly on application. The results from the study determined that both treatment groups experienced an improvement in the VAS and VRS scores as a function of time with no significant difference between the 2 treatment groups at any time point ($p < 0.05$). A significantly higher proportion of subjects in the P₁₁₋₄ treatment group reported that they were pain-free at the 7-day and 90-day time points compared to the ACC treatment group. The finding that the P₁₁₋₄ treatment group experienced the same level of dentine sensitivity symptom suppression upon receiving the application of P₁₁₋₄ treatment for only 7 days, when compared to an effective desensitising toothpaste used for the full 90-day trial, is significant as it suggests that the P₁₁₋₄ treatment is not only effective but also effective over a long period of time after treatment application. A SEM study was undertaken alongside this study and confirmed that the P₁₁₋₄ treatment

produced a layer on the surface of the dentine although it was stated by the author that no evidence of it penetrating down into the tubule was available, see Figure 7-3.

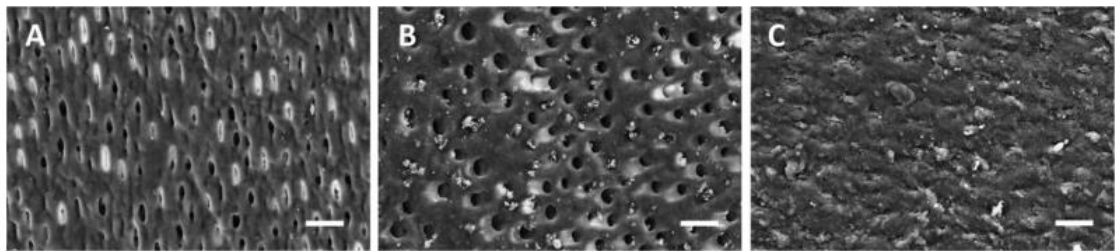


Figure 7-3 SEM images of A) the control dentine disks (after preparation, cleaning and without application of any agents); B) dentine disks treated with ACC toothpaste and C) dentine disks treated with P₁₁₋₄ gel product. Image reproduced with permission from Schlee *et al.* (2017).

The results reported in this thesis, see sections 6.3.3 and 6.3.4, suggested that application of 20 mM P₁₁₋₄ as a monomeric solution onto the surface of exposed and open dentine tubules promoted *de novo* mineralisation inside the dentine tubules, see Figure 6-13, at a distance of 20 μm from the surface. This would resist abrasion by tooth brushing or attrition removing the protective mineralised layer with a consequence of the painful symptoms of dentine sensitivity returning. As such, treatment with P₁₁₋₄ monomer could lack of immediate benefit after initial application which could be improved (see below).

A recent *in vitro* study by Chen *et al.* (2014) investigated the dentine permeability reducing properties of a range of desensitising treatments including Curodont Protect which contained assembled P₁₁₋₄ as its active ingredient. Dentine disks were acid-etched (n=5 per treatment group) and then split in half with one half acting as the control. Treatments were brushed onto the surface of the dentine disks for 2 minutes followed by fluid filtration measurement. The treated samples were compared to the control samples to determine the difference in fluid flow after treatment application. The results showed that the Curodont Protect treated samples had a mean decrease of $55.1 \pm 12.5\%$ which was a significantly larger decrease ($p < 0.05$) than that produced by UltraDex Recalifying and Whitening ($26.4 \pm 7.6\%$) and Colgate Sensitive Pro Relief ($27.6 \pm 6.8\%$). Curodont Protect treated samples were not statistically different to the Sensodyne Repair and

Protect ($64.9 \pm 18.5\%$) or the Sensodyne Rapid relief ($39.1 \pm 17.1\%$) treated samples ($p > 0.05$). This suggests that Curodont Protect is effective at reducing fluid flow in dentine after initial application but, due to the design of the study, does not assess the nucleation and crystal growth potential of Curodont Protect. To assess this, the treated samples would require incubation in an artificial saliva solution so that the active ingredient (P₁₁₋₄) can nucleate and support HA growth over a number of days, as discussed with regards to the Zhong *et al.* (2015) study above. The Chen *et al.* (2014) study only assessed how well the Curodont Protect gel can plug the tubules and prevent fluid flow without the formation of any mineral. That being said, if we compare Curodont Protect's fluid flow reducing properties ($55.1 \pm 12.5\%$, $n=5$) after initial application to the P₁₁₋₄ fluid flow reduction after initial application (12 ± 4 , $n=8$), it appears much more effective on initial application.

The need for a dentine sensitivity treatment to be rapid in action is one of the dentine sensitivity treatment gold standard requirements (Kimura *et al.*, 2000). For this reason, an almost instant alleviation of painful dentine sensitivity should be the goal of any treatment and the P₁₁₋₄ monomer treatment did not achieve this, as determined in this thesis. The issue with the application of P₁₁₋₄ in a monomer form is that it takes time for gelation to occur within the dentine tubule. The kinetics of P₁₁₋₄ have not been studied at short time scales although a self-supporting gel can be achieved within minutes when in a 5 mL glass vial with 5 mL volume. Once gelation has occurred it would take longer for the treatment to nucleate mineral to the extent that a reduction in fluid flow in dentine tubules occurred. The exact kinetics of P₁₁₋₄ nucleation under the conditions used in the fluid filtration study are currently unknown but this study confirmed that after 7 days, the dentine tubules had mineral-like deposits present after P₁₁₋₄ application. A study by Kirkham *et al.* (2007) showed that 15 mg/mL P₁₁₋₄ gels incubated in a mineralising solution produced deposits of poorly crystalline HA throughout the gel after 7 days incubation at 37 °C, similar to the conditions used in this work.

A potential solution to the inability of P₁₁₋₄ monomer to produce immediate results after application to the dentine, which was not tested in this thesis, would

be to combine the application of monomer P₁₁₋₄ solution followed by treatment with Curodont Protect. This could produce an effect similar to the hypothesised mode of action of the E8DS treatment described previously, see section 2.9. This could result in the penetration of P₁₁₋₄ monomer down into the dentine tubules promoting the formation of crystals occluding the tubules seen in this study, while the addition of Curodont Protect (P₁₁₋₄ in its assembled gel state) could provide the instant fluid flow reduction properties and provide dentine surface mineralisation over time.

For any P₁₁₋₄ based dentine sensitivity treatment to become commercially viable, the resulting dentine occlusion would have to be permanent or require infrequent (potentially annually) reapplication due to the associated costs of manufacture and the requirement for clinical application. The application of P₁₁₋₄ (monomeric) treatment is not as simple as a desensitising toothpaste and would require a dental healthcare professional to apply the solution. Previous studies (discussed above) have shown that patients are able to apply the D'senze treatment (this is identical to Curodont Protect and contains P₁₁₋₄ in its assembled gel form) themselves (which, at the time of writing, was € 16.80 per treatment) but the application of a P₁₁₋₄ solution would, due to the cost of treatment and precise application, require clinical application to the affected area. Unless the production of peptide-based treatments significantly decrease in cost through increased usage and become applicable by the patient, frequent application of P₁₁₋₄ may be prohibitively expensive and therefore ineffective compared to the current range of desensitising treatments already on the market. The clinical application of a P₁₁₋₄ solution followed by a repeated patient applied Curodont D'senze gel treatment could potentially be a more economically viable treatment method.

Chapter 8 – Summary and Conclusion

8.1 Summary

The main aim of this thesis was to assess and optimise a novel self-assembling peptide/nanoHA hybrid material with respect to its ability to occlude dentine tubules. The optimisation work was undertaken using the IVNCG while the assessment of the P_{11-13/14} nanoHA hybrid material and P₁₁₋₄ was undertaken using a dentine fluid filtration study.

Hydrothermal synthesis and characterisation of nanoHA was successfully achieved. Optimisation of the nanoHA seeding density in agarose with respect to phosphate mass (indicative of crystal growth) compared to the poly-L-glutamic acid positive control was determined as 30 µg/mL. The IVNCG assay proved capable of reliably determining the minimum nanoHA seeding density required to statistically increase the mass of mineral formed compared to the poly-L-glutamic positive control as 30 µg/mL when seeded in 1% agarose. This seeding density was then taken forward and combined with the self-assembling peptide component to create the hybrid material.

The IVNCG was then used to optimise the hybrid material with respect to its mineralisation potential. In contrast to the nanoHA seeding optimisation experiments, the use of the self-assembling peptide/nanoHA hybrid material in the IVNCG assay was found to be inappropriate and was unable to provide any experimental evidence that the hybrid material was capable of supporting the growth of the nanoHA crystals. Further experimental work using a novel precipitation well plate study suggested that the hybrid material was precipitating out of solution in the hydrogel when exposed to the conditions of the IVNCG assay, with the 6.5 mM concentration of ionic calcium being the main driver of hybrid material precipitation.

The analysis of the hybrid material components using ¹H NMR revealed that the peptide monomer P₁₁₋₁₃ was forming aggregates only under conditions of 6.5 mM ionic calcium and 30 µg/mL nanoHA. It was hypothesised that the formation of this aggregated P₁₁₋₁₃ was the result of surface mediated self-

assembly on the nanoHA seed crystals which resulted in the precipitation of the hybrid material when used in IVNCG experiments. It was concluded that the IVNCG assay technique was unsuitable for the optimisation of the hybrid material.

A dentine fluid filtration study was then undertaken with 2 peptide materials being assessed; the P_{11-13/14} nanoHA hybrid material and P₁₁₋₄, the latter being a known nucleator of HA. The results for the hybrid material 7 days after treatment application and incubation in AS solution showed a significant increase in fluid flow through dentine of $70 \pm 130\%$. The cause of this increase in fluid flow was hypothesised to be due to interaction of the charged face of the P₁₁₋₁₃ peptide monomers with the walls of the dentine tubule. This interaction would be expected to produce a hydrophobic coating on the tubule surface which would result in a compression of the “non-slip” layer. The compression of the “non-slip” layer would, due to the 1-2 μm diameter of the tubule, effectively increase the tubule volume susceptible to fluid flow producing increased dentine permeability.

The results for the P₁₁₋₄ treatment produced a significant $57 \pm 34\%$ reduction in fluid flow through dentine after 7 days incubation in AS solution compared to the negative control ($p < 0.05$). A SEM study concluded that the dentine surface remained clear of any visible mineral deposits but when the dentine samples were split and the tubules imaged, a 10 μm thick layer of crystals was visible 20 μm down the tubule. This suggests that the P₁₁₋₄ peptide is capable of forming mineral inside the dentine tubule; this would be an advantageous place with respect to treating dentine sensitivity due to it being difficult to abrade away through tooth brushing or similar processes. Comparisons with current P₁₁₋₄ based treatments in the literature suggest that the mineral deposition within the dentine tubules below the dentine surface is a new finding not previously seen in the use of P₁₁₋₄. The ability of monomer P₁₁₋₄ to penetrate the dentine tubules and promote sub-surface crystal growth makes it a candidate for further investigation and opens up the possibility of potentially combining it with Curodont D'Senze (gel-based P₁₁₋₄ desensitising agent) which has shown to decrease dentine permeability and promote dentine surface mineralisation

although lacks tubule penetration. Together, these 2 treatments could offer both immediate and enduring benefits for the treatment of dentine sensitivity.

8.2 Future work

- Determine if the IVNCG has the potential to be used as a high throughput for the assessment and optimisation of mineral nucleation and crystal growth with respect to other dentine sensitivity treatments that aim to produce mineral deposits to occlude dentine tubules. Further experiments with materials which can function in the IVNCG conditions would be required to test this.
- The use of P_{11-13/14} as a material for the support of hydroxyapatite crystal growth requires further analysis to determine the interaction of the peptide material with hydroxyapatite. No crystal growth supporting effect was seen in any technique used in this thesis.
- Although the results of this thesis suggest that P₁₁₋₁₃ may not be suitable for the applications described here due to its interaction with crystal surfaces and effect of increasing fluid flow through the dentine channels, it may be a candidate for use in other applications, for example as a potential internal coating for micro catheters and indwelling peripheral intravenous cannulae or as a mineral stabiliser/inhibitor of calcification. Surface modification chemistries for attachment of the P₁₁₋₁₃ peptide to the required surface would have to be investigated.
- Further analysis of the P₁₁₋₄ treatment on dentine. Multiple time points, for example testing every day, would provide more insight into how the P₁₁₋₄ treatment develops over time with respect to fluid flow reduction and mineralisation and provide insight in to mineralisation kinetics.
- Possible combination of P₁₁₋₄ treatment in a monomer state followed by application of self-assembled P₁₁₋₄ treatment may produce a dual effect of producing mineral deposits in the dentine tubule and promoting surface mineralisation. This hypothetical treatment could be investigated using the fluid filtration device.

8.3 Conclusion

In conclusion, this study has determined that the SAP/nanoHA hybrid material treatment was ineffective at reducing dentine permeability but has revealed new insight into the interaction of the individual peptides with calcium ions and HA crystal surfaces, as well as illustrating potential applications for P₁₁₋₁₃ in facilitating fluid flow in micro-channels. The P₁₁₋₄ treatment was shown to be effective in reducing dentine permeability 7 days after application and may be a promising candidate for further development as a dentine sensitivity treatment. Clinical trials would be needed to fully assess the effectiveness of the P₁₁₋₄ treatment with respect to treating dentine sensitivity.

Chapter 9 – Bibliography

- Abidi, S.S.A. and Murtaza, Q. 2014. Synthesis and Characterization of Nano-hydroxyapatite Powder Using Wet Chemical Precipitation Reaction. *Journal of Materials Science & Technology*. **30**(4), pp.307–310.
- Addy, M. and Dowell, P. 1983a. Dentine hypersensitivity - A review Aetiology, symptoms and theories of pain production. *Journal of Clinical Periodontology*. **10**(4), pp.341–350.
- Addy, M. and Dowell, P. 1983b. Dentine hypersensitivity- A review. Clinical and in vitro evaluation of treatment agents. *Journal of Clinical Periodontology*. **10**(4), pp.351–63.
- Addy, M. and Peace, N. 1994. Aetiological, Predisposing and Environmental Factors in Dentine Hypersensitivity. *Archives of Oral Biology*. **39**, p.33s–38s.
- Afshar, A., Ghorbani, M., Ehsani, N., Saeri, M.R. and Sorrell, C.C. 2003. Some important factors in the wet precipitation process of hydroxyapatite. *Materials Letters*. **57**(24–25), pp.4064–4069.
- Aggeli, A., Bell, M., Boden, N., Carrick, L.M. and Strong, A.E. 2003a. Self-Assembling Peptide Polyelectrolyte β -Sheet Complexes Form Nematic Hydrogels. *Angewandte Chemie - International Edition*. **42**(45), pp.5603–5606.
- Aggeli, A., Bell, M., Boden, N., Keen, J.N., Knowles, P.F., McLeish, T.C., Pitkeathly, M. and Radford, S.E. 1997. Responsive gels formed by the spontaneous self-assembly of peptides into polymeric β -sheet tapes. *Nature*. **386**(6622), pp.259–262.
- Aggeli, A., Bell, M., Carrick, L.M., Fishwick, C.W.G., Harding, R., Mawer, P.J., Radford, S.E., Strong, A.E. and Boden, N. 2003b. pH as a Trigger of Peptide β -Sheet Self-Assembly and Reversible Switching between Nematic and Isotropic Phases. *Journal of the American Chemical Society*. **125**(32), pp.9619–9628.

- Aggeli, A., Nyrkova, I.A., Bell, M., Harding, R., Carrick, L., McLeish, T.C.B., Semenov, A.N. and Boden, N. 2001. Hierarchical self-assembly of chiral rod-like molecules as a model for peptide β -sheet tapes, ribbons, fibrils, and fibers. *Proceedings of the National Academy of Sciences of the United States of America*. **98**(21), pp.11857–62.
- Al-Jadaa, A., Attin, T., Peltomäki, T., Heumann, C. and Schmidlin, P.R. 2014. Laboratory validation of a new gas-enhanced dentine liquid permeation evaluation system. *Clinical Oral Investigations*. **18**, pp.2067–2075.
- Anderson, H.C. 1995. Molecular Biology of Matrix Vesicles. *Clinical Orthopaedics and Related Research*. (314), pp.266–80.
- Ang, S.F., Saadatmand, M., Swain, M. V., Klocke, A. and Schneider, G.A. 2012. Comparison of mechanical behaviors of enamel rod and interrod regions in enamel. *Journal of Materials Research*. **27**(02), pp.448–456.
- Arana-Chavez, V.E. and Katchburian, E. 1998. Freeze-fracture studies of the distal plasma membrane of rat odontoblasts during their differentiation and polarisation. *European Journal of Oral Sciences*. **106**(S1), pp.132–136.
- Arana-Chavez, V.E. and Massa, L.F. 2004. Odontoblasts: the cells forming and maintaining dentine. *The International Journal of Biochemistry & Cell Biology*. **36**(8), pp.1367–73.
- Ash, A., Mulholland, F., Burnett, G.R. and Wilde, P.J. 2014. Structural and compositional changes in the salivary pellicle induced upon exposure to SDS and STP. *Biofouling*. **30**(10), pp.1183–1197.
- Avery, J.K. and Rapp, R. 1958. Demonstration of Cholinesterase in Teeth. *Stain Technology*. **33**(1), pp.31–37.
- Ayad, F., Ayad, N., Zhang, Y.P., DeVizio, W., Cummins, D. and Mateo, L.R. 2009. Comparing the Efficacy in Reducing Dentin Hypersensitivity of a New Toothpaste Containing 8.0% Arginine, Calcium Carbonate, and 1450 ppm Fluoride to a Commercial Sensitive Toothpaste Containing 2% Potassium Ion: An Eight-Week Clinical Study on Canadian Adult. *Journal of Clinical Dentistry*. **20**(1), pp.10–16.

- Bar-Cohen, Y. 2006a. Introduction to Biomimetics *In*: Y. Bar-Cohen, ed. *Biomimetics* [Online]. Boca Raton: CRC Press, pp.1–40. Available from: <http://dx.doi.org/10.1201/9781420037715.ch1>.
- Bar-Cohen, Y. 2006b. Biomimetics--using nature to inspire human innovation. *Bioinspiration & Biomimetics*. **1**(1), pp.P1–P12.
- Bartold, P.M. 2006. Dentinal hypersensitivity: a review. *Australian Dental Journal*. **51**(3), pp.212–8.
- Beddis, H., Soneji, P., Welford, S. and Ashley, M. 2013. Making Sense of Sensitivity. *Dental update*. **40**(5), pp.403–4, 406–8, 411.
- Beer, P., Gale, P. and Smith, D. 2003. *Supramolecular Chemistry* 1st ed. (J. Evans, ed.). Oxford: Oxford University Press.
- Bello, O.S., Adegoke, K.A. and Oyewole, R.O. 2013. Biomimetic Materials in Our World : A Review. *IOSR Journal of Applied Chemistry*. **5**(3), pp.22–35.
- Berzina-cimdina, L. and Borodajenko, N. 2012. Research of Calcium Phosphates Using Fourier Transform Infrared Spectroscopy *In*: T. Theophile, ed. *Infrared Spectroscopy - Materials Science, Engineering and Technology*. InTech, pp.123–148.
- Bhattacharjee, S. 2016. DLS and zeta potential - What they are and what they are not? *Journal of Controlled Release*. **235**, pp.337–351.
- Bhattacharyya, J., Bellucci, J., Weitzhandler, I., McDaniel, J., Spasojevic, I., Li, X., Lin, C., Chi, J. and Chilkoti, A. 2016. A Paclitaxel-Loaded Recombinant Polypeptide Nanoparticle Outperforms Abraxane in Multiple Murine Cancer Models. *Nature Communications*. **6**.
- Bilton, M., Brown, A.P. and Milne, S.J. 2010. Sol-gel synthesis and characterisation of nano-scale hydroxyapatite. *Journal of Physics: Conference Series*. **241**.
- Biondi, M., Ungaro, F., Quaglia, F. and Netti, P.A. 2008. Controlled drug delivery in tissue engineering. *Advanced Drug Delivery Reviews*. **60**(2), pp.229–242.

- Boskey, A.L. 1989. Hydroxyapatite Formation In A Dynamic Collagen Gel System - Effects Of Type-I Collagen, Lipids, And Proteoglycans. *Journal of Physical Chemistry*. **93**(4), pp.1628–1633.
- Boskey, A.L. 2003. Biomineralization: An Overview. *Connective Tissue Research*. **44**(1), pp.5–9.
- Boskey, A.L., Spevak, L., Tan, M., Doty, S.B. and Butler, W.T. 2000. Dentin Sialoprotein (DSP) Has Limited Effects on In Vitro Apatite Formation and Growth. *Calcified Tissue International*. **67**(6), pp.472–478.
- Boyde, A. 1967. The Development of Enamel Structure. *Journal of the Royal Society of Medicine*. **60**, pp.923–928.
- Bragg, W.L. 1913. The structure of some crystals as indicated by their diffraction of X-rays *In: Proceedings of the Royal Society of London. Series A, Containing Papers of a Mathematical and Physical Character.*, pp.248–277.
- Brannstrom, M. 1963. A hydrodynamic mechanism in the transmission of pain-producing stimuli through the dentine *In: D. J. Anderson, ed. Sensory Mechanisms In Dentine*. Oxford: Pergamon Press LTD., pp.73–79.
- Brown, W.E., Eidelman, N. and Tomazic, B. 1987. Octacalcium Phosphate as a Precursor in Biomineral Formation. *Advances in Dental Research*. **1**(2), pp.306–313.
- Brunton, P.A., Davies, R.P.W., Burke, J.L., Smith, A., Aggeli, A., Brookes, S.J. and Kirkham, J. 2013. Treatment of early caries lesions using biomimetic self-assembling peptides--a clinical safety trial. *British Dental Journal*. **215**(4), p.E6.
- Buonocore, M.G. and Bibby, B.G. 1945. The Effects of Various Ions on Enamel Solubility. *Journal of Dental Research*. (1), pp.103–108.
- Cao, Y., Liu, W., Ning, T., Mei, M.L., Li, Q.-L., Lo, E.C.M. and Chu, C.H. 2014. A novel oligopeptide simulating dentine matrix protein 1 for biomimetic mineralization of dentine. *Clinical Oral Investigations*. **18**(3), pp.873–81.

- Carlson, J., Ghaey, S., Moran, S., Tran, C.A., Kaplan, D.L., Moran, S. and Tran, C.A. 2006. Biological Materials in Engineering Mechanisms *In*: Y. Bar-Cohen, ed. *Biomimetics* [Online]. Boca Raton: CRC Press, pp.365–379. Available from: <http://dx.doi.org/10.1201/9781420037715.ch14>.
- Carrick, L.M., Aggeli, A., Boden, N., Fisher, J., Ingham, E. and Waigh, T.A. 2007. Effect of ionic strength on the self-assembly, morphology and gelation of pH responsive β -sheet tape-forming peptides. *Tetrahedron*. **63**(31), pp.7457–7467.
- Celata, G.Pi. 2004. Single-Phase Heat Transfer and Fluid Flow in Micropipes. *Heat Transfer Engineering*. **25**(3), pp.13–22.
- Cengiz, B., Gokce, Y., Yildiz, N., Aktas, Z. and Calimli, A. 2008. Synthesis and characterization of hydroxyapatite nanoparticles. *Colloids and Surfaces A: Physicochemical and Engineering Aspects*. **322**(1–3), pp.29–33.
- Chabanski, M.B. 1996. Prevalence of cervical dentine sensitivity in a population of patients referred to a specialist Periodontology Department. *Journal of Clinical Periodontology*. **23**(11), pp.989–992.
- Chabanski, M.B., Gillam, D.G., Bulman, J.S. and Newman, H.N. 1997. Clinical evaluation of cervical dentine sensitivity in a population of patients referred to a specialist periodontology department: a pilot study. *Journal of Oral Rehabilitation*. **24**(9), pp.666–72.
- Chen, P.S., Toribara, T.Y. and Warner, H. 1956. Microdetermination of Phosphorus. *Analytical Chemistry*. **28**(11), pp.1756–1758.
- Chen, X., Gillam, D.G., Mustafa, H., Lysek, D. and Hill, R.G. 2014. Dentine Tubule Occlusion of a Novel Self-assembling Peptide Containing Gel *In*: *2014 IADR/AMER General Session (Cape Town, South Africa)* [Online]. Cape Town, South Africa. [Accessed 4 August 2018]. Available from: <https://iadr.abstractarchives.com/abstract/14iags-188913/dentine-tubule-occlusion-of-a-novel-self-assembling-peptide-containing-gel>.
- Chrysanthakopoulos, N.A. 2011. Prevalence of Dentine Hypersensitivity in a General Dental Practice in Greece. *Journal of Clinical and Experimental Dentistry*. **33**(55), pp.445–51.

- Clayton, D.R., McCarthy, D. and Gillam, D.G. 2002. A study of the prevalence and distribution of dentine sensitivity in a population of 17-5 8-year-old serving personnel on an RAF base in the Midlands. *Journal of Oral Rehabilitation*. **29**(1), pp.14–23.
- Cochrane, N.J., Cai, F., Huq, N.L., Burrow, M.F. and Reynolds, E.C. 2010. New Approaches to Enhanced Remineralization of Tooth Enamel. *Journal of Dental Research*. **89**(11), pp.1187–97.
- Cornelisse, C.J. and van Duijn, P. 1973. A New Method for the Investigation of the Kinetics of the Capture Reaction in Phosphatase Cytochemistry. ii. Theoretical and Experimental Study Of Phosphate Diffusion from Thin Polyacrylamide Films. *The Journal of Histochemistry & Cytochemistry*. **21**(7), pp.614–622.
- Cunha-Cruz, J., Stout, J.R., Heaton, L.J. and Wataha, J.C. 2011. Dentin Hypersensitivity and Oxalates: a Systematic Review. *Journal of Dental Research*. **90**(3), pp.304–10.
- Cushing, B.L., Kolesnichenko, V.L. and O'Connor, C.J. 2004. Recent Advances in the Liquid-Phase Syntheses of Inorganic Nanoparticles. *Chemical Reviews*. **104**(9), pp.3893–3946.
- Dababneh, R.H., Khouri, A.T. and Addy, M. 1999. Dentine hypersensitivity — an enigma ? a review of terminology, epidemiology, mechanisms, aetiology and management. *British Dental Journal*. **187**(11), pp.606–611.
- Daculsi, G. and Kerebel, B. 1978. High-resolution electron microscope study of human enamel crystallites: size, shape, and growth. *Journal of Ultrastructure Research*. **65**(2), pp.163–172.
- Daculsi, G., Menanteau, J., Kerebel, L.M. and Mitre, D. 1984. Length and Shape of Enamel Crystals. *Calcified Tissue International*. **36**(1), pp.550–555.
- Dahl, E. and Mjör, I.A. 1973. The structure and distribution of nerves in the pulp-dentin organ. *Acta Odontologica Scandinavica*. **31**(6), pp.349–356.

- Davey, R. and Garside, J. 2000a. Nucleation *In*: R. Compton, S. Davies, J. Evans and L. Gladden, eds. *From Molecules to Crystallizers*. Oxford: Oxford University Press, pp.15–25.
- Davey, R. and Garside, J. 2000b. Crystal Growth *In*: R. Compton, S. Davies, J. Evans and L. Gladden, eds. *From Molecules to Crystallizers*. Oxford: Oxford University Press, pp.26–35.
- Davies, R.P.W., Aggeli, A., Beevers, A., Boden, N., Carrick, L.M., Fishwick, C.W.G., McLeish, T.C.B., Nyrkova, I. and Semenov, A.N. 2006. Self-assembling β -Sheet Tape Forming Peptides. *Supramolecular Chemistry*. **18**(5), pp.435–443.
- Day, M.A. 1990. The No-Slip Condition of Fluid Dynamics. *Erkenntnis*. **33**(3), pp.285–296.
- Deshpande, A.S., Fang, P.A., Zhang, X., Jayaraman, T., Sfeir, C. and Beniash, E. 2011. Primary Structure and Phosphorylation of Dentin Matrix Protein 1 (DMP1) and Dentin Phosphophoryn (DPP) Uniquely Determine Their Role in Biomineralization. *Biomacromolecules*. **12**(8), pp.2933–2945.
- Dimuzio, M.T. and Veis, A. 1978. The Biosynthesis of Phosphophoryns and Dentin Collagen in the Continuously Erupting Rat Incisor. *Journal of Biological Chemistry*. **253**(19), pp.6845–6852.
- Dogan, S., Fong, H., Yucesoy, D.T., Cousin, T., Gresswell, C., Dag, S., Huang, G. and Sarikaya, M. 2018. Biomimetic Tooth Repair: Amelogenin-Derived Peptide Enables in Vitro Remineralization of Human Enamel. *ACS Biomaterials Science and Engineering*. **4**(5), pp.1788–1796.
- Dorozhkin, S. V 2010. Nanosized and nanocrystalline calcium orthophosphates. *Acta biomaterialia*. **6**(3), pp.715–34.
- Dorvee, J.R., Boskey, A.L. and Estroff, L.A. 2012. Rediscovering Hydrogel-Based Double-Diffusion Systems for Studying Biomineralization. *CrystEngComm*. **14**(18), pp.5681–5700.

- Du, C., Falini, G., Fermani, S., Abbott, C. and Moradian-Oldak, J. 2005. Supramolecular Assembly of Amelogenin Nanospheres into Birefringent Microribbons. *Science*. **307**(5714), pp.1450–1454.
- Durucan, C. and Brown, P.W. 2000. Alpha-Tricalcium phosphate hydrolysis to hydroxyapatite at and near physiological temperature. *Journal of Material Science*. **1**(11), pp.365–371.
- Dykstra, M.J. and Reuss, L.E. 2003. Transmission Electron Microscopy *In: Biological Electron Microscopy Theory, Techniques, and Troubleshooting*. New York: Kluwer Academic/Plenum Publishers, pp.287–322.
- Earl, J.S. 2007. *Hydroxyapatite Nanoparticles and Dentine Tubule Infiltration*. Ph.D Thesis, The Univeristy of Leeds.
- Earl, J.S., Wood, D.J. and Milne, S.J. 2006a. Hydrothermal synthesis of hydroxyapatite. *Journal of Physics: Conference Series*. **26**, pp.268–271.
- Earl, J.S., Wood, D.J. and Milne, S.J. 2006b. Dentine Infiltration - A Cure For Sensitive Teeth. *American Ceramic Society Bulletin*. **85**(7), pp.22–25.
- Eastoe, J.E. 1960. Organic Matrix of Tooth Enamel. *Nature*. **187**, pp.411–412.
- Eisenburger, M., Addy, M., Hughes, J.A. and Shellis, R.P. 2001. Effect of Time on the Remineralisation of Enamel by Synthetic Saliva after Citric Acid Erosion. *Caries Research*. **35**(3), pp.211–215.
- Eisenmann, D.R. and Glick, P.L. 1972. Ultrastructure of Initial Crystal Formation in Dentin. *Journal of Ultrastructure Research*. **41**(1–2), pp.18–28.
- Eldarrat, A.H., High, A.S. and Kale, G.M. 2004. In vitro analysis of ‘smear layer’ on human dentine using ac-impedance spectroscopy. *Journal of Dentistry*. **32**(7), pp.547–54.
- Elliott, J.C., Holcomb, D.W. and Young, R.A. 1985. Infrared determination of the degree of substitution of hydroxyl by carbonate ions in human dental enamel. *Calcified Tissue International*. **37**(4), pp.372–375.

- Ertürk, M.S.O. and Kirzioğlu, Z. 2007. In vitro evaluation of dentin permeability of fluorotic primary teeth with a new electronic hydraulic conductance measurement system with photosensors. *Archives of Oral Biology*. **52**(11), pp.1057–63.
- Fan, T., Yu, X., Shen, B. and Sun, L. 2017. Peptide Self-Assembled Nanostructures for Drug Delivery Applications. *Journal of Nanomaterials*. **2017**.
- Fathi, M.H., Hanifi, A. and Mortazavi, V. 2008. Preparation and bioactivity evaluation of bone-like hydroxyapatite nanopowder. *Journal of Materials Processing Technology*. **202**(1–3), pp.536–542.
- Fearnhead, R.W. 1957. Histological Evidence for the Innervation of Human Dentine. *Journal of Anatomy*. **91**(2), pp.267–77.
- Featherstone, J.D.B. 1999. Prevention and reversal of dental caries: Role of low level fluoride. *Community Dentistry and Oral Epidemiology*. **27**(1), pp.31–40.
- Fincham, A.G., Moradian-Oldak, J. and Simmer, J.P. 1999. The structural biology of the developing dental enamel matrix. *Journal Of Structural Biology*. **126**(3), pp.270–99.
- Flynn, J., Galloway, R. and Orchardson, R. 1985. The incidence of 'hypersensitive' teeth in the West of Scotland. *Journal of Dentistry*. (3), pp.230–236.
- Fukumoto, S., Kiba, T., Hall, B., Iehara, N., Nakamura, T., Longenecker, G., Krebsbach, P.H., Nanci, A., Kulkarni, A.B. and Yamada, Y. 2004. Ameloblastin is a cell adhesion molecule required for maintaining the differentiation state of ameloblasts. *The Journal of Cell Biology*. **167**(5), pp.973–83.
- Gazitaeva, Z.I., Drobintseva, A.O., Chung, Y., Polyakova, V.O. and Kvetnoy, I.M. 2017. Cosmeceutical product consisting of biomimetic peptides: Antiaging effects in vivo and in vitro. *Clinical, Cosmetic and Investigational Dermatology*. **10**, pp.11–16.

- George, A. and Ravindran, S. 2010. Protein templates in hard tissue engineering. *Nano Today*. **5**(4), pp.254–266.
- Gibson, C.W., Golub, E., Ding, W., Shimokawa, H., Young, M., Termine, J. and Rosenbloom, J. 1991. Identification of the Leucine-Rich Amelogenin Peptide (LRAP) as the Translation Product of an Alternatively Spliced Transcript. *Biochemical and Biophysical Research Communications*. **174**(3), pp.1306–1312.
- Gillam, D.G., Aris, A., Newman, H., Ley, F., Swern, A., Friedman, M. and Curro, F. 2018. Clinical Evaluation of A 5% Potassium Nitrate Containing Mouthrinse in Relieving Dentine Hypersensitivity (DH). *Bio Accent Open Access Journal Dentistry*. **4**(1), p.039.
- Gillam, D.G., Bulman, J.S., Jackson, R.J. and Newman, H.N. 1996. Efficacy of a potassium nitrate mouthwash in alleviating cervical dentine sensitivity (CDS). *Journal of Periodontology*. **23**(11), pp.993–7.
- Gillam, D.G., Mordan, N.J. and Newman, H.N. 1997. The Dentin Disc Surface: A Plausible Model for Dentin Physiology and Dentin Sensitivity Evaluation. *Advances in Dental Research*. **11**(4), pp.487–501.
- Gillam, D.G., Mordan, N.J., Sinodinou, A.D., Tang, J.Y., Knowles, J.C. and Gibson, I.R. 2001. The effects of oxalate-containing products on the exposed dentine surface: an SEM investigation. *Journal of Oral Rehabilitation*. **28**(11), pp.1037–1044.
- Goldberg, H.A., Warner, K.J., Li, M.C. and Hunter, G.K. 2001. Binding of Bone Sialoprotein, Osteopontin and Synthetic Polypeptides to Hydroxyapatite. *Connective Tissue Research*. **42**(1), pp.25–37.
- Goldberg, M., Kulkarni, A.B., Young, M. and Boskey, A.L. 2011. Dentin: Structure, Composition and Mineralization: The role of dentin ECM in dentin formation and mineralization. *Frontiers in Bioscience (Elite Edition)*. **3**, pp.711–735.
- Goldberg, M. and Takagi, M. 1993. Dentine proteoglycans: composition, ultrastructure and functions. *The Histochemical Journal*. **25**(11), pp.781–806.

- Gotjamanos, T. 1969. Cellular Organization in the Subodontoblastic Zone of the Dental Pulp—I: A Study of Cell-Free and Cell-Rich Layers in Pulps of Adult Rat and Deciduous Monkey Teeth. *Archives of Oral Biology*. **14**(9), pp.1007–1010.
- Greenhill, J.D. and Pashley, D.H. 1981. The Effects of Desensitizing Agents on the Hydraulic Conductance of Human Dentin in vitro. *Journal of Dental Research*. **60**(3), pp.686–698.
- Gronthos, S., Mankani, M., Brahim, J., Robey, P.G. and Shi, S. 2000. Postnatal human dental pulp stem cells (DPSCs) in vitro and in vivo. *Proceedings of the National Academy of Sciences of the United States of America*. **97**(25), pp.13625–30.
- Gungormus, M., Fong, H., Kim, I.W., Evans, J.S., Tamerler, C. and Sarikaya, M. 2008. Regulation of in vitro Calcium Phosphate Mineralization by Combinatorially Selected Hydroxyapatite-Binding Peptides. *Biomacromolecules*. **9**(3), pp.966–973.
- Guo, C. and McMartin, K.E. 2005. The cytotoxicity of oxalate, metabolite of ethylene glycol, is due to calcium oxalate monohydrate formation. *Toxicology*. **208**(3), pp.347–355.
- Gwinnett, A.J. 1966. The Ultrastructure of the “Prismless” of Deciduous Teeth Enamel. *Archives of Oral Biology*. **11**, pp.1109–1115.
- Haefeli, M. and Elfering, A. 2006. Pain assessment. *European Spine Journal*. **15**(SUPPL. 1), pp.17–24.
- Hartgerink, J.D., Beniash, E. and Stupp, S.I. 2001. Self-Assembly and Mineralization of Peptide-Amphiphile Nanofibers. *Science (New York, N.Y.)*. **294**(5547), pp.1684–1688.
- Hartgerink, J.D., Granja, J.R., Milligan, R.A. and Ghadiri, M.R. 1996. Self-Assembling Peptide Nanotubes. *Journal of the American Chemical Society*. **118**(1), pp.43–50.

- Hashim, N.T., Gasmalla, B.G., Sabahelkheir, A.H. and Awooda, A.M. 2014. Effect of the clinical application of the diode laser (810 nm) in the treatment of dentine hypersensitivity. *BMC research notes*. **7**, p.31.
- Hatip Koc, M., Cinar Ciftci, G., Baday, S., Castelletto, V., Hamley, I.W. and Guler, M.O. 2017. Hierarchical Self-Assembly of Histidine-Functionalized Peptide Amphiphiles into Supramolecular Chiral Nanostructures. *Langmuir*. **33**, pp.7947–7956.
- He, G., Dahl, T., Veis, A. and George, A. 2003. Nucleation of apatite crystals in vitro by self-assembled dentin matrix protein 1. *Nature materials*. **2**(8), pp.552–8.
- He, G. and George, A. 2004. Dentin Matrix Protein 1 Immobilized on Type I Collagen Fibrils Facilitates Apatite Deposition in Vitro. *Journal of Biological Chemistry*. **279**(12), pp.11649–11656.
- Heasman, P.A., Ritchie, M., Asuni, A., Gavillet, E., Simonsen, J.L. and Nyvad, B. 2017. Gingival recession and root caries in the ageing population: a critical evaluation of treatments. *Journal of Clinical Periodontology*. **44**, pp.S178–S193.
- Hench, L.L. 1991. Bioceramics: From Concept to Clinic. *Journal of the American Ceramic Society*. **74**(7), pp.1487–1510.
- Hill, R.G., Chen, X. and Gillam, D.G. 2015a. In Vitro Ability of a Novel Nanohydroxyapatite Oral Rinse to Occlude Dentine Tubules. *International Journal of Dentistry*. **2015**, p.7.
- Hill, R.G. and Gillam, D.G. 2015. Future Strategies for the Development of Desensitising Products *In: D. Gillam, ed. Dentine Hypersensitivity: Advances in Diagnosis, Management, and Treatment*. Hiedelberg: Springer, pp.157–181.
- Hill, R.G., Gillam, D.G. and Chen, X. 2015b. The ability of a nano hydroxyapatite toothpaste and oral rinse containing fluoride to protect enamel during an acid challenge using ¹⁹F solid state NMR spectroscopy. *Materials Letters*. **156**, pp.69–71.

- Hiller, K.-A., Buchalla, W., Grillmeier, I., Neubauer, C. and Schmalz, G. 2018. In vitro effects of hydroxyapatite containing toothpastes on dentin permeability after multiple applications and ageing. *Scientific Reports*. **8**(1), p.4888.
- Hodosh, M. 1974. A superior desensitizer — potassium nitrate. *The Journal of the American Dental Association*. **88**(4), pp.831–832.
- Holland, G.R., Narhi, M.N., Addy, M., Gangarosa, L. and Orchardson, R. 1997. Guidelines for the design and conduct of clinical trials on dentine hypersensitivity. *Journal of Clinical Periodontology*. **24**(11), pp.808–13.
- Homma, K. 1990. Historical studies on the striae of Hunter-Schreger. *Dentistry in Japan*. **27**(1), pp.141–145.
- Housecroft, C.E. and Sharpe, A.G. 2008. Structures and energetics of metallic and ionic solids *In: Inorganic Chemistry*. London: Pearson Education Limited, pp.148–180.
- Hu, J.C.-C., Hu, Y., Lu, Y., Smith, C.E., Lertlam, R., Wright, J.T., Suggs, C., McKee, M.D., Beniash, E., Kabir, M.E. and Simmer, J.P. 2014. Enamelin Is Critical for Ameloblast Integrity and Enamel Ultrastructure Formation. *PLOS One*. **9**(3), p.e89303.
- Huang, S.B., Gao, S.S. and Yu, H.Y. 2009. Effect of nano-hydroxyapatite concentration on remineralization of initial enamel lesion in vitro. *Biomedical Materials*. **4**(3), p.034104.
- Hunter, G.K. and Goldberg, H.A. 1993. Nucleation of hydroxyapatite by bone sialoprotein. *Proceedings of the National Academy of Sciences of the United States of America*. **90**(18), pp.8562–8565.
- Hunter, G.K. and Goldberg, H.A. 1994. Modulation of crystal formation by bone phosphoproteins: role of glutamic acid-rich sequences in the nucleation of hydroxyapatite by bone sialoprotein. *The Biochemical Journal*. **302**, pp.175–179.
- Hunter, G.K., Grynpas, M.D., Cheng, P.T. and Pritzker, K.P.H. 1987. Effect of Glycosaminoglycans on Calcium Pyrophosphate Crystal Formation in Collagen Gels. *Calcified Tissue International*. **41**(3), pp.164–170.

- Hunter, G.K., Hauschka, P.V., Poole, A.R., Rosenberg, L.C. and Goldberg, H.A. 1996. Nucleation and inhibition of hydroxyapatite formation by mineralized tissue proteins. *The Biochemical Journal*. **317** (Pt 1, pp.59–64.
- Ide, M., Wilson, R.F. and Ashley, F.P. 2001. The reproducibility of methods of assessment for cervical dentine hypersensitivity. *Journal of Periodontology*. **28**(1), pp.16–22.
- Iggland, M. and Mazzotti, M. 2012. Population Balance Modeling with Size-Dependent Solubility: Ostwald Ripening. *Crystal Growth and Design*. **12**(3), pp.1489–1500.
- Iijima, M., Moriwaki, Y., Takagi, T. and Moradian-Oldak, J. 2001. Effects of bovine amelogenins on the crystal morphology of octacalcium phosphate in a model system of tooth enamel formation. *Journal of Crystal Growth*. **222**(3), pp.615–626.
- Imbeni, V., Kruzic, J.J., Marshall, G.W., Marshall, S.J. and Ritchie, R.O. 2005. The dentin-enamel junction and the fracture of human teeth. *Nature Materials*. **4**(3), pp.229–232.
- Ireland, R. 2006. *Clinical textbook of dental hygiene and therapy* [Online]. Blackwell Publishing. [Accessed 16 June 2014]. Available from: <https://www.dawsonera.com/readonline/9781405171861/startPage/15#>.
- Jahromi, M.T., Yao, G. and Cerruti, M. 2013. The importance of amino acid interactions in the crystallization of hydroxyapatite. *Journal of the Royal Society, Interface*. **10**(80), p.20120906.
- Johnson, G. and Brännström, M. 1974. The sensitivity of dentin changes in relation to conditions at exposed tubule apertures. *Acta Odontologica Scandinavica*. **32**(1), pp.29–38.
- De Jong, A.S., Hak, T.J. and van Duijn, P. 1980. The Dynamics of Calcium Phosphate Precipitation Studied with a New Polyacrylamide Steady State Matrix-Model: Influence of Pyrophosphate, Collagen and Chondroitin Sulfate. *Connective Tissue Research*. **7**(2), pp.73–79.

- De Jong, A.S., Hak, T.J., van Duijn, P. and Daems, W.T. 1978. New Dynamic-Model System for Study of Capture Reactions for Diffusible Compounds in Cytochemistry I. Description of Model with Special Attention to Phosphate Capture in Acid-Phosphatase Cytochemistry. *Journal of Histochemistry & Cytochemistry*. **26**(5), pp.331–339.
- Kaasalainen, M., Aseyev, V., von Haartman, E., Karaman, D.Ş., Mäkilä, E., Tenhu, H., Rosenholm, J. and Salonen, J. 2017. Size, Stability, and Porosity of Mesoporous Nanoparticles Characterized with Light Scattering. *Nanoscale Research Letters*. **12**(1).
- Karim, B.F. and Gillam, D.G. 2013. The Efficacy of Strontium and Potassium Toothpastes in Treating Dentine Hypersensitivity: A Systematic Review. *International Journal of Dentistry*. **2013**, p.573258.
- Kay, M.I., Young, R.A. and Posner, A.S. 1964. Crystal Structure of Hydroxyapatite. *Nature*. **204**, pp.1050–1052.
- Kerebel, B., Daculsi, G. and Kerebel, L.M. 1979. Ultrastructural Studies of Enamel Crystallites. *Journal of Dental Research*. **58**(Spec Issue B), p.844–51.
- Kimura, Y., Wilder-Smith, P., Yonaga, K. and Matsumoto, K. 2000. Treatment of dentine hypersensitivity by lasers: a review. *Journal of Clinical Periodontology*. **27**(10), pp.715–21.
- Kirkham, J., Firth, A., Vernals, D., Boden, N., Robinson, C., Shore, R.C., Brookes, S.J. and Aggeli, A. 2007. Self-assembling Peptide Scaffolds Promote Enamel Remineralization. *Journal of Dental Research*. **86**(5), pp.426–430.
- Kishore, A., Mehrotra, K.K. and Saimbi, C.S. 2002. Effectiveness of Desensitizing Agents. *Journal of Endodontics*. **28**(1), pp.34–5.
- Klein, R.D., Lewis, J. and Buffleben, M.S. 2012. Logging and turbidity in the coastal watersheds of northern California. *Geomorphology*. **139–140**, pp.136–144.

- Knight, N.N., Lie, T., Clark, S.M. and Adams, D.F. 1993. Hypersensitive Dentin: Testing of Procedures for Mechanical and Chemical Obliteration of Dentinal Tubuli. *Journal of Periodontology*. **64**(5), pp.366–73.
- Kosoric, J., Williams, R.A.D., Hector, M.P. and Anderson, P. 2007. A Synthetic Peptide Based on a Natural Salivary Protein Reduces Demineralisation in Model Systems for Dental Caries and Erosion. *International Journal of Peptide Research and Therapeutics*. **13**(4), pp.497–503.
- Kumta, P.N., Sfeir, C., Lee, D.-H., Olton, D. and Choi, D. 2005. Nanostructured calcium phosphates for biomedical applications: novel synthesis and characterization. *Acta biomaterialia*. **1**(1), pp.65–83.
- Kurt, S., Kırtıloğlu, T., Yılmaz, N.A., Ertaş, E. and Oruçoğlu, H. 2018. Evaluation of the effects of Er:YAG laser, Nd:YAG laser, and two different desensitizers on dentin permeability: in vitro study. *Lasers in Medical Science*., pp.1–8.
- Kuttler, Y. 1959. Classification Of Dentine Into Primary, Secondary, And Tertiary. *Oral Surgery, Oral Medicine, Oral Pathology*. **12**(8), pp.996–1001.
- Kyle, S., Aggeli, A., Ingham, E. and McPherson, M.J. 2009. Production of self-assembling biomaterials for tissue engineering. *Trends in Biotechnology*. **27**(7), pp.423–433.
- Kyle, S., Aggeli, A., Ingham, E. and McPherson, M.J. 2010. Recombinant self-assembling peptides as biomaterials for tissue engineering. *Biomaterials*. **31**(36), pp.9395–9405.
- Kyle, S., Felton, S.H., McPherson, M.J., Aggeli, A. and Ingham, E. 2012. Rational Molecular Design of Complementary Self-Assembling Peptide Hydrogels. *Advanced Healthcare Materials*. **1**(5), pp.640–645.
- De La Macorra, J.C. and Escribano, N.I. 2002. Comparison of Two Methods to Measure Permeability of Dentin. *Journal of Biomedical Materials Research*. **63**(5), pp.531–4.
- Leblond, C.P. and Warshawsky, H. 1979. Dynamics of Enamel Formation in the Rat Incisor Tooth. *Journal of Dental Research*. **58**(B), pp.950–979.

- LeFevre, M.L. and Manly, R.S. 1938. Moisture, Inorganic and Organic Contents of Enamel and Dentin from Carious Teeth, ,. *The Journal of the American Dental Association and The Dental Cosmos*. **25**(2), pp.233–242.
- LeGeros, R.Z. 1981. Apatites in Biological Systems. *Progress In Crystal Growth And Characterization*. **4**(1–2), pp.1–45.
- LeGeros, R.Z. 1994. Biological and Synthetic Apatites *In*: P. Brown and B. Constantz, eds. *Hydroxyapatite and Related Materials*. Boca Raton: CRC Press, pp.3–28.
- Legeros, R.Z., Kijkowska, R., Bautista, C. and Legeros, J.P. 1995. Synergistic Effects of Magnesium and Carbonate on Properties of Biological and Synthetic Apatites. *Connective Tissue Research*. **33**(1–3), pp.203–209.
- LeGeros, R.Z., Trautz, O.R., LeGeros, J.P., Klein, E. and Shirra, P.W. 1967. Apatite Crystallites: Effects of Carbonate on Morphology. *American Association for the Advancement of Science*. **155**(3768), pp.1409–1411.
- Leo, N.R., Liu, J., Archbold, I., Tang, Y. and Zeng, X. 2017. Ionic Strength, Surface Charge, and Packing Density Effects on the Properties of Peptide Self-Assembled Monolayers. *Langmuir*. **33**(8), pp.2050–2058.
- Li, L., Pan, H., Tao, J., Xu, X., Mao, C., Gu, X. and Tang, R. 2008. Repair of enamel by using hydroxyapatite nanoparticles as the building blocks. *Journal of Materials Chemistry*. **18**(34), p.4079.
- Liang, X., Wei, Z., Hu, D. and Ruan, J. 2017. Prevalence of dentin hypersensitivity among the residents of Xi'an city, China. *Acta Odontologica Scandinavica*. **75**(6), pp.387–393.
- Lilley, K.J., Gbureck, U., Knowles, J.C., Farrar, D.F. and Barralet, J.E. 2005. Cement from magnesium substituted hydroxyapatite. *Journal of Materials Science: Materials in Medicine*. **16**(5), pp.455–460.
- Lin, C.P. and Douglas, W.H. 1994. Structure-Property Relations and Crack Resistance at the Bovine Dentin-Enamel Junction. *Journal of Dental Research*. **73**(5), pp.1072–1078.

- Lin, X., de Groot, K., Wang, D., Hu, Q., Wismeijer, D. and Liu, Y. 2015. A Review Paper on Biomimetic Calcium Phosphate Coatings. *The Open Biomedical Engineering Journal*. **9**, pp.56–64.
- Linde, A. and Goldberg, M. 1993. Dentinogenesis. *Critical Reviews in Oral Biology and Medicine*. **4**(5), pp.679–728.
- Liou, S.C., Chen, S.Y., Lee, H.Y. and Bow, J.S. 2004. Structural characterization of nano-sized calcium deficient apatite powders. *Biomaterials*. **25**(2), pp.189–196.
- Liu, D.M., Troczynski, T. and Tseng, W.J. 2001. Water-based sol-gel synthesis of hydroxyapatite: process development. *Biomaterials*. **22**(13), pp.1721–1730.
- Liu, Y.K., Lu, Q.Z., Pei, R., Ji, H.J., Zhou, G.S., Zhao, X.L., Tang, R.K. and Zhang, M. 2009. The effect of extracellular calcium and inorganic phosphate on the growth and osteogenic differentiation of mesenchymal stem cells in vitro: implication for bone tissue engineering. *Biomedical Materials*. **4**(2), p.8.
- Lowenstam, H.A. and Weiner, S. 1989. Biomineralization Processes *In: On Biomineralization*. New York: Oxford University Press, pp.25–49.
- Majji, P. and Murthy, K.R.V. 2016. Clinical Efficacy of Four Interventions in the Reduction of Dentinal Hypersensitivity: A 2-month Study. *Indian Journal of Dental Research*. **27**(5), pp.477–482.
- Mandal, D., Nasrolahi Shirazi, A. and Parang, K. 2014. Self-assembly of peptides to nanostructures. *Organic & Biomolecular Chemistry*. **12**(22), pp.3544–61.
- Mann, S. 2001a. Chemical Control of Biomineralization *In: R. Compton, S. Davies and J. Evans, eds. Biomineralisation Principles and Concepts in Bioinorganic Materials Chemistry*. New York: Oxford University Press, pp.38–67.

- Mann, S. 2001b. General Principles of Biomineralization *In*: R. Compton, S. Davies and J. Evans, eds. *Biomineralisation Principles and Concepts in Bioinorganic Materials Chemistry*. New York: Oxford University Press, pp.24–37.
- Mantzourani, M. and Sharma, D. 2013. Dentine sensitivity: Past, present and future. *Journal of Dentistry*. **41 Suppl 4**, pp.S3-17.
- Marini, D.M., Hwang, W., Lauffenburger, D.A., Zhang, S. and Kamm, R.D. 2002. Left-Handed Helical Ribbon Intermediates in the Self-Assembly of a β -Sheet Peptide. *Nano Letters*. **2**(4), pp.295–299.
- Marini, M.G., Greggi, S.L.A., Passanezi, E. and Sant'ana, A.C.P. 2004. Gingival Recession: Prevalence, Extension and Severity in Adults. *Journal of Applied Oral Science*. **12**(3), pp.250–255.
- Markowitz, K., Bilotto, G. and Kim, S. 1991. Decreasing Intradental Nerve Activity in the Cat with Potassium and Divalent Cations. *Archives of Oral Biology*. **36**(1), pp.1–7.
- Matsuura, K., Murasato, K. and Kimizuka, N. 2005. Artificial Peptide-Nanospheres Self-Assembled from Three-Way Junctions of β -Sheet-Forming Peptides. *Journal of the American Chemical Society*. **127**(29), pp.10148–10149.
- Maude, S., Miles, D.E., Felton, S.H., Ingram, J., Carrick, L.M., Wilcox, R.K., Ingham, E. and Aggeli, A. 2011. De novo designed positively charged tape-forming peptides: self-assembly and gelation in physiological solutions and their evaluation as 3D matrices for cell growth. *Soft Matter*. **7**(18), p.8085.
- Melcher, M., Facey, S., Henkes, T., Subkkowski, T. and Hauer, B. 2016. Accelerated Nucleation of Hydroxyapatite Using an Engineered Hydrophobin Fusion Protein. *American Chemical Society*. **17**, pp.1716–1726.
- Mikkola, M.L. 2007. Genetic basis of skin appendage development. *Seminars in Cell & Developmental Biology*. **18**(2), pp.225–36.

- Miles, D.E. 2012. *Self-assembling peptide/glycosaminoglycan hydrogels for spinal therapies*. Ph.D. Thesis, The University of Leeds.
- Mitchell, J.C., Musanje, L. and Ferracane, J.L. 2011. Biomimetic dentin desensitizer based on nano-structured bioactive glass. *Dental Materials*. **27**(4), pp.386–393.
- Moreno, E.C., Zahradnik, R.T., Glazman, A. and Hwu, R. 1977. Precipitation of Hydroxyapatite From Dilute-Solutions Upon Seeding. *Calcified Tissue Research*. **24**(1), pp.47–57.
- Motskin, M., Wright, D.M., Muller, K., Kyle, N., Gard, T.G., Porter, A.E. and Skepper, J.N. 2009. Hydroxyapatite nano and microparticles: Correlation of particle properties with cytotoxicity and biostability. *Biomaterials*. **30**(19), pp.3307–3317.
- Müller, K.H., Motskin, M., Philpott, A.J., Routh, A.F., Shanahan, C.M., Duer, M.J. and Skepper, J.N. 2014. The effect of particle agglomeration on the formation of a surface-connected compartment induced by hydroxyapatite nanoparticles in human monocyte-derived macrophages. *Biomaterials*. **35**(3), pp.1074–1088.
- Muller, P. 1994. Glossary of Terms used in Physical Organic Chemistry. *Pure and Applied Chemistry*. **66**(5), pp.1077–1184.
- Murdock, R.C., Braydich-Stolle, L., Schrand, A.M., Schlager, J.J. and Hussain, S.M. 2008. Characterization of Nanomaterial Dispersion in Solution Prior to In Vitro Exposure Using Dynamic Light Scattering Technique. *Toxicological Sciences*. **101**(2), pp.239–253.
- MyScope™ 2014. *What is energy dispersive X-ray spectroscopy?* [Online]. Available from: <http://www.ammrf.org.au/myscope/analysis/eds/>.
- Nagayama, G., Matsumoto, T., Fukushima, K. and Tsuruta, T. 2017. Scale effect of slip boundary condition at solid–liquid interface. *Scientific Reports*. **7**(March), p.43125.

- Najibfard, K., K, R., Chedjieu, I. and Amaechi, B.T. 2011. Remineralization of Early Caries by Nano Hydroxyapatite Dentifrice. *The Journal of Clinical Dentistry*. **5**(January).
- Nakahira, A., Sakamoto, K., Yamaguchi, S., Kaneno, M., Takeda, S. and Okazaki, M. 1999. Novel Synthesis Method of Hydroxyapatite Whiskers by Hydrolysis of β -Tricalcium Phosphate in Mixtures of Water and Organic Solvent. *Journal of the American Ceramic Society*. **32**(8), pp.2029–2032.
- Nanci, A. 2013a. Structure of Oral Tissues *In: Ten Cate's Oral Histology*. St. Louis: Elsevier Mosby, pp.1–14.
- Nanci, A. 2013b. Dentin-Pulp Complex *In: Ten Cate's Oral Histology*. St. Louis: Elsevier Mosby, pp.165–204.
- Nanci, A. 2013c. Development of the Tooth and Its Supporting Tissues *In: Ten Cate's Oral Histology*. St. Louis: Elsevier Mosby, pp.70–94.
- Nanci, A. 2013d. Enamel: Composition, Formation, and Structure *In: Ten Cate's Oral Histology*. St. Louis: Elsevier Mosby, pp.121–164.
- Nanci, A. and Smith, C.E. 1999. Development and Calcification of Enamel *In: E. Bonucci, ed. Calcification in Biological Systems*. Boca Raton: CRC Press, pp.313–343.
- Nawrot, C.F., Campbell, D.J., Schroeder, J.K. and Valkenburg, M. Van 1976. Dental Phosphoprotein-Induced Formation of Hydroxylapatite During *In Vitro* Synthesis of Amorphous Calcium Phosphate. *Biochemistry*. **15**(16), pp.3445–3449.
- O'Toole, S. and Bartlett, D. 2017. The relationship between dentine hypersensitivity, dietary acid intake and erosive tooth wear. *Journal of Dentistry*. **67**(September), pp.84–87.
- Oliveira, M.A.H.D.M., Torres, C.P., Gomes- Silva, J.M., Chinelatti, M.A., Menezes, F.C.H. De, Palma- Dibb, R.G. and Borsatto, M.C. 2010. Microstructure and Mineral Composition of Dental Enamel of Permanent and Deciduous Teeth. *Microscopy Research and Technique*. **73**(5), pp.572–577.

- Olley, R.C., Pilecki, P., Hughes, N., Jeffery, P., Austin, R.S., Moazzez, R. and Bartlett, D. 2012. An in situ study investigating dentine tubule occlusion of dentifrices following acid challenge. *Journal of Dentistry*. **40**(7), pp.585–93.
- Orchardson, R. and Collins, W.J.N. 1987. Thresholds of hypersensitive teeth to 2 forms of controlled stimulation. *Journal of Clinical Periodontology*. **14**(2), pp.68–73.
- Orchardson, R. and Gillam, D.G. 2006. Managing dentin hypersensitivity. *The Journal of the American Dental Association*. **137**(7), pp.990–998.
- Pace, C.N., Trevino, S., Prabhakaran, E. and Scholtz, J.M. 2004. Protein structure, stability and solubility in water and other solvents. *Philosophical Transactions of the Royal Society B: Biological Sciences*. **359**(1448), pp.1225–1235.
- Pashley, D.H. 2013. How can sensitive dentine become hypersensitive and can it be reversed? *Journal of Dentistry*. **41 Suppl 4**, pp.S49-55.
- Pashley, D.H. and Galloway, S.E. 1985. The Effects of Oxalate Treatment on the Smear Layer of Ground Surfaces of Human Dentine. *Archives of Oral Biology*. **30**(10), pp.731–737.
- Pashley, D.H., Matthews, W., Zhang, Y. and Johnson, M. 1996. Fluid Shifts Across Human Dentine In Vitro in Response to Hydrodynamic Stimuli. *Archives of Oral Biology*. **41**(11), pp.1065–1072.
- Pashley, D.H., O'Meara, J.A., Kepler, E.E., Galloway, S.E., Thompson, S.M. and Stewart, F.P. 1984. Dentin permeability. Effects of desensitizing dentifrices in vitro. *Journal of Periodontology*. **55**(9), pp.522–525.
- Patterson, J., Martino, M.M. and Hubbell, J.A. 2010. Biomimetic materials in tissue engineering. *Materials Today*. **13**(1–2), pp.14–22.
- Petrou, I., Heu, R., Stranick, M., Lavender, S., Zaidel, L., Cummins, D., Sullivan, R.J., Hsueh, C. and Gimzewski, J.K. 2009. A Breakthrough Therapy for Dentin Hypersensitivity: How Dental Products Containing 8% Arginine and Calcium Carbonate Work to Deliver Effective Relief of Sensitive Teeth. *Journal of Clinical Dentistry*. **20**(1), pp.23–31.

- Pispa, J. and Thesleff, I. 2003. Mechanisms of ectodermal organogenesis. *Developmental Biology*. **262**(2), pp.195–205.
- Polhagen, L. and Brännström, M. 1971. The liquid movement in desiccated and rehydrated dentine in vitro. *Acta Odontologica Scandinavica*. **29**(1), pp.95–102.
- Pradeep, A.R. and Sharma, A. 2010. Comparison of Clinical Efficacy of a Dentifrice Containing Calcium a Placebo on Dentinal Hypersensitivity: Containing Potassium Nitrate and to Sodium Phosphosilicate to a Dentifrice A Randomised Clinical Trial. *Journal of Periodontology*. **81**(8), pp.1167–73.
- Priezjev, N. V., Darhuber, A.A. and Troian, S.M. 2005. Slip behavior in liquid films on surfaces of patterned wettability: Comparison between continuum and molecular dynamics simulations. *Physical Review E - Statistical, Nonlinear, and Soft Matter Physics*. **71**(4), pp.1–11.
- Qin, C., Xu, J. and Zhang, Y. 2006. Spectroscopic investigation of the function of aqueous 2-hydroxyethylmethacrylate/glutaraldehyde solution as a dentin desensitizer. *European Journal of Oral Sciences*. **114**(4), pp.354–359.
- Reeder, O.W., Walton, R.E., Livingston, M.J. and Pashley, D.H. 1978. Dentin Permeability: Determinants of Hydraulic Conductance. *Journal of Dental Research*. **57**(2), pp.187–193.
- Rees, J. 2000. The prevalence of dentine hypersensitivity in general dental practice in the UK. *Journal of Clinical Periodontology*. **27**(Addy 1999), pp.860–865.
- Rees, J. and Addy, M. 2002. A cross-sectional study of dentine hypersensitivity. *Journal of Clinical Periodontology*. **29**, pp.997–1003.
- Remya, N.S., Syama, S., Gayathri, V., Varma, H.K. and Mohanan, P. V. 2014. An in vitro study on the interaction of hydroxyapatite nanoparticles and bone marrow mesenchymal stem cells for assessing the toxicological behaviour. *Colloids and Surfaces B: Biointerfaces*. **117**, pp.389–397.

- Riman, R.E., Suchanek, W.L., Byrappa, K., Chen, C.W., Shuk, P. and Oakes, C.S. 2002. Solution synthesis of hydroxyapatite designer particulates. *Solid State Ionics*. **151**(1–4), pp.393–402.
- Robinson, C., Fuchs, P. and Weatherell, J.A. 1981. The Appearance of Developing Rat Incisor Enamel Using a Freeze Fracturing Technique. *Journal of Crystal Growth*. **53**(1), pp.160–165.
- Robinson, C., Kirkham, J., Brookes, S.J. and Shore, R.C. 1995. Chemistry of mature enamel *In: C. Robinson, J. Kirkham and R. Shore, eds. Chemistry of Mature Enamel in Dental Enamel: Formation to Destruction*. Boca Raton: CRC Press, pp.167–191.
- Robinson, C., Kirkham, J. and Hallsworth, A.S. 1988. Volume Distribution and Concentration of Protein, Mineral and Water in Developing Bovine Enamel. *Archives of Oral Biology*. **33**(3), pp.159–162.
- Robinson, C., Kirkham, J., Stonehouse, N.J. and Shore, R.C. 1989. Control of Crystal Growth During Enamel Maturation. *Connective Tissue Research*. **22**(1–4), pp.765–771.
- Rosner, B. 2011. *Fundamentals of Biostatistics* 7th ed. (M. Taylor, ed.). USA: Brooks/Cole Cengage Learning.
- Ruch, J. V., Lesot, H. and Begue-Kirn, C. 1995. Odontoblast differentiation. *International Journal of Developmental Biology*. **39**(1), pp.51–68.
- Sadat-Shojai, M., Atai, M., Nodehi, A. and Khanlar, L.N. 2010. Hydroxyapatite nanorods as novel fillers for improving the properties of dental adhesives: Synthesis and application. *Dental materials*. **26**(5), pp.471–82.
- Sadat-Shojai, M., Khorasani, M.-T., Dinpanah-Khoshdargi, E. and Jamshidi, A. 2013. Synthesis methods for nanosized hydroxyapatite with diverse structures. *Acta biomaterialia*. **9**(8), pp.7591–621.
- Sauro, S., Gandolfi, M.G., Prati, C. and Mongiorgi, R. 2006. Oxalate-containing phytocomplexes as dentine desensitisers: An in vitro study. *Archives of Oral Biology*. **51**(8), pp.655–664.

- Sauro, S., Watson, T.F. and Thompson, I. 2010. Dentine desensitization induced by prophylactic and air-polishing procedures: an in vitro dentine permeability and confocal microscopy study. *Journal of Dentistry*. **38**(5), pp.411–22.
- Sayed, J. 2013. *Self-Assembling Peptide (SAP) Biomimetic Scaffolds and Hydroxyapatite Nanoparticles for Skeletal and Dental Tissue Repair*. Ph.D. Thesis, University of Leeds.
- Scardi, P., Leoni, M. and Beyerlein, K.R. 2011. On the modelling of the powder pattern from a nanocrystalline material. *Zeitschrift fur Kristallographie*. **226**(12), pp.924–933.
- Schlee, M., Rathe, F., Bommer, C., Broseler, F. and Kind, L. 2017. Self-Assembling peptide matrix for treatment of dentin hypersensitivity: A randomized controlled clinical trial. *Journal of Periodontology*. (December 2017), pp.653–660.
- Schmidlin, P.R. and Sahrman, P. 2013. Current management of dentin hypersensitivity. *Clinical Oral Investigations*. **17**(SUPPL.1), pp.55–59.
- Shaw, D.J. 1991. *Introduction to Colloid and Surface Chemistry* 4th ed. Oxford: Butterworth-Heinemann.
- Shi, X., Zhou, K. and Wang, C. 2017. Interaction of hydroxyapatite nanoparticles with endothelial cells : internalization and inhibition of angiogenesis in vitro through the PI3K / Akt pathway. *International journal of nanomedicine*. **12**, pp.5781–5795.
- Shi, Z., Huang, X., Cai, Y., Tang, R. and Yang, D. 2009. Size effect of hydroxyapatite nanoparticles on proliferation and apoptosis of osteoblast-like cells. *Acta Biomaterialia*. **5**(1), pp.338–345.
- Shih, W.J., Chen, Y.F., Wang, M.C. and Hon, M.H. 2004. Crystal growth and morphology of the nano-sized hydroxyapatite powders synthesized from CaHPO₄·2H₂O and CaCO₃ by hydrolysis method. *Journal of Crystal Growth*. **270**(1–2), pp.211–218.

- Simmer, J.P. and Fincham, A.G. 1995. Molecular Mechanism of Dental Enamel Formation. *Critical Reviews in Oral Biology and Medicine*. **6**(2), pp.84–108.
- Sloan, A.J. and Smith, A.J. 2007. Stem cells and the dental pulp: Potential roles in dentine regeneration and repair. *Oral Diseases*. **13**(2), pp.151–157.
- Smith, A.J., Cassidy, N., Perry, H., Begue-Kirn, C., Ruch, J. V. and Lesot, H. 1995. Reactionary dentinogenesis. *International Journal of Developmental Biology*. **39**(1), pp.273–280.
- Smith, D.K. 1994. Calcium Phosphate Apatites In Nature. *In*: P. Brown and B. Constantz, eds. *Hydroxyapatite and Related Materials* [Online]. London: CRC Press, pp.29–44. Available from: http://books.google.co.uk/books?id=4Gwq_w9x_x8C&lpg=PP1&pg=PP1#v=onepage&q&f=false.
- Smith Jr., H.G. and Bauer, P.J. 1979. Light-Induced Permeability Changes in Sonicated Bovine Disks: Arsenazo III and Flow System Measurements. *Biochemistry*. **18**(23), pp.5067–5073.
- Solheim, T. 1992. Amount of secondary dentin as an indicator of age. *European Journal of Oral Sciences*. **100**(4), pp.193–199.
- Splieth, C.H. and Tachou, A. 2013. Epidemiology of dentin hypersensitivity. *Clinical Oral Investigations*. **17 Suppl 1**, pp.S3-8.
- Stanley, H.R., White, C.L. and McCray, L. 1966. Rate of Tertiary (Reparative) Dentine Formation in Human Tooth. *Oral Surgery, Oral Medicine, Oral Pathology, and Oral Radiology*. **21**(2), pp.180–189.
- Suchanek, W.L. and Riman, R.E. 2006. Hydrothermal Synthesis of Advanced Ceramic Powders. *Advances in Science and Technology*. **45**, pp.184–193.
- Sudarsanan, K. and Young, R.A. 1969. Significant precision in crystal structural details. Holly Springs hydroxyapatite. *Acta Crystallographica Section B Structural Crystallography and Crystal Chemistry*. **B25**(8), pp.1534–1543.

- Sun, J., Chen, C., Pan, H., Chen, Y., Mao, C., Wang, W., Tang, R.-K. and Gu, X. 2014. Biomimetic promotion of dentin remineralization using L-glutamic acid: inspiration from biomineralization proteins. *Journal of Materials Chemistry B*. **2**(28), p.4544.
- Tao, J., Pan, H., Zeng, Y., Xu, X. and Tang, R. 2007. Roles of Amorphous Calcium Phosphate and Biological Additives in the Assembly of Hydroxyapatite Nanoparticles. *The Journal of Physical Chemistry. B*. **111**(47), pp.13410–13418.
- Tarasevich, B.J., Howard, C.J., Larson, J.L., Snead, M.L., Simmer, J.P., Paine, M.L. and Shaw, W.J. 2007. The nucleation and growth of calcium phosphate by amelogenin. *Journal of Crystal Growth*. **304**(2), pp.407–415.
- Termine, J.D., Belcourt, A.B., Christner, P.J., Conn, K.M. and Nylen, M.U. 1980. Properties of Dissociatively Extracted Fetal Tooth Matrix Proteins I. PRINCIPAL MOLECULAR SPECIES IN DEVELOPING BOVINE ENAMEL. *Journal of Biological Chemistry*. **255**(20), pp.9760–9768.
- Thanatvarakorn, O., Nakashima, S., Sadr, A., Prasansuttiorn, T., Ikeda, M. and Tagami, J. 2013. In vitro evaluation of dentinal hydraulic conductance and tubule sealing by a novel calcium-phosphate desensitizer. *Journal of Biomedical Materials Research - Part B Applied Biomaterials*. **101 B**(2), pp.303–309.
- Thomson, B.M., Hardaker, L., Davies, R.P.W., Dennis, C., Bronowska, A., Aggeli, A., Kirkham, J. and Lysek, D.A. 2014. 61st ORCA Congress - A Second Generation Biocompatible, Self-Assembling Peptide with Potential to Promote Enamel Remineralisation *In: Caries Research* [Online]. Greifswald, Germany, Germany, pp.384–450. Available from: <https://www.karger.com/Article/FullText/360836>.
- Trauger, J.W., Kohli, R.M., Mootz, H.D., Marahiel, M.A. and Walsh, C.T. 2000. Peptide cyclization catalysed by the thioesterase domain of tyrocidine synthetase. *Nature*. **407**(6801), pp.215–218.

- Tretheway, D.C. and Meinhart, C.D. 2002. Apparent fluid slip at hydrophobic microchannel walls. *Physics of Fluids*. **14**(3), pp.9–12.
- Trowbridge, H.O. and Kim, S. 1994. Pulp development, structure and function *In*: S. Cohen and R. C. Burns, eds. *Pathways of the Pulp*. Orlando: Mosby, pp.296–336.
- Tsomaia, N. 2015. Peptide therapeutics: Targeting the undruggable space. *European Journal of Medicinal Chemistry*. **94**, pp.459–470.
- Tucker, A. and Sharpe, P. 2004. The Cutting-Edge of Mammalian Development; How the Embryo Makes Teeth. *Nature reviews. Genetics*. **5**(7), pp.499–508.
- Tugnait, A. and Clerehugh, V. 2001. Gingival recession - its significance and management. *Journal of Dentistry*. **29**(6), pp.381–394.
- Tye, C.E., Rattray, K.R., Warner, K.J., Gordon, J.A.R., Sodek, J., Hunter, G.K. and Goldberg, H.A. 2003. Delineation of the Hydroxyapatite-nucleating Domains of Bone Sialoprotein. *Journal of Biological Chemistry*. **278**(10), pp.7949–7955.
- Vano, M., Derchi, G., Barone, A., Pinna, R., Usai, P. and Covani, U. 2018. Reducing dentine hypersensitivity with nano-hydroxyapatite toothpaste: a double-blind randomized controlled trial. *Clinical Oral Investigations*. **22**(1), pp.313–320.
- Varoni, E.M., Zuccheri, T., Carletta, A., Palazzo, B., Cochis, A., Colonna, M. and Rimondini, L. 2017. In vitro efficacy of a novel potassium oxalate hydrogel for dentin hypersensitivity. *European Journal of Oral Sciences*. **125**(2), pp.151–159.
- Vetter, T., Iggland, M., Ochsenbein, D.R., Ha, F.S. and Mazzotti, M. 2013. Modeling Nucleation , Growth , and Ostwald Ripening in Crystallization Processes : A Comparison between Population Balance and Kinetic Rate Equation. *Crystal Growth & Design*. **13**(11), pp.4890–4905.
- Vlieghe, P., Lisowski, V., Martinez, J. and Khrestchatisky, M. 2010. Synthetic therapeutic peptides: science and market. *Drug Discovery Today*. **15**(1–2), pp.40–56.

- Wan, C., Yuan, G., Luo, D., Zhang, L., Lin, H., Liu, H., Chen, L., Yang, G., Chen, S. and Chen, Z. 2016. The Dentin Sialoprotein (DSP) Domain Regulates Dental Mesenchymal Cell Differentiation through a Novel Surface Receptor. *Scientific Reports*. **6**(May), pp.1–14.
- Wang, L., Zhou, G., Liu, H., Niu, X., Han, J., Zheng, L. and Fan, Y. 2012. Nano-hydroxyapatite particles induce apoptosis on MC3T3-E1 cells and tissue cells in SD rats. *Nanoscale*. **4**(9), pp.2894–2899.
- Wang, R., Wang, Q., Wang, X., Tian, L., Liu, H., Zhao, M., Peng, C., Cai, Q. and Shi, Y. 2014. Enhancement of nano-hydroxyapatite bonding to dentin through a collagen/calcium dual-affinitive peptide for dentinal tubule occlusion. *Journal of Biomaterials Applications*. **29**(2), pp.268–277.
- Wang, Z., Jiang, T., Sauro, S., Wang, Y., Thompson, I., Watson, T.F., Sa, Y., Xing, W., Shen, Y. and Haapasalo, M. 2011. Dentine remineralization induced by two bioactive glasses developed for air abrasion purposes. *Journal of Dentistry*. **39**(11), pp.746–756.
- Wang, Z., Sa, Y., Sauro, S., Chen, H., Xing, W., Ma, X., Jiang, T. and Wang, Y. 2010. Effect of desensitising toothpastes on dentinal tubule occlusion: a dentine permeability measurement and SEM in vitro study. *Journal of Dentistry*. **38**(5), pp.400–10.
- Wang, Z., Xu, Z., Zhao, W. and Sahai, N. 2015. A potential mechanism for amino acid-controlled crystal growth of hydroxyapatite. *Journal of Materials Chemistry B*. **3**(47), pp.9157–9167.
- West, N.X., Sanz, M., Lussi, A., Bartlett, D., Bouchard, P. and Bourgeois, D. 2013. Prevalence of dentine hypersensitivity and study of associated factors: A European population-based cross-sectional study. *Journal of Dentistry*. **41**(10), pp.841–851.
- Wewers, M.E. and Lowe, N.K. 1990. A Critical-Review of Visual Analog Scales in the Measurement of Clinical Phenomena. *Research In Nursing & Health*. **13**(4), pp.227–236.

- White, S.N., Luo, W., Paine, M.L., Fong, H., Sarikaya, M. and Snead, M.L. 2001. Biological Organization of Hydroxyapatite Crystallites Toughens and Controls into a Fibrous Continuum Anisotropy in Human Enamel. *Journal of Dental Research*. **80**(1), pp.321–326.
- Whitesides, G.M. and Boncheva, M. 2002. Beyond molecules: Self-assembly of mesoscopic and macroscopic components. *Proceedings of the National Academy of Sciences*. **99**(8), pp.4769–4774.
- Wilbur, K.M. 1984. Many Minerals , Several Phyla , and a Few Considerations. *American Zoologist*. **24**(4), pp.839–845.
- Williams, C.G.W., Macpherson, J.V.M., Unwin, P.R.U. and Parkinson, C.P. 2008. Laser Scanning Confocal Microscopy Coupled with Hydraulic Permeability Measurements for Elucidating Fluid Flow across Porous Materials : Application to Human Dentine. *Analytical Sciences*. **24**(April), pp.437–442.
- Wilson, R.M., Elliott, J.C., Dowker, S.E.P. and Rodriguez-Lorenzo, L.M. 2005. Rietveld refinements and spectroscopic studies of the structure of Ca-deficient apatite. *Biomaterials*. **26**(11), pp.1317–1327.
- Worthington, P., Pochan, D.J. and Langhans, S.A. 2015. Peptide hydrogels – versatile matrices for 3D cell culture in cancer medicine. *Frontiers in Oncology*. **5**(April), pp.1–10.
- Xu, H.H.K., Smith, D.T., Jahanmir, S., Romberg, E., Kelly, J.R., Thompson, V.P. and Rekow, E.D. 1998. Indentation Damage and Mechanical Properties of Human Enamel and Dentin. *Journal of Dental Research*. **77**(3), pp.472–480.
- Xu, J.L., Khor, K.A., Sui, J.J., Zhang, J.H. and Chen, W.N. 2009. Protein expression profiles in osteoblasts in response to differentially shaped hydroxyapatite nanoparticles. *Biomaterials*. **30**(29), pp.5385–5391.
- Yilmaz, H.G. and Bayindir, H. 2014. Clinical and scanning electron microscopy evaluation of the Er,Cr:YSGG laser therapy for treating dentine hypersensitivity: short-term, randomised, controlled study. *Journal of Oral Rehabilitation*. **41**(5), pp.392–8.

- Young, R.A. 1974. Implications of Atomic Substitutions and Other Structural Details in Apatites. *Journal of Dental Research*. **53**(2), pp.193–203.
- Yu, C. and Abbott, P. V 2007. An overview of the dental pulp : its functions and responses to injury. *Australian Dental Journal*. **52**(1 Suppl), pp.S4–S16.
- Zakaria, S.M., Hussein, S., Zein, S., Othman, M.R., Yang, F. and Jansen, J.A. 2013. Nanophase Hydroxyapatite as a Biomaterial in Advanced Hard Tissue Engineering : A Review. *Tissue engineering: Part B*. **19**(5), pp.431–441.
- Zhong, Y., Liu, J., Li, X., Yin, W., He, T., Hu, D., Liao, Y., Yao, X. and Wang, Y. 2015. Effect of a novel bioactive glass-ceramic on dentinal tubule occlusion: An in vitro study. *Australian Dental Journal*. **60**(1), pp.96–103.
- Zhou, H. and Lee, J. 2011. Nanoscale hydroxyapatite particles for bone tissue engineering. *Acta Biomaterialia*. **7**(7), pp.2769–2781.
- Zou, R., Wang, Q., Wu, J.J., Wu, J.J., Schmuck, C. and Tian, H. 2015. Peptide self-assembly triggered by metal ions. *Chemical Society Reviews*. **44**(15), pp.5200–5219.